In this work, we investigated very high quality carbon-doped two-dimensional hole gases (2DHGs). The first part deal with high-mobility GaAs/AlGaAs quantum wells (QWs). Optimizing the heterostructure design, the hole mobility was extremely increased. Quantum Hall effect, photoconductivity effect, Rashba spin splitting, fractional quantum Hall effect (revealing interesting anisotropy in the thermally activated transport) and the band structure were investigated. In the second part, we studied InAs/InGaAs/InAlAs QWs with high spin-orbit coupling. A great success was the preparation of a carbon p-type doping in QWs with high indium content. A conductivity type inversion from p- to n-type with changing composition was observed. The heterostructures exhibit weak-antilocalization, hole-hole interaction effect and strong transport anisotropy. The spin splitting can be engineered providing small changes in the structure design. Both topics are of major interest for spintronics research.

Universitätsverlag Regensburg

ISBN 978-3-86845-095-8

gefördert von:

Alumni der physikalischen Fakultät der Universität Regensburg e.V.

Universität Regensburg

Dissertationsreihe Physik - Band 29

Marika Hirmer

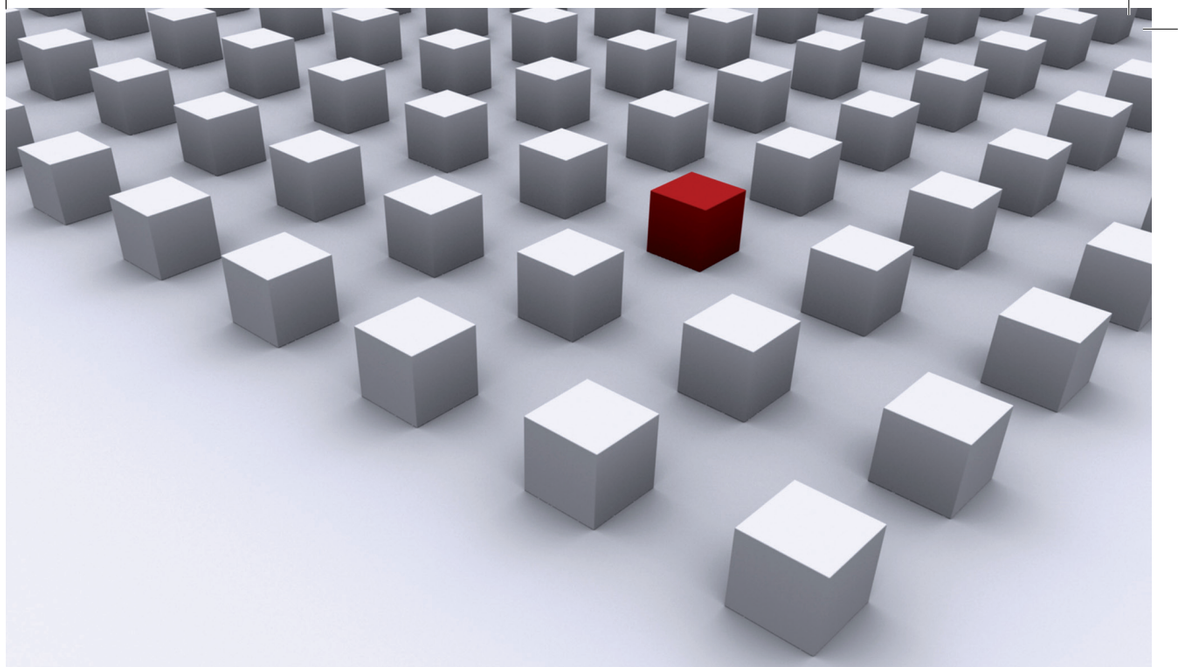

Marika Hirmer

High-mobility two-dimensional hole gases in III-V semiconductor heterostructures: growth and transport properties

Universitätsverlag Regensburg

29

Dissertationsreihe Physik

Marika Hirmer

High-mobility two-dimensional hole gases in III-V semiconductor heterostructures: growth and transport properties

High-mobility two-dimensional hole gases in III-V semiconductor heterostructures: growth and transport properties

Dissertation zur Erlangung des Doktorgrades der Naturwissenschaften (Dr. rer. nat.)
der Fakultät für Physik der Universität Regensburg
vorgelegt von

Marika Hirmer (geb. Kubová)
aus Zlín (Tschechische Republik)
August 2012

Die Arbeit wurde von Prof. Dr. Werner Wegscheider angeleitet.
Das Promotionsgesuch wurde am 13.08.2012 eingereicht.
Das Promotionskolloquium fand am 09.11.2012 statt.

Prüfungsausschuss: Vorsitzender: Prof. Dr. Thomas Niehaus
1. Gutachter: Prof. Dr. Werner Wegscheider
2. Gutachter: Prof. Dr. Dieter Weiss
weiterer Prüfer: Prof. Dr. Franz J. Gießibl

Dissertationsreihe der Fakultät für Physik der Universität Regensburg, Band 29

Herausgegeben vom Präsidium des Alumnivereins der Physikalischen Fakultät:
Klaus Richter, Andreas Schäfer, Werner Wegscheider, Dieter Weiss

Marika Hirmer

High-mobility two-dimensional hole gases in III-V semiconductor heterostructures: growth and transport properties

Universitätsverlag Regensburg

Bibliografische Informationen der Deutschen Bibliothek.
Die Deutsche Bibliothek verzeichnet diese Publikation
in der Deutschen Nationalbibliografie. Detailierte bibliografische Daten
sind im Internet über http://dnb.ddb.de abrufbar.

1. Auflage 2013

Leibnizstraße 13, 93055 Regensburg

Konzeption: Thomas Geiger
Umschlagentwurf: Franz Stadler, Designcooperative Nittenau eG
Layout: Marika Hirmer
Druck: Docupoint, Magdeburg
ISBN: 978-3-86845-095-8

Weitere Informationen zum Verlagsprogramm erhalten Sie unter:
www.univerlag-regensburg.de

High-mobility two-dimensional hole gases in III-V semiconductor heterostructures: growth and transport properties

Dissertation
zur Erlangung des Doktorgrades der Naturwissenschaften
(Dr. rer. nat.)
der Fakultät für Physik
der Universität Regensburg

vorgelegt von
Marika Hirmer (geb. Kubová)
aus Zlín (Tschechische Republik)

August 2012

Promotionsgesuch eingereicht am 13.08.2012
Die Arbeit wurde angeleitet von: Prof. Dr. Werner Wegscheider

Prüfungsausschuß:

Vorsitzender:	Prof. Dr. Thomas Niehaus
Erstgutachter:	Prof. Dr. Werner Wegscheider
Zweitgutachter:	Prof. Dr. Dieter Weiss
Weiterer Prüfer:	Prof. Dr. Franz J. Gießibl

Datum des Promotionskolloquiums: 09.11.2012

Contents

Chapter 1

Introduction

While the second half of the 20th century was marked by a strong improvement of transistor technology, now, at the beginning of the 21th century, this technology reaches soon the limits of miniaturization increasing the packing density (22 nm, structure size of Ivy Bridge processor from Intel, 2012). The development targeting at faster, smaller, more efficient and more powerful devices has led to tiny structures, where quantum effects start dominating the physical properties. In the past decades, new and promising concepts for the future computer have been presented such as: the spin transistor and the quantum computing.

In 1982, R. Feynman [1] introduced the idea of quantum computing, which uses quantum mechanics for performing computations instead of classical physics, providing an enormous speed advantage over the classical computer for certain algorithms. There are quite a few concepts of how to realize the quantum computer. One of the potential candidates is the fractional quantum Hall state $\nu = 5/2$ because it is supposed to show non-Abelian statistics (topological quantum computing developed by Kitaev, Freedman, and Preskill [2, 3, 4, 5, 6]). However, experimental studies of the $\nu = 5/2$ state require a high quality of the sample, especially concerning the carrier mobility. While two-dimensional electron gases (2DEGs) with electron mobilities on the order of $10^7\,\mathrm{cm}^2/\mathrm{Vs}$ have already been achieved, [7], the mobilities of holes in two-dimensional hole gases (2DHGs) are still at least one order of magnitude lower, [8]. This also limits the performance of common transistors. Nevertheless, great progress in the molecular beam epitaxy (MBE) of p-type GaAs/AlGaAs heterostructures was achieved by using a high-purity graphite-filament source for carbon modulation doping. This approach enables to grow 2DHGs of quality comparable with high-mobility 2DEGs, [9], exhibiting well-resolved fractional quantum Hall states, including the $\nu = 5/2$ state, [9, 10]. Recently, great progress has been achieved in the field of spintronics. The concept of the spin transistor proposed by S. Datta and B. Das in 1990, [11] is based on the manipulation of the electron spin instead of the electron charge to process information. The realization is challenging and requires: (a) high spin-orbit coupling as it allows the control of the spin via electric fields, (b) long spin dephasing times, and (c) effective spin injection between ferromagnetic electrodes and the 2D channel. Therefore, a lot of attention focuses on indium-containing narrow-gap semiconductors especially InAlAs/InGaAs/InAs heterostructures, since InAs exhibits a

high spin-orbit coupling, a high electron mobility compared with GaAs and highly transmissive metal-semiconductor interfaces. Indeed, in 2009, Koo *et al.* succeeded in fabricating the first spin-injected field effect transistor in a high-mobility InAs channel, [12].

Compared to electrons, holes offer some advantages for the spintronics applications. Due to the p-like symmetry of the hole wave function, the contact hyperfine interaction with the nuclei is considerably reduced, which leads to long spin coherence times of localized holes, [13, 14]. In a narrow p-doped GaAs/AlGaAs quantum well (QW), spin dephasing times exceeding tens of nanoseconds were reported by Korn *et al.* [13]. For this reason, localized hole spins are also interesting for future quantum computing schemes. In addition, the spin-orbit coupling effects are more important for holes due to their higher effective mass ($m_{eff} = 0.2 - 0.8\, m_0$, m_0 is the free electron mass) compared to electrons ($m_{eff} = 0.067\, m_0$), [15]. Very recently, the first direct Raman-spectroscopy measurements of the Rashba-induced spin splitting of the heavy-hole subband in a GaAs/AlGaAs QW revealed an extremely high energy of the spin splitting of a few meV, which is even comparable with the heavy-hole light-hole subband distance, [16]. Further demonstration of the strong spin-orbit interaction in GaAs/AlGaAs is the weak antilocalization observed by Grbic *et al.*, [17]. Because of the high ratio of Coulomb energy to the Fermi energy, holes are interesting for 2D carrier-carrier interaction physics including the fractional quantum Hall effect, [18, 19], which will also be discussed in this thesis. Owing to the high complexity of the GaAs valence-band structure, the 2DHGs are not well-explored yet. Nonetheless, this topic still covers a lot of interesting physical phenomena.

The presented thesis deals with two main themes: first, the MBE growth and characterization of carbon-doped high-mobility 2DHGs of exceptional quality in GaAs/AlGaAs QWs, and second, nonmagnetic p-type doping in indium-containing heterostructures with high spin-orbit coupling. Both topics are of major interest for spintronics research.

One of the goals of this work was to increase the hole mobility in carbon-doped GaAs/AlGaAs heterostructures. For this purpose, a new structure design with four doping layers (two on both sides of the QW) was applied, promising a reduction of interface roughness scattering and remote impurity scattering limiting the mobility in a widely-used single-sided-doped (ssd) QW. Optimization of the parameters enabled us to double the hole mobility (over the ssd-QW) near the current maximum [8], however in a completely different design. Subsequently, the properties of the highest mobility samples were studied via magnetotransport measurements. In this way, the activated transport of the fractional quantum Hall states was evaluated revealing a remarkable anisotropy. In literature dealing with carbon-doped 2DHGs, some reports concerning the persistent photoconductivity effect can be found, [20, 21]. However, its origin is not well understood, yet, also because carbon is not expected to create DX centers as silicon doping does in 2DEGs, [22, 23]. With regard to the influence of the growth conditions, the hole-density variations induced by illumination at low temperatures could be suppressed.

The second main challenge of this work was to prepare nonmagnetic

p-type doping in InAlAs/InGaAs/InAs heterostructures using carbon as a doping material. Apart from the manganese-modulation doping, which leads to interesting magnetic effects, [24], there have been no reports on hole conductivity in modulation-doped InAs QWs. Using a standard $In_xAl_{1-x}As$ step-graded metamorphic buffer layer, the structures have been grown on GaAs substrates. A conduction-type inversion from p- to n-type was observed as the indium content in the $In_xAl_{1-x}As$, $In_xGa_{1-x}As$ ternary compounds has been increased. Developing a new doping design, it was possible to overcome the natural tendency of carbon to incorporate as a donor in InAs and a good quality 2DHG was prepared in an $In_{0.75}Al_{0.25}As/In_{0.75}Ga_{0.25}As$ QW with an embedded InAs channel. Magnetotransport investigations at mK temperatures show the typical quantum Hall effect and Shubnikov-de Haas oscillations superimposed at intermediate magnetic fields by an extensive negative parabolic magnetoresistance pointing out a strong hole-hole interaction effect. An extremely pronounced weak-antilocalization minimum and a Rashba-induced spin splitting unambiguously prove a strong spin-orbit interaction. All transport parameters include a distinct anisotropy.

The thesis starts with an overview of the physical basics needed for the understanding of the physical effects discussed in the experimental chapters, in Chapter 2. The MBE method of layer growth is introduced in Chapter 3, together with a schematic description of our experimental set-ups and the sample preparation.

Chapter 4 focuses on the carbon-doped high-mobility GaAs/AlGaAs heterostructures. The first part is devoted to the optimization of the growth conditions and structure parameters, which induces low-temperature hole mobility of $2.1 \times 10^6\,cm^2/Vs$ without showing a persistent photoconductivity effect. In the second part, a comparison between a conventional single-sided-doped structure and an improved double-sided-doped structure is given in their magnetotransport parameters and calculated subband dispersion. Both are of excellent quality exhibiting a large number of fractional quantum Hall states enabling to investigate their activated transport. It follows an examination of a hole-hole interaction effect, which becomes noticeable as a negative parabolic magnetoresistance in the ssd-QW.

In Chapter 5 we investigated the MBE growth and magnetotransport properties of InAlAs/InGaAs/InAs heterostructures with a variety of indium contents. At the beginning, we discuss specifics of the carbon incorporation in the $In_xAl_{1-x}As$, $In_xGa_{1-x}As$ ternary compounds, especially the fabrication difficulties of p-type doping for high concentrations x. In this part we could successfully show the preparation of a 2DHG in the whole range of studied indium contents $x = 0.20-0.75$. Their magnetotransport data exhibit: (a) weak-antilocalization effect, from its theoretical fits phase-coherence and spin-orbit scattering times are extracted, (b) large negative parabolic magnetoresistance, from which we determined the hole-hole interaction time, (c) well-resolved Shubnikov-de Haas oscillations, and (d) pronounced transport anisotropy caused by several anisotropic scattering mechanisms discussed here as well. Additionally, multiband $\mathbf{k} \cdot \mathbf{p}$ simulations of the valence-band dispersion are used to explain the surprising experimental findings concerning the spin splitting. Finally, in Chapter 6, we summarize the results achieved in this thesis.

Chapter 2

Theory

In this work, we deal with two-dimensional hole systems of a high purity and mobility. In the theoretical chapter we introduce the general physical fundamentals necessary for understanding these systems and experiments done on them. It summarizes important equations used for the evaluation of characteristic sample parameters such as hole density and mobility, effective mass, scattering times, etc.

The first section presents a short introduction to the basics of the two-dimensional hole gas (2DHG), its characteristic parameters and magnetotransport phenomena such as: quantum Hall effect, Shubnikov-de Haas oscillations and fractional quantum Hall effect. The following sections concentrate on peculiarities of the valence band structure, especially spin splitting in 2DHGs. As a further manifestation of spin-orbit interaction, the weak antilocalization effect will be described. The chapter is concluded by an overview of research highlights done on similar materials and structures, as studied in this work, in recent years.

Detailed discussion to particular effects and their comparison with literature will be given separately in the related experimental sections.

2.1 Two-dimensional hole gas

A two-dimensional hole (electron) gas is a system, where the charge carriers are confined in one direction (typically growth direction) and can move freely in the plane perpendicular to it. The confinement potential, important for development of a two-dimensional charge-carrier system, can be realized on a heterojunction of two semiconductors with different band gaps (GaAs/AlGaAs interface) or in a quantum-well (QW) structure, where the material of lower band gap (GaAs, InAs) is enclosed by the semiconductor of a higher energy gap (AlGaAs, InAlAs). For 2D electrons, which have parabolic band dispersion resulting in a constant effective mass m^*, the two-dimensional density of states is constant and independent on energy:

$$D(E) = \frac{m^*}{\pi\hbar^2} = const \tag{2.1}$$

where $\hbar = h/2\pi$ is the reduced Planck constant. In 2D hole systems, where the nonparabolic effects are important, the effective mass is a function of E, [15], and

Eq. 2.1 is valid only in first approximation for small values of the in-plane wave vector $\mathbf{k}_{||}$.

At low temperatures, only the states near the Fermi energy contribute to the transport. Assuming parabolic bands[1] the Fermi energy is given as $E_F = \pi\hbar^2 p/m^*$, p is the carrier density, and for the Fermi wave vector follows:

$$k_F = \sqrt{2\pi p}. \tag{2.2}$$

To get knowledge about the quality and properties of the 2DHG, magnetotransport measurements at low temperatures are performed. The most interesting characteristics are hole density p and hole mobility μ. Using the Drude theory, both can be easily extracted from the magnetotransport data. In the Drude model, the carrier mobility is defined as a proportionality constant between the electric field $\vec{E}$ applied along the x-axis and the drift velocity $\vec{v}_D$:

$$\mu \equiv \frac{|\vec{v}_D|}{|\vec{E}|} = \frac{e\tau_t}{m^*}, \tag{2.3}$$

τ_t is the transport scattering time. In this section, three important effects arising in 2D carrier systems will be described: Hall effect, quantum Hall effect (QHE) (and related Shubnikov-de Haas oscillations) and fractional quantum Hall effect (FQHE).

Quantum Hall effect

In magnetic fields applied perpendicular to the 2DHG-plane, the components of the resistivity tensor can be expressed as:

$$\rho_{xx} = \rho_{yy} = \frac{1}{ep\mu} \tag{2.4}$$

$$\rho_{xy} = -\rho_{yx} = -\frac{B}{pe} \tag{2.5}$$

The Hall resistance ρ_{xy} increases linearly with the magnetic field (Hall effect) and the slope determines the carrier density p. The carrier mobility μ can be obtained from the sheet resistivity, which equals the longitudinal resistance ρ_{xx} at $B = 0\,\mathrm{T}$ multiplied by the geometry factor W/L (width/length), see also Section 3.2. The Drude model describes well the properties of the 2DHG only at weak magnetic field, where $\omega_c\tau_q < 1$, ($\omega_c = eB/m^*$ is the cyclotron frequency and τ_q is the quantum scattering time) and if no quantum effects take place.

At higher magnetic fields, the constant density of states is replaced by a sequence of δ-peaks, the Landau levels (LL), separated by $\hbar\omega_c$ in energy. In the experiment, due to the presence of scattering the Landau levels are broadened into bands of width $\Gamma = \hbar/2\tau_q$ (τ_q is the quantum scattering time). The degeneracy of the LLs is B-dependent and the number of states in each LL per unit area is $p_L = eBg_s/h$. At high magnetic fields, the LLs are spin split due to the Zeeman

[1] for holes satisfied at small values of the in-plane wave vector $\mathbf{k}_{||}$

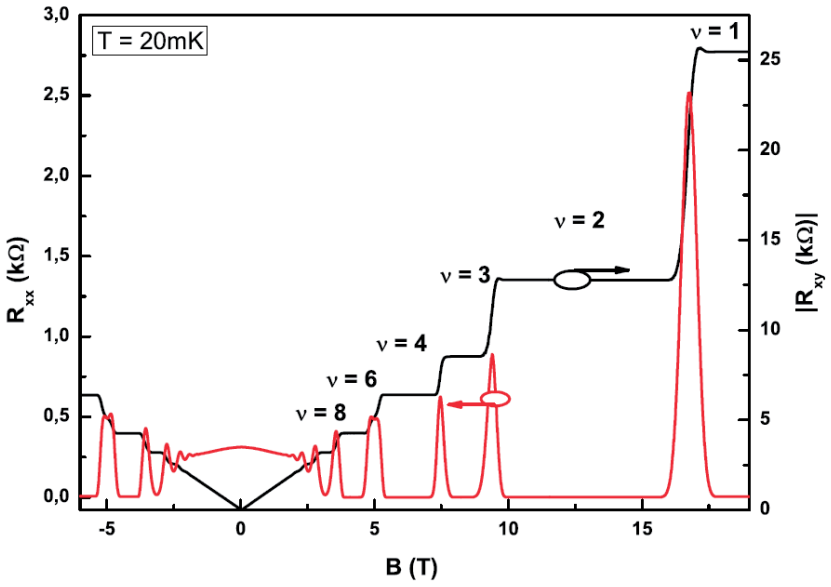

Figure 2.1: *[25], Magnetotransport of a Si-doped n-type $In_{0.75}Al_{0.25}As/In_{0.75}Ga_{0.25}As/InAs$ QW. Hall curve (black) exhibits plateaus at integer filling factors. Longitudinal magnetoresistance (red curve) shows Shubnikov-de Haas oscillations.*

energy $g^*\mu_B B$, (g^* is the effective g factor, μ_B is the Bohr magneton), and the degree of degeneracy is $g_s = 1$. If the two spins are counted as separated levels, the number of LLs below the Fermi level is given by the filling factor:

$$\nu = \frac{p}{p_L} = \frac{ph}{g_s eB} \tag{2.6}$$

In this definition, two spins are counted as separated levels.

As a consequence of formation of LLs, two effects in magnetotransport measurements are observed: the quantum Hall effect in the ρ_{xy} curve and the Shubnikov-de Haas oscillations in the ρ_{xx}. The Hall resistance ρ_{xy} displays plateaus, which develop exactly at the resistance values:

$$\rho_{xy} = \frac{1}{\nu}\frac{h}{e^2} \tag{2.7}$$

independent on material parameters, ν is integer, see Fig. 2.1. $R_H = h/e^2 = 25812.807\,\Omega$ is the von-Klitzing constant. The quantum Hall effect can be explained by means of the Landau-Büttiger formalism as a formation of edge channels, which arise due to the finite size of the sample. When the Fermi energy is located between two LLs, the current is carried only via edge states and back scattering is reduced. As a consequence ρ_{xy} exhibits a quantized value and ρ_{xx} a minimum. An overview about the QHE is given in [26, 27].

Shubnikov-de Haas oscillations

In the classical theory the longitudinal resistance is independent on the magnetic field, see Eq. 2.5. At high magnetic fields and low temperatures, oscillations in the longitudinal resistance arise as a consequence of the oscillations of the density of states at the Fermi edge. The so-called Shubnikov-de Haas (SdH) oscillations are $1/B$-periodic:

$$\Delta\left(\frac{1}{B}\right) = \frac{e}{ph}, \tag{2.8}$$

and this relation can be used for calculating the carrier density p. The SdH minima correspond to the plateaus in ρ_{xy} and in an ideal case they show zero resistance.

The envelope function of the SdH oscillations can be described by the Ando formula [28, 29, 30, 31, 32, 33]:

$$\frac{1}{2}\frac{\Delta\rho_{xx}}{\rho_0} = 4\frac{\chi}{\sinh(\chi)}\exp\left(\frac{-\pi}{\omega_c\tau_q}\right)\cos[\pi(2\nu-1)], \tag{2.9}$$

where $\chi = 2\pi^2 k_B T/\hbar\omega_c$, ω_c is the cyclotron frequency and ρ_0 is the zero-field resistance. Thermal damping of the amplitude is given by the Dingle factor $\chi/\sinh(\chi)$, which depends on the effective mass m*. At the ρ_{xx} extrema the cosine term is ± 1, [34]. According to Elhamri *et al.* [35], Eq. 2.9 can be simplified to:

$$\ln\left(\frac{A}{T}\right) \approx C_1 - \frac{2\pi^2 k_B m^*}{e\hbar B}T, \tag{2.10}$$

where A is the amplitude of SdH oscillations at a fixed magnetic field and C_1 is the temperature-independent term. From the slope of the plot $\ln(A/T)$ versus T, the effective mass can be calculated. This method was used for the estimation of the effective mass of 2D holes in AlGaAs/GaAs and InAlAs/InGaAs/InAs heterostructures in Sections 4.4.2 and 5.4.

The exponential term in Eq. 2.9 depends on the quantum scattering time τ_q, which determines the collision broadening of the Landau levels[2]. Using a "Dingle plot" τ_q can be evaluated from the amplitude of the oscillation at a fixed temperature, [32, 35, 36, 37, 30]:

$$\ln\left(\frac{1}{4}\frac{\Delta\rho_{xx}}{\rho_0}\frac{\sinh(\chi)}{\chi}\right) = C_2 - \left(\frac{\pi m^*}{e\tau_q}\right)\frac{1}{B}, \tag{2.11}$$

where C_2 represents the non-oscillating part. Plotting the term on the left hand side of the Eq. 2.11 versus $1/B$ with a knowledge of the effective mass, the quantum scattering time can be estimated. This procedure was applied in Sections 4.4.2 and 5.4.

[2]The $\Gamma = \hbar/2\tau_q$ is the full width at half maximum (FWHM) of a Landau level.

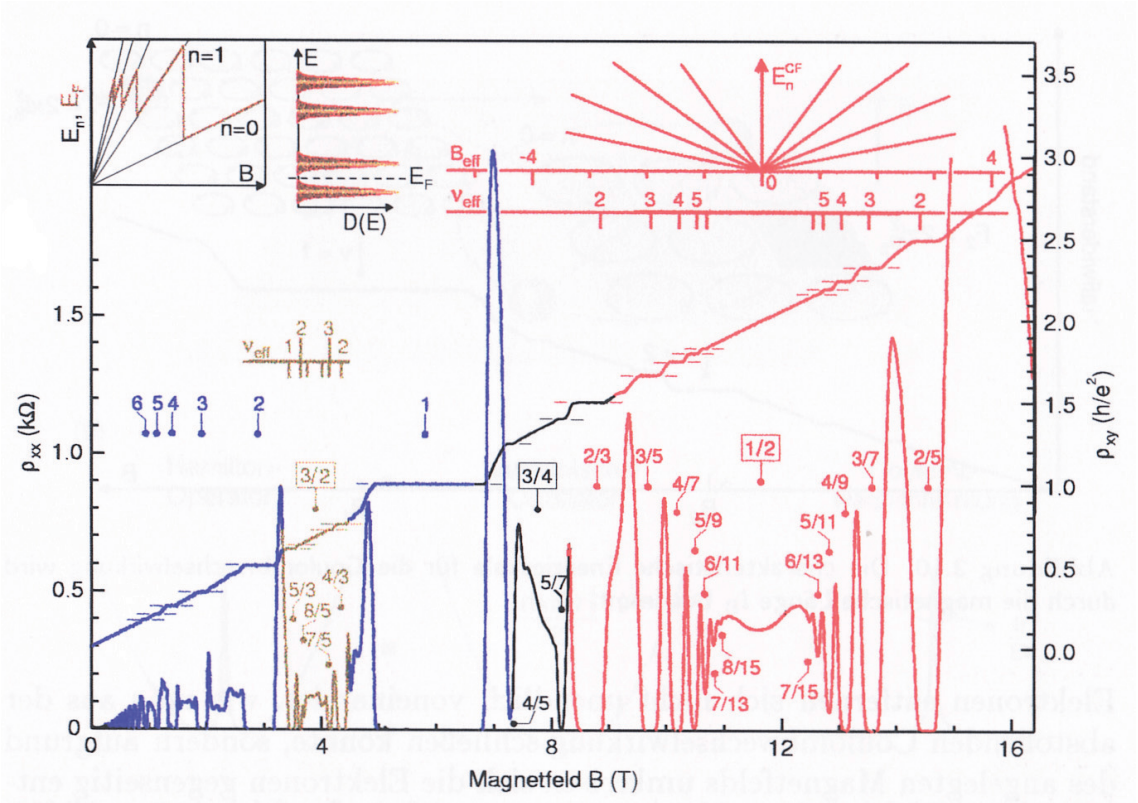

Figure 2.2: *[38] The integer and fractional QHE states. The integer QHE is marked with a blue color. Around the half fillings $\nu = 1/2$ and $\nu = 3/2$ a series of FQH states are grouped (red and brown colors). The similarity to the integer QHE is demonstrated by the effective magnetic field B_{eff} and the CF filling factor ν_{eff} in the upper part of the picture.*

Fractional quantum Hall effect

Fig. 2.2 shows plateaus in ρ_{xy} and minima in ρ_{xx} not only at the integer values of the filling factor ν, but also at $\nu = r/s$, where $r = 1, 2, 3, ...$, $s = 1, 3, 5, ...$ This is due to the fractional quantum Hall effect (FQHE) discovered by Tsui, Störmer, Gossard, [39]. It can be observed in samples with a very high mobility and at very low temperatures. For simplicity, we will discuss the FQHE for electrons.

In contrast to the integer QHE, the FQHE is a many-body effect and originates from the strong carrier-carrier Coulomb interaction. The relevant energy scale is the Coulomb repulsion $e^2/(4\pi\epsilon\epsilon_0 l_B) \propto \sqrt{B}$ (with ϵ the dielectric constant and $l_B = \sqrt{\hbar/eB}$ the magnetic length). The first description was done by Laughlin via a many-body wave function, [40]. Later, Jain [41] introduced a new theoretical model based on new quasiparticles, called composite fermions (CFs). They are composed of $2m$ magnetic flux quanta attached to each electron. For example, at $\nu = 1/2$ or $\nu = 1/4$ two or four magnetic flux quanta are attached to create a CF. In this way, the many-body system of strong interacting particles is translated into a simpler system of almost noninteracting quasiparticles. In other words, the FQHE resulting from complicated many-body interactions in the electron system could be understood as

the integer QHE but for non-interacting CFs. The CFs experience a reduced effective magnetic field:

$$B_{\mathit{eff}} = B - 2m\phi_0 n_e = B - B_{\nu=\frac{1}{2m}}, \tag{2.12}$$

$\phi_0 = h/e$ is the magnetic flux quantum, n_e is the average electron density. Since for the filling factor $\nu = 3/2$ the composite fermion density n_f differs from the electron density n_e, $n_f = n_e/3$, Eq. 2.12 has a form $B_{\mathit{eff}} = 3B - 2\phi_0 n_e$, [42]. The effective magnetic field B_{eff} vanishes exactly for filling factors with even denominator ($\nu = 1/2, 1/4, ...$ and also $\nu = 3/2, 3/4, ...$). At these states CFs fill up a Fermi sea with $k_F^{CF} = \sqrt{4\pi n_e}$. At $B_{\mathit{eff}} \neq 0$ Landau levels of the CFs build up and their filling factor is given as:

$$\nu_{\mathit{eff}} = \frac{n_e \phi_0}{B_{\mathit{eff}}} = \pm 1, 2, 3, ... \tag{2.13}$$

They are separated in energy by a cyclotron gap $\hbar\omega_c^{\mathit{eff}} = \hbar e B_{\mathit{eff}}/m_{\mathit{eff}}^{CF}$. Negative filling factors correspond to a negative effective magnetic field. The CF effective mass m_{eff}^{CF} has its origin in the electron-electron interaction[3] and is magnetic field-dependent as $m_{\mathit{eff}}^{CF} \propto \sqrt{B}$. For the relation between the electron filling factor ν and the CF filling factor ν_{eff} it follows:

$$\nu = \frac{|\nu_{\mathit{eff}}|}{2m\,\nu_{\mathit{eff}} \pm 1} \tag{2.14}$$

Around the $\nu = 1/(2m)$ filling factors a series of fractional quantum Hall (FQH) states develop, which consist of particle-hole symmetric counterparts arising symmetrically around the central half filling. This is demonstrated by series around $\nu = 3/2$ and $\nu = 1/2$ in Fig. 2.2. Further apparent is the similarity of the FQH states belonging to one series around $B_{\mathit{eff}} = 0\,\mathrm{T}$ to the SdH oscillations of electrons around $B = 0\,\mathrm{T}$. This fact was used by Manoharan *et al.* to calculate the CFs effective mass[4] in a 2DHG-sample in the vicinity of the $\nu = 1/2$. They found that the m_{eff}^{CF} is strongly dependent on the B_{eff} and divergent if one approaches $\nu = 1/2$, [34].

Attaching an odd number of flux quanta to the electron, the quantum statistics changes and composite bosons are formed. The most prominent representative is $\nu = 1/3$, which can be well described by the Laughlin many-body wavefunction, as well as other $\nu = 1/5, 1/7, ...$ An overview of the FQHE can be found in [42, 38, 44].

Recently, even denominator states were reported in higher Landau levels, $\nu = 5/2, 7/2, 9/2, 11/2, 13/2$ in both 2DEGs and 2DHGs as well. In contrast to the $\nu = 1/(2m)$ in the lowest LL, the $\nu = 5/2$ was reported to exhibit a plateau in the Hall resistance and activated transport in spite of its even denominator classification. It is believed that it arises from a p-wave pairing of the CFs described by either the Pfaffian or the anti-Pfaffian wave function, [45]. Some of these half fillings in higher LLs exhibit a pronounced anisotropy on crystallographic directions ascribed

[3] In contrast, the electron effective mass is a consequence of the kinetic energy.

[4] A similar experiment was done simultaneously by Du *et al.* on a 2DEG-sample, [43].

to formation of a striped phase, [46]. This behavior was investigated on 2DHGs by Manfra *et al.* [19], and on 2DEGs by Du *et al.* [47] and by Lilly *et al.* [48].

In Section 4.4.3 we will describe some remarkable features, which we observed on FQH states $2 > \nu > 1$. At this point, it should be mentioned that these FQH states possess another interesting property; they undergo a transition from a spin-unpolarized to a spin-polarized state in tilted magnetic fields [49, 50, 51, 52]. This is accompanied with successive emergence and destruction of the $\nu = 4/3$ and $\nu = 7/5$ ($\nu = 8/5$ and $\nu = 11/7$) states and is also manifested in sharp changes of the activation energy (see the definition below) with the total magnetic field. Experiments done in Refs. [50, 51] on 2DEGs, and in Refs. [49, 52] on 2DHGs, showed that the transition can be driven by tilting the sample relative to the external magnetic field, varying the carrier density or changing the symmetry of the confinement potential.

One of the experimental signatures of a FQH state is the thermally activated transport. This is associated with a finite energy gap, which must be present in the density of states in order to be able to observe the integer and the fractional QHE. The activation gap equals the energy necessary to create a quasiparticle-quasihole pair, which moves then independently across the system and contributes to the transport. It can be calculated from the temperature dependence of the minimum in the longitudinal magnetoresistance corresponding to the FQH state using an Arrhenius plot:

$$\rho_{xx}(T) = \rho_0 \exp(-\frac{\Delta}{2T}). \tag{2.15}$$

A derivation of this equation can be found in Ref. [45]. However, the measured activation gap is lower than the ideal gap Δ_{id}, because of disorder broadening of the CF LLs. Very recently, d'Ambrumenil, Halperin and Morf presented a new model of dissipative transport in the FQH regime, [53]. They found out that the gap extracted from the Arrhenius plot is reduced by tunneling effects through saddle points in the effective potential for excitations created by ionized impurities, [53].

2.2 Spin-orbit coupling

Spin-orbit coupling is the interaction of the electron spin with its orbital motion. It is a consequence of relativistic effects, where the electron moves in an electric field $\vec{E} = (-1/q)(\nabla V(\vec{r}))$. By a relativistic transformation of fields $\vec{B} = (1/c^2)\vec{v} \times \vec{E}$, the electric field of the core is transformed into the magnetic field, which couples with the electron spin. This coupling leads to a correction term to the Hamilton operator:

$$H_{SO} = -\frac{\hbar}{4m_0^2c^2}\vec{\sigma} \cdot (\vec{p} \times \nabla V(\vec{r})) \tag{2.16}$$

where $\hbar$ is Planck constant, m_0 is the free electron mass[5], c is the velocity of light in vacuum, $\vec{p}$ is the momentum operator and $\vec{\sigma} = (\sigma_x, \sigma_y, \sigma_z)$ is the vector of the Pauli

[5] $m_0 = 9.1 \cdot 10^{-31}$ kg

spin matrices, and $V(\vec{r})$ is the Coulomb potential of the atomic core. In semiconductors $V(\vec{r})$ includes the potential of ions, defects and deviations due to phonons, etc., [54].

2.3 GaAs valence-band structure

GaAs is a III-V semiconductor, which crystalizes in the zinc-blende crystal structure. It is a direct semiconductor with an energy gap of 1.42 eV at room temperature. Its conduction band has s-like symmetry (the orbital angular momentum $l = 0$). The valence band has p-like symmetry ($l = 1$). Spin-orbit interaction leads to the splitting of the uppermost valence band into subbands with a total angular momentum $j = 3/2$ and $j = 1/2$. The $j = 1/2$ is the split-off (SO) band and is twofold degenerated. The $j = 3/2$ states are fourfold degenerated at the Γ point. A qualitative sketch of the GaAs valence band structure near the Γ point is depicted in Fig. 2.3(a). Fig. 2.3(b) shows the calculated dispersion of the GaAs bulk crystal.

In contrast to the bulk, in 2DHGs a size quantization along the growth axis z takes place. As a consequence, the fourfold degeneracy of the $j = 3/2$ states (Γ_8 valence band) is lifted. There are two subbands separated in energy at the in-plane wave vector $k_{||} = 0$: the heavy-hole (HH) subband with a z component of the angular momentum $m = \pm 3/2$ and the light-hole (LH) subband with $m = \pm 1/2$. Both are twofold degenerate concerning the spin. For comparison, the lowest conduction band Γ_6 has $j = 1/2$ and is twofold degenerate concerning the spin. The HH (LH) subbands refer to the higher (lower) effective mass of holes for the motion along the growth axis. For the in-plane motion their character is reversed. The subband structure of a 2DHG consists of individual HH and LH subbands. The HH-LH splitting causes a mixing of the HH and LH states at higher values of the in-plane wave vector $\mathbf{k}_{||}$ and the HH-LH anticrossing takes place, see scheme in Fig. 2.3(c). In Fig. 2.3(d) a subband dispersion calculated for 2D holes in a 15 nm wide GaAs quantum well is shown. More information about the theoretical calculations of the valence-band dispersion can be found in Ref. [15].

2.4 Spin splitting in 2D hole systems

In III-V semiconductor heterostructures, the spin splitting of the spin degenerate states was observed in both: conduction [56] and valence band [16]. It arises as a consequence of the bulk inversion asymmetry (BIA) of the zinc-blende crystal structure and the structure inversion asymmetry (SIA) even at $B = 0$ T. As a third origin the microscopic asymmetry of the interfaces should be remarked, [57]. The BIA spin splitting is described by the Dresselhaus term and is a fixed material property. Its relevance depends on the QW width and the Fermi wave vector, [15]. Even though BIA spin splitting is an intrinsic property of GaAs, in an asymmetric structure the SIA-induced spin splitting is more dominant, [58, 59]. It originates from internal or external electric fields, thus it can be tuned. The SIA spin-orbit interaction causes an in-plane effective magnetic field, which tends to orient the

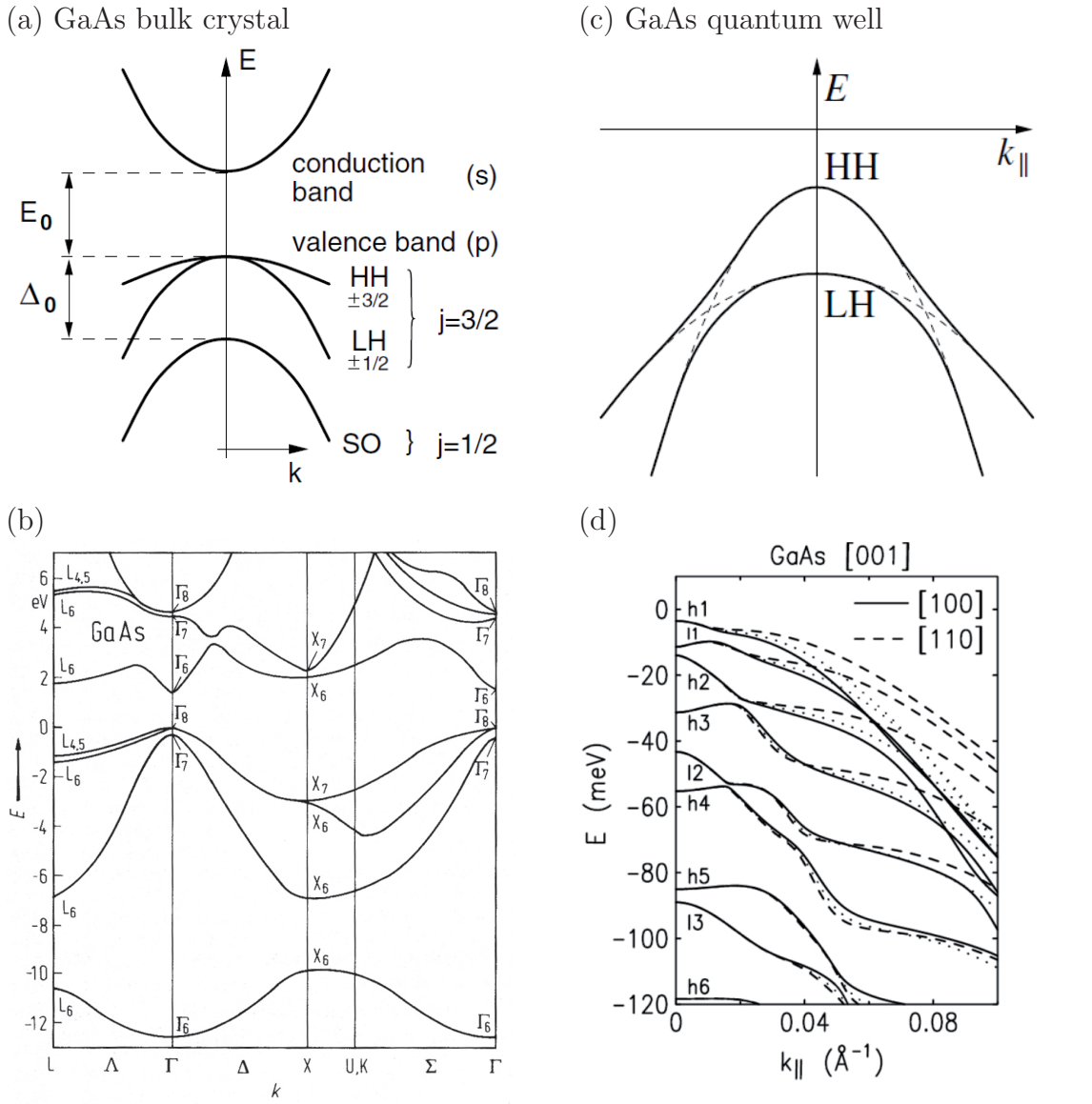

Figure 2.3: *(a) [15], qualitative sketch of GaAs band structure near the* Γ *point. (b) [55], calculated band structure of bulk GaAs. (c) [15], scheme of the HH-LH anticrossing in a p-type GaAs QW. The HH-LH splitting appears as a consequence of the quantum confinement in a QW, see text. (d) [15], calculated subband structure of a 2DHG confined in a 15 nm wide GaAs QW.*

quantization axes in plane. On the contrary, the quantization axis of the angular momentum is perpendicular to the 2DHG-plane. Hence, the spin splitting of the HH states competes with the HH-LH splitting and as a consequence it is a higher order effect. The dominant component to the spin splitting of the HH states is then cubic in $k_{||}$, but for the LH states with $m = \pm 1/2$ the spin splitting is linear in $k_{||}$ (satisfied for small $k_{||}$), see Fig. 2.4(a). In contrast to electrons, the energy of the spin splitting is very high for holes. Even more, it is comparable to the subband

separation, [16].

Most important for the SIA Hamiltonian is the Rashba term. The effective Rashba Hamiltonian for the HH states with the electric field oriented perpendicular to the 2DHG-plane (z direction) is given as, [60]:

$$H_{SO}^{h} = \beta_R^h \mathcal{E}_z i(k_+^3\sigma_- - k_-^3\sigma_+), \tag{2.17}$$

with $\sigma_\pm = 1/2(\sigma_x \pm i\sigma_y)$ and $k_\pm = k_x \pm ik_y$, where σ_x and σ_y are the Pauli spin matrices in the x and y directions, respectively. The effective electric field $\mathcal{E}_z = ep/(2\epsilon\epsilon_0)$, ϵ is the dielectric constant), is proportional to the 2D hole density p, [61]. As a consequence, the internal electric field can be increased by both: increasing the doping or decreasing the thickness of the spacer layer.

In the usual case of a quantum well containing a 2DHG with hole density of $p \sim 10^{11}\,\mathrm{cm}^{-2}$, only the HH subband as the uppermost subband in the valence band is occupied. The spin-split HH-subband dispersion can be approximated by, [61]:

$$E_\pm^h(\mathbf{k}_{||}) = \langle\mu_h\rangle k_{||}^2 \pm \langle\beta_R^h E_z\rangle k_{||}^3, \tag{2.18}$$

where μ_h (times $2/\hbar^2$) stays for the reciprocal effective mass and $\langle\beta_R^h E_z\rangle$ is the effective Rashba coefficient for the cubic splitting, further assigned as β, which can be calculated from the experimental magnetotransport data, [15]:

$$\beta = \sqrt{\frac{2}{\pi}}\langle\mu_h\rangle \frac{p(\tilde{p_+} - \tilde{p_-}) + \Delta p(\tilde{p_+} + \tilde{p_-})}{6p^2 + 2\Delta p^2}, \tag{2.19}$$

where $\tilde{p}_\pm = \sqrt{p \pm \Delta p}$, $\Delta p = |p_1 - p_2|$, p_1, p_2 are the densities in the two spin subbands and p is the total hole density. Then for the spin splitting it follows $\Delta_{SO} = 2\beta k_{||}^3$, [15].

The anisotropic spin splitting

Taking into account both BIA and SIA, the spin splitting of the HH subband will be direction-dependent and to first approximation it can be written as [62]:

$$\Delta E^{HH}(\mathbf{k}) = 2k_{||}^3\sqrt{\alpha_R^2\mathcal{E}_z^2 + \beta_D^2 - 2\alpha_R\mathcal{E}_z\beta_D sin(2\varphi)}, \tag{2.20}$$

where β_D is the Dresselhaus coefficient, $\alpha_R\mathcal{E}_z$ the effective Rashba coefficient. The dominant contributions for the spin splitting are considered to be cubic in k.

In Ref. [62], Eq. 2.20 was used to calculate the Fermi contour $k_{F,+}$ and $k_{F,-}$ of the spin-split HH subbands, see Fig. 2.4(b). It is apparent that the interference of BIA and SIA causes small spin splittings along the [110] direction. In contrast, the $[1\bar{1}0]$ direction exhibits the largest spin splitting. The fourfold symmetry of the dispersion is now reduced to a twofold with one symmetry axes along these two directions. The directions [100] and [010] exhibit intermediate values of the spin splitting.

More accurate numerical calculations of the BIA term show, that its effective field changes its orientation with increasing k along the [110] and $[1\bar{1}0]$

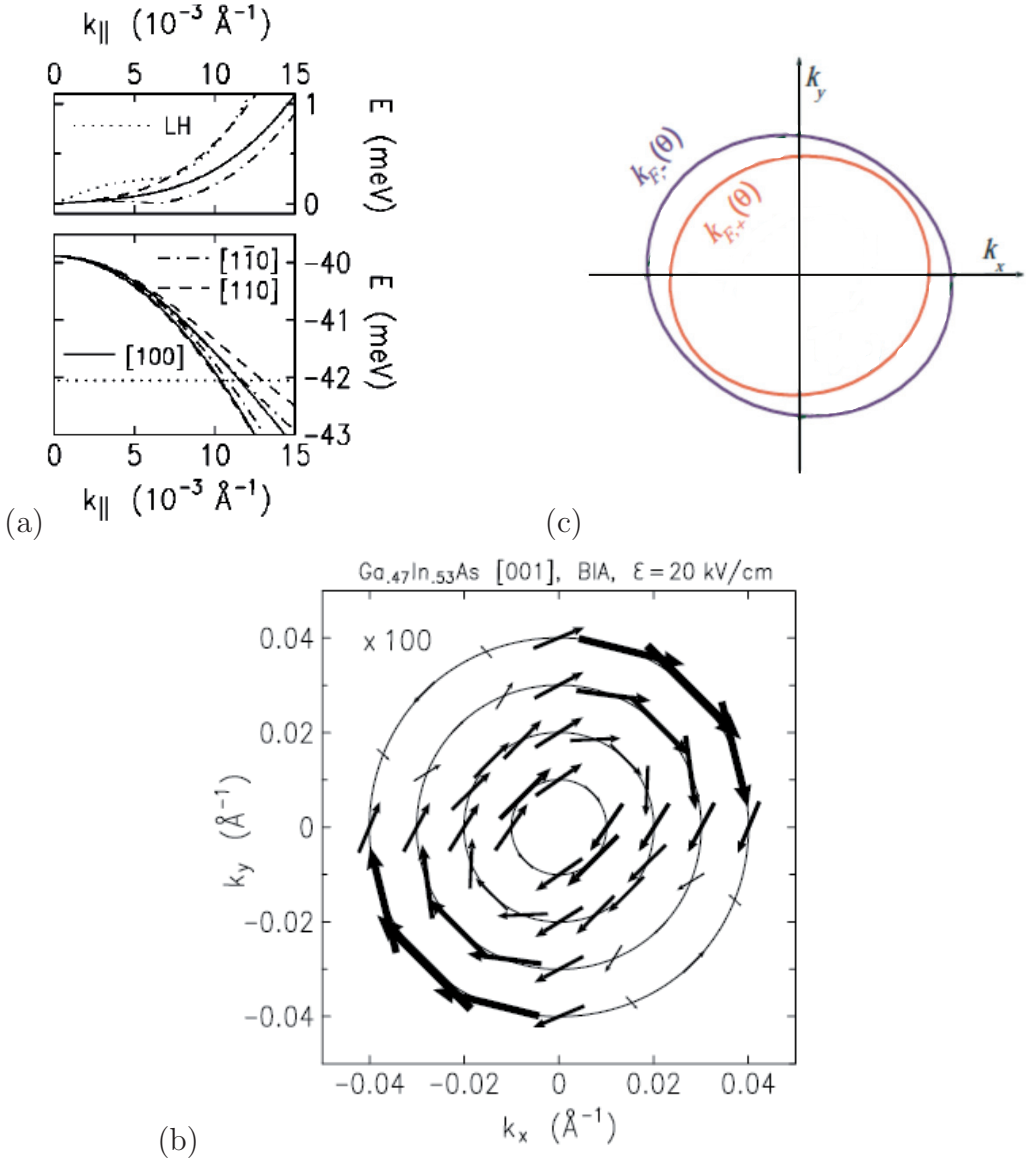

Figure 2.4: *(a) [59], Calculated spin splitting $E_+(k_{||}) - E_-(k_{||})$ (upper) and subband dispersion $E_\pm(k_{||})$ (lower) of the HH subband of a $GaAs/Al_{0.50}Ga_{0.50}As$ heterostructure grown in [001] direction. The horizontal line indicates the Fermi energy E_F.(b) [15], The effective field when both BIA and SIA spin splittings are taken into account, calculated for a $Ga_{0.47}In_{0.53}As$-InP QW. The length of the arrows is proportional to the intensity of the field. (c) [62], The angular anisotropy of the spin-split HH subbands of a 2DHG. Solid lines are the Fermi contours for $k_{F,+}$ and $k_{F,-}$ Fermi wave vectors.*

directions. On the contrary, the Rashba effective field is perpendicular to the in-plane wave vector $\mathbf{k}_{||}$ and keeps to point clockwise (or anticlockwise) exhibiting a rotational symmetry, [15]. The superposition of both effective fields is displayed in Fig. 2.4(c). As a consequence, it is possible to tune the interference from destructive to constructive with varying the density and so the Fermi wave vectors of the spin subbands $k_{F,+}$ and $k_{F,-}$. Further, it is worth to note that with increasing wave vector

k the subbands proceed more non-parabolically and the warping[6] plays an important role. Both effects contribute to the anisotropy of the spin splitting.

2.5 Weak-antilocalization effect

The weak-antilocalization (WAL) effect originates from interference on time-reversed paths, see Fig. 2.5(a). It appears in systems with strong spin-orbit interactions, where the phase-coherence length l_φ of the charge carriers is longer than their mean free path l. In disordered conductors the ring path of charge carriers is given by the arbitrary distribution of defects, see Fig. 2.5. Due to scattering events the spin orientation is randomized along the path leading to phase differences and destructive interference of the electron partial waves running along the time-reserved path. This results in a reduction of the backscattering probability and is demonstrated as a positive magnetoresistance around $B = 0\,\mathrm{T}$, see top curves in Fig. 2.5(b).

In contrast, the weak-localization (WL) effect arises due to constructive interference, if the spin-orbit interaction is negligible. The backscattering is enhanced in this case. In applied magnetic fields both partial waves obtain a different phase shift, the time-reversal symmetry is broken, and it leads to a negative magnetoresistance around $B = 0\,\mathrm{T}$, see the bottom curves in Fig. 2.5(b). The appearance of WAL or WL is strongly influenced by the strength of the spin-orbit interaction, demonstrated in Ref. [63]. Fig. 2.5(b) shows a pronounced transition from WAL to WL if the SIA of the InGaAs QW is changed from high to small, [63].

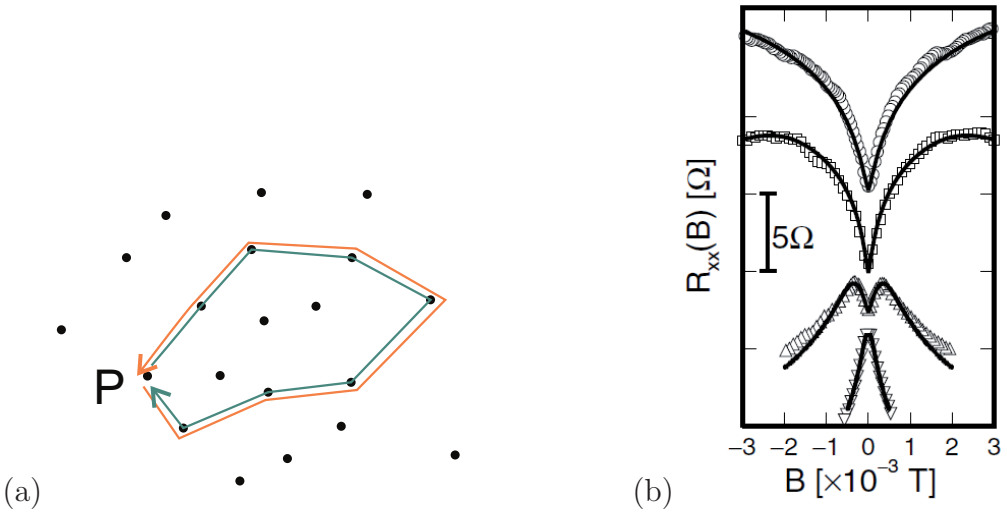

Figure 2.5: *(a) Constructive interference of partial waves on the time-reversal paths leads to weak localization. (b) [63], Transition from positive (WAL) to negative (WL) magnetoresistance as a consequence of the tuning of the SIA in the QW from large to small.*

[6]Warping is the anisotropic rosette-like valence-band dispersion, which originates from the p-like GaAs valence band.

There are two important theories which describe these quantum mechanical effects. The first one is the Hikami-Larkin-Nagaoka (HLN) theory, [64]. It was originally developed for metallic samples and assumes the Elliott-Yafet skew-scattering mechanism. In semiconductor heterostructures, the Dyakonov-Perel spin-relaxation mechanism is more important, [65, 66]. It is used in the theory by Iordanskii, Lyanda-Geller and Pikus (ILP), [65]. The ILP theory was successfully applied in a qualitative description of 2DEGs confined in an InAs channel in a $In_{0.75}Ga_{0.25}As/In_{0.75}Al_{0.25}As$ heterostructure, [67], or in InGaAs QWs [63, 66].

In this work we investigate similar structures, containing a 2DHG. In contrast to the spin splitting of electrons and LH states proportional to $k_{||}$, the uppermost subband in the valence band of GaAs and InAs, the HH subband, is exhibiting a spin splitting proportional to $k_{||}^3$, [15]. The ILP theory involves both the linear and cubic k terms for the spin splitting. Neglecting the terms linear in k, it gives the same results as the HLN theory, [65]. Therefore, for 2D hole systems the HLN theory is more appropriate to be used, as was successfully shown in Ref. [17]. Recently, Golub developed a theoretical model of WAL for high-mobility 2D systems [68], but its application for fitting the experimental data is not straightforward. For these reasons, in Section 5.4.3 the HLN theory is used to quantitatively describe the WAL effect.

2.6 State of research in the growth and transport properties of 2DHGs

Carbon is a very important acceptor material for heterostructures based on GaAs. In recent years, high-mobility two-dimensional hole gases in (100)-oriented GaAs/$Al_xGa_{1-x}As$ heterostructures have been realized experimentally. For the first time in C-doped p-type GaAs/AlGaAs heterostructures, the integer and fractional quantum Hall effect was measured by Grbic *et al*, [69]. The investigations were performed on samples with a hole mobility of $0.15 \times 10^6\,cm^2/Vs$ at 100 mK. Further progress in fabrication was made by Gerl *et al.*, [9], and Manfra *et al.*, [20], who enhanced the mobility up to $10^6\,cm^2/Vs$ at mK temperatures. Simultaneously, Gerl *et al.* extended the method of preparation of C-doped 2DHGs on the nonpolar (110)-oriented GaAs wafers as well and exceeded $\mu = 1.1 \times 10^6\,cm^2/Vs$ at 30 mK there, [21]. Currently, the highest mobility achieved was reported by Watson *et al.*, [8]. In their case, the 2DHG of a very low hole density, $p = 0.62 \times 10^{11}\,cm^{-2}$ was confined in an asymmetric quantum well and exhibited a hole mobility of $\mu = 2.6 \times 10^6\,cm^2/Vs$ at $T = 50$ mK. The authors further indicated that background impurity scattering and remote ionized impurity scattering are the most important scattering mechanisms limiting the hole mobility in the highest quality samples. Nevertheless, these values are still one order of magnitude lower than the highest electron mobilities in 2DEGs, $\mu = 35 \times 10^6\,cm^2/Vs$ at 360 mK reported by Umanski *et al.*, [7].

Unlike electrons in GaAs, holes have a higher effective mass[7] resulting in stronger carrier-carrier interaction. Therefore, these structures have been used to study 2D hole-hole interaction physics, including the metal-to-insulator transition, [18], and the fractional quantum Hall effect, [19, 72, 52, 34]. New reports deal, for example, with fractional quantum Hall physics in the 2nd Landau level, [72], and charge density wave formation in partially filled Landau levels, [73, 19]. Kumar *et al.* presented evidence of a fractional quantum Hall state at $\nu = 8/3$ in a 2DHG, [72]. The strong spin-orbit coupling in these heterostructures is apparent in a beating pattern of the Shubnikov-de Haas oscillations due to the two spin-split subbands and weak antilocalization, [17]. The long phase-coherence length of holes of 2.5 μm, extracted in Ref. [17], is promising for the fabrication of phase-coherent p-type nanodevices such as Aharonov-Bohm rings, [74]. Moreover, a modulation p-doped AlGaAs/GaAs heterojunction is part of the spin Hall effect transistor realized in Ref. [75].

Recently, InAlAs/InGaAs heterostructures were subject of intensive research due to their strong spin-orbit coupling and their promising applications in spintronics devices, [11]. Due to the large lattice mismatch between GaAs and InAs, the In-containing epitaxial layers grown on GaAs substrates are strongly strained and crystal defects can build up. These problems were overcome by the concept of a step-graded metamorphic buffer layer with gradually increasing indium content, see an example in Ref. [76]. This concept makes growth of almost unstrained $In_xAl_{1-x}As/In_xGa_{1-x}As$ heterostructures with high indium content x on GaAs substrates possible. Most of the publications concentrate on the properties of two-dimensional electron gases. In $In_{0.75}Ga_{0.25}As/In_{0.75}Al_{0.25}As$ heterostructures with embedded strained InAs channel, 2DEGs were achieved without any intentional doping, [77, 78], or using silicon as a doping material, [79]. They reached electron mobilities of up to $\mu = 5 \times 10^5\,\mathrm{cm}^2/\mathrm{Vs}$, [80]. Furthermore, a significant weak antilocalization, weak localization and Rashba effect were observed in [63, 81, 67], which are unambiguous evidence of a very strong spin-orbit interaction in these structures with $x > 0.50$. The authors in Ref. [63] demonstrated that the zero-field spin splitting is induced and controlled by the structure inversion asymmetry of the $In_{0.53}Ga_{0.47}As$ quantum well lattice-matched to InP. They observed a clear transition from positive to negative magnetoresistance by changing the asymmetry of the QW. A large spin splitting of 6.08 meV was reported in Ref. [81]. From the weak antilocalization analysis a long mean free path on order of $\sim \mu$m was estimated, [67]. The transport properties of the 2DEGs were found to be correlated with surface morphology, [80]. With a very simple change of the buffer layer, the residual strain in the active layer can be tuned from compressive to tensile, [82, 83]. Moreover, an enhancement of the carrier density due to generation of piezoelectric fields in strained layers grown on [311]A and [111]B oriented GaAs substrates was found, [84].

Recently, manganese-modulation-doping was used to prepare a 2DHG in strained InAs quantum wells, [25]. It has led to interesting magnetic effects. Especially, a phase transition at $T = 600\,\mathrm{mK}$ from a paramagnetic to a ferromagnetic

[7] The effective mass of holes was studied in dependence on different sample parameters in Refs. [70, 71].

phase was indicated in the transport behavior in a normal-doped structure, [85]. Further, a Mn-inverted-doped structure revealed an insulator-to-metal transition driven by a magnetic field, [24]. However, publications on nonmagnetic p-type doping in comparable InAlAs/InGaAs/InAs heterostructures are missing. For this reason carbon was applied as a doping material in the present work.

Chapter 3

Experimental methods

In this chapter, the experimental arrangements used for the growth, preparation and characterization of carbon-doped III-V semiconductor heterostructures will be described. The samples were grown using the molecular beam epitaxy (MBE) technique and analyzed via magnetotransport measurements. Quick characterization was performed in van-der Pauw geometry in a ^{4}He cryostat at temperatures of 4.2 K and 1.3 K. Using optical lithography and wet chemical etching, L-shaped Hall bars were defined and precise measurements were carried out in a dilution refrigerator and a ^{3}He cryostat in the temperature range between 20 mK and 1 K. To characterize the surface morphology of the grown heterostructures, atomic force microscopy (AFM) and X-ray diffraction were applied.

3.1 Molecular beam epitaxy

The most precise method for preparing high quality crystalline structures is molecular beam epitaxy (MBE). In this work, this method was applied to grow heterostructures of III-V compound semiconductors. The crystal constituents, stored in separate cells, are heated up to evaporate or sublimate and to create molecular beams. When the molecular beams impinge on the surface of the heated wafer (in our case (100) oriented GaAs crystals), the epitaxial growth takes place. In the Frank-van der Merwe growth mode, the atoms complete monolayer by monolayer.[1] The molecular beams can be interrupted by closing tantalum shutters mounted on the cell openings. In this way, the growth is controlled with a precision of fractions of one monolayer. If more cells are simultaneously open, compound crystals such as AlGaAs, InGaAs and InAlAs can be prepared. The MBE method is controlled with three temperatures: the temperature of the group III materials (gallium, aluminum, indium), group V materials (arsenic) and the temperature of the GaAs substrate. The growth rate is governed by the temperature of the group III elements, which controls the flux, while the arsenic is in abundance. It is very important to ensure

[1] All of the GaAs/AlGaAs and InAs/InGaAs/InAlAs heterostructures discussed in this work were prepared in this growth mode. Other growth mechanisms are listed, e.g., in [86].

(a) the In cell (b) the C cell

Figure 3.1: *(a) The downward-looking SUMO® source for indium. (b) The carbon filament source.*

UHV[2] conditions in the MBE chamber to keep a low concentration of background impurities in the grown layer.

3.1.1 The MBE system in Regensburg

In this work, a modified Veeco GEN II solid source molecular beam epitaxy system was used. This system consists of two MBE chambers called C ("spintronic") and D ("high mobility"), which can be operated separately. They are connected with a UHV channel for sample transfer between the chambers and a loading chamber (entry). The background pressure is below 10^{-11} mbar. All samples presented here were grown in the D chamber. It was designed for the growth of high mobility 2DEGs, and contains two gallium (Ga) cells, two aluminum (Al) cells, an indium (In) cell, an arsenic valved cracker cell and two filament cells for the doping materials: silicon (Si) and carbon (C). The materials in the effusion cells are stored in pyrolytic boron nitride crucibles of conical or SUMO® shape[3], for pictures see [87] or [88]. The In cell is directed downwards and therefore it has the special form of the downward-looking SUMO®, see Fig. 3.1(a). For the p-type doping we used a resistively heated carbon filament source, a modified SUKO-D from Dr. Eberl MBE-Komponenten GmbH, see Fig. 3.1(b). The technical details of the C cell are given in [21]. For easy handling the wafer is mounted on a tantalum holder using liquid gallium, which provides good thermal contact with the manipulator heater in the growth chamber. To ensure a homogeneous thickness of the epitaxial layer on the whole substrate, the wafer rotates (typically 7 rpm) during the growth process. The temperature of the substrate is measured using Ircon and IMPAC pyrometers for temperatures $T > 400$°C and $T < 400$°C, respectively. For *in-situ* characterization of the grown surface, a RHEED[4] gun is installed in the chamber. By analyzing the RHEED oscillations the growth rates are calibrated, see for example [25]. Further, the samples

[2]ultra high vacuum

[3]Usually, the conventional MBE effusion cells are equipped with a crucible with a large exit aperture. In contrast, the SUMO® crucible has a cylindrical form with a small tapered orifice, which is heated separately to prevent the emergence of droplets at the cell opening and to minimize shutter-related flux transients.

[4]reflection high energy electron diffraction

can be cleaved *in-situ* and the cleaved edge can be overgrown (CEO)[5].[6] A detailed description of this MBE machine can be found in [89] and some more details are also given in [87, 21, 25].

There are several options on how to create 2DHGs in $GaAs/Al_xGa_{1-x}As$ heterostructures. Recently, silicon and beryllium have often been used as doping materials. Yet, both have significant disadvantages such as a strong mobility anisotropy in the case of silicon, [90] or high diffusion and segregation in the case of beryllium, [91]. In contrast, carbon has a low diffusion and segregation, [92], and very high hole mobilities of more than $10^6\,cm^2/Vs$ can be achieved in heterostructures grown on [100] and [110] oriented GaAs substrates, [93]. As a group IV element, carbon incorporates on the As sides in the GaAs crystal lattice and works as an acceptor. As a carbon source, resistively heated high-purity graphite filaments have been widely implemented, [94], and were also used in this work. We achieved excellent crystal properties of GaAs using a growth rate of $1\,\mu m/h$ ($1\,monolayer/s$) under As_4-rich conditions ($6.5 - 7.1 \times 10^{-6}\,Torr$ As_4 beam equivalent pressure) when the substrate temperature was maintained at $T_G = 640°C$, apart from the growth of the doping layers, during which the temperature was reduced to compensate for the high thermal impact of the carbon cell, see Section 4.2.[7]

In Section 5, carbon was used as a doping material in $In_xAl_{1-x}As/In_xGa_{1-x}As/InAs$ heterostructures. The generation of 2DHGs in these structures is not straight forward because carbon acts as a donor in InAs, [95, 96]. The specifics of the growth are described in Section 5.1 and Section 3.1.3 details the calibration of the In cell. The growth rate was typically $1.2\,\mu m/h$ under As_4-rich conditions ($7.8 - 8.6 \times 10^{-6}\,Torr$ As_4 beam equivalent pressure) and the substrate temperature was varied between 430°C and 340°C for low and high In content. Additional information is given in [97] as well.

3.1.2 Calibration of the carbon cell

The carbon cell has the form of a thin graphite filament, which is heated up by applying a current. To get information about the doping density at different currents, the carbon cell was calibrated. During this procedure, a series of homogeneously-doped $1\,\mu m$ thick GaAs bulk layers were grown. For each value of filament current samples were measured at $4.2\,K$. In Fig. 3.2, the hole density as a function of the filament current is plotted. The error bars represent the measurement errors resulting in different densities if flat or corner contacts were used. Interestingly, the temperature of the substrate during the doping T_D seems to have a strong influence on the gained hole density. This is demonstrated in Fig. 3.2 on samples doped with the same filament current of $53\,A$. The sample grown at $T_D = 620°C$ (black circle) exhibits approximately 1.5 times higher hole density than the sample grown at higher

[5] cleaved edge overgrowth

[6] With each applied CEO-growth process it is possible to reduce the dimension of the electron (hole) system from 2DEG (2DHG) to quantum wire or quantum dot, [87].

[7] Growth on (110)-oriented GaAs surface requires different growth conditions, for more information see [21, 87].

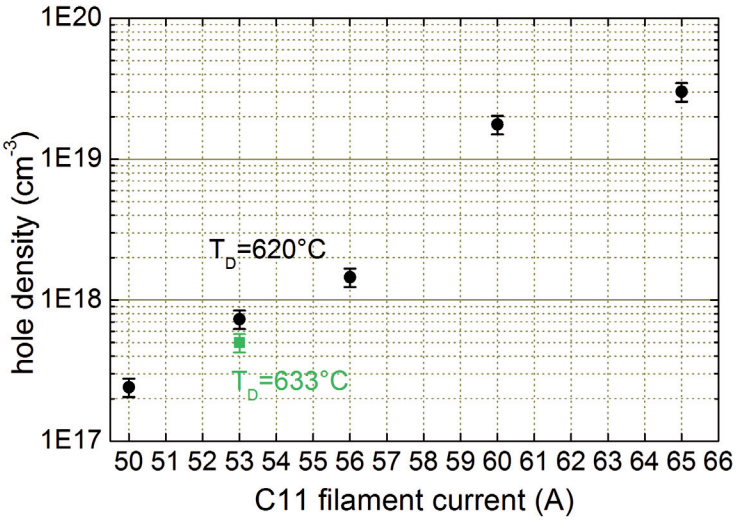

Figure 3.2: *Calibration of the C cell: Hole density measured in van-der Pauw geometry at 4.2 K versus filament current. Error bars represent differences in the hole density if flat or corner contacts of the van-der Pauw sample were used.*

temperature 633°C (green square). More detailed information on the reduction of T_D during the doping process will be given in Section 4.2.

3.1.3 Calibration of the indium cell

For preparation of $In_xGa_{1-x}As$, $In_xAl_{1-x}As$ epitaxial layers with different indium content and for growth of the buffer layer, where the In content is increased stepwise, see Section 5.1.1, careful adjustment of the InAs growth rate is needed. In this work, the calibration of the In cell proceeds via RHEED oscillations. Due to the high cost of an InAs substrate and the demanding surface preparation procedure before RHEED oscillations can be observed, we used a common RHEED sample[8]. The method is based on comparing the growth rates of the AlAs and InAlAs compounds. The RHEED oscillations of both materials are shown in Fig. 3.3(a). First, we established the rate of AlAs, then the In cell was opened and oscillations of InAlAs were recorded. The difference of both rates gives the InAs growth rate. We overcame the problem of the high lattice mismatch due to the presence of indium by applying a strong overshoot of Al mixed with only a small fraction of In in the $In_xAl_{1-x}As$ ternary compound. In doing so, the growth of thin layers proceeded pseudomorphically. To increase the accuracy the procedure was repeated at least three times for a certain temperature of the In cell. Before each AlAs/InAlAs growth step, the RHEED sample was smoothed by growth of a thick layer of GaAs and a GaAs/AlAs superlattice at high temperatures of about 600°C. Fig. 3.3(b) demonstrates the evolution of the InAs growth rate in a wide range of In cell temperatures. As such a calibration takes a long time it has not been executed for each growth process but at regular intervals.

In contrast to the Ga and Al cells, the In cell is oriented downwards in the MBE chamber. Fig. 3.1(a), in Section 3.1, shows the special form of the crucible with an extended front part (downward-looking SUMO® source) designed for the

[8] A small (approx. $4 \times 4\,mm^2$) piece of a GaAs wafer, mainly used for calibrating the AlAs and GaAs growth rates.

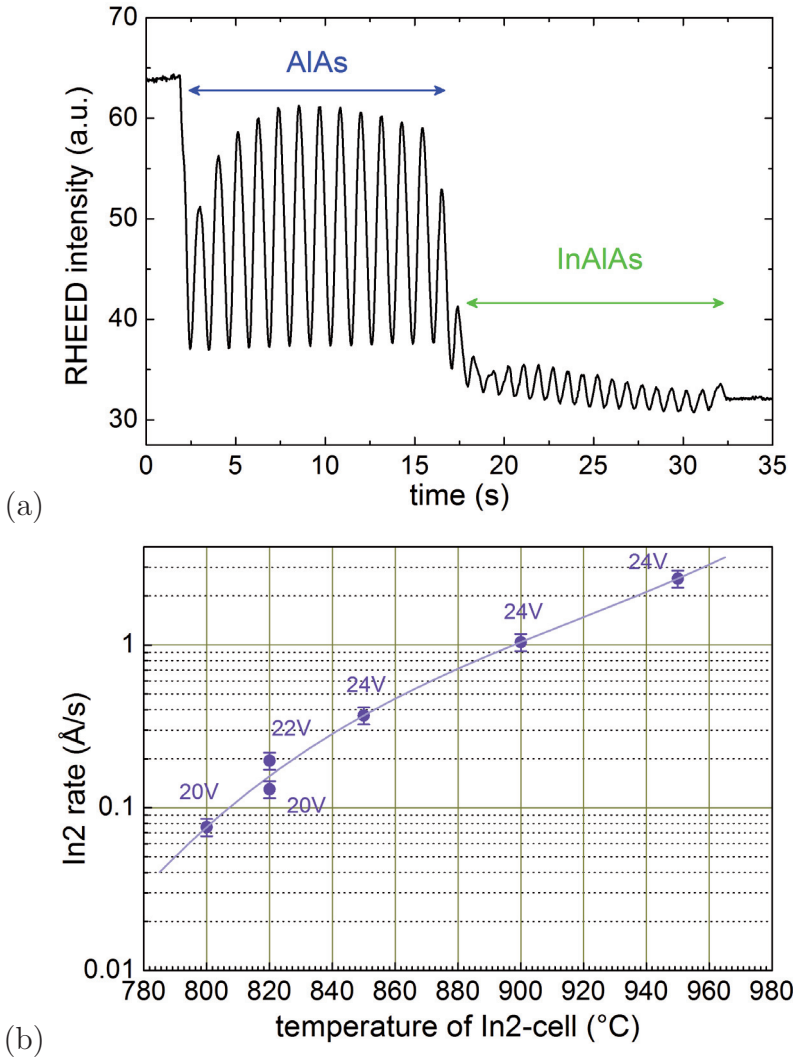

Figure 3.3: *(a) RHEED oscillations of AlAs and InAlAs used for calibration the InAs growth rate. (b) Calibration of the In cell. The points are marked with values of the applied tip voltage.*

molten source group-III materials in downward-facing ports. The front part of the cell is heated separately from the bulk to prevent recondensation at the exit cone and therefore changes the overall flux coming from the In cell. This is illustrated in Fig. 3.3(b): The two points taken at the In-bulk temperature of 820°C demonstrate the strong influence of the tip voltage on the InAs growth rate. Thus, a careful adjustment of the In-bulk temperature and the tip voltage is necessary.

The validity of our calibration method was confirmed by X-ray diffraction measurements on the buffer layers with different final In content done by M. Lohr [98]. For the buffer layer terminated at $x = 0.75$ indium the discrepancy was only about 2.5%, [98]. In the sample with desired $x = 0.60$, the X-ray diffraction established an $x = 0.575 \pm 0.014$ indium, see also Section 5.4.5.

3.2 Sample preparation

To characterize the grown heterostructures electrically, the samples were either contacted in the van-der Pauw or the L-shaped Hall-bar geometry. We used the van-der Pauw method [99], see scheme in Figs. 3.4(a), (c), to get quick information about the carrier density and mobility. For van-der Pauw measurements, $5 \times 5\,\mathrm{mm}^2$ pieces were cut from the wafer and eight ohmic contacts were made on the corners and flats of the sample. In four-terminal measurements, the sheet resistivity can be determined by cyclic permutation of the contacts. The equation describing this method is given in Ref. [100]. The carrier density was derived from the slope of the Hall curve, see Eq. 2.5. In the van-der Pauw geometry, the quantum Hall effect and SdH oscillations can be observed as well. However, it is not possible to extract any information about the different properties in different crystallographic directions.

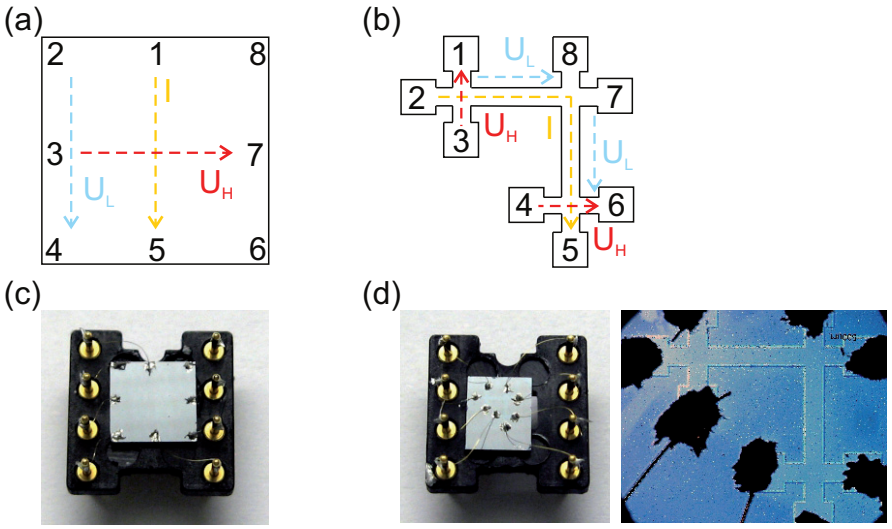

Figure 3.4: *Schemes of (a) the van-der Pauw and (b) the L-shaped Hall-bar geometry. I stands for the current, U_H is the Hall resistance and U_L is the longitudinal resistance. (c) and (d) are photographs of the samples fabricated in the van-der Pauw and the L-shaped Hall-bar geometry, respectively.*

For this purpose, we prepared L-shaped Hall bars[9], see Fig. 3.4(b), (d), with the arms oriented along two orthogonal directions, here [011], [01$\bar{1}$], or [001], [010]. This kind of geometry makes it possible to record magnetotransport properties of both directions simultaneously. In order to define the L-shaped Hall-bar geometry, standard optical lithography and wet chemical etching were applied. A detailed overview of the parameters used in this procedure is given in Appendix A. To maintain the information about the crystal directions the samples were cut into $4 \times 5\,\mathrm{mm}^2$ pieces from the wafer. The p-contacts were made using an InZn mixture, which ensures good ohmic contact, more information is listed in Appendix A.

[9]We fabricated L-shaped Hall bars of dimensions: $200\,\mu\mathrm{m}/1000\,\mu\mathrm{m}$, $200\,\mu\mathrm{m}/1600\,\mu\mathrm{m}$ (width/length).

3.3 Measurement set-up

Dewar cryostat

For a fast characterization of the carrier density and mobility at temperatures 4.2 K and 1.3 K, the dewar cryostat at the Chair of Prof. Wegscheider was used. It consists of a magnet rod and a sample rod, which are both lowered into a dewar with liquid ^{4}He for cooling, see Fig. 3.5(a). On the magnet rod, a superconducting coil providing a magnetic field up to ± 5.8 T is mounted. The internal space is vacuum isolated and can be connected to or disconnected from the ^{4}He reservoir by a needle valve. Pumping on the ^{4}He, temperatures as low as 1.3 K can be achieved. A quick record of the Hall curve and the SdH oscillations is done using a standard lock-in technique. Samples can be illuminated by a red light-emitting diode (LED) at low temperatures.

^{3}He cryostat

Using the rare ^{3}He isotope instead of the ^{4}He isotope, temperatures in the range between 300 mK and 1 K can be achieved. This is done by pumping the ^{3}He from a reservoir containing liquid ^{3}He. The measurements performed in this work were carried out in three ^{3}He cryostats of different design: a self-made system at the Chair of Prof. Wegscheider at the University of Regensburg, and two commercial systems from Oxford Instruments at the ETH Zurich (year of construction 2009) and at the Walter Shottky Institute (WSI) in Munich (year of construction 1988). All three systems are operating in the same way, see Fig. 3.5(b). The gaseous ^{3}He condensates on the 1 K pot, which is held at $T = 1.5$ K, and accumulates in the bottom of the rod. The liquid ^{3}He has now the temperature of the 1 K pot. When decreasing the temperature of the sorption pump to $T = 4.2$ K, the sorb starts to pump on the liquid ^{3}He, and its temperature decreases slowly to approximately 300 mK. Individual constructions vary: either the sample is immersed[10] in liquid ^{3}He, or the cryostat can be configured as a cold finger, where the sample, placed in vacuum, is cooled due to the thermal contact with the liquid ^{3}He reservoir[11].

Dilution refrigerator

Due to the high effective mass of holes, very low temperatures are needed to get well-developed SdH oscillations and quantum Hall plateaus. In order to cool down the sample to temperatures below 300 mK, a dilution refrigerator is needed, see Fig. 3.5(c). It uses the special properties of the ^{4}He and ^{3}He mixture. At temperatures lower than the critical temperature of 0.87 K, two phases are created in the mixture. The lighter concentrated phase consists predominantly of ^{3}He and swims on top of the heavier dilute phase. The dilute phase is rich in ^{4}He and contains approximately 6.6% of ^{3}He. The cool-down process proceeds due to pumping out the ^{3}He from

[10] the self-made system at the Chair of Prof. Wegscheider at the University of Regensburg and the ^{3}He cryostat at the WSI in Munich

[11] the setup at the ETH Zurich

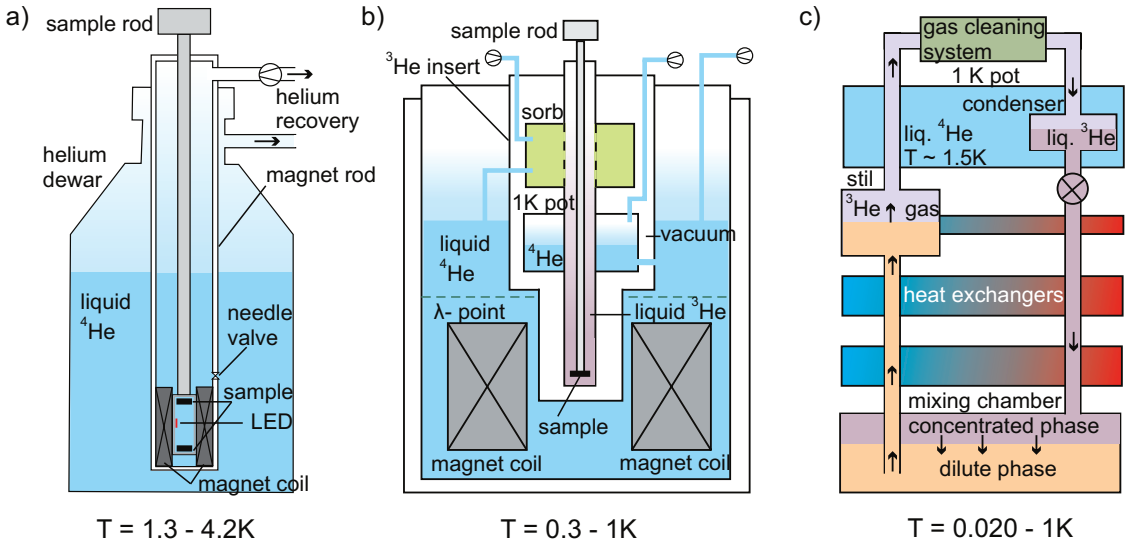

Figure 3.5: *The scheme of (a) the dewar cryostat, (b) the ^{3}He cryostat, and (c) the dilution refrigerator.*

the dilute phase[12]. To maintain the constant concentration in the mixture, the ^{3}He atoms pass from the concentrated phase to the dilute phase and provide the cooling because of the different enthalpy of the ^{3}He in both phases. In this work we used the dilution refrigerator at the Chair of Prof. Weiss with a base temperature of 20 mK. The measurements were carried out using a standard lock-in technique at a frequency of 17 Hz and a constant current of 10 nA.

Spectromag

Magnetotransport measurements up to room temperature were done in the Spectromag cryostat from Oxford Instruments at the WSI in Munich. In this system the temperature can be varied from 1.5 K up to 300 K due to two heaters: one on the sample rod and another one on the bottom of the variable temperature insert (VTI). The cool-down process can be regulated very accurately via a needle valve, which connects the VTI with the liquid ^{4}He reservoir. The temperature of the sample is then determined as the temperature difference between the temperature measured in the VTI and on the sample holder. The difference was adjusted to be lower than 3 K at $T < 180\,K$ and 5 K at $T \geq 180\,K$. Using the λ-plate[13], magnetic fields up to 8 T can be achieved.

[12] ^{3}He has lower latent heat than ^{4}He and evaporates approximately three orders of magnitude better than ^{4}He at $T = 0.6$ K.

[13] The superconductive coil is cooled down below 4 K.

Room-temperature magnet

To determine the sheet resistivity, carrier density and mobility at room temperature, the measurement setup made by B. Hacker at the Chair of Prof. Wegscheider was used [101]. Two water-cooled magnet coils generate a magnetic field of up to 1 T. As measurement instruments a lock-in amplifier and a Keithley multimeter are implemented. The sample can be illuminated using an LED.

3.4 Postgrowth surface characterization methods

Atomic force microscopy

In order to study the morphological properties of the surface of the indium-containing heterostructures, an atomic force microscope was used. The raw data were recorded on a Nanoscope III Scanning Probe Microscope and a Veeco Dimension Icon Atomic Force Microscope with ScanAsyst[14] in tapping mode using a common Si-tip.

X-ray diffraction

The X-ray diffraction analysis was done to get more information about strain relaxation and the lattice constant along different crystallographic directions in the indium-containing heterostructures; see Section 5.4.5. More information about the method and the experimental arrangements can be taken from [102, 98].

3.5 Nextnano^3 simulation of the valence-band structure

The simulations of the valence band structure were performed with the nextnano^3 program package [103]. This software was developed by P. Vogl and his group at the WSI in Munich. Now, it is supported by S. Birner.

For the calculation of the electronic structure of layered semiconductors, the envelope function approximation (EFA) is commonly used. In this approximation, the wave function is expanded in terms of Bloch functions in the quickly oscillating lattice-periodic part, which is modulated by a slowly varying envelope function. The effective-mass approximation for single isotropic parabolic bands provides a basic insight into the subband structure. It is a good starting point for the 2D electrons, which have almost parabolic and isotropic dispersion, [15]. While the hole dispersion E($\mathbf{k}$) is highly anisotropic and nonparabolic, a more detailed valence band structure can be obtained in the framework of $\mathbf{k}\cdot\mathbf{p}$-method and EFA. It is based on the multiband Hamiltonian and assumes nonparabolicity, spin splitting and coupling between heavy holes and light holes. Very accurate results were achieved with the 8×8 band $\mathbf{k}\cdot\mathbf{p}$-method, taking not only the coupling between Γ_8

[14] Chair of Prof. Weiss

and Γ_7 valence bands into account, but also the interactions with the Γ_6 conduction band. Further information about the calculation of the dispersion relations of p-type quantum wells can be found in Refs. [15], [104].

All methods described above are implemented in the nextnano^3 program package and can be applied to our heterostructures. The sample structure, as well as the overall simulation parameters, such as the computation method, simulation dimension, lattice temperature, crystal orientation etc., are defined in the input data file. In our case of quantum wells with quantum confinement along the z-axis (growth direction), a 1D simulation dimension is sufficient[15]. The crystal is approximated with a grid. The grid lines and their spacing can be set as needed. All calculations are performed on the grid points. Nextnano^3 contains an extended database, in which all material parameters are listed. The computation process proceeds as follows. First, the input file and the database are read in and particular materials are assigned to each grid point. Then, the strain is calculated. Only pseudomorphic growth can be considered, where the in-plane lattice constant matches to the substrate and the out-of-plane is extended or compressed. For the predefined "quantum region", typically the quantum well and its close neighborhood, the Poisson equation and the 8×8 band $\mathbf{k} \cdot \mathbf{p}$-Schrödinger equation are solved self-consistently. More information about this software can be found on the webpage [105]. There are also some detailed examples.

[15] In nextnano^3 also 2D and 3D simulations of quantum wires and quantum dots are possible, [87].

Chapter 4

Carbon-doped GaAs/AlGaAs heterostructures

A goal of this work was to improve the performance of 2DHGs confined in GaAs/AlGaAs quantum wells and to investigate their magnetotransport properties. To prepare a p-type doping, we used a high purity carbon filament source, with which a record hole mobility $\mu = 1.2 \times 10^6\,\mathrm{cm}^2/\mathrm{Vs}$ was obtained in a previous study by C. Gerl [9]. Because the carrier mobility is an important indicator of the sample quality, we optimized the structure and growth conditions in order to enhance the hole mobility further. An overview will be given in Section 4.1.

It is well known that the illumination of a 2DEG sample at low temperatures causes an enhancement of the electron density due to the activation of DX centers induced by silicon impurities. Although carbon is not expected to create DX centers, some photoconductivity effect was reported in literature [21, 20]. Our investigations on this topic, especially the possibility to suppress the persistent photoconductivity effect in 2DHGs by varying the growth parameters, will be introduced in Section 4.2.

Engineering the band structure, samples of symmetrical and asymmetrical confinement potential were prepared and their properties will be compared in Section 4.4. We will support our experimental findings with theoretical simulations of the valence-band structure, which are summarized in Section 4.3.

4.1 Growth

4.1.1 Sample structure

In this work, the modulation-doping technique is used to prepare high-mobility 2DHGs in GaAs/$Al_xGa_{1-x}As$ quantum-well structures. This method is based on the separation of the carbon-doping layer from the QW by an AlGaAs spacer layer, which leads to a significant reduction of the ionized impurity scattering.

Recently, the most investigated structure has been the single-sided-doped QW (ssd-QW). The parameters of this structure were optimized by Manfra *et al.* in Ref. [20]. In a 15 nm wide GaAs QW with an 80 nm thick $Al_xGa_{1-x}As$ spacer layer,

the authors obtained a peak hole mobility on the order of $10^6\,\mathrm{cm}^2/\mathrm{Vs}$ at 300 mK. Further modification of this structure, especially the reduction of the Al content to $x = 0.16$ in the barrier material, led to an enhancement of the hole mobility to $\mu = 2.6 \times 10^6\,\mathrm{cm}^2/\mathrm{Vs}$ at $T = 50$ mK. The layer sequence is given in [8].

For these reasons, the ssd-QW was the starting point also for this study of the high-mobility samples. It represents the basis for further development of novel structure designs. The detailed sample structure is shown in Fig. 4.1. It consists of a 15 nm wide QW separated by an $Al_{0.30}Ga_{0.70}As$ spacer (80 nm) from a carbon δ-doping[1] layer of 330 s. In spite of the high value of the low-temperature hole mobility, which was achieved in this structure (see above), there still remain some problems, which must be solved. One of the most important mechanisms limiting the mobility is interface roughness scattering. The calculated valence-band edge is shown in the upper part of Fig. 4.1. Because the ssd-QW structure has only one doping layer above the QW, the QW is strongly asymmetric and the carrier density profile is situated close to the barrier/well interface. As a consequence, the free holes are strongly influenced by the quality of the interface, which introduces an additional scattering mechanism. Furthermore, the asymmetrical confinement potential generates a strong internal electric field, causing a significant Rashba effect, [15].

These effects can be overcome by arranging the QW more symmetrically using the double-sided-doped-QW (dsd-QW) structure having two doping layers: one on each side of the QW. C. Gerl used the dsd-QW structure. Optimizing the structure parameters such as QW width and spacer thickness, he reached a 2DHG with a mobility of $1.21\times10^6\,\mathrm{cm}^2/\mathrm{Vs}$ and density of $2.3\times10^{11}\,\mathrm{cm}^{-2}$ at $T = 30$ mK, [21, 9]. These results represent the highest hole mobility achieved in this MBE chamber prior to this work. In order to compensate the surface states, the carbon dopant concentration in the δ-doping layer close to the surface is much higher (typically 330 s, [21]) than in the δ-doping layer closer to the substrate ($\sim$ 100 s, [21]). Thus, it is rather complicated to adjust the QW to be exactly symmetrical in this case. Gerl *et al.* reported a spin splitting of the HH subband of 4.4% as a consequence of the residual structure anisotropy, [9, 21].[2]

In this work, we used a modified dsd-QW structure with four carbon doping layers C1-C4, two on each side of the QW. The layer sequence is shown in Fig. 4.2. A 15 nm GaAs QW is confined between two $Al_xGa_{1-x}As$ spacer layers of 80 nm thickness[3]. The carbon δ-doping layers C2 and C3 around the QW are identical. The motivation for using this design was reaching an electron mobility of $\sim 19 \times 10^6\,\mathrm{cm}^2/\mathrm{Vs}$ in a similar structure, [106]. The additional C4 and C1 layers compensate the surface states and substrate charges, respectively. Further, they are supposed to reduce remote ionized impurity scattering, limiting the mobility in the standard dsd- and ssd-QW. Moreover, the band profile close to the QW can more easily be designed symmetrically. The calculated valence-band edge is shown in the upper part of Fig. 4.2. In this case, the QW is symmetric and the carrier

[1] δ-doping means that only the carbon cell and the arsenic cracker cell were opened during this part of the growth procedure. The time of opening of the carbon cell is given in seconds.

[2] In this case, BIA was considered to be negligible.

[3] The parameters of the standard dsd-QW structure were optimized in [9].

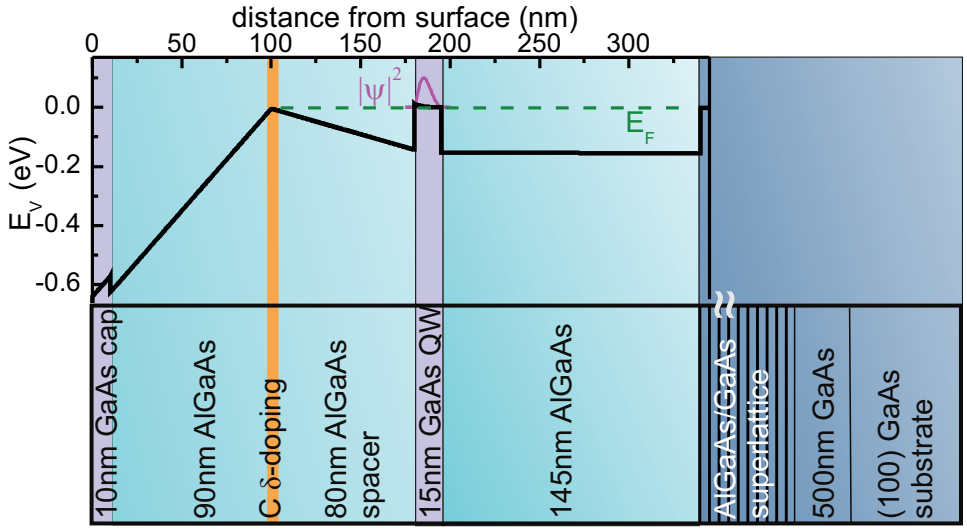

Figure 4.1: *Layer sequence of the ssd-QW structure and its valence-band edge calculated using nextnano³ for sample ssd-A. The QW is asymmetric and the carrier density profile (violet line) is situated close to the QW/barrier interface.*

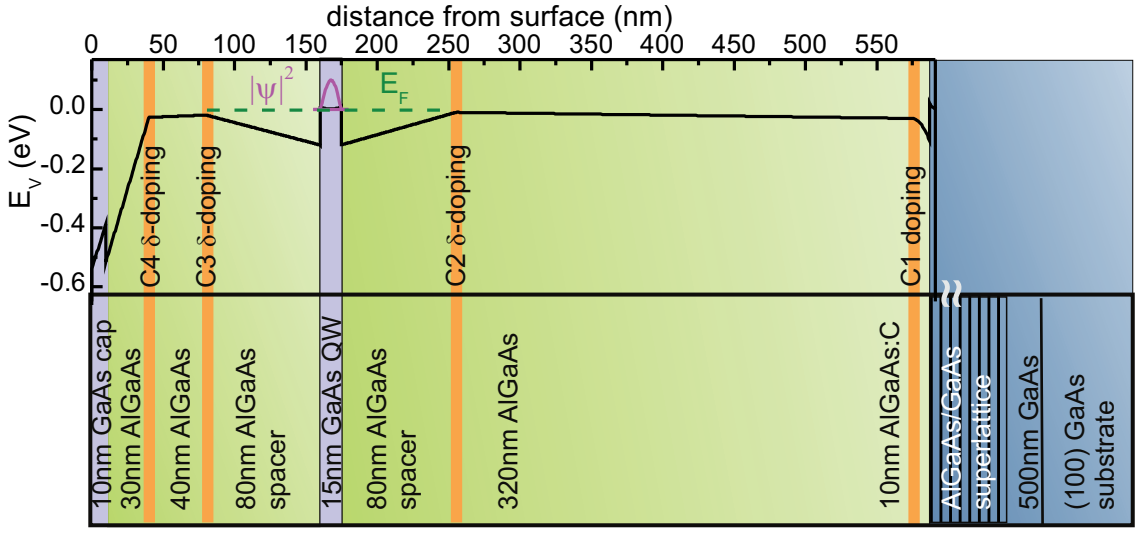

Figure 4.2: *Layout of the dsd-QW structure and its valence-band edge along the growth direction calculated using nextnano³ for sample dsd-B. Due to the additional doping layers C1 and C4, the QW is symmetric and the carrier density profile is situated in the middle of the QW.*

density profile is situated in the middle of the QW. Therefore, interface roughness scattering is expected to be reduced in contrast to the ssd-QW. In summary, the modified dsd-QW structure has following advantages: reduced interface roughness scattering due to symmetric QW, and reduced remote ionized impurity scattering due to the additional C1 and C4 doping layers. Finally, it enables us to reduce the Rashba effect, see Section 4.3.

The valence-band edge shown in Figs. 4.1 and 4.2 was calculated for two particular samples ssd-A and dsd-B, which will be defined in the next section. In Figs. 4.1 and 4.2 the position of the Fermi level is marked with the dashed line. In both structures only the first subband is occupied.

All samples were grown on a (100) GaAs semi-insulating substrate material. Between the electrically active layer and the substrate a 500 nm thick GaAs layer was inserted, followed by a superlattice consisting of 100 periods of 10 nm AlGaAs and 3 nm GaAs. Both serve to smooth the surface and to electrically decouple the 2DHG from the substrate. The whole structure was capped with 10 nm GaAs. Typical Al content of the $Al_xGa_{1-x}As$ barrier was $x = 0.30$, but we also will present results on samples where x was in the range between 0.20 and 0.35.

4.1.2 Ultra-high hole mobility

Because we report here the first application of the modified dsd-QW structure on 2DHGs, optimal growth conditions in order to get a very high hole mobility had to be found. Some of the important parameters are doping concentration, growth temperature and Al content in the barrier.[4]

Variation of the doping concentration

The layer sequence of the dsd-QW is quite complex, thus we decided to adjust the doping concentration first in order to get a high quality 2DHG. In this section, samples with $x = 0.30$ Al content in the barrier will be discussed exemplarily.

In the first experiment, a series of samples were grown, where the doping concentration of the C4 δ-doping layer, which is the doping layer closest to the surface, was varied. At the same time, the other three doping layers were held constant at C1 = 29 s and C2 = C3 = 80 s. The doping concentration was tuned by varying the opening time of the carbon cell. At the same time the flux of the carbon cell was kept constant[5] for all samples. The results are plotted in Fig. 4.3. The two-dimensional hole density increases with increasing doping concentration of C4. The holes from the C4 doping go into the C3 layer. The hole mobility shows a peak value at C4 = 200 s. This could be explained by a reduction of remote ionized impurity scattering, as the holes coming from the C4 doping neutralize the ionized

[4]Optimal values of the QW width and spacer thickness for the dsd structure with two carbon δ-doping layers on the opposite sides of the QW were found to be 15 nm and 80 nm, respectively, Ref [21].

[5]The flux of the carbon cell is controlled via the current applied through the carbon filament, see also Section 3.1. For all samples discussed in this chapter, we applied the current of 50 A, which gives a carbon doping concentration of $(2.4 \pm 0.4) \times 10^{17}\,\mathrm{cm}^{-3}$, see Fig. 3.2.

acceptors in the C3-doping layer. The sharp decrease of the mobility at the high doping concentration is most probably caused by intersubband scattering, because at so high hole density not only the first HH, but also the first LH subband is occupied.

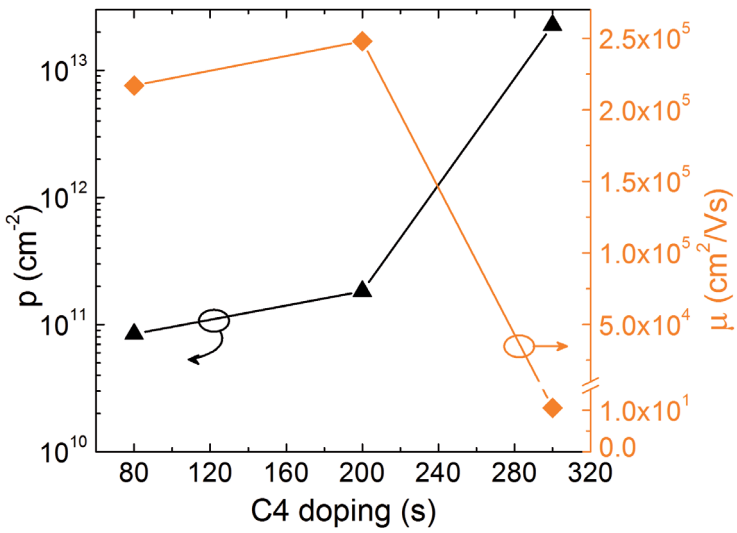

Figure 4.3: *Optimization of the doping concentration of the C4-doping layer in the dsd-QW structure. C2 = C3 = 80 s and C1 = 29 s were maintained constant. Magnetotransport data were measured at 4.2 K. All samples have x = 0.30 Al content in the barrier. The lines are guides to the eyes.*

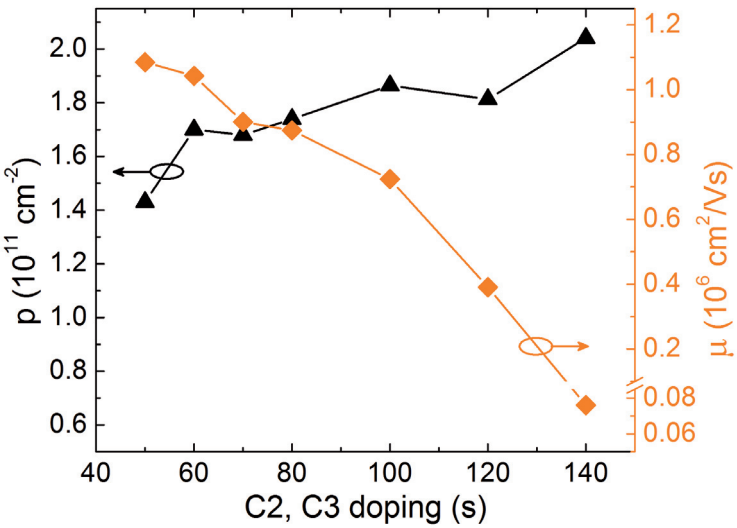

Figure 4.4: *Optimization of the doping concentration of C2 = C3 doping layers in the dsd-QW structure. C4 = 200 s and C1 = 29 s were held constant. Magnetotransport data were measured at 1.3 K. All samples have x = 0.30 Al content in the barrier. The lines are guides to the eyes.*

In the second experiment, the C4 doping was held constant at C4 = 200 s and the doping concentration of the C2- and C3-doping layers was varied. According to the expectation, the hole density increases with increasing the doping concentration (aside from some runaway values), see Fig. 4.4. For all plotted samples, the hole mobility decreases with increasing doping concentration. This phenomenon that at high densities the mobility drops with increasing density is specific for 2DHGs and was described in literature to changes in the effective mass [70] and/or intersubband scattering [9]. Further samples grown with low doping concentration of C2 = C3 = 40 s and 30 s (not plotted in Fig. 4.4) were insulating at low temperatures. The maximum of mobility at C2 = C3 = 50 s and 60 s can be ascribed to enhanced

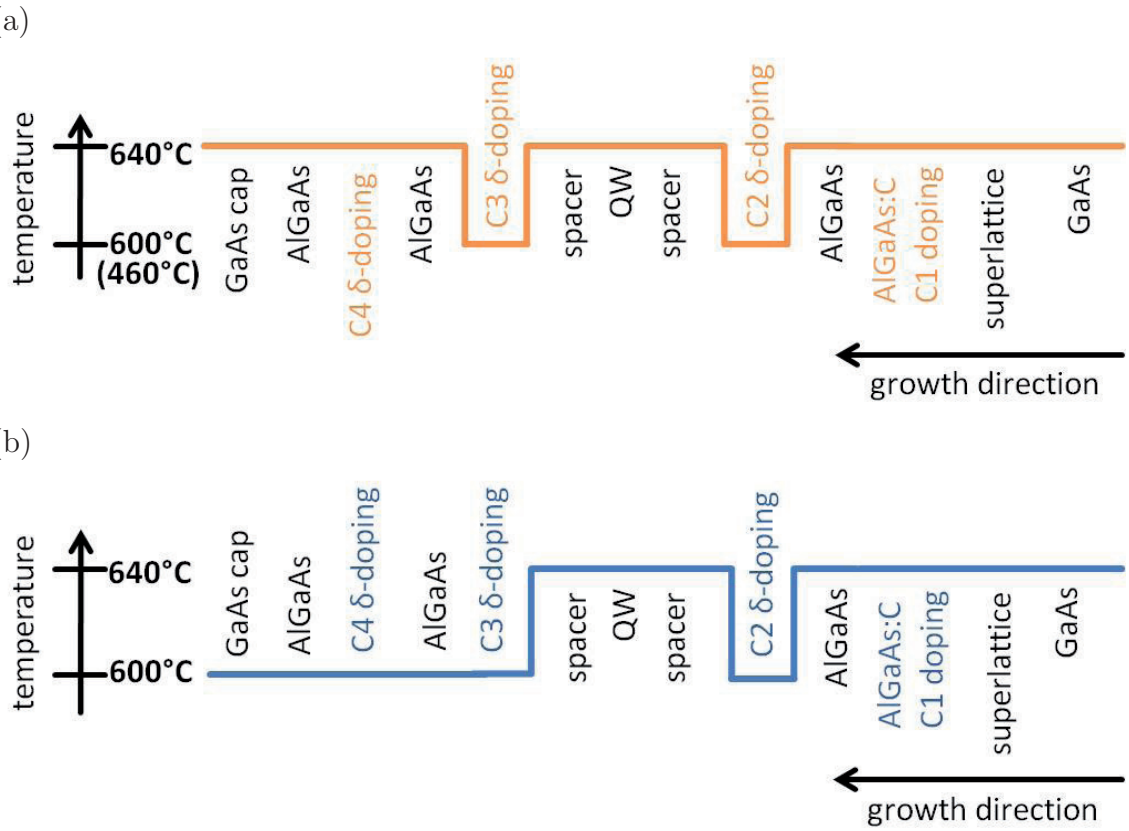

Figure 4.5: *Scheme of the temperature profile during the whole growth process. To compensate the additional heating of the carbon doping cell, the substrate temperature was reduced during doping.*

screening due to increasing hole density. Since both samples with C2 = C3 = 50 s and 60 s exceeded the mobility $1 \times 10^6\,\mathrm{cm}^2/\mathrm{Vs}$ at 1.3 K, their parameters were used in subsequent optimizing procedures.

In both experiments, the C1 = 29 s was kept constant. Its function is only to pin the band edge after the superlattice. The doping is far away from the active region (distance of 400 nm), thus we expect less influence.

In summary, we optimized the doping concentration of C4 and C2 = C3 layers and prepared high quality 2DHGs with mobility exceeding $1 \times 10^6\,\mathrm{cm}^2/\mathrm{Vs}$ at 1.3 K and with low carrier density $1 - 2 \times 10^{11}\,\mathrm{cm}^{-2}$.

Reduction of the growth temperature during the δ-doping process

Now, we will show how the temperature profile during the growth process affects the hole mobility. In this section, we will consider only samples with $x = 0.30$ Al content in the barrier. In this experiment, we used the optimized doping concentration C2 = C3 = 50 s, C4 = 200 s, C1 = 29 s. The flux of the carbon cell was kept

constant for all samples.[6] Usually for the growth of 2DEGs, the substrate temperature is lowered during the doping. Typically, the 2DEG samples are doped at 480°C to prevent the diffusion of silicon at higher temperatures. Substrate temperatures substantially lower than 480°C lead to the formation of crystal defects, [106]. In our case, we have to compensate the high temperature impact of the carbon cell, which typically achieves filament temperatures of ~ 2200°C. This can be done by varying the temperature profile of the active layer.

Fig. 4.5(a) displays schematically the first tested T-profile. Almost the whole structure was grown at 640°C. The substrate temperature was reduced only for the C2- and C3-doping layers to ~ 460°C. These conditions lead to a rather low hole mobility of $0.8 \times 10^6\,\mathrm{cm^2/Vs}$ at 1.3 K ($p = 1.2 \times 10^{11}\,\mathrm{cm^{-2}}$). Applying the temperature $T_D = 600$°C instead of 460°C, the mobility was improved to $1.1 \times 10^6\,\mathrm{cm^2/Vs}$ ($p = 2.0 \times 10^{11}\,\mathrm{cm^{-2}}$). Since all other growth parameters including carbon flux and doping concentration were constant, the significant enhancement of the hole density can be attributed to the change of the growth temperature T_D. This indicates that T_D crucially influences the incorporation of carbon in the crystal lattice. There are two possible scenarios what happened if T_D was too low: either some carbon atoms incorporated not as acceptors but as neutral atoms not providing free holes, or they created n-type defects, which neutralized free holes. The possibility of formation of As antisites is rather improbable at such high temperatures, [107].

Fig. 4.5(b) shows the second applied T-profile. In this case, the temperature was reduced to $T_D = 600$°C not only for C2 and C3 but also for all layers following after the C3-doping layer. Owing to this modification we achieved a very high value of the hole mobility of $\mu = 1.3 \times 10^6\,\mathrm{cm^2/Vs}$ at 1.3 K ($p = 2.0 \times 10^{11}\mathrm{cm^{-2}}$).

Finally, the T-profile affects not only the hole mobility and the hole density but also the persistent photoconductivity effect in our samples, which will be discussed in Section 4.2.

Variation of the aluminum content x in the $Al_xGa_{1-x}As$ barrier

We studied the influence of the Al content x of the $Al_xGa_{1-x}As$ barrier in the dsd-QW on the magnetotransport properties. We applied the improved temperature profile illustrated in Fig. 4.5(b), optimized doping concentration and grew a variety of samples with different Al contents in the range between $x = 0.20$ and 0.35.

First, we concentrate on samples with C2 = C3 = 50 s. In Fig. 4.6, the measured density and mobility is plotted as a function of the Al content x. The peak mobility of $\mu = 1.3 \times 10^6\,\mathrm{cm^2/Vs}$ was obtained in the sample with $x = 0.30$ Al in the barrier material. Interestingly, the hole density increased with increasing Al content x. This observation is in agreement with studies on $Al_xGa_{1-x}As$ bulk layers, where the hole density was reported to increase in our interval of interest $x = 0.20 - 0.35$, [95]. In QWs, the linear enhancement of p in dependence on Al content x was confirmed by Watson *et al.* [108] as well. It is worth to note that these

[6] For all samples discussed in this chapter, we applied the current of 50 A, which gives a carbon doping concentration of $(2.4 \pm 0.4) \times 10^{17}\,\mathrm{cm^{-3}}$, see Fig. 3.2.

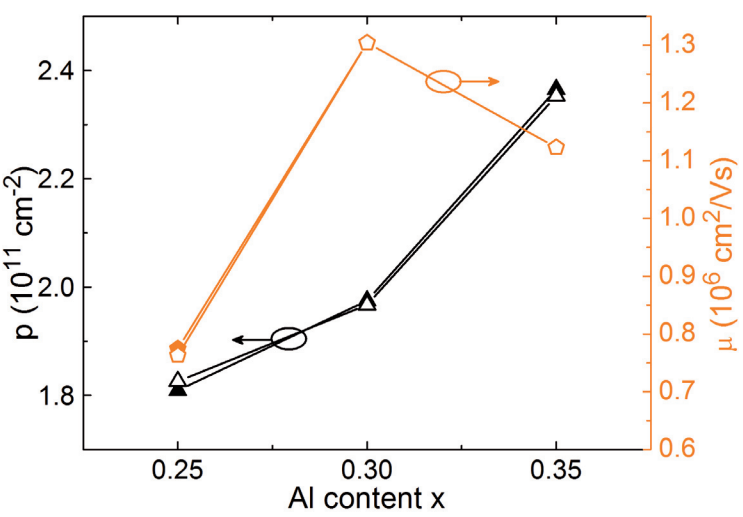

Figure 4.6: *Hole density and mobility versus the Al content x of the $Al_xGa_{1-x}As$ barrier material. All samples have C2 = C3 = 50 s and C4 = 200 s. Measurements were performed at 1.3 K without illumination (full symbols) and after illumination with red light (open symbols).*

samples do not show any pronounced changes of p and μ after illumination, see Fig. 4.6.

Second, samples grown with the doping concentration C2 = C3 = 60 s exhibit similar behavior as illustrated in Fig. 4.6. A very high hole mobility of $\mu = 1.6 \times 10^6\,\mathrm{cm^2/Vs}$ at 1.3 K was reached in the structure with barrier material containing $x = 0.25$ Al. The increase of Al content to $x = 0.35$ resulted in a slightly lower mobility $\mu = 1.0 \times 10^6\,\mathrm{cm^2/Vs}$, but the mobility decreased rapidly for $x = 0.20$ to $\mu \sim 10^4\,\mathrm{cm^2/Vs}$. We want to stress that $\mu = 1.6 \times 10^6\,\mathrm{cm^2/Vs}$ at 1.3 K is the highest hole mobility reported to be grown in this MBE chamber.[7] This sample (in following called dsd-B, see Section 4.4) has a hole density of $p = 1.8 \times 10^{11}\,\mathrm{cm^{-2}}$ and, what is even more important, it does not show any persistent photoconductivity effect.

In addition, we observed a variation of the hole density in dependence on the Al content x also in the ssd-QW structure. The samples with $x = 0.20$ and $x = 0.30$ Al content had the same hole mobility of $\mu = 0.2 \times 10^6\,\mathrm{cm^2/Vs}$ at 4.2 K, but the sample with $x = 0.30$ had an almost two times higher hole density $p_{(x=0.30)} = 1.1 \times 10^{11}\,\mathrm{cm^{-2}}$ than the sample containing $x = 0.20$ aluminum ($p_{(x=0.20)} = 0.6 \times 10^{11}\,\mathrm{cm^{-2}}$). After illumination with red light at 4.2 K and cooling down to 1.3 K, p and μ further increased in both samples, but only the sample (in following called ssd-A, see Section 4.4) with $x = 0.30$ achieved a mobility above $10^6\,\mathrm{cm^2/Vs}$. This value $\mu = 1.2 \times 10^6\,\mathrm{cm^2/Vs}$ represents the highest mobility achieved with the ssd-QW structure in this work. In comparison, the μ of the sample with $x = 0.20$ improved only to $\mu = 0.5 \times 10^6\,\mathrm{cm^2/Vs}$ after cooling it down to 1.3 K.

In conclusion, via development of the symmetric dsd-QW structure with four doping layers and optimizing the growth parameters such as: the doping concentration of the C4, C2 = C3 doping layers, the temperature profile during the growth process and the Al content of the $Al_xGa_{1-x}As$ barrier material, we suc-

[7] For earlier values see Ref. [93, 9].

ceeded in a strong enhancement of the mobility of 2D holes. The best sample has $x = 0.25$ Al content in the barrier and was doped C2 = C3 = 60 s, C4 = 200 s at reduced substrate temperature of $T_D = 600°C$. It exhibits a hole mobility of μ(dsd-B) $= 1.6 \times 10^6\,\mathrm{cm^2/Vs}$ at $T = 1.3\,\mathrm{K}$, which further increases to $\mu = 2.1 \times 10^6\,\mathrm{cm^2/Vs}$ at 20 mK. For comparison, in the asymmetric ssd-QW structure we achieved μ(ssd-A) $= 1.2 \times 10^6\,\mathrm{cm^2/Vs}$ at 1.3 K. Moreover, we suppressed the persistent photoconductivity effect in the dsd-QW samples, for more details see Section 4.2. In the following sections, magnetotransport properties of the best representatives of both sample structures, namely samples ssd-A and dsd-B, will be discussed and quantitatively described.

4.2 Photoconductivity effect

In this section we will study the effect of illumination in our modified dsd-QW structure, see Fig. 4.2. We will concentrate only on the samples with $x = 0.30$ Al in the barrier including the highest mobility samples. The parameters of the samples are listed in Table 4.1. Hole density and mobility were measured at 4.2 K. When we illuminated the sample with a red light emitting diode with a photon energy above the energy gap of the $Al_{0.30}Ga_{0.70}As$ barrier, we observed changes in the p and μ in comparison to the non-illuminated case. In 2DEGs, in which the incorporation of silicon leads to the formation of DX centers (distorted configurations of substitutional Si donors in the $Al_xGa_{1-x}As$ lattice), illumination at low temperatures causes enhancement of the electron concentration, [22, 23]. In contrast, no such effect is considered to take place using carbon as a doping material, even though some comments in literature pointed out changes in the hole density of carbon-doped 2DHGs after illumination, [20, 21]. Yet, there is no model published to explain this effect.

Fig. 4.7 demonstrates the change of the hole density p with the time of illumination with a red LED in three different samples: dsd-I, dsd-II, dsd-III. Their growth parameters and magnetotransport properties are summarized in Table 4.1. As mentioned, the photon energy was higher than the band gap of, both; the GaAs QW and the barrier. Generally, these samples represent three different kinds of behavior, which we observed in our C-doped GaAs/AlGaAs 2DHGs: positive, negative and no persistent photoconductivity (PC), see Fig. 4.7. The data shown in Fig. 4.7 were recorded in the following cycle. The first value at $t = 0$ s was measured in dark environment after cooling the samples to 4.2 K without any previous illumination. Subsequently, the samples were exposed to red light for $t = 20$ s and their density was measured again in the darkness. Then, the samples were illuminated for a further 120 s etc. It is worth to mention that before we noted the value of p we waited for a time until p was constant. All data points were taken subsequently without resetting the hole density to the value at $t = 0$ s by warming up the sample (during the whole measurement procedure the temperature was maintained at 4.2 K). In this sense, the time axis in Fig. 4.7 indicates the overall illumination length.

After illumination, the density changes or stayed constant, as shown in Fig. 4.7. First, sample dsd-I represented by the red curve exhibited an increase of

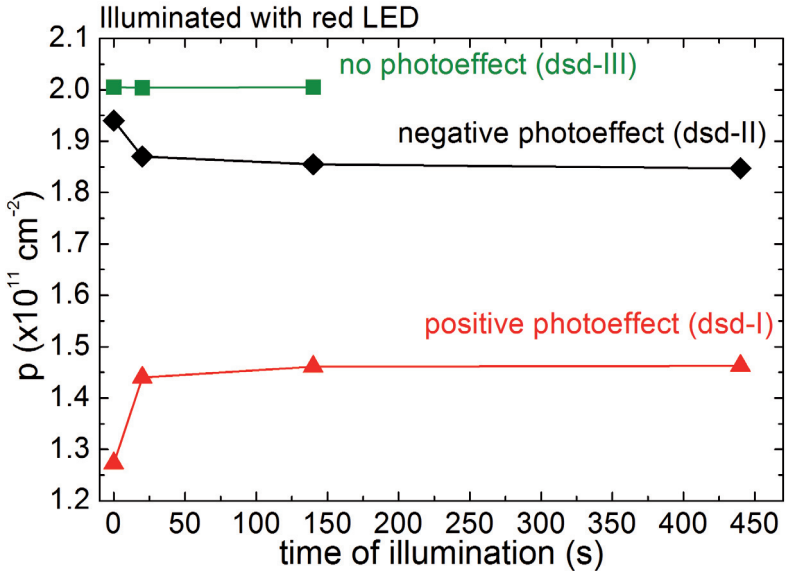

Figure 4.7: *Hole density as a function of the overall time of exposure to red light. The density was measured in the dark environment at a stable temperature of 4.2 K. The value at $t = 0$ s was without any previous illumination. The subsequent data points were taken after illumination, see text. The samples are general examples of different kinds of behavior, found in the carbon-doped GaAs/AlGaAs 2DHGs grown in this work, exhibiting a positive, negative and no persistent PC. The lines are guides to the eyes.*

the hole density. It means, it has a positive persistent PC. Second, the density of sample dsd-II (black curve) decreased after illumination and the sample showed a negative persistent PC. Third, in sample dsd-III (green curve) the illumination did not affect the hole density and mobility (not shown). By a close inspection of the data in Fig. 4.7, it is obvious that the most significant change of p occurs after 20 s exposure to red light. There is also a small change if we illuminated the samples subsequently for an extra 120 s. But further illumination did not seem to have any influence on the carrier density. Thus, it is necessary to illuminate for some minutes to get a constant density.

For a better understanding of this effect we recorded the time-dependent change of the Hall voltage before, during and after the illumination. To make sure that the samples are completely cooled down to 4.2 K and the conditions are stable, we registered U_{xy} for some time in the darkness until no change was observed. In the experiment we used the red LED like before. Fig. 4.8(a) displays the hole density during the whole experimental procedure for the three samples: dsd-I, dsd-II and dsd-III. The value of p at $t = 0$ min represents the starting value measured in the dark. As the red LED was turned on, the hole density decreased rapidly. This is a consequence of building electron-hole pairs in the barrier and recombination of the drifted electrons with holes in the QW. After the LED was turned off, the hole density began to relax towards its final value. In comparison to its initial value, the final density was observed to be higher, lower or the same, pointing out positive, negative or no persistent PC in sample dsd-I, dsd-II and dsd-III, respectively.

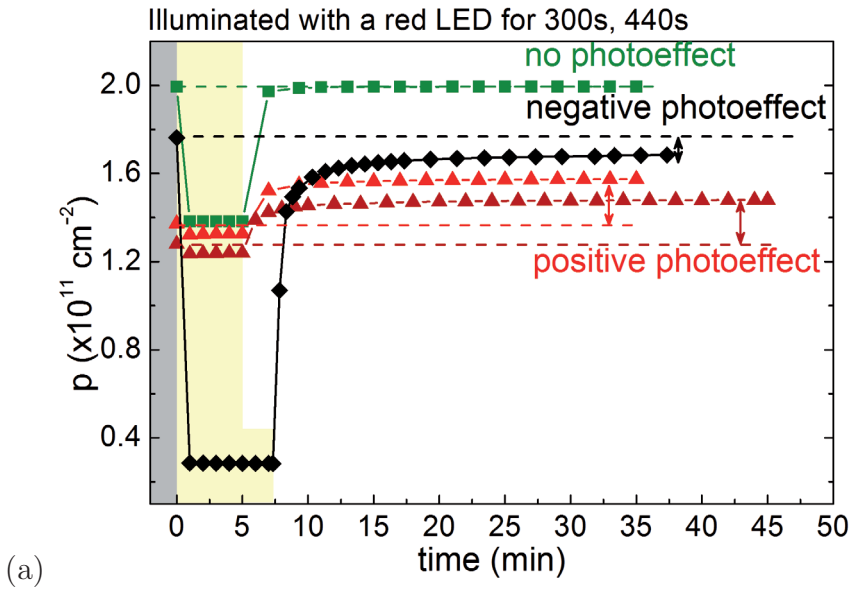

(a)

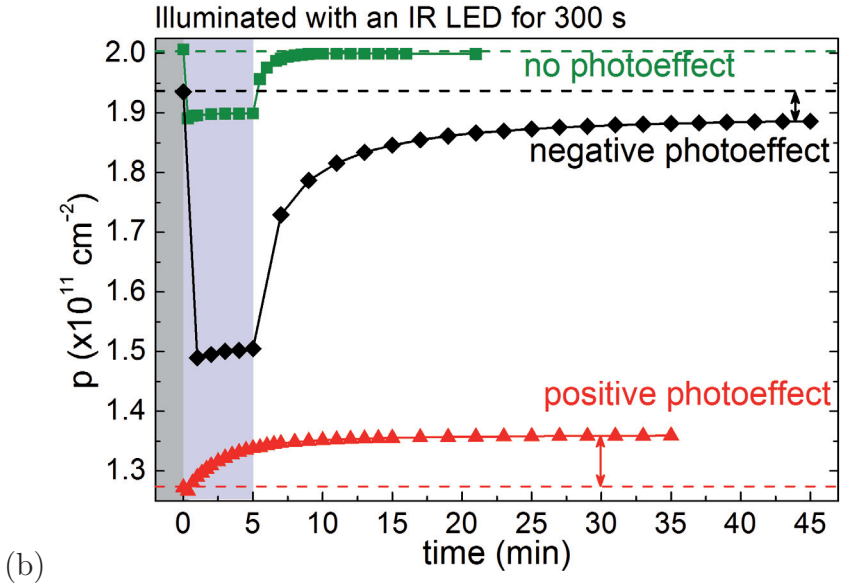

(b)

Figure 4.8: *Temporal evolution of the hole density during illumination (yellow/blue area) and after illumination. The first value at $t = 0\,s$ was measured in the darkness before exposure to light. The curves correspond to three different samples: (red ▲) sample dsd-I, (black ♦) sample dsd-II and (green ■) sample dsd-III, which exhibit positive, negative and no persistent PC effect, respectively. The lines are guides to the eyes. (a)/(b) displays measurements after illumination with a red/an IR LED. Note different scaling of the density axes in (a) and (b).*

In order to get more information about the possible origin of the persistent PC, we repeated the procedure with an infrared (IR) LED. The IR LED emitted at 1300 nm at room temperature and exhibited a peak at 1250 nm with a FWHM of ~ 25 nm at 4.2 K. Hence, the photon energy was below the band gap energy of the $Al_{0.30}Ga_{0.70}As$ barrier and even below the band gap of the GaAs QW. Fig. 4.8(b)

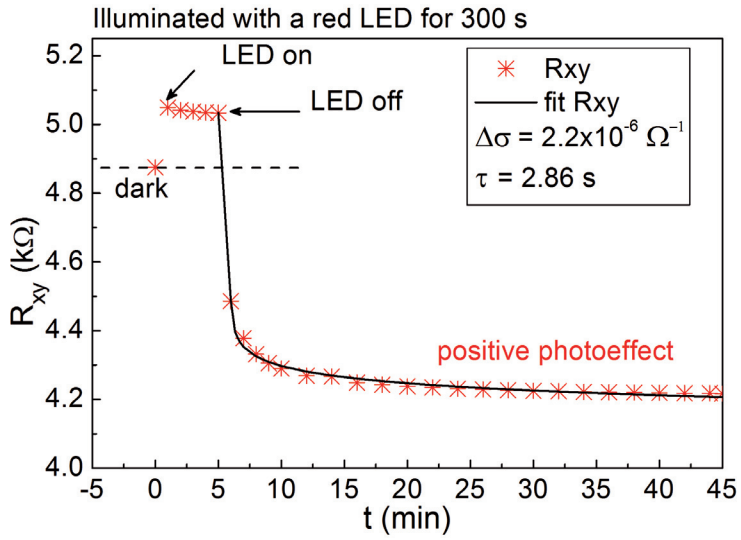

Figure 4.9: *Fit of the Hall resistance of sample dsd-I using the non-exponential decay given in Eq. 4.1, after illumination with red light.*

shows the time-dependence of the hole density measured during the experimental procedure. In two samples we observed a negative PC during the illumination and a non-exponential increase of the hole density afterwards, which is a behavior very similar to Fig. 4.8(a). Interestingly, sample dsd-I (positive persistent PC) exhibited a somewhat different phenomenon: after turning on the LED, the density decreased for only a few seconds below the initial value and then kept increasing continuously. If the initial and final values of p were taken into account, samples dsd-I, dsd-II and dsd-III kept showing positive, negative and no persistent PC, respectively. Because of the qualitatively very similar temporal evolution of the hole density (apart from the small discrepancy by sample dsd-I) after the illumination with the IR LED as well as with the red LED, it is possible to infer that there must be some defect levels in the band gap responsible for these density changes. Further, it is important to emphasize that the negative PC during the illumination with IR LED is much less distinct (i.e. resulting in a smaller change of the density) than with the red LED, cf. the scale of the y-axis in Figs. 4.8(a) and (b).

An analogous time decay of the Hall resistance has been reported on Be-

Sample	Persis. PC	C2, C3 (s)	C4 (s)	T_D(C2, C3) (°C)	T_D(C4) (°C)	p (10^{11} cm^{-2})	μ (10^6 cm^2/Vs)
dsd-I	pos.	50	200	460	640	1.3	0.8
dsd-II	neg.	80	140	460	640	1.9	0.9
dsd-III	no	50	200	600	600	2.0	1.3

Table 4.1: *Table of growth parameters and magnetotransport properties. The second and third column list the time for C2, C3 and C4 δ-doping layers, T_D is the substrate temperature during the doping process, see Section 4.1.2. The hole density p was measured in the dark environment without illumination at 4.2 K. The hole mobility μ was determined without illumination at 1.3 K.*

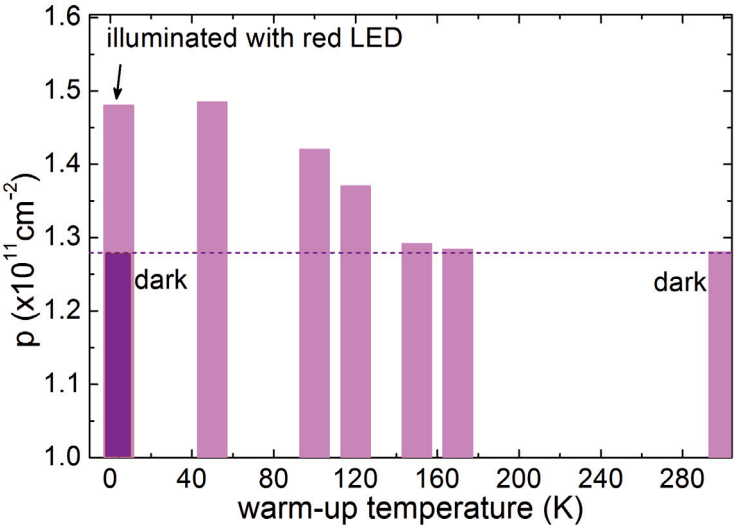

Figure 4.10: *The initial value of the hole density can be restored by warming-up the sample above 170 K. For the description of the measurement procedure see text.*

doped GaAs/$Al_{0.50}Ga_{0.50}$As heterojunctions, [109], and GaAs/$Al_{0.50}Ga_{0.50}$As standard dsd-QWs [110]. The non-exponential decay of the Hall resistance after switching off the LED could be phenomenologically described by a logarithmic law [109, 111]:

$$\frac{1}{R_{xy}} = \frac{1}{R_0} + \Delta\sigma \left[\ln\left(\frac{t - t_0}{\tau} + 1 \right) \right]^{\gamma} \tag{4.1}$$

where R_0 is the Hall resistance at t_0 when the LED was switched off, $\Delta\sigma$ is an amplitude factor, τ is a time constant characteristic of the decay and γ is a power term. We used Eq. 4.1 to fit our data presented in Fig. 4.8. The parameters, which provided the best fit to the experimental data are listed in Table 4.2. Fig. 4.9 demonstrates an excellent match between the theoretical curve and measured points for sample dsd-I.

Comparison of the fit parameters for both LEDs revealed that the measurements with the IR LED have a lower amplitude factor $\Delta\sigma$ and of about one order of magnitude longer characteristic time τ. In literature, $\Delta\sigma$ was reported to be dependent on the intensity of illumination and to increase with increasing cur-

Sample	Persistent PC	Illumination		$\Delta\sigma$ ($10^{-6}\,\Omega^{-1}$)	τ (s)	γ
		Time	LED			
dsd-I	positive	300 s	red	2.2	2.9	1
		300 s	IR	0.9	30.6	1
dsd-II	negative	440 s	red	7.1	3.8	1
		300 s	IR	5.4	17.2	1
dsd-III	none	300 s	red	decays very quickly		
		300 s	IR	1.8	5.4	1

Table 4.2: *Fitting parameters determined by the fit of the non-exponential decay of the Hall resistance by Eq. 4.1. An example of the fit is shown in Fig. 4.9.*

rent through the LED, [109]. Although the intensity of illumination with the IR LED was greater than with the red LED in our case[8], the amplitude factor $\Delta\sigma$ is lower. Furthermore, the persistent changes of the density after illumination were not so pronounced using the IR LED. If we compared the initial hole density at $t = 0\,\text{min}$ with its stable value at $t = 30\,\text{min}$ of sample dsd-I, it increased by $\Delta p(\text{red LED}) = 0.20 \times 10^{11}\,\text{cm}^{-2}$, but only by about $\Delta p(\text{IR LED}) = 0.09 \times 10^{11}\,\text{cm}^{-2}$ using an IR LED. Moreover, the negative PC effect, which arose during the illumination and caused significant non-persistent reduction of p, was much more pronounced when using a red LED. For illustration, the density of sample dsd-II lowered even by one order of magnitude from $p_{initial} = 1.76 \times 10^{11}\,\text{cm}^{-2}$ to $p = 0.29 \times 10^{11}\,\text{cm}^{-2}$ during the exposure to red light in contrast to $\Delta p(\text{IR LED}) = 0.45 \times 10^{11}\,\text{cm}^{-2}$, cf. the values in the shaded areas in Figs. 4.8(a) and (b).

Kraak *et al.* [110] studied the effect of illumination in a Be-doped GaAs/$Al_{0.50}Ga_{0.50}As$ QWs and explained it with some donor-like states, which are present in the AlGaAs barrier. According to the investigations, the whole process can be understood as sketched in Fig. 4.11. In the initial state, the donor-like states lie below the Fermi energy and are neutral. When illuminating the structure with a red LED, the electrons are excited from these shallow levels into the conduction band and relax quickly into the QW. Then, these photoexcited electrons recombine with 2D holes in the QW and a negative PC is observed. After switching off the LED, holes tunnel slowly back from the donor-like states into the QW, causing a non-exponential increase of the hole density. Moreover, some electrons can be trapped at deep levels situated at the GaAs/AlGaAs inverted interface (confirmed by deep level spectroscopy in Ref. [112]). The trapped electrons cannot recombine with holes in the QW and an overshoot of holes arises, resulting in a positive persistent PC.

Nevertheless, this model cannot be directly applied to our observations without corrections because there are some discrepancies between our measurements and those presented by Kraak *et al.* [110]. First and very important, it is the different barrier composition. The authors in Ref. [110] used an $Al_{0.50}Ga_{0.50}As$ barrier. This composition exhibits higher band-gap energy than the photon energy emitted by a red LED. Hence, the authors could assume excitation from shallow levels. In our case, the band-gap energy at the Γ point of our $Al_{0.30}Ga_{0.70}As$ barrier is $\sim 1.7\,\text{eV}$ and it is lower than the photon energy of the red LED $\sim 1.9\,\text{eV}$ that we used. This implies that we excited the electrons over the band gap of the $Al_{0.30}Ga_{0.70}As$ barrier, from the valence band to the conduction band. Second, the authors in Ref. [110] did not observe any changes in the density after illumination with an IR LED. This is in stark contrast to our measurements. We found that the negative PC and the non-exponential decay persist and exhibit a similar shape when using an IR LED for illumination (apart from sample dsd-I, where the negative PC part is not so distinct, see Fig. 4.8). Moreover, our IR LED has photon energy of $\sim 0.99\,\text{eV}$, which is even below the band gap of the GaAs QW ($\sim 1.51\,\text{eV}$ at $4.2\,\text{K}$). In summary, the model presented by Kraak *et al.* is able to explain the negative PC effect arising during exposure to light (red or IR) in our samples. However, our experiments with

[8]Here, we applied significantly higher current through the IR LED and it was aimed directly at the sample.

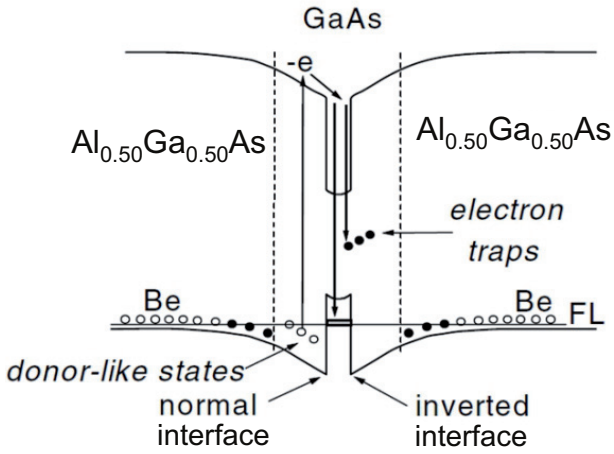

Figure 4.11: *[110], Diagram explaining a negative PC and a positive persistent PC of Be-doped 2DHG in an $Al_{0.50}Ga_{0.50}As/GaAs/Al_{0.50}Ga_{0.50}As$ heterostructure. Kraak* et al. *assumed that there are some donor-like states in the AlGaAs barrier, which are responsible for the effect of illumination. FL marks the Fermi level.*

the IR LED point out some deep defect levels in the band gap, rather than shallow donor-like states, in our carbon-doped heterostructures.

The initial value of p in darkness could be recovered if we warmed up the sample above 170 K. We did the experiment demonstrated in Fig. 4.10 for sample dsd-I exhibiting a positive persistent PC. At 4.2 K, we recorded p in darkness and after illumination with a red LED. Then we warmed up the sample to 50 K, cooled it down to 4.2 K and measured the value of p again. We repeated this warming-up and cooling-down procedure for a series of temperatures up to room temperature and observed a continuous decrease of the hole density. As a result we found that the initial value could be recovered by warming up the sample above 170 K.

It is worth to note here that small differences in the cooling down process can lead to slight variations of the low-temperature density. This is obvious especially in Fig. 4.8(a), where both red curves correspond to sample dsd-I. They represent the same measurement done in another cooling cycle. Although the initial values of p were not exactly equal, the shape of the curve was maintained as well as the difference $\Delta p = 0.20 \times 10^{11}\,\mathrm{cm}^{-2}$ between $p_{initial}$ at $t = 0$ min and p_{final} at $t = 30$ min. This could be a sign of some defect levels in this sample.

Reduction of the growth temperature during the δ-doping process

A possible explanation for the behavior described above can be found if we have a closer look at the growth conditions, especially the substrate temperature while doping. As already mentioned in Section 3.1, the carbon cell has to be heated up for the doping procedure and can reach very high temperatures up to 2200°C during the doping process. For comparison, the operating temperatures of Ga and Al cells are much lower at about $T(\mathrm{Ga}) = 930 - 960$°C and $T(\mathrm{Al}) = 1050 - 1090$°C. Due to this additional heating of the carbon cell, the substrate temperature has to be reduced to compensate for the thermal impact, otherwise the substrate temperature can rise significantly, which leads to formation of crystal defects.

In this work, we modified the T-profile during the growth process as illustrated in Figs. 4.5(a) and (b) and observed strong impact on the hole mobility and density, see Section 4.1.2. Now, we will discuss their influence on the persistent

PC, i.e. persistent change of the density Δp after illumination. In the first tested case (Fig. 4.5(a)), almost the whole structure was grown at 640°C, only the C2- and C3-doping layers were grown at lower temperature T_D. If we reduced the temperature to $T_D = 460$°C, the hole density increased after illumination with a red LED by $\Delta p \sim 19\%$, see sample dsd-I in Table 4.3(a). The hole mobility enhanced by 40% after illumination and achieved values on the order of $10^6\,\mathrm{cm^2/Vs}$. Similarly, sample dsd-II exhibiting a negative persistent PC was grown under the same growth conditions. Afterwards, we modified this T-profile and used $T_D = 600$°C, see sample dsd-IV in Table 4.3(a). In comparison to sample dsd-I, sample dsd-IV has an almost two times higher carrier density and, more interestingly, Δp is only 5% in this case. Additionally, it still exhibits a mobility above $10^6\,\mathrm{cm^2/Vs}$.

Applying the second T-profile sketched in Fig. 4.5(b), we succeed in eliminating the persistent PC effect. In this case we adjusted $T_D = 600$°C not only for the C2- and C3-doping layers, but also for all layers following after the C3-doping layer, including C4. For comparison, the C4-doping layer was grown at $T_D = 640$°C as the rest of the structure in the first T-profile, cf. Fig. 4.5(a). As a result, sample dsd-III did not show any persistent PC ($\Delta p = 0\%$), see Table 4.3(b).[9] Moreover, the hole mobility remained constant before and after the illumination and achieved $\mu = 1.30 \times 10^6\,\mathrm{cm^2/Vs}$ at 1.3 K, which is a much higher value than provided by the previous samples, cf. Table 4.3.

In conclusion, we succeeded in suppressing the persistent PC effect in our carbon-dsd GaAs/AlGaAs heterostructures. The persistent PC data did not show any significant trend in other parameters than in dependence on the substrate temperature while doping, which seems to play a crucial role in carbon incorporation into the crystal lattice. If the growth temperature is too low or too high it can lead to the formation of defect levels. Time-dependent magnetotransport measurements show a negative PC during the illumination and a non-exponential increase of the hole density upon it. This relaxation of the Hall resistance is well-described with Eq. 4.1. The samples exhibited a positive and a negative persistent PC not only after exposure to red light but also by using an IR LED with a photon energy below the band gap of the GaAs QW. This indicates that possible defect levels must be situated deep in the band gap. Despite comparing all samples, no obvious indication could be found to clarify the responsible mechanism behind the fact that some samples show positive and some negative persistent PC. In addition, a presence of deep levels in carbon-doped heterostructures was demonstrated by C. Gerl in Ref. [21], where the author described a hysteretic change of the hole density with an applied gate voltage. For a detailed analysis of the defect levels, further experiments, such as deep level transient spectroscopy (DLTS) are needed, but this is beyond the scope

[9] The persistent PC was examined on the ssd-QW structure, too, see also [21, 93]. As a barrier material, $Al_{0.30}Ga_{0.70}As$ was grown. The overall growth temperature was kept at 640°C and we varied the temperature T_D of the δ-doping layer. It seems as if the optimum could be achieved in the sample doped at $T_D = 580$°C. In this case, the 4.2 K-hole density did not change significantly after exposure to red light. The reduction of the substrate temperature to $T_D = 560$°C and 550°C led to $\Delta p = 11\%$ and 10%, respectively. The hole mobility was maximal in the sample with $T_D = 580$°C and decreased with decreasing T_D in the other samples.

(a)

Sample	T_D(C2, C3) (°C)	p_{dark} (10^{11} cm^{-2})	p_{ill} (10^{11} cm^{-2})	Δp	μ_{dark} (10^6 cm^2/Vs)	μ_{ill} (10^6 cm^2/Vs)	$\Delta\mu$
dsd-I	460	1.20	1.43	19%	0.78	1.09	40%
dsd-IV	600	2.05	2.16	5%	1.10	1.06	-4%

(b)

Sample	T_D(C4) (°C)	p_{dark} (10^{11} cm^{-2})	p_{ill} (10^{11} cm^{-2})	Δp	μ_{dark} (10^6 cm^2/Vs)	μ_{ill} (10^6 cm^2/Vs)	$\Delta\mu$
dsd-IV	640	2.05	2.16	5%	1.10	1.06	-4%
dsd-III	600	1.97	1.97	0%	1.30	1.30	0%

Table 4.3: *Hole density and hole mobility at 1.3 K measured before (dark) and after illumination with a red LED (ill) in dependence on substrate temperature during the growth of the carbon δ-doping layers C2, C3 and C4. (a) summarizes samples grown with T-profile shown in Fig. 4.5(a): a variation of T_D(C2) = T_D(C3), T_D(C4) = 640° C was kept constant, (b) samples grown with T-profile sketched in Fig. 4.5(b): a change of T_D(C4) while T_D(C2,C3) = 600° C was kept constant.*

of this work. Samples in which the persistent PC effect was suppressed, demonstrate the highest hole mobility, indicating low defect density.

4.3 Nextnano^3 simulations of the valence-band structure

In this section we will present 8 × 8-band $\mathbf{k}\cdot\mathbf{p}$-calculations of the valence-band dispersion using the nextnano^3 program package. The theoretical basics and computational procedure were described in Section 3.5. For the theoretical investigations we chose samples ssd-A and dsd-B. Both samples were extensively studied experimentally and the results will be shown in Section 4.4. The main part of the sample structure is a 15 nm wide QW separated from the carbon-doping layers by an 80 nm thick spacer layer consisting of $Al_{0.30}Ga_{0.70}As$ in sample ssd-A and of $Al_{0.25}Ga_{0.75}As$ in sample dsd-B. The exact layer sequences are depicted in Figs. 4.1 and 4.2. The calculations of the valence-band profile show great differences between these two structures. We will show that the symmetry of the structure is very important regarding the SIA-induced spin splitting.

Fig. 4.12 compares the valence-band structure of both samples. The three uppermost subbands: HH1 (heavy-hole), LH1 (light-hole) and HH2 are plotted versus the in-plane wave vector $k_{||}$. The energy axis is rescaled with respect to the Fermi level E_F, which is defined as $E = 0$ meV and its position is marked with a dashed line corresponding to the hole density of p(ssd-A)= 1.2×10^{11} cm^{-2} and p(dsd-B)= 1.9×10^{11} cm^{-2} in Figs. 4.12(a) and (b), respectively. In both samples only the first HH1 subband is occupied. The subbands exhibit strongly nonparabolic shape.

This is a consequence of the coupling between HH and LH states, which are separated in energy due to quantum confinement in the GaAs QW, see also Section 2.3. At higher $k_{||}$ values the bands come closer to each other and an anti-crossing takes place; compare HH1 and LH1 subbands in Figs. 4.12(a), (b) with the scheme in Fig. 2.3. Aside from the nonparabolicity, the band structure exhibits distinct anisotropy between the [011] and the [001] crystallographic directions (solid and dashed lines in Fig. 4.12). As a consequence, the dispersion has a rosette-like shape, see Figs. 4.12(c), (d). This kind of anisotropy (called warping) reflects the p-like origin of the GaAs valence band, see also Section 2.3. For the asymmetric QW, a comparison with literature confirms a good qualitative agreement between our calculations of the band structure and those in Ref. [15]. The inset in Fig. 4.12(b) illustrates that the wave function of sample dsd-B is situated in the middle of the QW underlining the symmetry of this structure in contrast to the ssd-QW, see inset in Fig. 4.12(a).

SIA-induced splitting is one of the most interesting features of the band structures and can be determined from the nextnano^3 simulations. Due to the structure inversion asymmetry, the twofold degeneracy of the subbands is lifted and they split into two subbands with different spin orientations. Hence, the spin splitting is most expected in the asymmetric QW of sample ssd-A. Indeed, this is clearly recognizable in Fig. 4.12(a) cf. the black and red curves. From the Fermi wave vectors k_1 and k_2 of both spin-splitted subbands of the HH1 subband and comparing the densities p_1 and p_2 we estimated a theoretical spin splitting of $\approx 8\%$ in sample ssd-A. On the basis of these considerations, one would not expect any Rashba splitting in the symmetric QW of sample dsd-B. However, our calculations revealed some small spin splitting also in this sample (not recognizable in Fig. 4.12(b) due to the selected scaling). In this case, the spin-splitted subbands have only slightly different Fermi wave vectors and from their densities we determined a very low carrier imbalance of $\approx 1\%$. Apparently, in this symmetric-as-grown sample some small asymmetry must still be present as well. Comparison with the experimentally determined values from the beating pattern of the SdH oscillations will be given in Section 4.4.1.

The spin splitting calculated from the theoretical band structure reflects the Rashba spin splitting directly. The reason is that in nextnano^3, the Dresselhaus term is not included. Irrespective of the symmetry of the QW, a spin splitting of the subbands must still occur as a consequence of bulk inversion asymmetry, see Section 2.4. However, the findings in literature show that the bulk inversion asymmetry can be neglected besides the structure inversion asymmetry concerning the magnitude of the spin splitting for similar ssd-QW structures as investigated in our case, [59]. Nevertheless, the missing Dresselhaus term in the simulations makes it difficult to compare the results with magnetotransport measurements, because its superposition with the Rashba term introduces an additional anisotropy into the subband dispersion. This is illustrated in Figs. 2.4(b) and (c). In the simulations done by nextnano^3, the [011] and the [01$\bar{1}$] orthogonal directions are identical, see Figs. 4.12(a),(b). The BIA term, if included, leads to a reduction of the symmetry of the rosette-like shape of the dispersion from 4-fold (see Figs. 4.12(c), (d)) to 2-fold, as reported by Winkler [15].

In addition, we calculated the effective mass theoretically. The effective

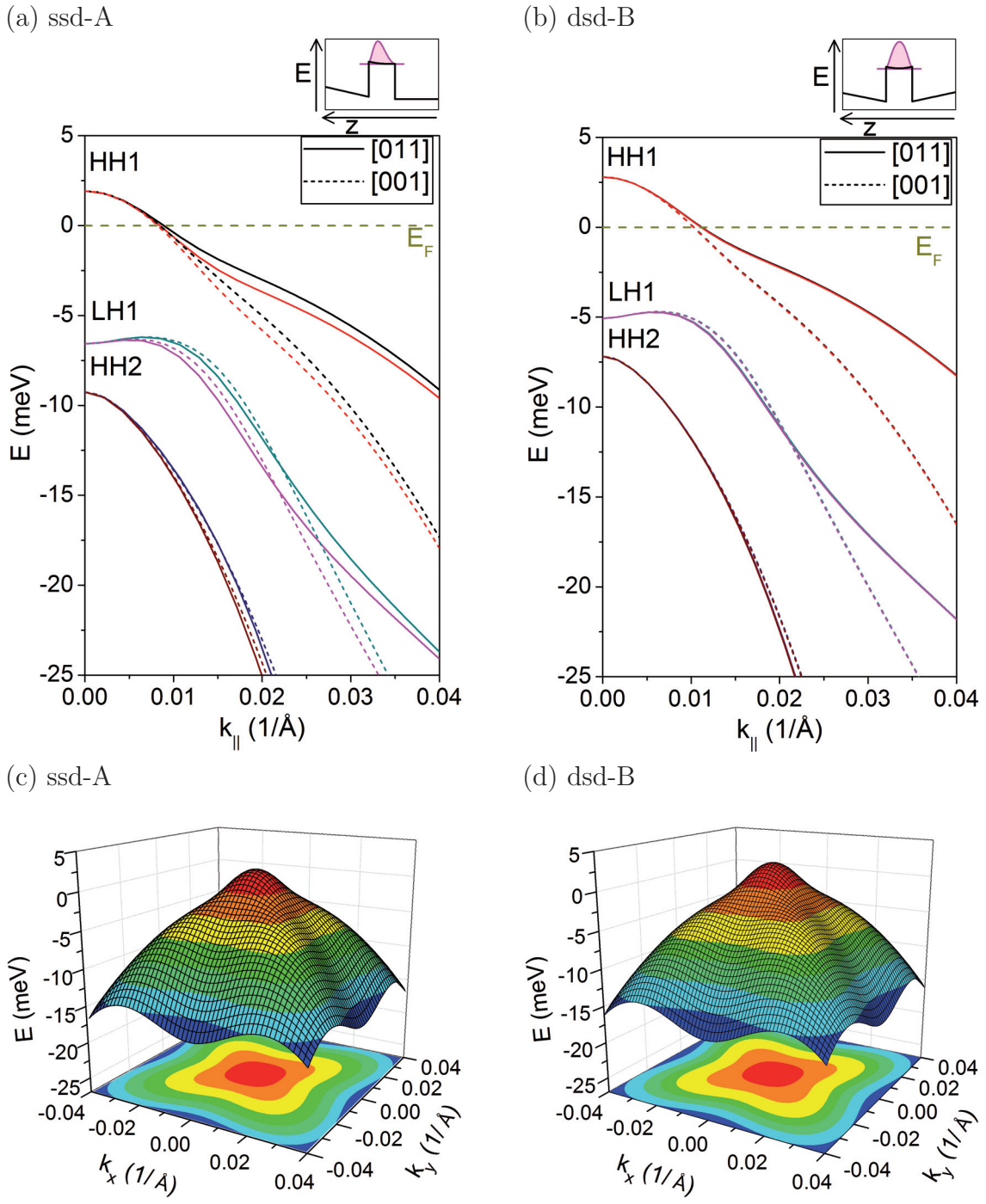

Figure 4.12: *Anisotropic valence-band dispersion of sample (a) ssd-A and (b) dsd-B. The 2DHG is confined in the 15 nm GaAs QW with $Al_xGa_{1-x}As$ barrier with $x = 0.30$ and 0.25 for sample ssd-A and dsd-B, respectively, see also Figs. 4.1 and 4.2. The valence-band structure was calculated by means of a 8×8-band $\mathbf{k} \cdot \mathbf{p}$ method using the nextnano³ program package. Horizontal lines represent position of the Fermi energy. In both samples, the subband dispersion is nonparabolic with distinct HH-LH anti-crossings (shown for HH1 and LH1), and is anisotropic (compared for the [011] and [001] crystallographic directions). The asymmetric sample ssd-A, shown in (a), exhibits pronounced spin splitting of the subbands. Inset (a), (b): Scheme of the valence-band edge of the QW, shaded area stands for the carrier density profile. (c) and (d) show the dispersion of the HH1 subband of samples ssd-A and dsd-B, respectively.*

mass is defined as $m^* = \hbar^2(d^2E/dk^2)^{-1}$. For the 2D electrons near the Γ point, where the conduction band proceeds roughly parabolic in $k_{||}$, the effective mass can be taken as constant. However, such a simple method cannot be applied on 2D holes. Contrary to electrons, the subbands in the valence band are strongly nonparabolic (cf. Fig. 4.12) and as a consequence m_{eff}, calculated as a second derivative, changes with $k_{||}$. Moreover, close to the point of inflection of the dispersion curve, m_{eff} is very likely to achieve values greater than one or negative (in units of m_0). We will shortly illustrate the problems arising from the evaluation of the effective mass from the band dispersion on sample dsd-B. In Fig. 4.12(b), the HH1 subband is the only occupied subband and it exhibits a point of inflection near the Fermi level. For its uppermost subband we derived $m_{eff} = 0.52\,m_0$ at $k_{||} = 1.1 \times 10^8\,\mathrm{m}^{-1}$ along the [011] direction but along the [001] we got m_{eff} = -0.80 m_0. Small deviations in the Fermi wave vector induce large variations of m_{eff}. Thus, the error in this estimation of m_{eff} is large. Furthermore, it is important to note that also the lower spin-splitted subband of the HH1 subband contributes to the transport. It has a slightly different band profile at the Fermi energy and also its contribution to m_{eff} must be taken into account. As the discussion above shows, a single effective mass is not sufficient to describe the valence-band physics. Especially, near the Fermi energy m_{eff} changes abruptly. Hence we did not try further to estimate effective masses from simulation.

4.4 Magnetotransport measurements

Transport properties of samples ssd-A and dsd-B were measured in a dilution refrigerator at a base temperature of 20 mK. Measurements were performed in a 4-terminal geometry under an applied ac current of 10 nA. The samples were fabricated in L-shaped Hall-bars with a width of $W = 200\,\mu$m and a length of $L = 1200\,\mu$m.

In Fig. 4.13 ρ_{xx} and ρ_{xy} are plotted as a function of a magnetic field applied perpendicular to the 2DHG plane. The high quality of both heterostructures is documented by the observation of pronounced integer quantum Hall plateaus, fractional quantum Hall states and well-developed SdH oscillations. For example, ν = 5/3, 4/3, 2/3, 3/5 are marked in Fig. 4.13. At these fractional states, sample dsd-B exhibits fully-developed minima with $\rho_{xx} = 0\,\Omega$. Moreover, in sample ssd-A

Sample	Crystal direction	p ($10^{11}\,\mathrm{cm}^{-2}$)	μ ($10^6\,\mathrm{cm}^2/\mathrm{Vs}$)	m_{eff} (m_0)	τ_t (ps)	τ_q (ps)	τ_t/τ_q
ssd-A	[011]	1.20	0.80	0.41	186	16.0	12
	[01$\bar{1}$]	1.14	0.96	0.40	218	19.8	11
dsd-B	[011]	1.94	2.01	0.53	606	5.6	108
	[01$\bar{1}$]	1.94	2.14	0.53	646	6.6	98

Table 4.4: *Table of the most important magnetotransport data from the whole Section 4.4, measured at 20 mK in the dark. The accuracy of m_{eff}, τ_t, τ_q derived from the fitting procedure is 10%.*

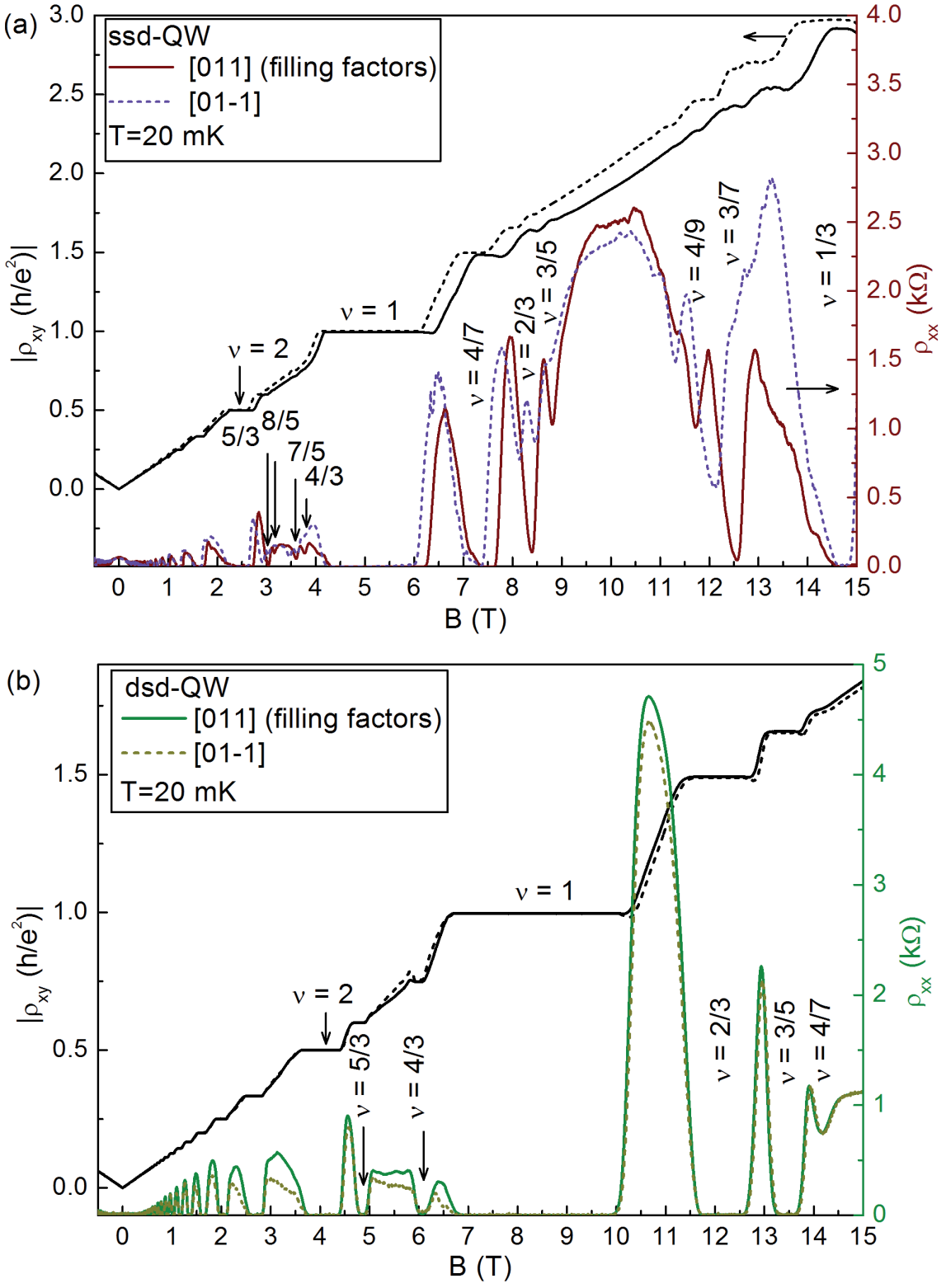

Figure 4.13: *Hall resistance ρ_{xy} (black lines) and longitudinal magnetoresistance ρ_{xx} (a) (red and magenta line) of sample ssd-A (asymmetric QW); (b) (olive and green line) of sample dsd-B (symmetric QW). Measurements were done at 20 mK along [011] (solid lines) and [01$\bar{1}$](dashed lines) crystal directions.*

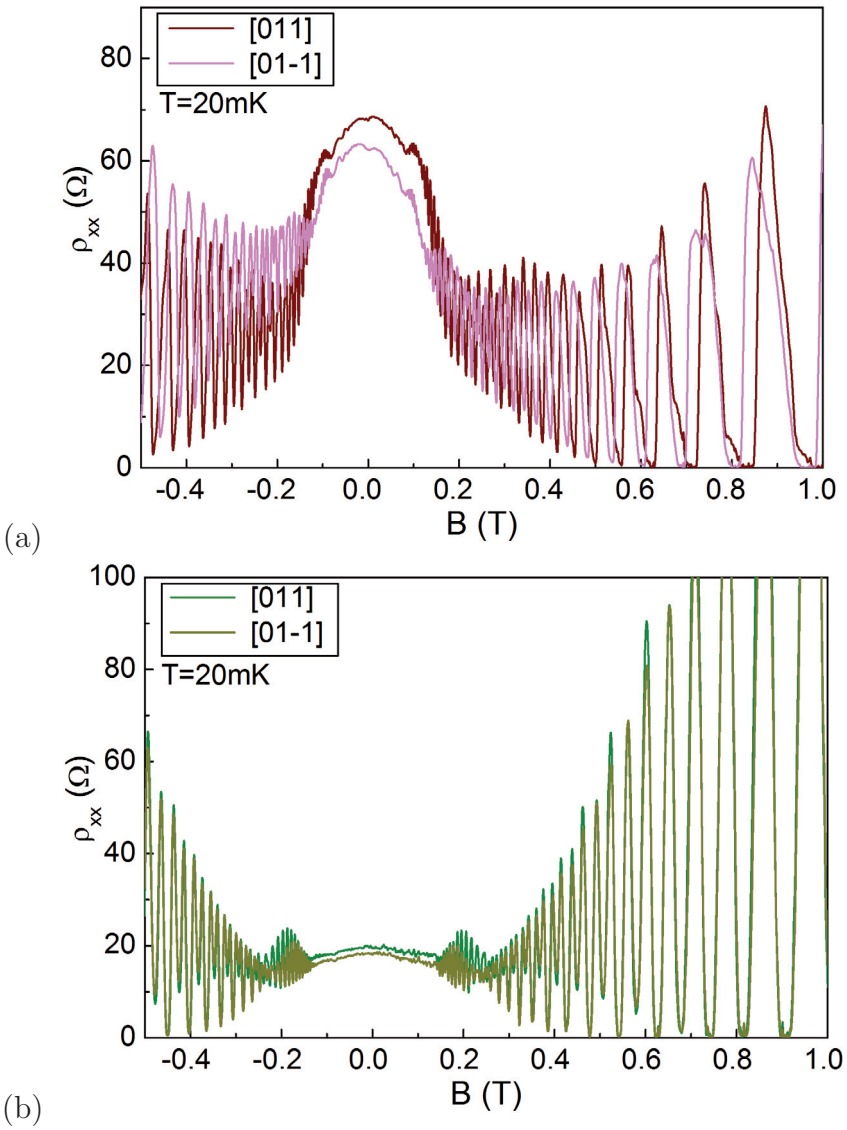

Figure 4.14: *Beating pattern of SdH oscillations of (a) sample ssd-A and (b) sample dsd-B at $T = 20\,mK$.*

further fractional states $\nu = 8/5,\ 7/5,\ 4/9,\ 3/7$ are present, not only as minima in longitudinal resistance, but also as plateaus in Hall resistance.

Both samples generate well-pronounced SdH oscillations. At higher magnetic fields, the ρ_{xx} minima are approaching $0\,\Omega$. Thus, the presence of a parallel conducting layer in these structures can be excluded, [113]. At low magnetic fields up to 0.7 T, a beating pattern of the SdH oscillations appears, see Fig. 4.14. This superposition of two different frequencies indicates a spin splitting of the uppermost HH subband and will be discussed in detail in Section 4.4.1. In sample ssd-A, a negative magnetoresistance dominates the ρ_{xx} curve around $B = 0\,\mathrm{T}$. It originates from the hole-hole interaction effect, which will be quantitatively investigated in Section 4.4.4.

Moreover, there is a distinct difference between the two orthogonal crystallographic directions. First, the SdH minima in sample ssd-A are shifted relative to each other. This indicates different carrier densities along [011] and [01$\bar{1}$] directions. From the slope of the Hall curve, we derived $p_{[011]} = 1.20 \times 10^{11}\,\mathrm{cm}^{-2}$ and $p_{[01\bar{1}]} = 1.14 \times 10^{11}\,\mathrm{cm}^{-2}$. Although both values do not differ significantly, the effect in magnetotransport measurements is clearly recognizable as shifted minima of SdH oscillations and different slopes of the Hall curves. Because the magnetotransport data for both directions were recorded simultaneously on a single piece of sample, which was fabricated in L-shaped Hall-bar geometry, density fluctuations between different sample pieces can be excluded. Since the SdH measurements probe the whole Fermi surface, one would not expect any density differences between crystallographic directions. This topic will be discussed in detail in Section 4.4.1. Sample dsd-B, doped at both sides of the QW, exhibits a hole density of $p = 1.94\times10^{11}\,\mathrm{cm}^{-2}$, which is almost twice as high as the density of sample ssd-A. Second, the hole mobility calculated from the sheet resistivity at $B = 0\,\mathrm{T}$ is anisotropic and reaches a higher value along the [01$\bar{1}$] direction in comparison to the [011], cf. Table 4.4.

In sample dsd-B, we got a very high hole mobility of $\mu = 2.14\times10^{6}\,\mathrm{cm}^2/\mathrm{Vs}$. In literature, some authors report a hole mobility of about $1\times10^{6}\,\mathrm{cm}^2/\mathrm{Vs}$, [20, 9, 93]. Yet, such a high value of μ was only achieved in Ref. [71] in an asymmetric structure with a very low hole density. Sample ssd-A exhibits $\mu = 0.96 \times 10^{6}\,\mathrm{cm}^2/\mathrm{Vs}$ along [01$\bar{1}$] direction. All data presented here have been recorded in darkness without any previous illumination of the samples and are summarized in Table 4.4.

4.4.1 Structure inversion asymmetry

More information about the symmetry of the quantum well can be derived from the SdH oscillations at low magnetic fields. In a magnetic-field interval up to $\pm0.5\,\mathrm{T}$, both heterostructures ssd-A and dsd-B develop a beating pattern of the SdH oscillations, see Fig. 4.14. It arises from a superposition of two different frequencies corresponding to two spin-splitted subbands of the uppermost HH subband.

The longitudinal-resistance curves ρ_{xx} were measured at 20 mK in the L-bar geometry oriented along the two orthogonal crystal directions [011], [01$\bar{1}$]

Sample	Crystal direction	p_1 ($10^{11}\,\mathrm{cm}^{-2}$)	p_2 ($10^{11}\,\mathrm{cm}^{-2}$)	p_{FFT} ($10^{11}\,\mathrm{cm}^{-2}$)	p_{Hall} ($10^{11}\,\mathrm{cm}^{-2}$)	β ($10^{-29}\,\mathrm{eVm}^3$)	Δ_{SO} (meV)
ssd(A)	[011]	0.54	0.62	1.16	1.20	7	0.08
	[01$\bar{1}$]	0.52	0.59	1.11	1.14	7	0.08
dsd(B)	[011]	0.91	1.01	1.92	1.94	3	0.07
	[01$\bar{1}$]	0.92	0.99	1.92	1.94	2	0.06

Table 4.5: *Hole densities determined from fast Fourier transformation of SdH oscillations; p_1, p_2 subband densities, p_{FFT} the total density, and p_{Hall} determined from the slope of the Hall curve. The Rashba parameter β was calculated using Eq. 2.19. Δ_{SO} is the lower bound of the Rashba splitting, see text.*

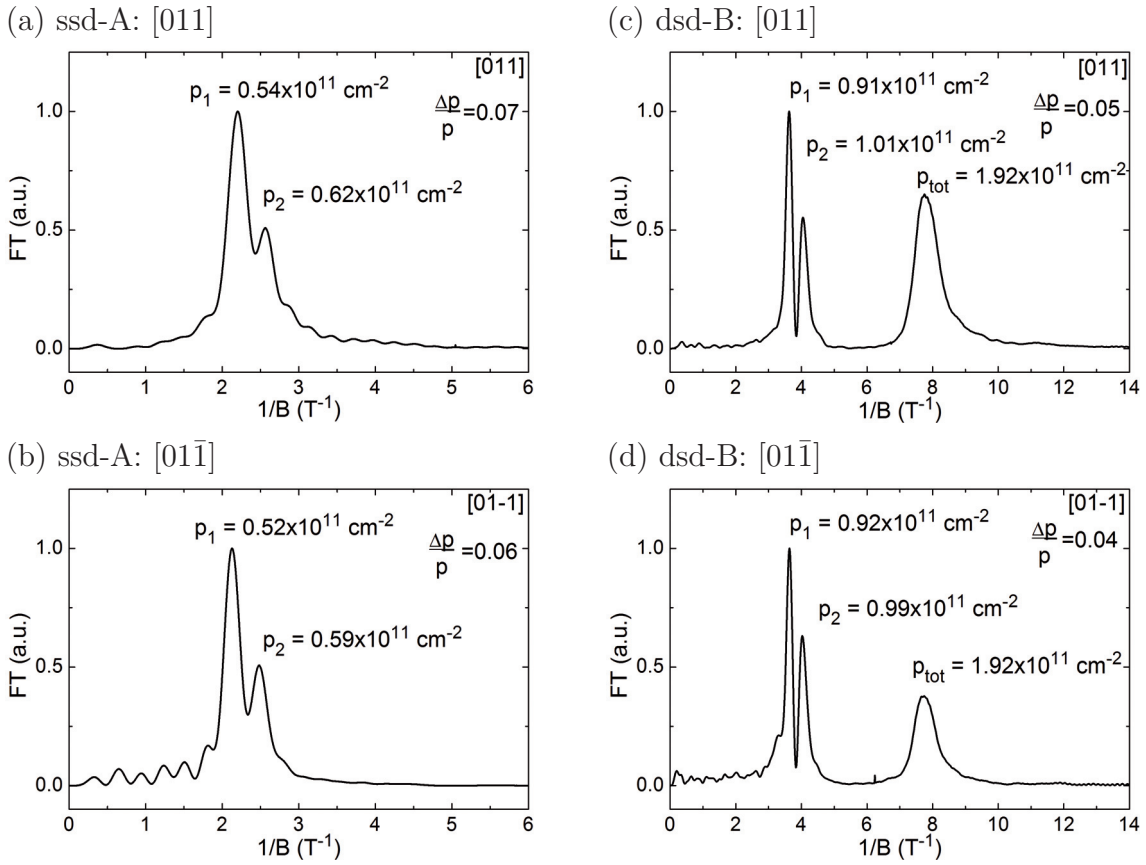

Figure 4.15: *FFT spectra of the low-field SdH oscillations of sample (a), (b) ssd-A and (c), (d) dsd-B, along the two orthogonal crystallographic directions [011] and [01$\bar{1}$]. The fast Fourier transformation was applied on magnetotransport data shown in Fig. 4.14.*

with an applied current of 10 nA. For the extraction of the densities of both spin-splitted subbands we used the procedure described in Appendix B. The fast Fourier transformation (FFT) spectra of sample ssd-A are shown in Figs. 4.15(a), (b) and of sample dsd-B in Figs. 4.15(c), (d).

The presence of two peaks in the spectrum of sample ssd-A confirms the existence of two spin-splitted subbands. A peak corresponding to the total density should develop at $\sim 5\,\mathrm{T}^{-1}$ but is missing in Figs. 4.15(a) and (b). The densities p_1 and p_2 and other estimated parameters are listed in Table 4.5. From the densities we calculated the relative carrier imbalance, which is related to the magnitude of the spin splitting, as $\Delta p/p = 7\%$ and 6% along [011] and [01$\bar{1}$] directions, respectively. Although the SdH measurements probe the whole Fermi surface and therefore no anisotropy is expected, we registered substantial differences by comparison of both orthogonal directions, cf. values in Table 4.5. This phenomenon was only reported in Ref. [114] on samples grown during this work. In contrast to the commonly used van-der Pauw geometry, in our precise L-shaped Hall bar structures the current direction is defined along the [011] or [01$\bar{1}$] crystallographic direction. Possibly, the carrier imbalance can be explained by the transport process. By applying a volt-

age, the Fermi surface moves along the voltage direction. Since the band structure is anisotropic in our case (see Section 4.3), the enclosed Fermi surface changes if measured along different crystal directions, [114].

The Fermi wave vectors corresponding to both occupied subbands are $k_1 = 0.82 \times 10^8\,\mathrm{m}^{-1}$, $k_2 = 0.88 \times 10^8\,\mathrm{m}^{-1}$ along [011] and $k_1 = 0.81 \times 10^8\,\mathrm{m}^{-1}$, $k_2 = 0.86 \times 10^8\,\mathrm{m}^{-1}$ along [01$\bar{1}$]. Using the relation $\Delta_{SO} = 2\beta k_{||}^3$, [59], the lower boundary of the spin splitting of the HH subband at the Fermi energy was estimated to be approximately $\Delta_{SO} \approx 0.08\,\mathrm{meV}$ along both crystallographic directions. The results point out a structure inversion asymmetry of sample ssd-A, cf. sample structure in Fig. 4.1, which was also predicted by simulations of the valence-band structure, see Section 4.3.

Despite the fact that the QW in sample dsd-B was grown to be symmetric, having identical spacer layers and the C2 = C3 doping layers on both sides, three peaks in its FFT spectra are present, see Figs. 4.15(c), (d). Beginning at low values of $1/B$, the peaks correspond to the densities in the spin-splitted subbands p_1, p_2 and the total density p_{tot}. They satisfy well the relation $p_{tot} = p_1 + p_2$. From the densities, summarized in Table 4.5, we derived the relative carrier imbalance $\Delta p/p = 5\%$ and 4% along [011] and [01$\bar{1}$] directions, respectively. The corresponding wave vectors at the Fermi level are $k_1 = 1.07 \times 10^8\,\mathrm{m}^{-1}$, $k_2 = 1.13 \times 10^8\,\mathrm{m}^{-1}$ along [011] and $k_1 = 1.08 \times 10^8\,\mathrm{m}^{-1}$, $k_2 = 1.12 \times 10^8\,\mathrm{m}^{-1}$ along [01$\bar{1}$]. The lower bound for the spin-splitting of the HH subband at the Fermi energy was estimated $\Delta_{SO}[011] \approx 0.07\,\mathrm{meV}$ and $\Delta_{SO}[01\bar{1}] \approx 0.06\,\mathrm{meV}$.

In Table 4.5, the hole densities we extracted from the FFT analysis, are compared to the densities determined from the slope of the Hall curve. According to selected intervals of the magnetic field, where the FFT was applied to, the values of the subband densities p_1, p_2 varied slightly. Based on these results we estimated the accuracy of the calculated FFT density to be 3%. The hole density derived using both methods is in good agreement.

The spin splitting of both samples (the symmetric dsd-B and the asymmetric ssd-A) is of the same magnitude (see Table 4.5) and β is about a factor of 2 higher in sample ssd-A. Nevertheless, one would expect a much stronger difference. At this point, the density dependence of the spin splitting must be stressed, as the position of the Fermi energy is tuned with the carrier density. The spin splitting of the HH subband $E_{1,2}^h(k_{||})$ is proportional to $k_{||}^3$ and is rather small for small densities, [59]. Because the hole density of sample dsd-B is almost twice as high as that of sample ssd-A, the Fermi energy E_F crosses the dispersion at higher values of the in-plane wave vector $k_{||}$. Similarly, the Rashba spin splitting increases. Hence, the structure inversion asymmetry has a stronger effect at higher densities.

Against expectations, the experimentally determined spin-splitting in sample dsd-B is not equal to zero. Owing to the bulk inversion asymmetry, in symmetric GaAs QW there must still occur a spin splitting caused by the Dresselhaus term. Finally, we cannot exclude some small asymmetry also in this symmetric-as-grown sample.

Theoretical calculations of the valence-band structure of both samples were done in Section 4.3. They predicted a relative carrier imbalance of 8% and

1% in sample ssd-A and dsd-B, respectively. The values are slightly different from the experimentally determined 6-7% (sample ssd-A) and 4-5% (sample dsd-B). The small discrepancy is most likely caused by the missing Dresselhaus term in the simulations, see Section 4.3. Additionally, the observed anisotropy between the [011] and the [01$\bar{1}$] directions in the experimentally determined spin splitting can most probably be explained as a superposition of Rashba and Dresselhaus effects, see Section 2.4.

Comparison to high-density QWs

For better understanding of the spin-orbit coupling in the high-mobility samples, we examined highly-single-sided-doped samples where the spin-splitting is expected to be large. This allows to compare the GaAs QW with the In-containing heterostructures because they exhibit high hole densities, as will be shown in Chapter 5. Furthermore, in the high-mobility samples ssd-A and dsd-B we observed some anisotropy in the spin-splitting between [011] and [01$\bar{1}$] directions. The relative carrier imbalance was $\Delta p/p[011] > \Delta p/p[01\bar{1}]$.

According to Eq. 2.17, the Rashba spin splitting is in first order proportional to the electric field in the sample $\mathcal{E}_z$ perpendicular to the 2DHG-plane. In ssd-QW $\mathcal{E}_z$ depends directly on the hole density, $\mathcal{E}_z \propto p$.

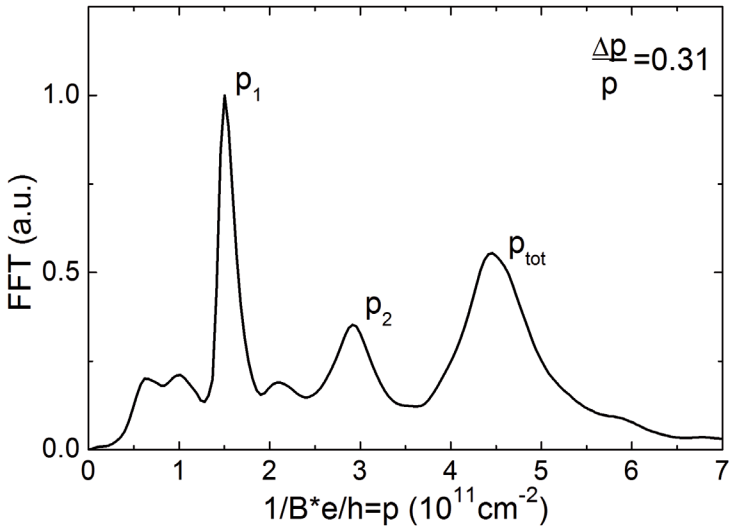

Figure 4.16: *FFT spectra of the low-field SdH oscillations of a ssd-sample with high hole density* $p = 4.7 \times 10^{11}\ cm^{-2}$ *and hole mobility* $\mu = 0.2 \times 10^6\ cm^2/Vs$. *The magnetotransport data were taken at* $T = 350\ mK$.

First, we will consider spin splitting in a highly-doped ssd-QW with a hole density $p = 4.7 \times 10^{11}\,\mathrm{cm}^{-2}$ and a hole mobility $\mu = 0.2 \times 10^6\,\mathrm{cm}^2/\mathrm{Vs}$ at 1.3 K. The mobility is much lower in comparison to the high-mobility samples ssd-A and dsd-B. Magnetotransport data were measured in van-der Pauw geometry at $T = 350\,\mathrm{mK}$. At low magnetic fields the sample exhibited a beating-pattern of SdH-oscillations and, applying the Fourier analysis, we got the spectrum shown in Fig. 4.16. The presence of well-separated peaks p_1, p_2, p_{tot} clearly demonstrates a distinct spin splitting. The relative carrier imbalance achieves the extremely high value $\Delta p/p = 31\%$. This is about 5-times higher than in the high-mobility sample ssd-A discussed above. The lower bound for the spin-splitting was estimated to

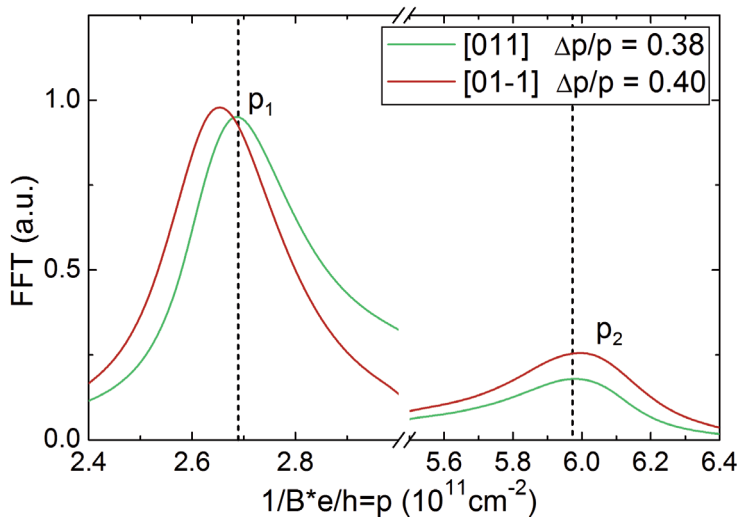

Figure 4.17: *FFT spectra of the low-field SdH oscillations of a ssd-sample with a very high hole density* $p = 8.6 \times 10^{11}\ cm^{-2}$ *and exhibiting a hole mobility* $\mu = 0.09 \times 10^{6}\ cm^2/Vs$. *The magnetotransport data were taken at* $T = 280\ mK$ *in L-bar geometry along [011] and [01$\bar{1}$] directions. The dashed lines are guides to the eyes.*

$\Delta_{SO} \approx 0.8\,\text{meV}$, which represents even 10-times stronger spin-splitting than listed in Table 4.5 for the high-mobility samples.

Second, we investigated the anisotropy in a ssd-QW of a very high hole density $p = 8.6 \times 10^{11}\,\text{cm}^{-2}$ exhibiting a hole mobility $\mu = 0.09 \times 10^{6}\,\text{cm}^2/\text{Vs}$ at $T = 280\,\text{mK}$ fabricated in L-shaped Hall-bar geometry oriented along the [011] and [01$\bar{1}$] directions. The FFT spectra of the beating pattern of the SdH oscillations are shown in Fig. 4.17. There are two peaks p_1 and p_2 belonging to each crystallographic direction confirming that the spin splitting in this sample is enormous. The shift of the peak position highlights significant differences between [011] and [01$\bar{1}$] crystal directions. This suggests that there is an anisotropic spin-splitting in the SdH measurements. Moreover, the spin splitting is higher along the [01$\bar{1}$] direction in contrast to the [011] direction. We calculated the relative carrier imbalance as $\Delta p/p[011] = 38\% < \Delta p/p[01\bar{1}] = 40\%$. This must originate in the interplay of BIA and SIA as discussed in the previous section. However, both effective fields interfere in the opposite way than observed in the high-mobility samples ssd-A and dsd-B of much lower density. Our observations are in consensus with theoretical predictions. In Section 2.4, Fig. 2.4(b) illustrates the interference of BIA and SIA effective fields for a variety of in-plane wave vectors $\mathbf{k}_{||}$.

Finally, we want to emphasize that for both discussed samples the longitudinal resistance vanished at low filling factors, excluding the existence of a parallel conducting channel, and only one subband was occupied.

In conclusion, we have shown that the high-mobility samples exhibit anisotropic spin-splitting similar to the highly-single-sided-doped QWs. As expected, in the highly-doped samples the spin splitting is extremely large in contrast to samples ssd-A and dsd-B of much lower density. Because the enhancement of the hole density was accompanied by a reduction of the hole mobility, the following investigations concentrate only on samples ssd-A and dsd-B. The spin-orbit coupling phenomena in the highly-doped samples were extensively studied via Raman spectroscopy in Ref. [114].

4.4.2 Temperature dependence

It is necessary to cool the samples containing a 2DHG down to very low temperatures (below 500 mK) to be able to discern the SdH oscillations and the quantum Hall plateaus. Already at 1 K, the longitudinal-magnetoresistance curve becomes U-shaped with a few dips indicating SdH minima, but no detailed structure can be recognized. This is in contrast to 2DEGs, for which SdH oscillations at 1.5 K are well-developed. The reason are the different effective masses of holes and electrons, which govern the T-damping of the SdH oscillations. In literature, $m_{eff} = 0.51\,m_0$ was reported for holes in the HH subband of GaAs and a much lower value $m_{eff} = 0.067\,m_0$ for electrons in the conduction band, [115].

From the temperature dependence of the longitudinal magnetoresistance a lot of important transport parameters can be obtained, see Section 2.1. As already mentioned above, the temperature damping of the amplitude of the SdH oscillations is dominated by the effective mass, and the value of m_{eff} can be calculated from it, see Eq. 2.10. Since we know m_{eff}, the quantum scattering time τ_q and the transport scattering time τ_t can be deduced, see Eq. 2.11. Additionally, the electron-electron interaction exhibits a typical T-dependence and will be further discussed in Section 4.4.4.

The longitudinal magnetoresistance ρ_{xx}(B) of sample ssd-A and dsd-B was recorded at temperatures from 20 mK to 1 K under an applied current of 10 nA along both orthogonal directions [011] and [01$\bar{1}$] of the L-shaped Hall-bar structure. In order to get the values of m_{eff} in our samples, we applied the method described in Section 2.1. The effective mass calculated from the T-damping of the amplitude of the SdH oscillations is dependent on the B field, and its value at $B = 0$ T was derived from the linear extrapolation. The values are summarized in Table 4.4. For sample ssd-A, we determined $m_{eff} = 0.41\,m_0$ and $m_{eff} = 0.40\,m_0$ along [011] and [01$\bar{1}$] directions, respectively. Sample dsd-B exhibits a higher effective mass $m_{eff} = 0.53\,m_0$ along both orthogonal directions. The experimental error from the fitting procedure was estimated at $\pm 0.03\,m_0$. Publications on similar kinds of structures containing asymmetric QWs reported $m_{eff} = 0.36\,m_0$, [10], and $0.34\,m_0$, [71]. For a standard dsd-QW, $m_{eff} = 0.54\,m_0$ was presented in Ref. [71]. We can conclude that the hole effective mass is a function of many sample-dependent parameters, including the confining potential (the barrier height, the QW width, and the doping configuration, etc.), the 2D hole density, and the Miller index of the growth surface. This was extensively investigated in Ref. [71].

From the sheet resistivity, the hole mobility was calculated and its temperature dependence is plotted in Fig. 4.18 for both studied samples. In the range between 20 mK and 1 K, the mobility changes only a little, but for $T > 1$ K it decreases rapidly. Furthermore, we used the known m_{eff} and μ and evaluated the transport scattering time τ_t from Eq. 2.3. In both samples, τ_t achieves very high values on the order of 10^2 ps, even higher than reported for comparable 2DHGs in Refs. [21, 10]. This is a consequence of the extremely high hole mobility of our samples. The transport scattering time copies the T-dependence of the mobility and below $T = 1$ K it remains almost constant in both samples, see Fig. 4.19.

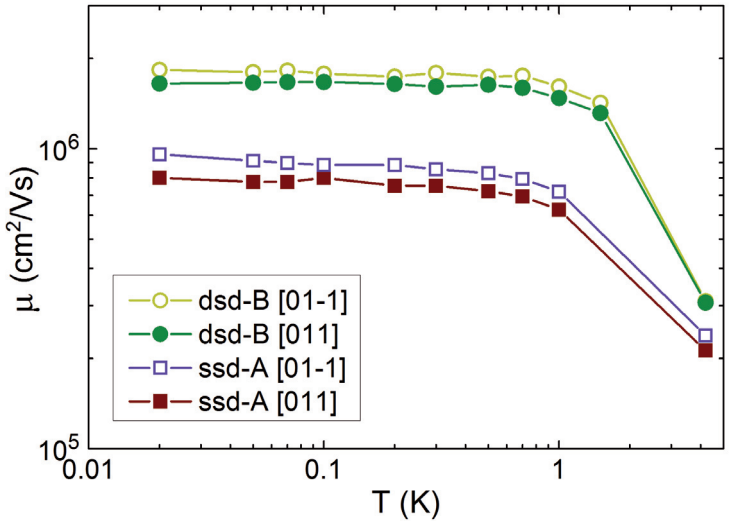

Figure 4.18: *Temperature dependence of the hole mobility of sample ssd-A and dsd-B. Filled/open symbols mark the [011]/[01$\bar{1}$] directions. The lines are guides to the eyes.*

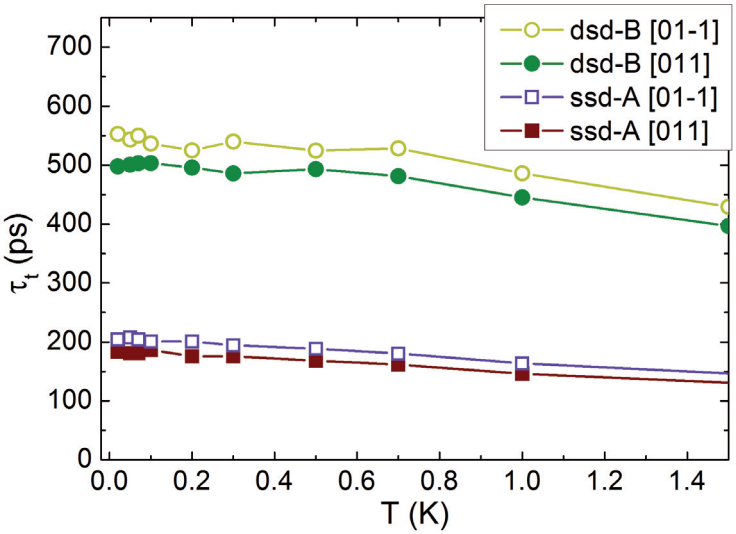

Figure 4.19: *Temperature dependence of the transport scattering time of sample ssd-A and dsd-B. Filled/open symbols mark the [011]/[01$\bar{1}$] directions. The lines are guides to the eyes.*

Hole mobilities and transport scattering times measured at the base temperature of the cryostat $T = 20\,\mathrm{mK}$ are summarized in Table 4.4. Like the hole mobility, the transport scattering time exhibits strong anisotropy. Along the [01$\bar{1}$] direction, τ_t is much longer than that determined along the [011] direction corresponding to the high- and low-mobility direction. Comparing both samples, the mobility of sample dsd-B is approximately twice as high as that of sample ssd-A and τ_t is three times longer in this sample.

In addition, we determined the quantum scattering time τ_q from the longitudinal-magnetoresistance curves, see Table 4.4. The method was described in Section 2.1. For sample ssd-A we obtained $\tau_q[011] = 16.0\,\mathrm{ps}$ and $\tau_q[01\bar{1}] = 19.6\,\mathrm{ps}$ along both orthogonal directions. Interestingly, the very-high-mobility sample dsd-B exhibits shorter quantum scattering times $\tau_q[011] = 5.6\,\mathrm{ps}$ and $\tau_q[01\bar{1}] = 6.6\,\mathrm{ps}$. Qualitatively similar results were reported by C. Gerl for heterostructures grown on [110] GaAs substrates: a standard dsd-QW showed a shorter quantum scattering time than an asymmetric ssd-QW, [21]. The error of τ_q was estimated from the

fitting procedure to be $\approx 10\%$.

The ratio of the scattering times enables us to determine whether a long-range or a short-range scattering potential is more important. We found that $\tau_t/\tau_q \approx 10$ in sample ssd-A and $\tau_t/\tau_q \approx 100$ in sample dsd-B, see Table 4.4. This indicates that a long-range scattering potential leading to a small-angle scattering is dominant in both samples. Additionally, as quoted above, the quantum scattering time of sample dsd-B is much shorter than that of sample ssd-A, pointing out higher small-angle scattering in this sample. This is also well demonstrated in Fig. 4.13: sample ssd-A exhibits much more well-developed FQH minima than sample dsd-B. We surmise that the enhanced small-angle scattering in sample dsd-B must result from the presence of two remote-doping layers on both sides of the QW in contrast to only one doping layer in sample ssd-A.

4.4.3 Anisotropic activated transport of fractional quantum Hall states

We utilized T-dependent longitudinal resistance data for evaluation of activated transport of fractional quantum Hall states in our samples. The experimental details were described in the previous section. At dilution-refrigerator temperatures, both investigated samples, ssd-A and dsd-B, exhibit a large amount of fully quantized FQH states in the lowest LLs, see Figs. 4.13(a) and (b). Especially, in the range of $2 > \nu > 1$, FQH states $\nu = 5/3$ and $4/3$ are well-developed in both samples. Moreover, higher-order states $\nu = 7/5$ and $8/5$ could be resolved in sample ssd-A, see Fig. 4.13(a). The FQH states are visible as distinct minima in ρ_{xx} and plateaus in ρ_{xy} curves. Furthermore, FQH states $\nu = 5/3$ and $\nu = 4/3$ with longitudinal resistance dropping to zero were detected in sample dsd-B, see Fig. 4.13(b). ρ_{xx} curves recorded at different temperatures show that these FQH states vanish with increasing temperature, cf. Figs. 4.20(a), (b) for sample ssd-A and Figs. 4.20(c), (d) for sample dsd-B. Note that along both orthogonal directions the FQH states are similarly strong pronounced, compare Fig. 4.20(a) with (b), or Fig. 4.20(c) with (d).

In order to quantitatively examine the T-dependence of the FQH states, we plotted the minima of ρ_{xx} belonging to a specific FQH state as a function of $1/T$ on logarithmic scale (Arrhenius plot). A representative example of an Arrhenius plot of the FQH state $\nu = 5/3$ is shown in Figs. 4.21(a), (b) for samples ssd-A and dsd-B, respectively. We found activated regions fulfilling the relation in Eq. 2.15, see the linear fits in Fig. 4.21. Deviation from the activation law at the lowest temperature may indicate a transition from activated transport to hopping conduction, [116]. Fig. 4.21(a) reveals some astonishing features. Data of sample ssd-A exhibit two different slopes according to the crystallographic direction of current flow [011] or $[01\bar{1}]$. This is in contrast to almost identical slopes for [011] and $[01\bar{1}]$ directions in sample dsd-B, see Fig. 4.21(b). This behavior was observed for other FQH states as well. From the linear fits and using Eq. 2.15 we extracted quasiparticle excitation energy gaps Δ, see Fig. 4.22.

Fig. 4.22 displays our most remarkable findings. It shows the activation energy Δ of various FQH states plotted versus the perpendicular magnetic field

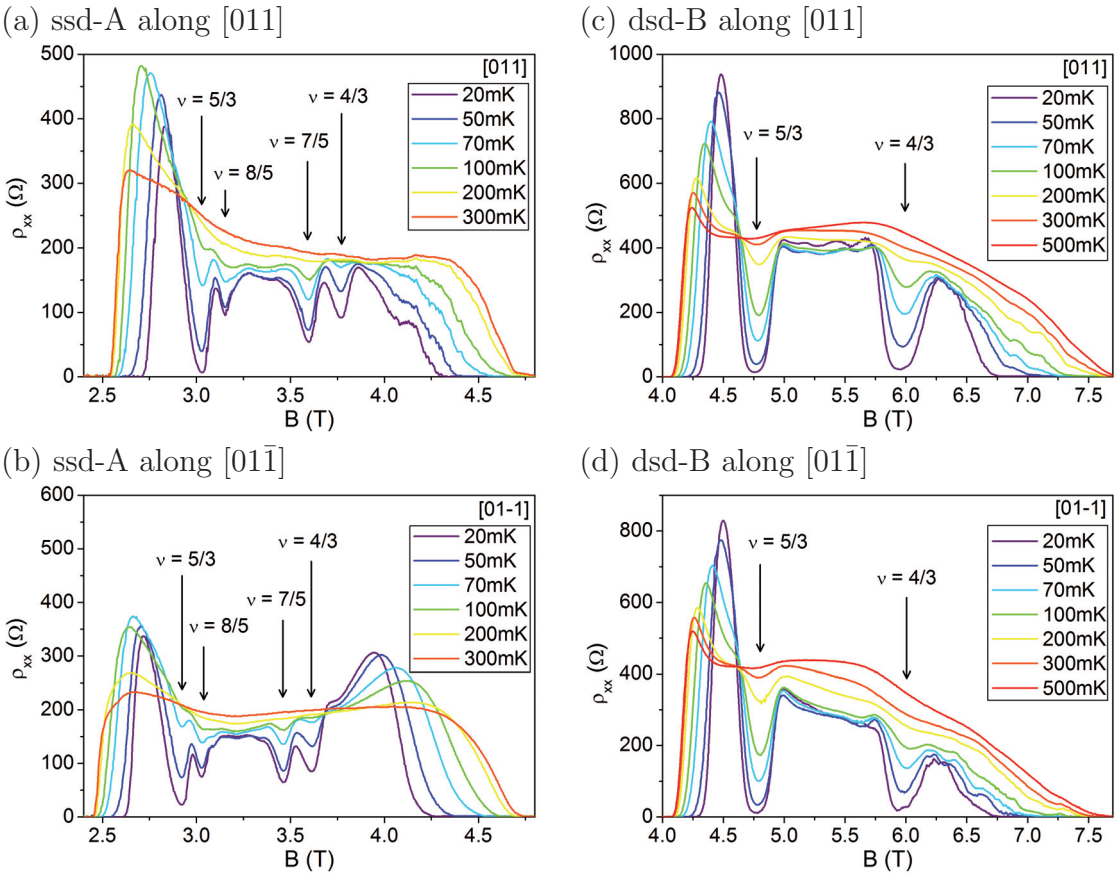

Figure 4.20: *T-dependence of FQH states in the range of* $2 < \nu < 1$*: Longitudinal resistance* ρ_{xx} *is plotted versus the perpendicular magnetic field: (a), (b) of sample ssd-A recorded along [011] and [01*$\bar{1}$*] directions, and (c), (d) of sample dsd-B along [011] and [01*$\bar{1}$*] directions, respectively.*

B. The activation energy of the same FQH state exhibits significant differences between [011] and [01$\bar{1}$] crystallographic directions. Fig. 4.22(a) shows FQH states in the range of filling factors $2 > \nu > 1$. The anisotropy in the activation gap is most apparent for $\nu = 5/3$ for sample ssd-A, where we observed a gap reduction of about 40% along [01$\bar{1}$] in comparison to the [011] direction. The FQH states $\nu = 4/3$, $\nu = 7/5$ and $\nu = 8/5$ of sample ssd-A (red symbols) exhibit changes in Δ of $\sim 10 - 20\%$. More interestingly, the anisotropy vanishes for sample dsd-B (blue symbols). Fig. 4.21 depicts this for the FQH state $\nu = 5/3$ in a more demonstrative way as two different slopes. The fits of the data of sample ssd-A corresponding to activated transport along [011] and [01$\bar{1}$] deviate strongly from each other, see Fig. 4.21(a), the slopes of sample B are rather similar, see Fig. 4.21(b).

We extracted a strong difference between $\Delta_{[011]}$ and $\Delta_{[01\bar{1}]}$ in sample ssd-A. Previous studies done on samples with a metallic topgate to modulate the hole density, confirm a linear dependence of Δ on B for the FQH state $\nu = 2/3$, [117]. For the density $1.2 \times 10^{11}\,\mathrm{cm}^{-2}$, the authors estimated an activation gap $\Delta = 1.6\,\mathrm{K}$,

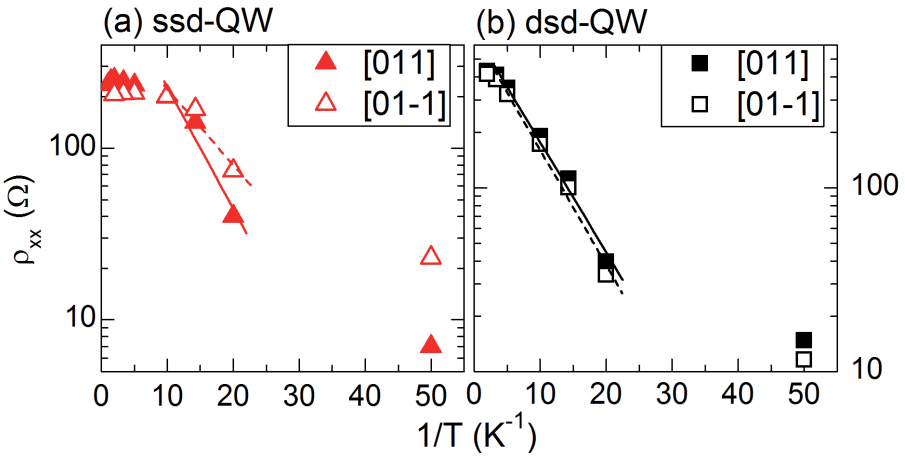

Figure 4.21: *Arrhenius plots for the FQH state $\nu = 5/3$ in (a) sample ssd-A and (b) sample dsd-B. Filled (open) symbols are data measured along [011] ([01$\bar{1}$]) direction. The solid lines are fits to $\rho_{xx} \propto \exp(-\Delta/2T)$, where Δ is the activation gap. Striking is the pronounced anisotropy of the data of sample ssd-A (a) whereas the curves for sample dsd-B have identical slopes (b).*

which is in excellent agreement with our measurements, see Fig. 4.22(b). From the density-dependent study in Ref. [117] follows that such a big change of the activation energy of 0.6 K, which we observed in sample ssd-A, must be caused by a change of the carrier density of about $0.2 \times 10^{11}\,\mathrm{cm}^{-2}$. As listed in Table 4.4, the SdH oscillations indicate slightly different densities along the orthogonal crystallographic directions. However, the difference is one order of magnitude lower than expected from the investigations in Ref. [117]. Hence, this cannot explain our observations. In literature, comparable density-dependent studies for the range of $2 > \nu > 1$ are missing.

A pronounced anisotropy was already reported on some of the even-denominator FQH states in higher $N \geq 2$ Landau levels. These experiments were carried out on both 2DEGs [48, 47] and 2DHGs [19, 118] prepared in GaAs/AlGaAs heterostructures. In 2DHGs grown on a (100) GaAs substrate, similar to our samples, Manfra *et al.* described a pronounced transport anisotropy at filling factors: $\nu = 7/2$, $\nu = 11/2$, $\nu = 13/2$, which can be altered by varying the hole density and the symmetry of the confining potential [19]. This is demonstrated by the development of a sharp maximum or minimum in the longitudinal resistance at half fillings depending on the in-plane current direction through a square sample and is ascribed to the formation of a many-particle state: quantum smectic or quantum nematic phases[10], [19]. No such kind of anisotropies were observed in $N = 0$ and $N = 1$ LLs [47, 48]. However, these investigations were performed only using the van-der Pauw configuration and an accurate examination of the crystal direction anisotropy of the FQH states using more exact L-shaped Hall-bar geometry was missing up to now. In addition, the van-der Pauw geometry was shown to exagger-

[10]More information about the liquid-crystal phases of quantum Hall systems can be found in Ref. [46]

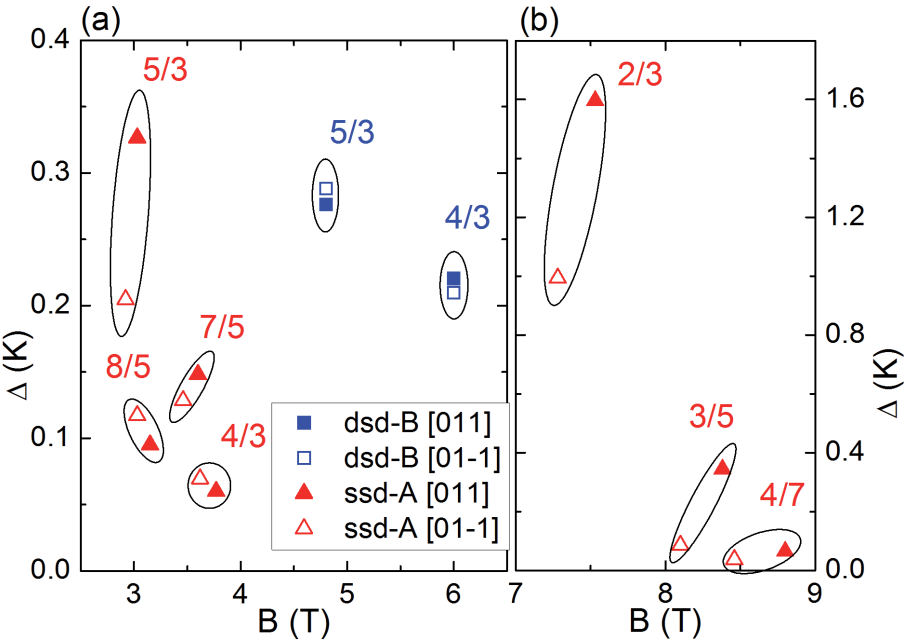

Figure 4.22: *Activation gaps of FQH states in the range of (a) $2 > \nu > 1$ of samples ssd-A (red symbols) and dsd-B (blue symbols), (b) $1 > \nu$ of sample ssd-A. Filled (open) symbols stand for measurements along the [011] ([01$\bar{1}$]) crystallographic direction. Data corresponding to the same FQH state are grouped as a guide to the eyes. Remarkable is the pronounced anisotropy between $\Delta_{[011]} \neq \Delta_{[01\bar{1}]}$ in sample ssd-A in contrast to almost isotropic values $\Delta_{[011]} \sim \Delta_{[01\bar{1}]}$ in sample dsd-B.*

ate the anisotropy because of a non-uniform current distribution [119]. For a 2DEG, Du *et al.* determined the activation energy of the FQH state $\nu = 9/2$ from the T-dependence of the ρ_{xx} peak and minimum. As a result, the authors got same values of Δ for both orthogonal directions, in other words: They detected an isotropic activation energy. In summary, up to now no anisotropy was reported in $N = 1$ and $N = 0$ LLs and in the activated transport as well. All these experiments are in stark contrast to our observations. Let us stress that we report anisotropy in the activation energy of the FQH states but not the transport anisotropy in longitudinal magnetoresistance. Moreover, along both directions [011] and [01$\bar{1}$] we found no peak at a particular filling factor but well-developed resistance minima, compare Figs. 4.20(a) with (b) and Figs. 4.20(c) with (d).

Although we do not have any exact theoretical explanation for our observation yet, there could be found some indications of a possible origin. In Ref. [19], Manfra *et al.* observed a transport-anisotropy-to-isotropy transition driven by a change of the symmetry of the confinement potential from symmetric to strongly asymmetric. They explained this phenomenon by spin-orbit coupling, which depends not only on the hole density but also on the electric field in the QW, and which alters the ground state of a FQH state, [19]. In our case, simulations of the valence-band structure, see Fig. 4.1, show that in sample ssd-A the QW is asymmetric and the charge distribution of holes is placed near the barrier/QW interface. On the con-

trary, in sample dsd-B the QW is highly symmetric and the charge distribution is located in the middle of the QW, compare Fig. 4.2. Furthermore, the asymmetry of the confinement potential is demonstrated in the development of different FQH states in the range of $2 > \nu > 1$, [52]. In full agreement with Ref. [52], we found in sample dsd-B similarly pronounced FQH states $\nu = 5/3$ and $\nu = 4/3$ but no higher-order structure was resolved here, see Fig. 4.13(b). This is a further evidence of the symmetric confinement potential in this double-sided-doped QW. Making the QW potential asymmetric, the resistance minimum at $\nu = 4/3$ vanishes and a new minimum emerges at $\nu = 7/5$, [52], in correspondence to the single-sided-doped QW in sample ssd-A, see Fig. 4.13(a).

Additionally, a new model of dissipative conductance in FQH states was recently reported by d'Ambrumenil *et al.*, [53]. The model assumes that the slowly varying potential caused by remote ionized impurities leads to an inhomogeneous system, were compressible regions containing quasiparticles or quasiholes are separated by percolating regions of incompressible fluid, [120]. Then the dissipative transport is carried out in terms of thermally assisted tunneling through a saddle point. First calculations done by d'Ambrumenil based on this theoretical model seem to confirm the existence of two gaps [120] but for the explanation further theoretical investigations are necessary. Nevertheless, we have experimentally demonstrated anisotropic Δ for $2 > \nu > 1$ and $1 > \nu$.

4.4.4 Hole-hole interaction induced magnetoresistance

High-mobility 2D electron and hole gases were reported to show negative parabolic magnetoresistance in the range of classically strong magnetic fields ($\omega_c\tau > 1$), [121, 122, 123]. We observed this effect in sample ssd-A, see Fig. 4.23(a). There exist several sources, which cause an enhancement of the longitudinal resistance around $B = 0\,\mathrm{T}$, but due to its typical B-field- and T-dependence this feature is commonly ascribed to the electron-electron (here hole-hole) interaction effect.

At first, the electron-electron interaction correction to the classical Drude conductivity was investigated by Altshuler and Aronov [124] in a diffusive transport regime where $k_BT\tau/\hbar \ll 1$. Choi *et al.* [125] improved this theory and it will be applied in Section 5.4.4 to the strong negative parabolic magnetoresistance observed in our InAlAs/InGaAs/InAs heterostructures. Afterwards, Gornyi and Mirlin [126, 127] extended the theory also for the ballistic transport regime ($k_BT\tau/\hbar \gg 1$) describing the high-mobility 2DEGs and 2DHGs.

In our high-mobility samples, the ionized impurities are separated from the QW containing the 2DHG with a large undoped spacer layer. In this way, the scattering on the ionized impurities was reduced, but the remote impurities still cause a long-range scattering potential with a correlation length determined by the spacer thickness d. Additionally, a short-range scattering induced by background impurities (reflecting the purity of the MBE chamber) and interface roughness is present. It becomes more important with increasing spacer thickness and can limit the mobility. Such a real situation is implemented in the mixed-disorder model developed by Gornyi and Mirlin, [127]. It combines a smooth random potential charac-

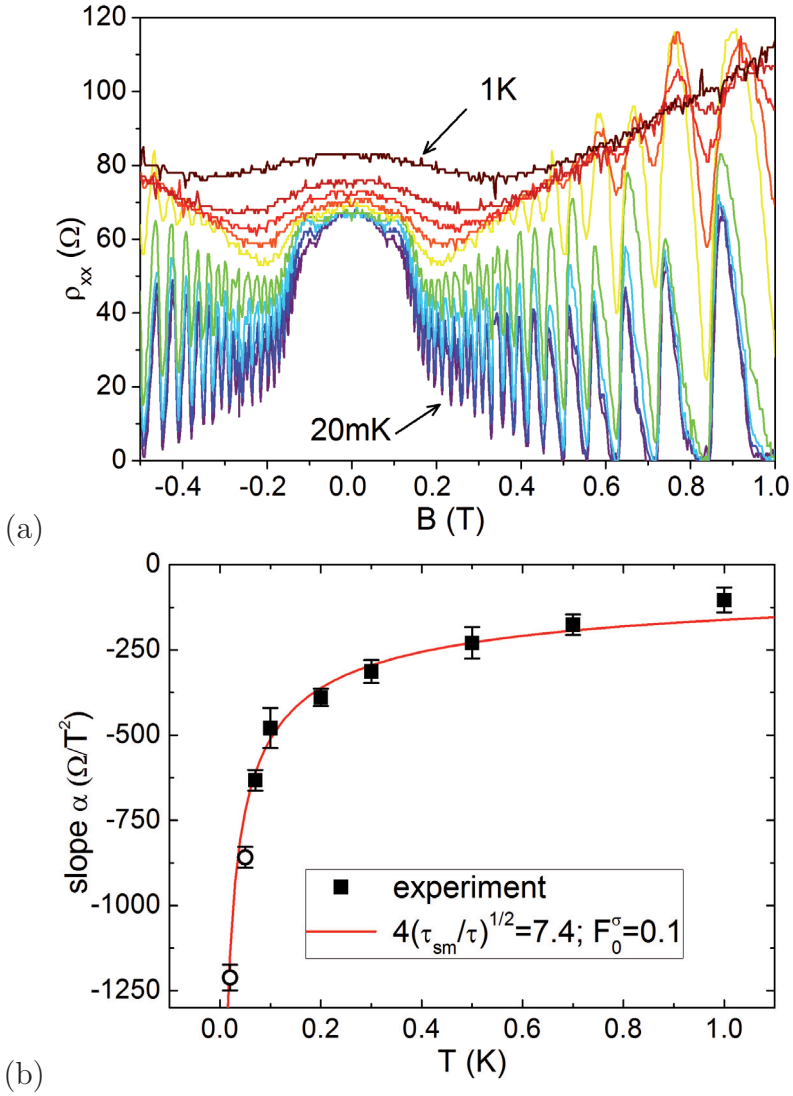

Figure 4.23: *(a) Sample ssd-A exhibits negative parabolic magnetoresistance in the $\rho_{xx}(B)$ curve, which is temperature-dependent between 0.02 K and 1 K. (b) Slope $\alpha = d\rho_{xx}/dB^2$ versus temperature T and the fit of the data with Eq. 4.2. The temperatures 0.02 K and 0.05 K (open symbols) do not suit the condition for ballistic transport, see text.*

terized by a transport relaxation time τ_{sm} and single-particle (quantum) relaxation time $\tau_{sm,q}$, and a white-noise disorder with a characteristic time τ_{wn}. The overall transport relaxation rate is then $\tau^{-1} = \tau_{wn}^{-1} + \tau_{sm}^{-1}$ and is dominated by short-range scattering $\tau_{wn} \ll \tau_{sm}$. However, the damping of the SdH oscillation is given by the smooth random potential $\tau_{sm,q} \ll \tau_{wn}$. The theory predicts:

$$\rho_{xx} = -\rho_0 \frac{c_0 \mu^2}{\pi k_F l_e} \left(\frac{k_B T \tau}{\hbar}\right)^{-1/2} 4 \left(\frac{\tau_{sm}}{\tau}\right)^{1/2} \left(6\frac{F_0^\sigma}{1+F_0^\sigma} + \frac{1}{2}\right) B^2 + \rho_0 \qquad (4.2)$$

$c_0 \simeq 0.276$ is a constant, F_0^σ is a Fermi-liquid interaction parameter and is used as

a fitting parameter.[11] The longitudinal resistance ρ_{xx} scales as $B^2T^{-1/2}$. Eq. 4.2 is valid for ballistic transport and strong interaction where $\kappa/k_F \ll 1$.

To evaluate the negative parabolic magnetoresistance in sample ssd-A, see Fig. 4.23(a), we plotted ρ_{xx} versus B^2 and found a linear dependence. Since the theory is valid for $\omega_c\tau \gg 1 \gg \omega_c\tau_q$, we fitted the data in the interval $13\,\mathrm{mT} < B < 150\,\mathrm{mT}$, which we obtained by inserting our values of the transport parameters listed in Table 4.4 in the inequality. The experimental curves taken at a variety of temperatures were fitted with equation $\rho_{xx} = \alpha B^2 + \rho_0$. From that, we extracted the slope α and investigated its temperature dependence, see Fig. 4.23(b). The error bars in Fig. 4.23(b) represent the error of this fitting procedure. The slope α demonstrates a $T^{-1/2}$ functional dependence very well.

In addition, we must check whether the condition of ballistic transport is satisfied. For temperatures between 0.07 K and 1 K, $k_BT\tau/\hbar$ changes from 1.7 to $24 > 1$ and confirms that the data belong to the ballistic regime. Nevertheless, the measurements at $T = 0.02\,\mathrm{K}$ and $T = 0.05\,\mathrm{K}$ do not justify the condition. At these temperatures $k_BT\tau/\hbar$ is equal to 0.5 and 1.2, which is not significantly greater than 1. Therefore these points were not included in the following analysis. Previous results confirm that the fluctuation potential is indeed long-range $\tau_t \gg \tau_q$, see Table 4.4, which is further supported by $k_Fd = 6.9 > 1$ in this sample with a spacer thickness $d = 80\,\mathrm{nm}$. The condition of a strong interaction $\kappa/k_F = 14 > 1$ is satisfied and we can use Eq. 4.2. The fit of the experimental data with Eq. 4.2 is shown in Fig. 4.23(b). For the fitting parameters we got: $4(\tau_{sm}/\tau)^{1/2} = 7.4$ and $F_0^\sigma = 0.1$. The fit remained stable within this accuracy, even if the starting values were changed. We estimated the ratio of $\tau_{sm}/\tau = 3.5$ and from the overall transport relaxation rate we got $\tau_{wn}/\tau_{sm} = 0.4$. The latter ratio indicates that the transport relaxation rate is dominated by short-range scattering. Our results are comparable with the findings in literature: $F_0^\sigma = 0.1 - 0.2$ for 2DEG [121, 123], $F_0^\sigma = 0.25 - 0.45$ for 2DHG with a very low density [122]. In high-mobility 2DEGs, $\tau_{wn}/\tau_{sm} = 0.3$ was obtained, [123].

In Fig. 4.23(b), the open symbols at $T = 0.02\,\mathrm{K}$ and $T = 0.05\,\mathrm{K}$ lie also on the fitted curve. However, they were not included in the fitting procedure. For $k_BT\tau/\hbar < 1$, one would rather expect a diffusive transport regime. In this case, Eq. 5.6 supposing $\ln(1/T)$-dependence of the slope α should be applied, see Section 5.4.4. Here, the temperature dependence of α is rather like $T^{-1/2}$ and completely matches the experimental values. These two data points can be assigned to the intermediate regime or transition from the diffusive to the ballistic regime, reported also for high-mobility 2DEGs in Ref. [121].

In conclusion, the negative magnetoresistance in sample ssd-A is B-field-dependent as a function of B^2 and temperature-dependent as a function of $T^{-1/2}$ and can be therefore ascribed to the hole-hole interaction effect. From the analysis it follows that $\tau_{wn} < \tau_{sm}$. That means that the mobility is limited by the short-range scattering potential governed by background impurities present in the QW and interface roughness scattering. In contrast, sample dsd-B does not show any strong increase of the longitudinal magnetoresistance around $B = 0\,\mathrm{T}$. We emphasize that

[11] $\kappa = 2/a_B$ is the inverse screening length; a_B is the Bohr radius. For holes in GaAs $\kappa = 1.102 \times 10^9\,\mathrm{m}^{-1}$.

the samples differ in the symmetry of the confinement potential, see Figs. 4.1 and 4.2. While sample dsd-B is symmetric with the wave function situated in the middle of the QW, sample ssd-A is asymmetric and the wave function penetrates into the AlGaAs spacer layer. Hence, the 2DHG in sample ssd-A is strongly influenced by the quality of the AlGaAs/GaAs interface. Moreover, both samples were grown in the same MBE chamber and shared the same growth conditions. Therefore, we can assume that the concentration of the background impurities is approximately the same in both cases. As a result, the dominating scattering mechanism in sample ssd-A must be interface roughness scattering.

Chapter 5

Carbon-doped InAlAs/InGaAs/InAs heterostructures

Indium-containing heterostructures are interesting due to their strong spin-orbit interaction. In fact, the first device approaching the function of a spin transistor is based on a high-mobility InAs channel. There are a lot of investigations done on 2DEGs confined in the InAlAs/InGaAs/InAs structure, but the 2DHGs (apart of the manganese-doped 2DHGs, where the properties of the heterostructure are superimposed by magnetic effects coming from the manganese impurity) are not well explored yet. Due to a lot of experience with carbon p-type doping, which we earned by optimizing the growth of C-doped GaAs/AlGaAs quantum wells summarized in Chapter 4, we decided to use carbon for preparation of 2DHGs also in In-containing heterostructures. To be able to realize heterostructures with high indium content on a GaAs wafer, we engineered the strain via step-graded metamorphic buffer layers and thereby prepared relaxed substrates for the indium-containing active layers. The specifics of the growth are listed in Section 5.1. Of particular importance for the investigations is the behavior of carbon impurities, if the indium content of the ternary compound was changed, see Section 5.2. The properties of 2DHGs in the $In_xAl_{1-x}As/In_xGa_{1-x}As/InAs$ heterostructures with different x were intensively studied using magnetotransport measurements (Section 5.4) and compared with simulations of the valence-band structure (Section 5.3). These In-containing 2DHGs exhibit strong spin-orbit coupling, demonstrated by an extraordinarily pronounced weak-antilocalization effect, strong hole-hole interactions and significant crystal-direction anisotropy of transport parameters, pointing out the dominant scattering mechanisms in these structures. Finally, in Section 5.5 we will introduce how we succeeded in engineering of the spin-splitting by performing small changes in the structure design.

5.1 Growth

5.1.1 Buffer layer

As a substrate material for the active layers with high In content, we used a (100)-oriented GaAs wafer. In contrast to the lattice-matched GaAs/AlGaAs heterostructures described in Chapter 4 the growth process is not straightforward due to the large difference in the lattice constants between InAs and GaAs. Table 5.1 summarizes the lattice constants of the binary and ternary compounds discussed in this work. The lattice mismatch between GaAs and InAs is about 7%. In this case, where $a_{substrate}$(GaAs)< a_{layer}(InAs), the epitaxial layer is compressively strained.[1] The growth of a material having a lattice constant differing from that of the substrate proceeds at first pseudomorphically. The in-plane lattice constant of the layer matches the substrate but the out-of-plane constant expands to accommodate the misfit. With increasing thickness, the strain in the layer increases up to the critical thickness. Above the critical thickness the elastic energy collected in the layer is so high that it is favorable to build crystal defects and the lattice constant relaxes towards its equilibrium value in the bulk. To release the strain, typically misfit dislocations form. As a consequence a whole row of atoms parallel to the interface is missing. Misfit dislocations are confined in the plane parallel to the interface and cannot move through the crystal. As a further important crystal defect threading

[1]The opposite case $a_{layer} < a_{substrate}$ leads to a tensile-strained epitaxial layer.

Binary Compounds

	a (Å)	E_g (eV)	m_e^* (m_0)	m_{hh}^* (m_0)
GaAs	5.65325	1.51	0.067	0.51
InAs	6.0583	0.417	0.026	0.39
AlAs	5.660	2.24(ind.)	0.15	0.76

Ternary Compounds

	a (Å)	E_g (eV)	m_e^* (m_0)	m_{hh}^* (m_0)
$In_xGa_{1-x}As$	6.058-0.405(1-x)	0.417x+1.51(1-x) -0.477x(1-x)	0.063-0.040x	0.57
$In_xAl_{1-x}As$	6.058-0.397(1-x)	0.417x+3.1(1-x) -0.70x(1-x)	0.15-0.127x	0.76-0.19x
$Al_xGa_{1-x}As$	5.6533+0.0078x	1.420+1.087x+ +0.438x^2	0.063+0.087x	0.57+0.19x

Table 5.1: *Material parameters of III-V binary and ternary semiconductor compounds, [55, 115, 128]: lattice constant a (at 300 K), band gap energy E_g (at 4.2 K), and effective mass of electrons m_e^* and heavy holes m_{hh}^* at the Γ-point. AlAs has an indirect band gap.*

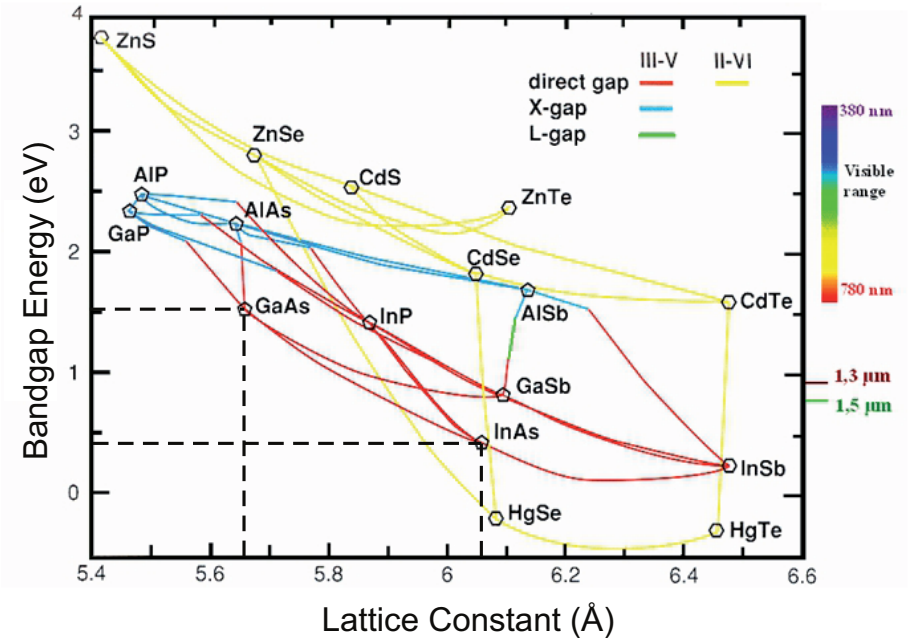

Figure 5.1: *Bandgap energy and lattice constants of the most important binary semiconductors. The lines correspond to the ternary compounds. Taken from [129].*

dislocations should be noted. They propagate through the whole structure and can act as scattering sources for the charge carriers. Hence, they should be avoided. The type of growth process above the critical thickness is called metamorphic and is used to accommodate the strain and the lattice constant. Here, we made use of it and grew a step-graded metamorphic buffer layer.

In order to get a defect-free active region, we grew an $In_xAl_{1-x}As$ step-graded metamorphic buffer layer. The sample structure is shown schematically in Fig. 5.2. The buffer layer consisted of a series of 50 nm thick $In_xAl_{1-x}As$ layers, where the indium content was increased in $\Delta x = 0.05$ steps from $x = 0.08$ in the first layer up to the required final indium composition. The progress is sketched in Fig. 5.2 up to $x = 0.75$. The growth process was controlled via the In rate, while the Al rate was maintained constant. The temperature of the wafer was kept at 340°C for a buffer layer ending at $x = 0.75$ indium concentration and at 430°C for $x = 0.20$. The layer sequence was capped with a thick layer of a constant composition, which served as a lattice-matched virtual substrate for the active region of the same indium content. In this work, we investigated samples with indium content in the active layer of $x = 0.75, 0.60, 0.50, 0.40, 0.30$ and 0.20.

5.1.2 Sample structure

The overall sample structure consists of three main regions: a superlattice, a buffer and an active layer, see Fig. 5.2(left). The growth on the (100) GaAs substrate starts with a 100 nm thick GaAs layer followed by a superlattice of 5 nm $Al_{0.5}Ga_{0.5}As$ and 5 nm GaAs repeated 10 times. The superlattice has crucial influence on the

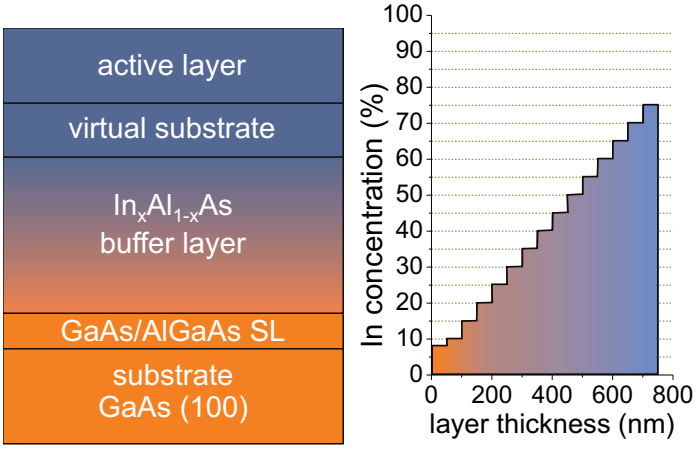

Figure 5.2: *(left) Overall sample structure. (right) Layer sequence of the $In_xAl_{1-x}As$ metamorphic buffer layer terminating at a final indium concentration of $x = 0.75$.*

suppression of the threading dislocations, see Ref. [130]. In this part of the growth process the temperature of the substrate was maintained at 620°C. In the middle area of the structure, the strain between the GaAs substrate and the quantum well with high indium content is accommodated via an $In_xAl_{1-x}As$ step-graded metamorphic buffer layer, described in Section 5.1.1. It creates a lattice-matched virtual substrate for the active layer. The main part of the structure is the active layer containing a 2DHG.

In this work, various designs of the active layer were investigated: a normal and an inverted-doped structure, a simple $In_xGa_{1-x}As$ QW or an $In_xGa_{1-x}As$ QW with an embedded InAs channel. The three most interesting combinations are illustrated in Fig. 5.3. Samples with high indium content (above $x = 0.50$) were prepared with a layer sequence shown in Fig. 5.3(a). The core is an $In_xGa_{1-x}As$ QW with an embedded strained InAs channel. A similar structure with a final indium content of $x = 0.75$ was extensively studied for 2DEGs by Ercolani *et al.*, [83, 82]. They showed that by embedding a thin channel of InAs the electron mobility can be increased, in comparison to a simple $In_{0.75}Ga_{0.25}As$ QW. This can be explained as a reduction of alloy disorder scattering if the carrier density profile is confined in the binary compound[2] [83]. Ercolani *et al.* achieved the highest electron mobility of 320000 cm^2/Vs in a 4 nm thick InAs channel [82, 83]. Simultaneously, they experimentally established the critical thickness of the pseudomorphically grown InAs on the $In_{0.75}Ga_{0.25}As$ layer as 7 ± 1 nm, [83]. For thicknesses larger than 6 nm, a rapid reduction of the electron mobility was observed, [82, 83]. Further, U. Wurstbauer used this structure for growth of manganese-doped 2DHGs, [25, 85]. However, in both references concerning either the 2DEGs or 2DHGs, the authors concentrated only on heterostructures with final indium content of $x = 0.75$. A systematic examination of the influence of the indium content x on the properties of the 2D charge carrier systems is still missing. To have direct comparison with the literature we applied this layout to our nonmagnetic carbon-doped 2DHGs.

For samples with low indium content (below $x = 0.50$), the structure was simplified and a simple $In_xGa_{1-x}As$ QW was grown, see Fig. 5.3(b). The reason is the large lattice mismatch between the $In_xGa_{1-x}As$ with $x < 0.50$ and the InAs channel

[2]Our results on 2DHGs will be shown in Section 5.4.5.

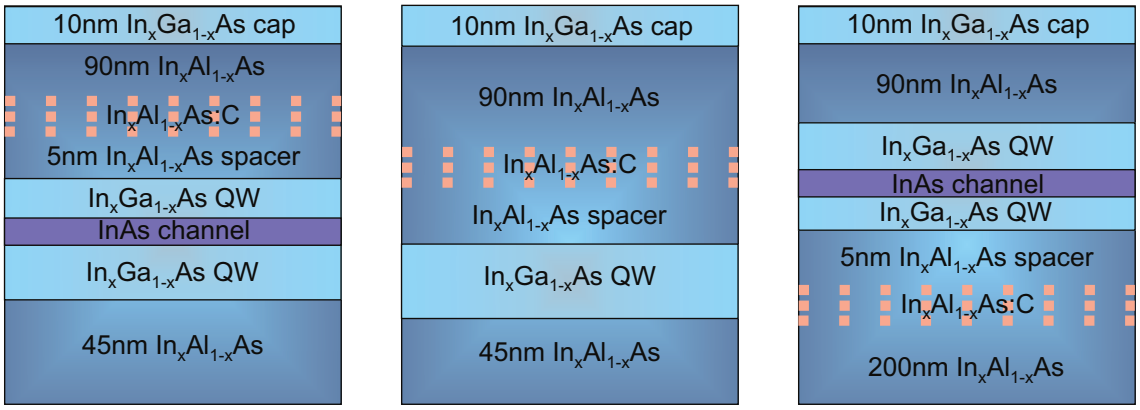

(a) InGaAs QW with embedded InAs channel

(b) InGaAs QW

(c) inverted-doped InGaAs QW

Figure 5.3: *Different designs of the active layer grown.*

leading to crystal defects with a consequence of structure damage, see below.

Fig. 5.3(c) sketches a layer sequence of an inverted-doped structure, where the carbon-doping layer was grown before the QW. It was prepared as a direct comparison to the manganese-doped inverted structures, in which magnetic effects were observed due to the presence of Mn-impurity in the QW, [24]. Wurstbauer *et al.* reported an insulator-to-metal transition driven by a magnetic field and exhibiting abrupt and hysteretic changes of the resistance, [24]. These phenomena originate in exchange coupling between a hole and the parent Mn acceptor and coexist with the quantum Hall effect at high magnetic fields. However, direct comparison with a p-type nonmagnetic inverted-doped structure was missing up to now.

Samples were fabricated with a different indium composition of $x = 0.75, 0.60, 0.50, 0.40, 0.30$ and 0.20. The structure was covered with a 90 nm InAlAs upper barrier. In order to prevent oxidation in samples with high Al fraction in the barrier, an additional 10 nm thick InGaAs capping layer was grown. This was not necessary for samples with high In content. The growth temperature was adjusted according to the final indium content in the active layer. The optimal range was found to be between 430°C and 340°C for $x = 0.20$ to 0.75. All structures were modulation doped[3] using two different doping techniques: a homogeneous doping in an $In_xAl_{1-x}As$ layer (for most of the 2DHG-samples except for those with $x = 0.75$ indium concentration) and a digital-alloy doping (for samples with $x = 0.75$ In content). The differences between them and the reason behind will be provided in Section 5.2.

Table 5.2 gives an overview of single-sided doped samples with active layers shown in Figs. 5.3(a) and (b) one inverted-doped sample, see Fig. 5.3(c). Comparison of samples A, E and F in Table 5.2 demonstrates the importance of incorporating of the InAs channel into the QW for the development of a good-quality 2DHG. All three samples were successively grown and contain $x = 0.75$

[3]It means that the doping layer and the QW were separated by a spacer layer.

indium. Sample F, which consists of a simple $In_{0.75}Ga_{0.25}As$ QW, was insulating at low temperatures. Then, we embedded a 2 nm thin InAs channel into the QW and detected a 2DHG with a low-temperature mobility of $\mu = 2500\,cm^2/Vs$ in sample E. We could further increase the mobility up to $\mu = 6600\,cm^2/Vs$ at $T = 1.3\,K$ by increasing the channel thickness to 4 nm in sample A. Our results are in agreement with experiments done on 2DEGs in Ref. [82, 83], discussed above.

In order to stay below the critical thickness of the InAs channel and prevent damage of the structure on one hand, and to get well-developed 2DHGs on the other, we reduced the thickness of the InAs layer simultaneously with decreasing the indium content of the ternary compound. In this way, we succeeded in preparing a 2DHG in a normal-doped $In_{0.60}Ga_{0.40}As$ QW containing a 2 nm thin InAs channel (sample B) and in an inverted-doped $In_{0.50}Ga_{0.50}As$ QW with an embedded 1 nm thin InAs layer (sample *inv* in Table 5.2). They achieved hole mobilities of $\mu = 6300\,cm^2/Vs$ (sample B) and $\mu = 4500\,cm^2/Vs$ (sample *inv*) at 1.3 K. Further experiments showed that for an In concentration of $x = 0.30$ (sample G) even a 0.65 nm thick strained InAs film inserted into the $In_{0.30}Ga_{0.70}As$ QW blocked the building of a 2DHG. Even such a thin layer obviously lead to the formation of dislocations which destroyed the structure. In conclusion, the critical thickness of the InAs channel is strongly dependent on the indium content x of the underlying $In_xGa_{1-x}As$ layer and must be taken into account by growth.

Examination of magnetotransport properties in dependence on indium content were done on exemplary samples A, B, C and D, and will be presented in Section 5.4. Samples A, B were grown with high indium content (above $x = 0.50$) and their QW contains an InAs channel, see the sketch of the active layer in Fig. 5.3(a). On the contrary, samples C, D consist of an $In_xGa_{1-x}As$ QW with $x < 0.50$, see the layer sequence in Fig. 5.3(b). The inverted-doped structure will be considered separately in Section 5.4.6.

Sample	In content x	InGaAs (nm)	InAs (nm)	InGaAs (nm)	Spacer (nm)	Doping	2DHG
A	0.75	13.5	4	2.5	5	dig.	✓
B	0.60	15.5	2	2.5	5	homog.	✓
C	0.40	20	-	-	20	homog.	✓
D	0.20	20	-	-	5	homog.	✓
E	0.75	15.5	2	2.5	5	dig.	✓
F	0.75	20	-	-	5	dig.	-
G	0.30	16.5	0.65	2.5	5	homog.	-
inv	0.50	10	1	10	20	homog.	✓

Table 5.2: *Overview of normal-doped samples with different In concentrations in the active layers, see Fig. 5.3(a), (b), and one inverted-doped sample, see Fig. 5.3(c). Columns 3-5 represent the structure of the QW. In columns 6-8 the spacer thickness, type of doping, homogeneous or digital, and the existence of 2DHG are stated. Transport properties of samples A-D will be discussed in Section 5.4.*

5.1.3 Surface morphology

The surface of the metamorphic buffer layer exhibits a cross-hatch pattern, which has a different periodicity and RMS[4] roughness along the [011] and [01$\bar{1}$] crystallographic directions. This typical surface topography was also observed on Ge_xSi_{1-x} grown on Si substrates [131], $In_xAl_{1-x}As$ on InP [132], and $In_xAl_{1-x}As$ on GaAs [78, 133, 134], etc. Its origin was reported to be associated with: (i) spatially varying strain fields due to networks of misfit dislocations resulting in local changes of growth rate [131, 135, 136], (ii) surface displacement due to the building of networks of dislocation clusters [137] or (iii) lateral mass transport tending to eliminate the surface steps [138]. The cross-hatch pattern is repeated in all interfaces in the active region.

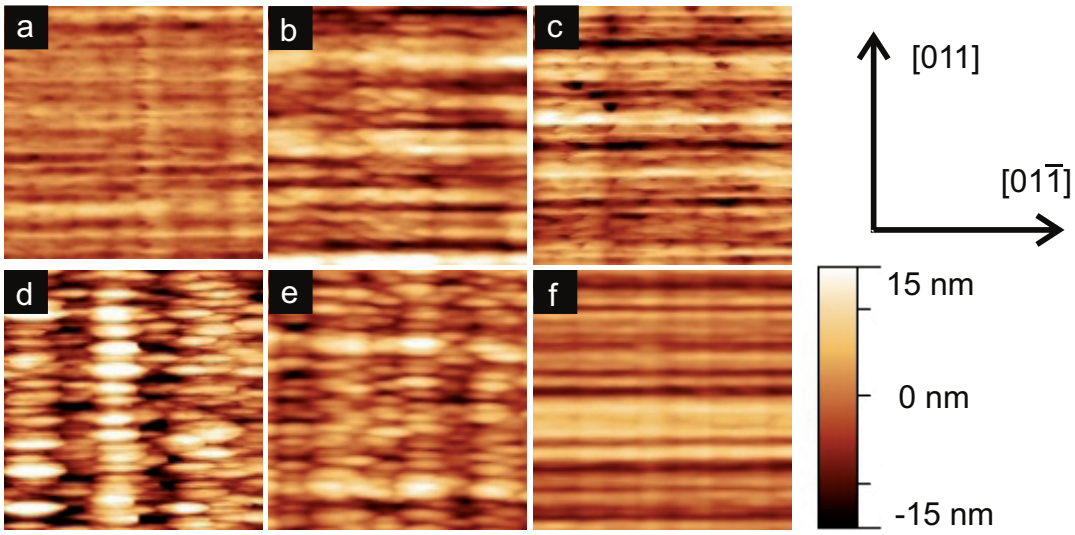

Figure 5.4: *10×10 μm^2 AFM surface topographies of samples having different In contents in the active layer: (a) $x = 0.75$, (b) $x = 0.60$, (c) $x = 0.50$, (d) $x = 0.40$, (e) $x = 0.30$ and (f) $x = 0.20$. The color scale varies from 15 nm to -15 nm. The roughness parameters are listed in Table C.1 in Appendix C.*

In all our samples we found a pronounced cross-hatch pattern already using an optical microscope. Quantitatively we investigated the morphological properties of the surface using atomic force microscopy (AFM). Fig. 5.4 shows AFM images of a variety of samples. The data were analyzed using the program Gwyddion and the roughness parameters along different crystallographic directions were extracted, see Appendix C Table C.1. We found that the surface morphology of all samples is strongly anisotropic. The RMS roughness is highest along [011] with $\sim 2-4$ nm, accompanied by a very short periodicity $< 1\,\mu$m of the pattern. In contrast, the [01$\bar{1}$] direction exhibits low RMS roughness of ~ 1 nm and a very long periodicity of $\sim 1-2\,\mu$m. Further, the diagonal directions [010] and [001] cross the pattern in a 45° angle and combine thus the characteristics of both [011] and [01$\bar{1}$] directions. Consequently, they express intermediate properties. The influence of this

[4] root mean square

strong anisotropy on transport of charge carriers will be discussed in Section 5.4.5.

Fig. 5.4 provides an overview of the topography of a variety of samples with different indium content from $x = 0.20$ to 0.75. Despite some deviations in the RMS roughness, the periodicity of the cross-hatch pattern was maintained for all samples. As a result, the AFM analysis of the surface parameters, listed in Table C.1 in Appendix C, shows no dependence of the cross-hatch pattern on the indium content x. This confirms that the buffer layer and the virtual substrate efficiently relax the strain and are of a good quality. In addition, we investigated the influence of the strained InAs channel on the surface morphology. Samples A, E and F have the same indium content $x = 0.75$, but they differ in the design of the QW including 4 nm, 2 nm and 0 nm thick InAs channels in the $In_{0.75}Ga_{0.25}As$ QW, respectively, see Table 5.2. From comparison of the AFM data summarized in Table C.1 in Appendix C, we found that the incorporation of the strained InAs channel did not significantly alter the surface properties.

5.2 Switching from n-type to p-type conductivity

In the known literature, a 2DHG in InAs has not been reported, yet, except of that doped with manganese, which introduces magnetic effects. It is not straightforward to get a p-type conductivity using carbon as a doping material in heterostructures with high indium content. There are some phenomena which act against this.

First, similar In-containing heterostructures as those investigated in this work were reported to exhibit electron conductivity even without any intentional doping. Capotondi *et al.* described the formation of a 2DEG with an electron density of $2 - 3 \times 10^{11}\,\mathrm{cm}^{-2}$ and mobility of $2.15 \times 10^5\,\mathrm{cm}^2/\mathrm{Vs}$ in completely undoped $In_{0.75}Ga_{0.25}As/In_{0.75}Al_{0.25}As$ quantum wells, [77]. Further, D. Ercolani improved the transport properties of the 2DEG by embedding a strained InAs channel into the QW and reached an electron density of $5\times10^{11}\,\mathrm{cm}^{-2}$ and a mobility of $5\times10^5\,\mathrm{cm}^2/\mathrm{Vs}$, [83]. The PICTS analysis[5] done in Ref. [77] identified deep donor-like levels at energies 0.12 eV and 0.17 eV below the conduction band edge of the $In_{0.75}Al_{0.25}As$. The levels lay within the $In_{0.75}Al_{0.25}As$ barrier and the $In_{0.75}Ga_{0.25}As$ QW conduction band discontinuity, and are most probably responsible for the formation of the 2DEG, [77].

Second, carbon as a group IV member is amphoteric in III-V semiconductors and can act as a donor or acceptor. In GaAs at typical growth conditions, carbon incorporates primarily on the arsenic sides in the crystal lattice and provides free holes. Therefore, in GaAs/AlGaAs heterostructures, as discussed extensively in Chapter 4, it is applied as a standard p-type doping material. But in InAs carbon was reported to be a donor, [95, 96]. Further, carbon doping results in electron conductivity, in InP, for example, [139].

In order to get more information about the kind of incorporation of carbon in the $In_xAl_{1-x}As$ and $In_xGa_{1-x}As$ ternary compounds with high In content x, we prepared bulk layers homogeneously doped with carbon. The structure consists of

[5] Photoinduced Current Transient Spectroscopy

a step-graded metamorphic buffer layer terminating at $x = 0.75$ and covered with a virtual substrate, on which the growth of a 0.5 μm thick bulk layer of $In_{0.75}Al_{0.25}As$:C or $In_{0.75}Ga_{0.25}As$:C followed. Both samples exhibit a p-type conductivity with 3D hole densities of $p_{(InAlAs)} = 8.7 \times 10^{13}\,cm^{-3}$ and $p_{(InGaAs)} = 6.1 \times 10^{13}\,cm^{-3}$ at 4.2 K. After exposure to red light, the hole density further increased to $p_{(InAlAs)} = 9.0 \times 10^{13}\,cm^{-3}$ and $p_{(InGaAs)} = 6.3 \times 10^{13}\,cm^{-3}$. For comparison, we grew an undoped $In_{0.75}Al_{0.25}As$ bulk layer. Here, in agreement with Ref. [77], no free carriers could be registered. With regard to these examinations, carbon seems to release free holes if incorporated into the ternary compounds with $x = 0.75$.

Let us switch back to the 2D systems. Despite both mentioned facts contributing to the n-type conductivity in $In_xAl_{1-x}As/In_xGa_{1-x}As$ heterostructures with high x, we succeeded in achieving p-type doping using carbon as a doping material. Section 5.2.1 summarizes the properties of samples exhibiting a 2DEG. Comparing the transport characteristics of samples with different x, we observed conductivity type inversion between $x = 0.60$ and $x = 0.75$, specified in Section 5.2.2. In Section 5.2.3, we will introduce our novel doping design, with which we overcame our problems described above and we will also present results on a carbon-doped 2DHG in a sample with $x = 0.75$.

5.2.1 Carbon-doped 2DEGs

In this section, we will consider samples with a 4 nm thick InAs film embedded in the $In_{0.75}Ga_{0.25}As$ layer. In these structures, only a 2DEG was observed to form under carbon homogeneous or δ-doping. However, some indications could be detected that carbon partly occupies also the acceptor sites. Table 5.3 lists the properties of some exemplary samples exhibiting a 2DEG. Sample 2DEG-A is completely undoped. It exhibits a distinct 2DEG with a high electron mobility of $3.4 \times 10^4\,cm^2/Vs$, in consistence with observations in Ref. [77, 83]. By comparison, the homogeneously doped sample 2DEG-B, grown at the same conditions, exhibits a lower electron density. This indicates that some carbon atoms are incorporated at acceptor sites.

Further, we found a pronounced dependence of the electron density on the growth temperature. The high temperature of $T_G = 470°C$ resulted in an almost

Sample	C-doping	T_G (°C)	n_{dark} ($10^{12}\,cm^{-2}$)	n_{ill} ($10^{12}\,cm^{-2}$)	μ_{dark} ($10^3\,cm^2/Vs$)	μ_{ill} ($10^3\,cm^2/Vs$)
2DEG-A	no	330	-0.3	-0.4	24	34
2DEG-B	yes	330	-0.2	-0.3	12	29
2DEG-C	yes	470	-0.7	-0.8	12	13

Table 5.3: *Magnetotransport properties of 2DEGs which develop in carbon-homogeneously-doped heterostructures with an indium content of $x = 0.75$. T_G is the growth temperature. Electron density n and mobility μ were measured at 4.2 K in the dark and after illumination with a red LED.*

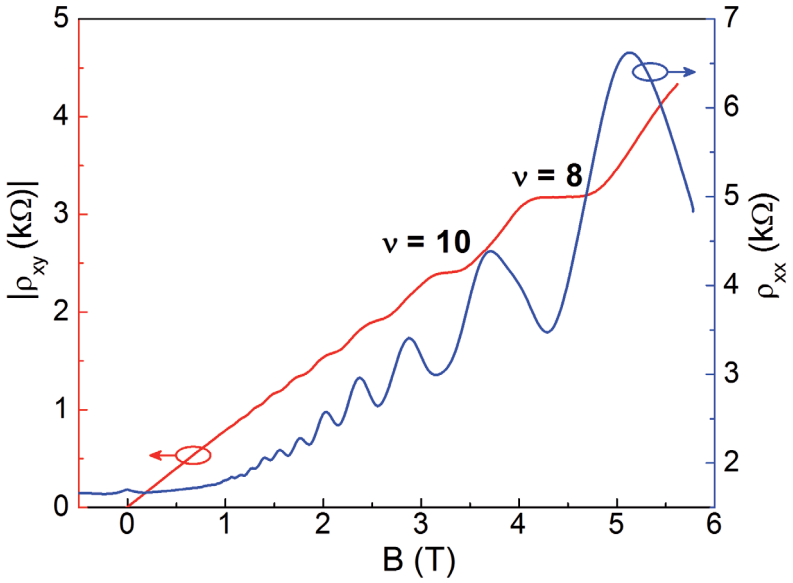

Figure 5.5: *Hall and longitudinal resistance of sample 2DEG-C recorded in van-der Pauw geometry at 4.2 K after illumination with red light. The negative slope of the Hall curve indicates the electron conductivity.*

4-times higher electron density in sample 2DEG-C compared to sample 2DEG-B grown at $T_G = 330°C$, see Table 5.3. In the following experiments, we made use of this behavior and grew the samples designed to develop a 2DHG at a lower temperature of $T_G = 330°C$.

Magnetotransport measurements on all 2DEG samples recorded at low temperatures show Hall plateaus and a negative slope of the Hall curve. In longitudinal resistance, distinct Shubnikov-de Haas oscillations were detected. A representative example is shown in Fig. 5.5, where magnetotransport data of sample 2DEG-C, taken at 4.2 K, are plotted. Additionally, both, the electron density and mobility increase after illumination with a red LED, see Table 5.3.

It is worth to note that the 2DEG samples provide about one order of magnitude higher carrier mobilities compared to the later grown samples containing a 2DHG, see Section 5.2.3.

5.2.2 Conductivity-type inversion as a function of indium content

In this section, we study the relation between the indium content x in the active layer and the type of the conductivity. We have grown carbon-homogeneously-doped samples with $x = 0.20, 0.40, 0.50, 0.60$ and 0.75 and characterized them at 4.2 K. The magnetotransport properties are summarized in Table 5.4.

In Fig. 5.6(a), the carrier density is plotted versus the indium content x. Here, the positive (negative) sign of the density indicates the p-type (n-type) conductivity. The samples with indium content between $x = 0.20$ to 0.60 exhibit hole conductivity. But the sample with the highest indium content of $x = 0.75$ provides

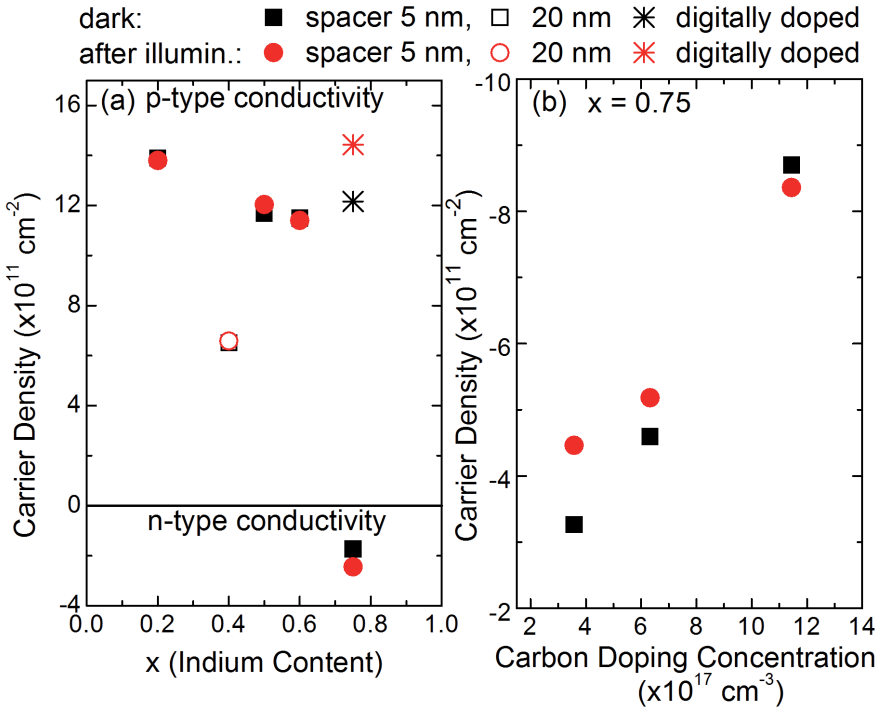

Figure 5.6: *[97], (a) Carrier density as a function of indium content x in the active layer, (b) electron density in dependence on doping concentration in samples with $x = 0.75$ indium content, measured at 4.2 K. Black points were measured in the dark, red points after illumination with a red LED, at 4.2 K. Positive (negative) carrier density means hole (electron) density. Asterisks represent the digitally doped sample discussed in Section 5.2.3.*

a 2DEG. Thus, the conductivity changes from p- to n-type between $x = 0.60$ and $x = 0.75$. These observations are in disagreement with the literature, where the conduction type inversion occurs at $x = 0.90$ and $x = 0.60$ for strained $In_xAl_{1-x}As$ and $In_xGa_{1-x}As$ bulk layers, respectively, [95]. Similarly, our bulk layers demonstrated p-type conductivity for $x = 0.75$ indium content. Together with other experiments, the results point out the amphoteric nature of carbon impurities. Additionally, in Fig. 5.6(a), there is also the digitally doped sample (sample A) included, marked with asterisks, which will be discussed separately in Section 5.2.3.

Based on the results discussed in Section 5.2.1, in which the free electron density was reduced by applying carbon doping in comparison to the undoped case, we tried to compensate the intrinsic electron conductivity by increasing the doping concentration in these heterostructures. We concentrated on samples with $x = 0.75$ and varied the doping concentration. Here, the thickness of the doping layer was kept constant at 90 nm and the doping concentration was regulated with the filament current: 51 A, 53 A and 56 A.[6] In Fig. 5.6(b), the electron density is plotted as a function of the carbon doping concentration. All samples present a well-developed 2DEG. Moreover, the electron density increases with increasing carbon doping level.

[6]For the calibration of the C cell see Section 3.1.

As a consequence, it is not possible to obtain hole conductivity by only incorporating more carbon atoms into the layer and another concept had to be developed, see Section 5.2.3.

In addition, we illuminated the samples with a red LED at low temperatures; compare the red points in Fig. 5.6. In Fig. 5.6(b), the 2DEG samples of a relatively low doping concentration exhibited an enhancement of the electron density. But the electron density of the sample with the highest doping level decreased after exposure to red light. This effect of illumination is most likely related to the self-compensation of carbon atoms at high doping densities. Carbon as a group IV member behaves amphoteric in III-V semiconductors and shows strong self-compensation in these materials, resulting in conduction type inversion with changing composition, [95].

5.2.3 Carbon-doped 2DHGs with high indium content

In the previous sections, we discussed homogeneously doped samples with $x = 0.75$ In concentration, where the carbon doping in the $In_{0.75}Al_{0.25}As$ layer led to the creation of a 2DEG. Developing a novel doping design, we overcame the problems described above with carbon incorporation. Based on the observations in Fig. 5.6(a), we made use of the fact that carbon acts as an acceptor in $In_xGa_{1-x}As$ and $In_xAl_{1-x}As$ compounds with low indium content and designed digital-alloy doping. It consists of a series of $\sim 0.34\,nm$ $In_{0.75}Al_{0.25}As$ layer, $\sim 0.26\,nm$ AlAs layer, both homogeneously doped with carbon, and 100 s carbon δ-doping layer. This sequence is repeated four times. This results in an overall indium content of $x = 0.40$ in the doping layer.

Using the digital-alloy-doping technique, we successfully created a 2DHG in the $In_{0.75}Al_{0.25}As/In_{0.75}Ga_{0.25}As$ heterostructures. Fig. 5.7 displays magnetotransport data of such a sample with a 4 nm thick InAs channel embedded in the $In_{0.75}Ga_{0.25}As$ QW (sample A). The positive slope of the Hall curve confirms the hole conductivity. The sample provides a very high hole density of $p = 1.1 \times 10^{12}\,cm^{-2}$ and a hole mobility of $\mu = 6.6 \times 10^3\,cm^2/Vs$ at 280 mK. The Hall resistance ρ_{xy}

Indium content x	Carrier density ($10^{12}\,cm^{-2}$)	Carrier mobility ($10^3\,cm^2/Vs$)
0.20	1.5	1.8
0.40	0.7	2.0
0.50	1.2	1.7
0.60	1.2	3.7
0.75 (homogeneously doped)	-0.2	12.1
0.75 (digitally doped)	1.2	6.0

Table 5.4: *[97], Magnetotransport properties of carbon-homogeneously-doped $In_{0.75}Al_{0.25}As/In_{0.75}Ga_{0.25}As/InAs$ heterostructures at 4.2 K without illumination. Positive carrier density stands for holes, negative for electrons.*

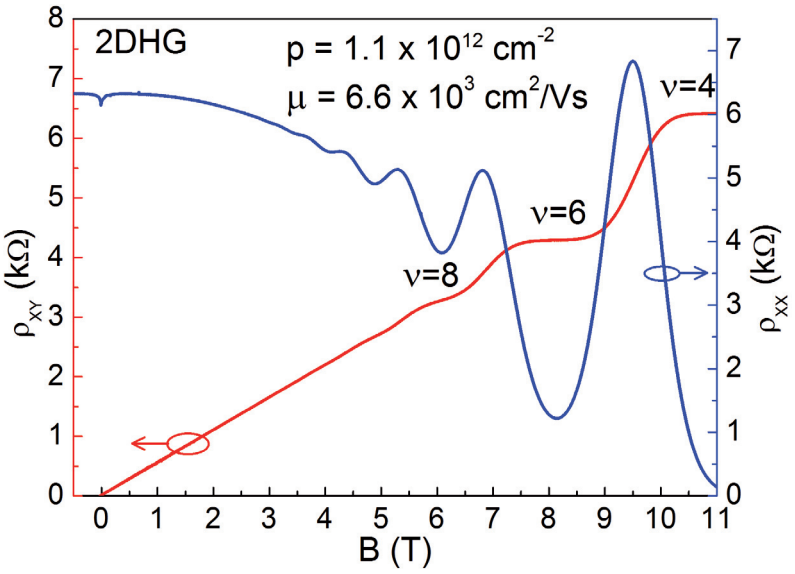

Figure 5.7: *[97], (red) Hall curve and (blue) SdH oscillations of the digitally doped sample A exhibiting a 2DHG, recorded at 280 mK.*

demonstrates distinct quantum Hall plateaus at even filling factors. The longitudinal resistance ρ_{xx} exhibits pronounced SdH oscillations already at 1.3 K, which are not observable at this temperature when high-mobility 2DHGs in GaAs/AlGaAs QWs are measured, [140]. The most probable reason is the lower effective mass of holes in InAs ($m_{eff} = 0.39\,m_0$, [115]) in comparison to GaAs ($m_{eff} = 0.51\,m_0$, [115]). In Section 5.4 it will be shown that the effective mass of holes is only about $m_{eff} \approx 0.10\,m_0$ in these structures.

Apart from the SdH oscillations, the strong feature dominating the ρ_{xx} curve in Fig. 5.7 is the negative parabolic magnetoresistance. By contrast, it is completely missing in sample 2DEG-C displayed in Fig. 5.5. The strong minimum of the longitudinal resistance around $B = 0$ T can be ascribed to a weak-antilocalization effect. Conversely, the peak at $B = 0$ T in Fig. 5.5 corresponds to weak localization. These observations point out that the phase-coherence length l_φ is significant in these heterostructures.

In conclusion, we succeeded for the first time in growing carbon-doped $In_xAl_{1-x}As/In_xGa_{1-x}As$ heterostructures which show p-type conductivity in the whole investigated range of indium concentration x. Developing a new doping design, we overcame the carbon nature leading to the donor-like behavior in ternary compounds with high indium content, and prepared a good quality 2DHG also in samples with $x = 0.75$. These structures are especially interesting because strong spin-orbit-coupling effects and a low hole effective mass are expected. The magnetotransport phenomena of the 2DHGs will be described in Section 5.4.

5.3 Nextnano^3 simulations of the valence-band structure

In this section we will discuss the specifics of the valence-band structure of the indium-containing heterostructures. The nextnano^3 program package was used to perform 8×8-band $\mathbf{k} \cdot \mathbf{p}$ simulations, with more details described in Section 3.5. Here, we concentrated on two samples representing the main differences. They differ in the indium content of the active layer, but more importantly in the design of the QW. First, we considered sample A, where the 2DHG is confined in the 4 nm thick strained InAs channel embedded in the $In_{0.75}Ga_{0.25}As$ QW. In the second case, we investigated the pure 20 nm wide $In_{0.40}Ga_{0.60}As$ QW of sample C. In both samples the QW is strongly asymmetric because the doping layer has been grown only on one side (the top side) of the QW. The layer sequence is schematically shown in Fig. 5.3(a), (b) and summarized in Table 5.2.

The calculated valence-band structure is presented in Fig. 5.8. Apparently it deviates from the results on the GaAs/AlGaAs heterostructures discussed in Section 4.3 and highlights pronounced differences. In Fig. 5.8(a), the immense separation between the first HH subband and the LH subband of sample A is surprising. It originates from the strong quantum confinement due to the InAs channel, which pushes the subbands away from each other. By contrast, the subbands in the valence band of sample C are close to each other owing to the relatively wide InGaAs QW, see Fig. 5.8(b).

The different quantum confinement in sample A and C has crucial influence on the spin splitting.[7] In the first case, due to the huge distance between the HH and LH subband, they couple at high values of the in-plane wave vector $\mathbf{k}_{||}$. This results in an almost isotropic dispersion of the HH-subband shown in Fig. 5.8(c) and a small spin splitting at the Fermi energy of about 1.4 meV. The situation is different in sample C. Here, because of the low subband separation, the anticrossing between HH and LH subbands occurs already at the Fermi energy and the subbands are strongly warped exhibiting pronounced spin splitting, see Fig. 5.8(b). As a consequence, the HH subband proceeds strongly anisotropically, see Fig. 5.8(d). We estimated the spin splitting of the uppermost subband in sample C at the Fermi energy in the range of 0.7 - 2 meV along the [001] and between 0.7 - 4 meV along the [011] direction. Both samples were studied extensively experimentally, see Section 5.4. The magnetotransport data of sample C exhibit varying amplitudes of the SdH oscillations. The analysis using fast Fourier transformation is given in Section 5.4.2. No spin splitting was observed in sample A, in agreement with the theoretical predictions.

Finally, the Fermi contour in 2D-$\mathbf{k}_{||}$-space in Fig. 5.8(c) and (d) is 4-fold symmetric due to the missing BIA, [15]. In sample C, Fig. 5.8(d), the Fermi contour has the typical rosette-like shape, which comes from warping. Adding BIA, the symmetry is reduced to 2-fold, [15]. The reason therefore is the omitted Dresselhaus term in the nextnano^3 calculations, discussed in Section 4.3. The first observation

[7] Here, only the SIA-induced spin splitting is considered due to the limitations of nextnano^3.

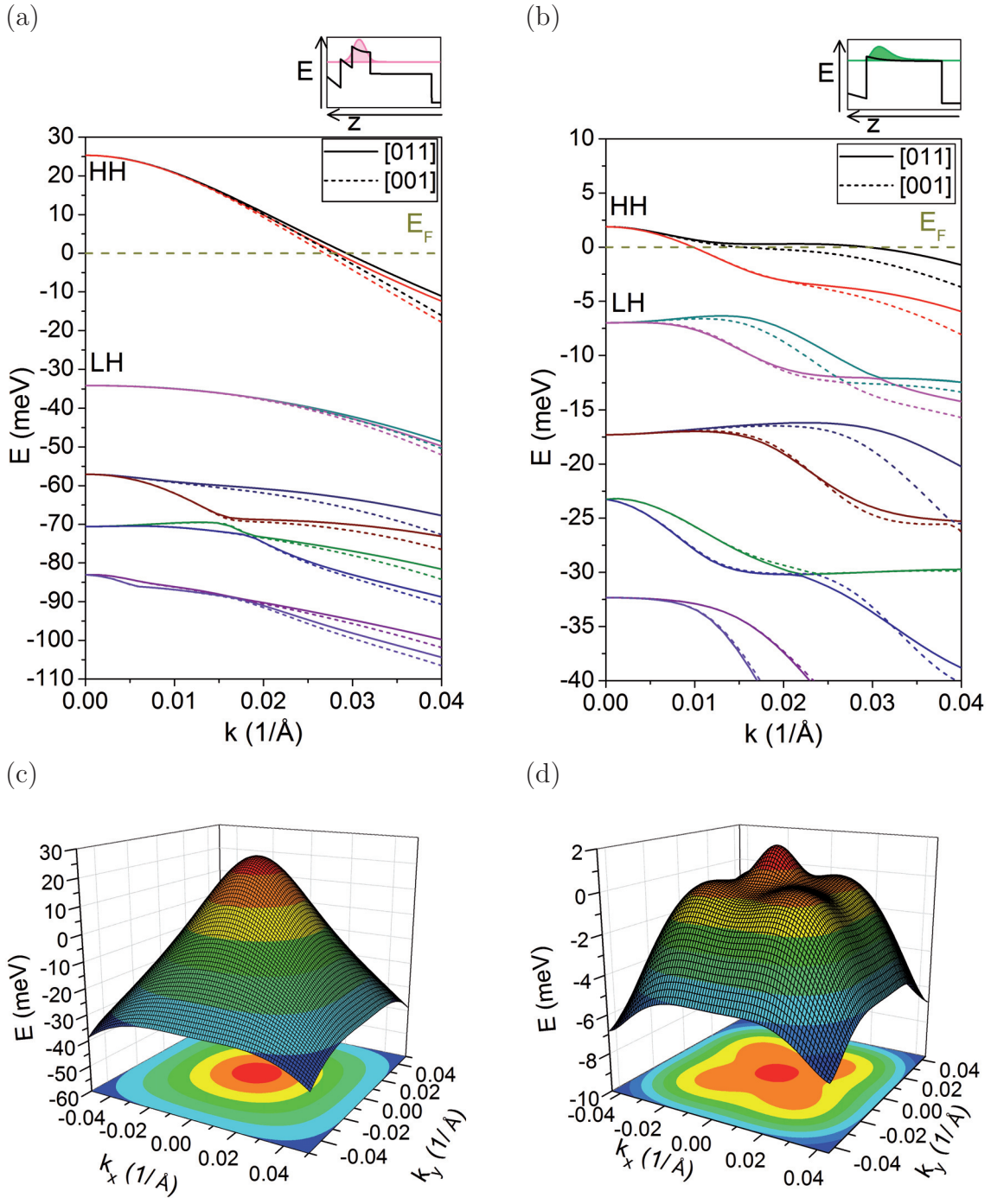

Figure 5.8: *Valence-band structure (a) of sample A containing a 4 nm thick strained InAs channel in the $In_{0.75}Ga_{0.25}As$ QW, (b) of sample C having a 20 nm wide $In_{0.40}Ga_{0.60}As$ QW. Inset (a), (b): Scheme of the valence-band edge of the QW, shaded area stands for the carrier density profile. (c) and (d) show the dispersion of the uppermost HH subband of samples A and C, respectively.*

of breaking the 4-fold symmetry of the Fermi contour to the 2-fold symmetry was reported in highly-doped GaAs/AlGaAs QWs in Ref. [16].

5.4 Magnetotransport measurements

We investigated magnetotransport properties of sample A with a final indium content of $x = 0.75$ and sample B having $x = 0.60$ at dilution-refrigerator temperatures and magnetic fields up to 17 T. Both samples were prepared in L-shaped Hall-bar geometry. A constant current of 10 nA was applied across the whole L-bar and the data were taken along both [011] and [01$\bar{1}$] crystallographic directions. The results are presented in Fig. 5.9. In both samples the Hall curve exhibits well-developed quantum Hall plateaus at even filling factors with a small signature of the filling factor $\nu = 3$, see Fig. 5.9 at $B = -15$ T ($B = -12$ T) in sample A (sample B). The positive Hall coefficient confirms the p-type conductivity in both samples.

The longitudinal magnetoresistance curve can be separated into three parts according to the magnetic field, which will be considered separately in the following sections. In the range of very low magnetic fields, a small dip around $B = 0$ T is present. This sharp decrease of the longitudinal resistance is most pronounced at mK temperatures and decreases in magnitude with increasing T up to approximately 20 K, where it vanishes. We ascribe it to the weak antilocalization effect and it will be discussed in more detail in Section 5.4.3. In the intermediate field range between -6 T and 6 T, a strong negative parabolic magnetoresistance dominates the ρ_{xx} curve. Due to its temperature- and B-dependence, it can be attributed to the hole-hole interaction effect in the diffusion channel. The temperature dependence of this effect was used to determine the hole-hole interaction time in Section 5.4.4. At high magnetic fields pronounced Shubnikov-de Haas oscillations develop. ρ_{xx} vanishes at the minima corresponding to the filling factors $\nu = 6, 4, 2$ and $\nu = 4, 2$ for samples A and B, respectively. This confirms the good quality of both samples. In this region, the Landau levels are twofold-degenerate, containing both spins. In Fig. 5.9, there is a double peak structure present as the spin-splitted minimum at $\nu = 3$ begins to emerge.

In Fig. 5.9, there is a significant difference in the longitudinal magnetore-

Sample	In content x	Crystal direction	p (10^{12} cm^{-2})	μ (cm^2/Vs)	τ_t (ps)	τ_q (ps)	τ_t/τ_q
A	0.75	[011]	1.1	5700	0.3	0.05	6
		[01$\bar{1}$]	1.1	7200	0.4	0.06	7
B	0.60	[011]	0.9	2200	0.2	0.08	3
		[01$\bar{1}$]	0.9	7100	0.6	0.09	7

Table 5.5: *Table of magnetotransport properties measured at 20 mK: hole density p, hole mobility μ, transport scattering time τ_t, quantum scattering time τ_q. The samples have different indium content x in the active layer.*

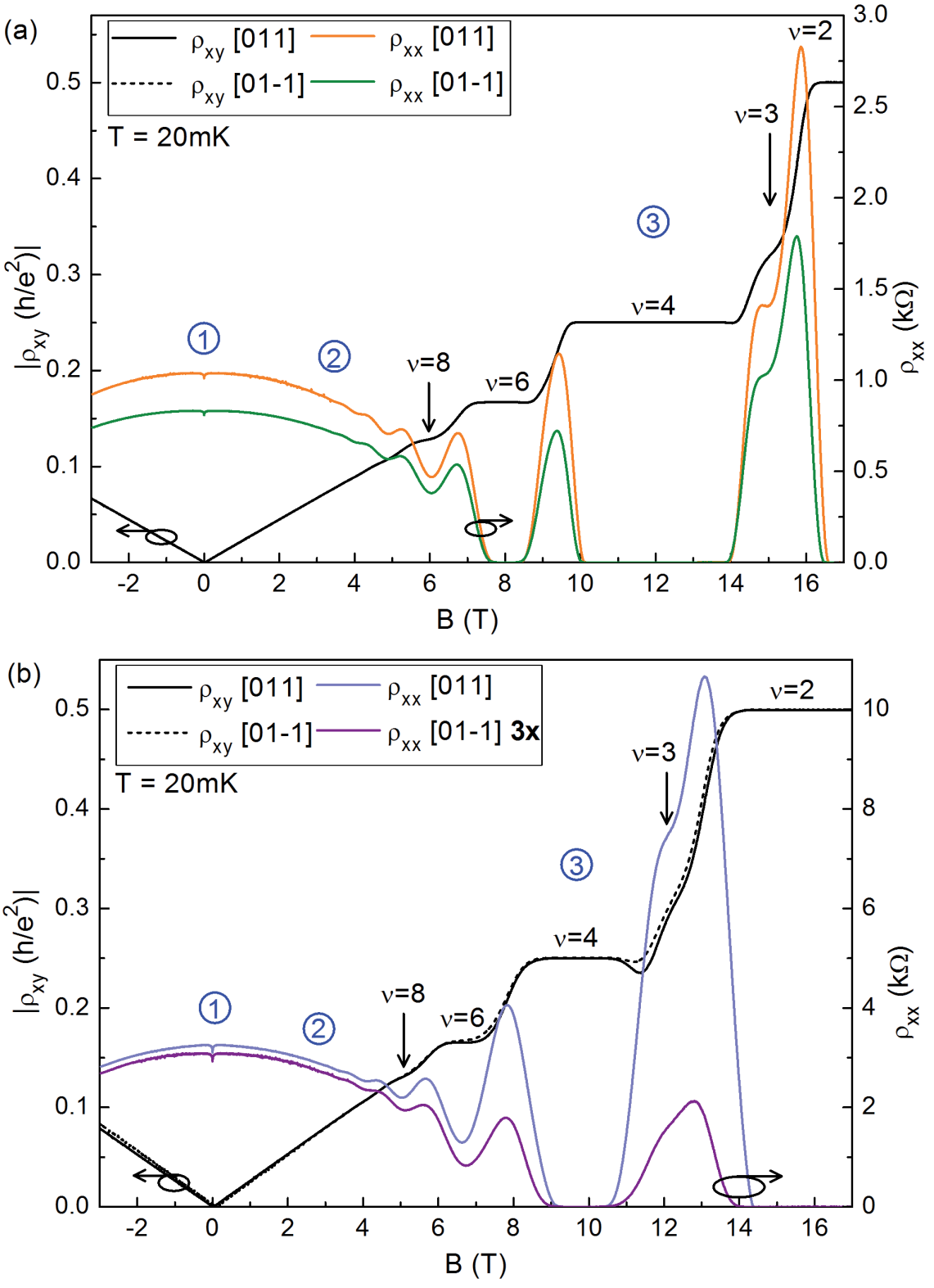

Figure 5.9: *Magnetotransport measurements at 20 mK (a) on sample A containing $x = 0.75$ indium, (b) on sample B with $x = 0.60$ indium in the active layer (the longitudinal resistance along [01$\bar{1}$] was multiplied by a factor of 3). The longitudinal-magnetoresistance curves show a pronounced anisotropy between the two orthogonal directions [011] and [01$\bar{1}$]. Numbers mark three specific parts of the ρ_{xx} curve according to the magnetic field, where: (1) weak antilocalization, (2) hole-hole interaction effect, and (3) SdH oscillations dominate.*

sistance measured along [011] and [01$\bar{1}$] crystal directions apparent. The zero-field resistance is by a factor of 1.3 higher in sample A and even by a factor of 3 higher in sample B along [011] compared to that along [01$\bar{1}$]. The crystal direction anisotropy and its possible origin will be discussed in Section 5.4.5. The highest mobility in the indium-containing heterostructure grown in this work, was achieved in sample A along the high mobility direction [01$\bar{1}$], $\mu = 7200\,\mathrm{cm}^2/\mathrm{Vs}$. Both samples have a very high hole density of roughly $10^{12}\,\mathrm{cm}^{-2}$. The carrier density and mobility are summarized in Table 5.5. We found consensus in the hole density calculated from the slope of the Hall curve and by using the fast Fourier transformation of the SdH oscillations. This fact, in combination with the vanishing ρ_{xx} at the minima of the SdH oscillations, confirms that no parallel conducting channel is present, neither in the doping layer nor as a second occupied subband in both these samples.

Beside the three dominant features, described above, the samples with low indium content ($x < 0.50$) show some specifics. These will be described in Section 5.4.2. In this work, we studied the inverted-doped structure as well. The results will be presented in Section 5.4.6. For the discussion of the effects dominating the magnetotransport, fundamental parameters of the 2DHG are needed and were extracted from the high-field region as shown in Section 5.4.1.

5.4.1 Transport parameters of heterostructures with a thin InAs channel

Longitudinal magnetoresistance curves were recorded at different temperatures in the range from 20 mK to 1 K. From the temperature damping of the amplitude of the SdH oscillations, we determined the effective mass of holes using the conventional Ando formula shown in Eq. 2.9 and an approximation according to Elhamri *et al.* [35], see Section 2.1. In order to get the correct amplitude of the SdH oscillations, the parabolic background was subtracted and then the resistance traces were normalized to the zero-field resistance $\rho_{xx}(B = 0\,T)$. The raw data and the extracted amplitudes for sample A are shown in Fig. 5.10. At a fixed magnetic field, m_{eff} was calculated from the slope of $\ln(Amplitude/T)$ versus T. Plotting $m_{eff}(B)$ versus B, the points give a straight line with a slope different from zero. Linear extrapolation of the data to $B = 0\,\mathrm{T}$ suggests $m_{eff} \approx 0.10\,m_0$ and $m_{eff} \approx 0.15\,m_0$ for samples A and B, respectively. Owing to the parabolic background and high magnetic fields we assume only an accuracy of ±30% whether applying the simplified fit or the non-simplified Eq. 2.9. We evaluated m_{eff} along different crystallographic directions. The values were found to vary sightly, but the differences lie within the inaccuracy of this method.

From the hole mobility and by using the values of effective mass discussed above, we derived the transport scattering time τ_t, see Table 5.5. In consistence with the observed anisotropy in μ, τ_t shows higher values along the [01$\bar{1}$] direction: $\tau_t = 0.4\,\mathrm{ps}$, $\tau_t = 0.6\,\mathrm{ps}$ for samples A and B, respectively. For both samples τ_t are in comparison with the high-mobility 2DHGs in GaAs/AlGaAs heterostructures three orders of magnitude lower, cf. Table 4.4. This corresponds to the lower hole mobility in the In-containing samples. The quantum scattering time τ_q was extracted

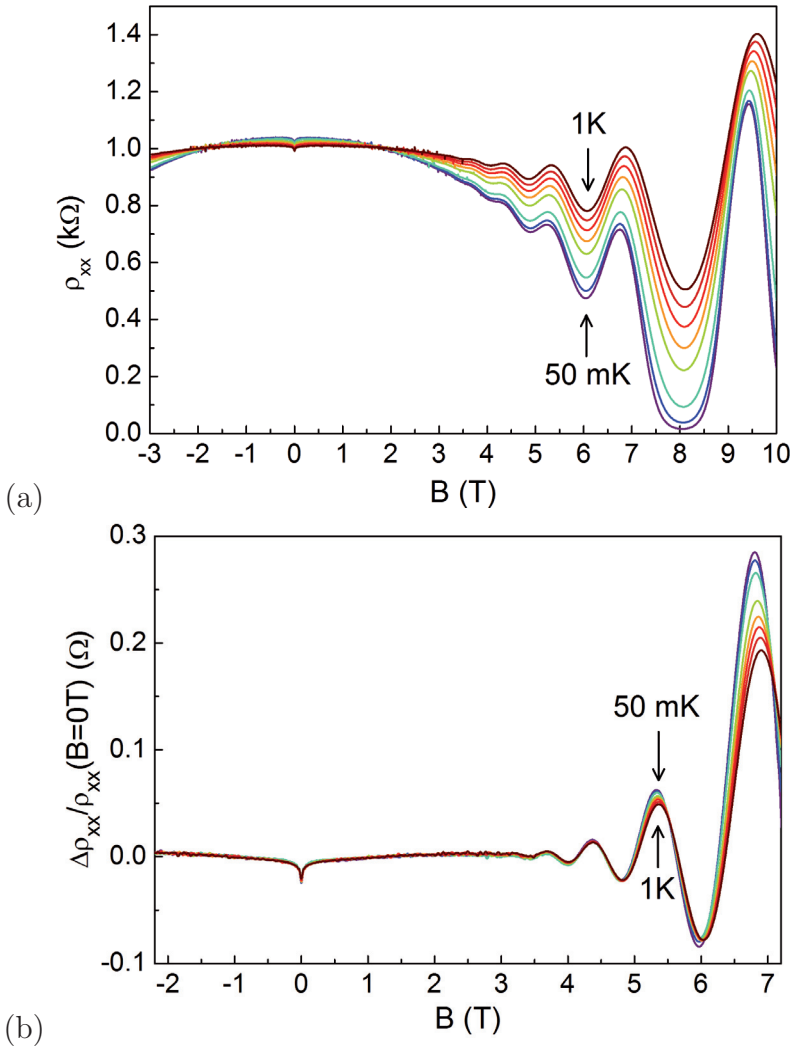

Figure 5.10: *Temperature dependence of the SdH oscillations of sample A used to evaluate the effective mass. The temperature was varied between 50 mK and 1 K. (a) Raw data were taken along the [011] direction. (b) Longitudinal resistance after substraction of the second-order polynomial background and normalization to the zero-field resistance.*

from the Dingle plot of our data, see Section 2.1. At a fixed temperature we plotted the changing amplitude $\Delta\rho_{xx}(B)$ versus $1/B$, see Eq. 2.11. From the slope of the straight line τ_q was calculated using the established m_{eff}. The values of τ_q are listed in Table 5.5. During the evaluation, we detected consistently longer quantum scattering times along the $[01\bar{1}]$ direction, also at other temperatures. The ratio of the scattering times τ_t/τ_q is approximately $3-7$, depending on the sample and the crystal direction, indicating a high fraction of a small-angle scattering in these samples. More information about the scattering mechanisms playing a role in these heterostructures is given in Section 5.4.5. In theory, the quantum scattering time is in direct connection to the width of the Landau levels, $\Gamma = \hbar/2\tau_q$. Explicitly, the lower τ_q, the higher is the broadening of the Landau levels. This fact, in combination

with a rather low carrier mobility and high carrier density in these samples, explains why we observe a small number of SdH oscillations.

To analyze the g factor of the In-containing heterostructures we will first introduce the theory. The Zeeman interaction for holes is more complex than for electrons. In bulk semiconductors there are two terms contributing to the Zeeman interaction, [15, 54]:

$$H_Z^h = 2\kappa\mu_B \mathbf{B}\cdot\mathbf{J} + 2q\mu_B \mathbf{B}\cdot\mathcal{J} \qquad \text{with} \qquad \mathcal{J} = (J_x^3, J_y^3, J_z^3) \tag{5.1}$$

Here, κ and q are the isotropic and anisotropic valence band g factors, respectively, μ_B is the Bohr magneton. According to Ref. [54], q is much smaller than κ and the anisotropic Zeeman term can be neglected. For the HH states with $m = \pm 3/2$, the perpendicular magnetic field gives rise to a Zeeman splitting $\Delta E_Z^{HH} = 6\mu_B\kappa B_z$. For the LH states with $m = \pm 1/2$ it results in $\Delta E_Z^{LH} = 2\mu_B\kappa B_z$, [141]. It follows $g_z^{HH} = 6\kappa$ and $g_z^{LH} = 2\kappa$, [15].

In this work, we evaluated the g factor of the 2DHG in sample A in a perpendicular magnetic field (out-of-plane g factor) as follows. It is assumed that the SdH oscillations first appear at magnetic field B_1, if the distance $\hbar\omega_c (= \hbar eB/m_{eff})$ between two Landau levels is larger than the collision broadening of the Landau levels Γ. Similarly, the first spin splitting in the SdH oscillations can be observed at magnetic field B_2, where the Zeeman energy $\Delta E_Z = \mu_B g^* B$ just exceeds Γ, g^* is the effective g factor. Taking Γ as a reference energy, we obtained for the g factor: $g^* = (\hbar eB_1)/(\mu_B B_2 m_{eff})$, [142, 143]. In Fig. 5.9(a), the SdH oscillations appear at $B_1 = 2.96\,\mathrm{T}$ and the minimum corresponding to the filling factor $\nu = 3$ occurs at $B_2 = 14.98\,\mathrm{T}$. It yields $g^* \approx 4$. For a second estimation, we used the quantum scattering time τ_q, see Table 5.5 and determined the broadening of the Landau levels $\Gamma = \hbar/2\tau_q$. To observe the spin splitting $\mu_B g^* B \geq \Gamma$ must be satisfied, [143]. Taking the equality in this expression, we got $g^* = \hbar/(2\tau_q \mu_B B_2)$, which gives for our data $g^* \approx 6$. The discrepancy in the approximated values of the g factor between these two methods stems most likely from the high uncertainty of τ_q. In summary, we estimated the effective g factor of our 2D holes in the 4 nm wide InAs channel embedded in $In_{0.75}Ga_{0.25}As$ QW to be $g^* \approx 4-6$ in perpendicular magnetic field. A comparable structure containing a 2DEG exhibits g factors of about 6, [144].

In conclusion, we determined the effective mass of holes in samples with an embedded InAs channel to be low, $m_{eff} \approx 0.10\, m_0$ and $m_{eff} \approx 0.15\, m_0$, in comparison to the 2DHG confined in a GaAs QW. The ratio of the transport scattering time and the quantum scattering time τ_t/τ_q is approximately $3-7$ indicating a high fraction of a small-angle scattering in these heterostructures. The out-of-plane g factor estimated from the SdH oscillations in a perpendicular magnetic field is $g^* \approx 4-6$.

5.4.2 Specifics of magnetotransport of InGaAs QWs with low indium content

In this section we will summarize the specific properties of heterostructures containing a 20 nm wide $In_xGa_{1-x}As$ QW with a low indium content of $x = 0.40$ (sample C)

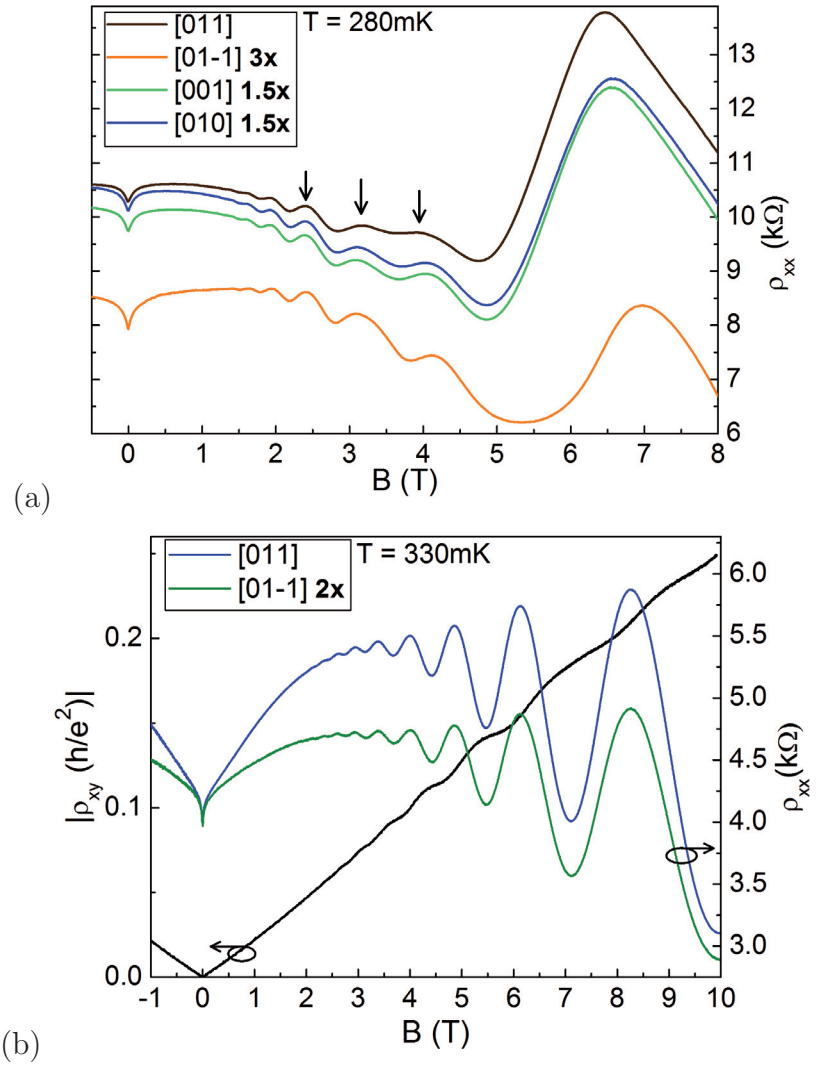

Figure 5.11: *(a) Longitudinal magnetoresistance of sample C with $x = 0.40$ indium, recorded at 280 mK along [011], [01$\bar{1}$], [001] and [010] crystal directions. Vertical arrows mark the varying amplitude of the SdH oscillations. Due to the large resistance anisotropy the ρ_{xx} curves along [01$\bar{1}$], [001] and [010] directions were multiplied by the indicated factors in order to increase the readability of the picture. (b) Magnetotransport of sample D with $x = 0.20$ indium at 330 mK. The longitudinal-magnetoresistance curve, taken along [01$\bar{1}$] direction, was multiplied by a factor of 2.*

and $x = 0.20$ (sample D). These samples enable us to investigate the influence of the indium content on the spin splitting and to compare directly the results with the GaAs/AlGaAs QWs described in Section 4.4.1. Further, it is interesting to examine if there are differences to the QWs with an embedded InAs channel and high indium content discussed in the previous section.

The ρ_{xx} and ρ_{xy} curves were measured in different ^{3}He cryostats at base temperatures of 280 mK and 330 mK in samples C and D, respectively. Magne-

totransport experiments were performed on L-shaped Hall-bar structures oriented along the [011], [01$\bar{1}$] and [001], [010] crystal directions. Similar features, as discussed above for samples A and B, could be identified in samples C and D as well. Longitudinal magnetoresistance exhibits three specific ranges according to the magnetic field, where successively the weak-antilocalization effect, the hole-hole-interaction effect and the SdH oscillations play a dominant role, see also the following Sections 5.4.3, 5.4.4. Further, a strong crystal-direction anisotropy influences the magnetotransport. The differences in the zero-field resistivity of sample C exceed 70% along the high-mobility direction [01$\bar{1}$] and 35% along the diagonal directions [001] and [010] in comparison to the low-mobility direction [011]. In sample D, the [01$\bar{1}$] direction exhibits 50% lower zero-field resistivity in contrast to the [011] direction. The resistivity anisotropy is directly reflected in the hole mobility, see Table 5.6. Section 5.4.5 will be devoted to this topic. Moreover, there are some additional features present in the ρ_{xx} curves of the 2DHG confined in a $In_xGa_{1-x}As$ QW.

Following the prediction of the $\mathbf{k} \cdot \mathbf{p}$ simulation of the valence-band structure in Section 5.3, there should be a strong spin splitting of the uppermost HH subband at the Fermi level in sample C. This was indeed confirmed by applying a Fourier transformation to the SdH oscillations. In Fig. 5.11(a), the oscillating amplitude is marked with vertical arrows. However, the beating pattern of the typical form as observed in high-mobility 2DHGs (cf. Section 4.4.1) is missing, probably due to the low number of developed SdH oscillations. According to Appendix B, we analyzed the different frequencies between 1.5 T and 5 T and the results are summarized in Table 5.6. In the FFT spectra we found two peaks corresponding to the two spin-splitted subbands and calculated their densities p_1 and p_2. The total density was represented as a separated peak and fits the relation $p = p_1 + p_2$.

From Eq. 2.19 and by using $m_{eff} \approx 0.21\, m_0$, determined from the temperature dependence of the amplitude between 300 mK and 1 K, the effective Rashba parameter β was calculated. The relative carrier imbalance amounts to about $\Delta p/p \approx$ 32% along the [011], [001], [010] directions and $\Delta p/p \approx 50\%$ along [01$\bar{1}$]. Inserting the mean value of (k_1, k_2) for the wave vector in $\Delta_{SO} = 2\beta k_{||}^3$ (cf. Eq. 2.18) we got the mean spin splitting of the HH subband at the Fermi energy, see Table 5.6(a). By comparing the crystallographic directions, significant differences emerge. Actually, there is no direction dependence of the densities extracted from the SdH oscillations to be expected because this method probes the whole Fermi surface. Nevertheless, we observed some variations of the densities in the high-mobility 2DHGs too, see Section 4.4.1. In the case of sample C, the highest spin splitting develops along the [01$\bar{1}$] direction. The spin splitting is lower along [011] direction and lowest along both diagonal directions [001] and [010]. This anisotropy can be a sign of interplay between BIA and SIA in this one-sided-doped QW. A further contribution to the anisotropy of the spin splitting can provide the effective mass, which is direction-dependent (not considered here) due to the warping.

Finally, we should note the limiting factors of this analyzing procedure. The low number of the developed SdH oscillations has large impact on the accuracy. This fact, in combination with uncertainty in m_{eff} (see discussion in Section 5.4), signalizes that the values in Table 5.6(a) must be considered as a rough estimate. The

(a) sample C, $x = 0.40$

Crystal direction	p_1	p_2	p	μ	β	Δ_{SO}
	$(10^{11}\,\mathrm{cm}^{-2})$			$(\mathrm{cm}^2/\mathrm{Vs})$	$(10^{-28}\,\mathrm{eVm}^3)$	(meV)
[011]	1.6	3.1	4.7	1300	3	3.2
[01$\bar{1}$]	1.2	3.5	4.7	5000	5	4.4
[001]	1.5	2.9	4.4	2200	3	3.0
[010]	1.5	2.9	4.4	2100	3	3.0

(b) sample D, $x = 0.20$

Crystal direction	p $(10^{12}\,\mathrm{cm}^{-2})$	μ $(\mathrm{cm}^2/\mathrm{Vs})$
[011]	1.0	1500
[01$\bar{1}$]	1.0	2900

Table 5.6: *Magnetotransport properties at 300 mK of samples containing a* $\mathrm{In_xGa_{1-x}As}$ *QW with low indium content x. (a) Results of the Fourier analysis of the SdH oscillations of sample C. The* p_1*,* p_2 *are the densities of the spin subbands, p is the total density,* μ *is the hole mobility,* β *is the effective Rashba parameter calculated from Eq. 2.19 and* Δ_{SO} *is the mean spin splitting of the HH subband. The values of the total density slightly vary because the experiments along [011], [01*$\bar{1}$*] and [001], [010] were performed on two different sample pieces cut from the same wafer.*

relation $\Delta_{SO} = 2\beta k_{||}^3$ is based on Eq. 2.18, which is satisfied for small $k_{||}$ considering a parabolic dispersion of the HH subband. Owing to the simulated band structure in Fig. 5.8, in such an extreme sample with high carrier density, it is a very rough approximation. Our further approach was done using the mean value of the effective mass in Eq. 2.18. Both spin subbands have different band bendings resulting in a different value of the effective mass. Nevertheless, the calculated spin splitting in sample C is in good agreement with the theoretical prediction derived from the valence-band simulations in Section 5.3. Further, its magnitude is much higher than that observed in the high-mobility 2DHGs investigated in Section 4.4.1. Moreover, comparable GaAs/AlGaAs QWs with a similar hole density of $p = 4.7 \times 10^{11}\,\mathrm{cm}^{-2}$ and heterostructure designs exhibit a spin-splitting of about 1.2 meV, cf. Section 4.4.1 and Ref. [16]. This is 3-times lower than in our sample. The factor responsible for the increased spin splitting must be the increased spin-orbit coupling due to the presence of $x = 0.40$ indium in sample C. Hence, there is a direct influence of the indium content on the spin-orbit interaction.

Apart from the three discussed parts, the ρ_{xx} curve of sample D exhibits an increase of the longitudinal resistance between 0.2 T and 2.5 T, see Fig. 5.11(b). This positive magnetoresistance was observed only in this sample containing $x = 0.20$ indium in the QW and at all investigated temperatures in the range between 300 mK and 4.2 K. Following Fig. 5.11, its magnitude is higher along [011] direction, which can point out an increased scattering rate along this crystal direction. In

addition, it did not show any dependence on temperature.

In conclusion, besides the three dominant features: WAL minimum, negative parabolic magnetoresistance and distinct SdH oscillations developed in samples with high In content and InAs channel as well, the sample consisting of a simple $In_{0.40}Ga_{0.60}As$ QW exhibit a changing amplitude of the SdH oscillation. This evidences significant spin splitting of the HH subband up to $\sim 5\,\mathrm{meV}$, which represents a large enhancement to the similar GaAs QW. Additionally, a strong crystal direction anisotropy of the magnetotransport data and of the related transport parameters was present also in these QWs.

5.4.3 Weak antilocalization

The formation of a weak-antilocalization dip is a sign of a strong spin-orbit interaction. In 2D hole systems, where the spin splitting of the HH subband is proportional to k^3, the Hikami-Larkin-Nagaoka (HLN) theory [64] was successfully applied to quantitatively investigate the weak-antilocalization effect, [17, 145]. Within this theory the quantum correction to the conductivity is [64, 65]:

$$\begin{aligned}\Delta\sigma(B) &= -\frac{e^2}{\pi h}\left[\frac{1}{2}\psi\left(\frac{1}{2}+\frac{B_\varphi}{B}\right)-\frac{1}{2}\ln\left(\frac{B_\varphi}{B}\right)-\psi\left(\frac{1}{2}+\frac{B_\varphi+B_{so}}{B}\right)\right.\\ &\left.+\ln\left(\frac{B_\varphi+B_{so}}{B}\right)-\frac{1}{2}\psi\left(\frac{1}{2}+\frac{B_\varphi+2B_{so}}{B}\right)+\frac{1}{2}\ln\left(\frac{B_\varphi+2B_{so}}{B}\right)\right] \qquad (5.2)\end{aligned}$$

The expression contains two fitting parameters $B_\varphi = \hbar/(4De\tau_\varphi)$ and $B_{so} = \hbar/(4De\tau_{so})$, from which the phase-coherence time τ_φ and the spin-orbit scattering time τ_{so} can be evaluated. D is the diffusion constant and other constants are of common meaning.

In all our indium-containing heterostructures we clearly recognized a sharp WAL resistance minimum in the vicinity of $B = 0\,\mathrm{T}$, see Figs. 5.9 and 5.11. It corresponds to the sharp peak in the longitudinal conductivity $\Delta\sigma(B) = [\sigma(B) - \sigma(0)]$, which is most pronounced at low temperatures and can be observed in a wide temperature range from 20 mK to 20 K. We used the HLN theory to fit the magnetotransport data of sample A and B. Before we proceed with the evaluation of the WAL, we should discuss the range of validity of the theory. Eq. 5.2 is valid in the diffusive regime for magnetic fields lower than the transport magnetic field $B < B_t = \hbar/(4De\tau_t)$. B_t depends on magnetotransport parameters such as hole density and mobility, and it was calculated for each sample separately. In all studied samples the WAL feature is extremely pronounced and extends up to $\pm 0.2\,\mathrm{T}$ or $\pm 0.4\,\mathrm{T}$ which is much more than the range given by the transport magnetic field B_t. This confirms the expectations of a strong spin-orbit interaction in these heterostructures.

It is worth to note that although the HLN theory is valid only below the transport field B_t, we found excellent agreement between the theoretical curve and the measured data up to $B = 6\,B_t$ (sample A), where the WAL feature spreads out. The fitting parameters (the scattering times τ_{so} and τ_φ) do not change significantly

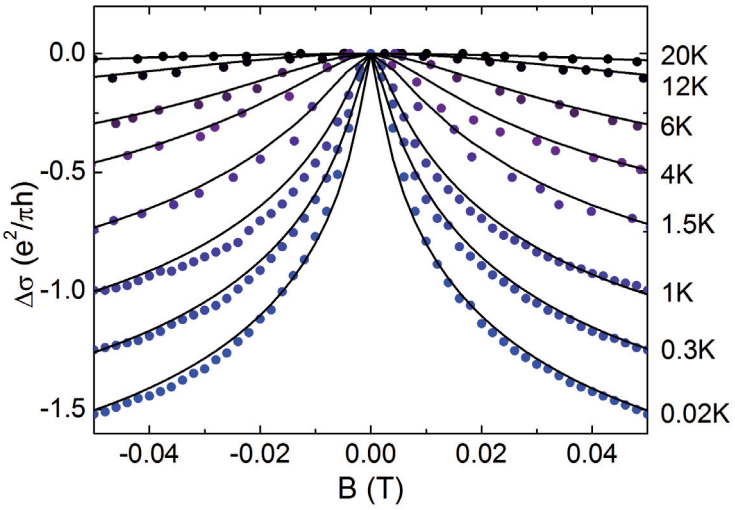

Figure 5.12: *Temperature dependence of the WAL peak present in the conductivity of sample A along the [011] crystal direction. The solid lines represent theoretical fits by Eq. 5.2.*

with changing the fitting interval. The inaccuracy in the scattering times was about 5%. In addition, fitting with the ILP theory, represented by the equation in Ref. [65], does not yield satisfactory consensus with the experimental curve, see also Section 2.5.

In the first part of this section we will investigate the temperature dependence of the phase-coherence time and the spin-orbit scattering time extracted from the WAL data of sample A. The second part of this section concentrates on a very striking phenomenon: an anisotropy of quantum-interference-related effects, which takes place in sample B.

Temperature dependence of τ_φ and τ_{so}

We investigated the temperature dependence of the WAL conductivity peak in sample A from tens of millikelvin up to tens of kelvin. The experimental data at selected temperatures are plotted in Fig. 5.12. The fitting interval had to be taken slightly larger than the transport magnetic field ($B_t = 0.03\,\mathrm{T}$) to get a reasonable number of data points. As obvious from Fig. 5.12, the theoretical curves match well with the experimental data. From the fits, we extracted the phase-coherence time τ_φ and the spin-orbit scattering time τ_{so} and investigated their temperature dependence.

In 2D systems the phase-breaking rate is determined by electron-phonon (here hole-phonon) scattering and electron-electron (here hole-hole) scattering, [146]:

$$\frac{1}{\tau_\varphi} = \frac{1}{\tau_{ep}} + \frac{1}{\tau_{ee}} \tag{5.3}$$

At low temperatures the hole-phonon scattering time τ_{ep} is much longer than the hole-hole scattering time τ_{ee}, thus the phase-breaking rate is dominated by the hole-hole scattering, [147, 148, 146]:

$$\frac{1}{\tau_\varphi} \approx \frac{1}{\tau_{ee}} \tag{5.4}$$

There are two mechanisms contributing to the hole-hole scattering, [147]: (a) hole-hole collisions with small-energy transfer leading to functional dependence of the

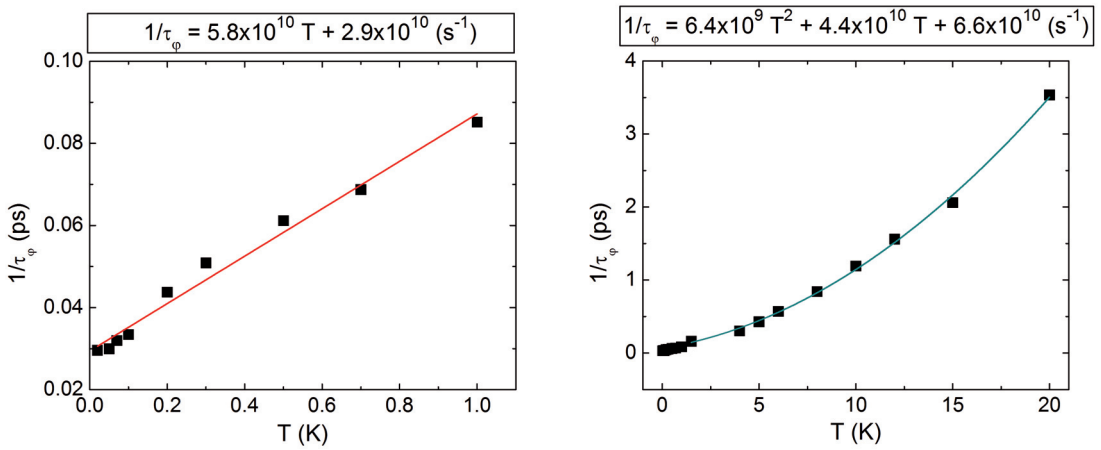

(a) for $T < 1\,\mathrm{K}$: $1/\tau_\varphi \propto T$ (b) for $T > 1\,\mathrm{K}$: $1/\tau_\varphi \propto T^2$

Figure 5.13: *Temperature dependence of the phase-breaking rate $1/\tau_\varphi$ extracted from the fits in Fig. 5.12. (a) at $T < 1$ K the phase-breaking rate exhibits linear dependence on T. (b) at $T > 1$ K, the phase-breaking rate increases as T^2.*

phase-breaking rate on temperature: $1/\tau_\varphi \propto T$ at $T < \hbar/k_B\tau_t$, and (b) hole-hole collisions with large-energy transfer resulting in the phase-breaking rate $1/\tau_\varphi \propto T^2$ at $T > \hbar/k_B\tau_t$.

We observed a rapid reduction of the phase-coherent time τ_φ with increasing temperature: from $\tau_\varphi = 38\,\mathrm{ps}$ at 20 mK it decreased by two orders of magnitude to $\tau_\varphi = 0.3\,\mathrm{ps}$ at 20 K. Fig. 5.13 shows the evolution of the phase-breaking rate $1/\tau_\varphi$ with temperature. We found two different functional dependencies: (a) for $T < 1\,\mathrm{K}$ the phase-breaking rate increases linearly with temperature, $1/\tau_\varphi \propto T$, see Fig. 5.13(a), (b) whereas for $T > 1\,\mathrm{K}$ the phase-breaking rate is proportional to $1/\tau_\varphi \propto T^2$, see Fig. 5.13(b). For the comparison with the theory of the electron-electron scattering, we must calculate the critical temperature first. Using the known transport scattering time $\tau_t = 0.3\,\mathrm{ps}$, we obtained the critical temperature $T_c = \hbar/k_B\tau_t \sim 25\,\mathrm{K}$, which is far beyond the investigated temperature range in Fig. 5.13. This result allows us to assume that the linear dependence at $T < 1\,\mathrm{K}$ originates from the small-energy-transfer mechanism. However, the T^2-dependence cannot be clearly assigned to the large-energy-transfer mechanism, because the experimental results are still below the critical temperature $T_c \sim 25\,\mathrm{K}$. Moreover, a quadratic dependence on the temperature originating from the hole-phonon scattering was often found in literature, [149, 147]. Probably, at temperatures higher than 1 K the hole-phonon scattering can play an important role, [150]. However, in thin films at liquid-helium temperatures, it is very difficult to separate these two mechanisms, [149].

Theoretically, τ_φ should diverge as $T \longrightarrow 0\,\mathrm{K}$ if there exist only inelastic hole-hole and hole-phonon scattering, [147]. Many recent experiments found rather a finite value of τ_φ as $T \to 0\,\mathrm{K}$, [147, 151]. For example, this behavior was reported on 2DEGs in an InGaAs/InP QW [152]. In agreement with the earlier observation, a saturation of τ_φ occurs at low temperatures, which is demonstrated as a nonzero

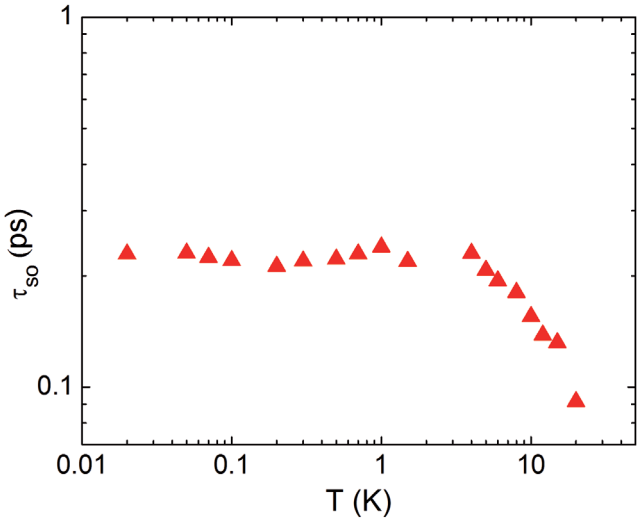

Figure 5.14: *Temperature dependence of the spin-orbit scattering time τ_{so} extracted from the fits in Fig. 5.12. At low temperatures the spin-orbit scattering time remains constant, but for temperatures higher than 4 K it starts to decrease.*

intercept of the straight line in Fig. 5.13(a). The saturation implies that there must exist some additional phase-breaking mechanisms. As a possible origin literature proposes: inhomogeneous distribution of the alloy composition, the interface roughness or variations of the doping concentration, [152].

From the theoretical fits in Fig. 5.12 we extracted the spin-orbit scattering time τ_{so} and evaluated its temperature dependence between 20 mK and 20 K, plotted in Fig. 5.14. At low temperatures between 20 mK and 4 K, the spin-orbit scattering time remains constant $\tau_{so} = 0.2$ ps, but for temperatures higher than 4 K it decreases with increasing temperature. Moreover, τ_{so} is reduced by a factor of 2 towards $\tau_{so} \sim 0.1$ ps at 20 K. The change of the spin-orbit scattering time with T is striking and was not observed in literature yet. Up to now, the experimental studies reported T-independent τ_{so}, [153, 152, 145, 154, 155].

Anisotropic phase-coherent transport

Similar to sample A, we observed in sample B with $x = 0.60$ indium a very distinct WAL dip pointing out strong spin-orbit interaction, see Fig. 5.9(b). In this sample we investigated the crystal direction anisotropy. For this reason, we used L-shaped Hall bars with arms fabricated along the [011], [01$\bar{1}$] and [001], [010] crystallographic directions. Fig. 5.15 presents the experimental data. A close inspection of the magnetoresistance curves reveals peculiar differences. Beginning with the direction [01$\bar{1}$], where the mobility is the highest, the red curve in Fig. 5.15(a) exhibits a very pronounced WAL minimum. The curve form changes if we apply the current along the [011] direction. A clear WAL dip is still present around the $B = 0$ T but moreover it seems to be superimposed on a sharp weak-localization peak, cf. black curve in Fig. 5.15(a). The WL peak is also clearly recognizable in Fig. 5.15(b) along both diagonal directions [001] and [010], and even most pronounced along the [010] direction, cf. blue curve in Fig. 5.15(b). Simultaneously, the graphs demonstrate a well-formed WAL minimum as well.

Equally to sample A, we applied the HLN theory, perfectly matching

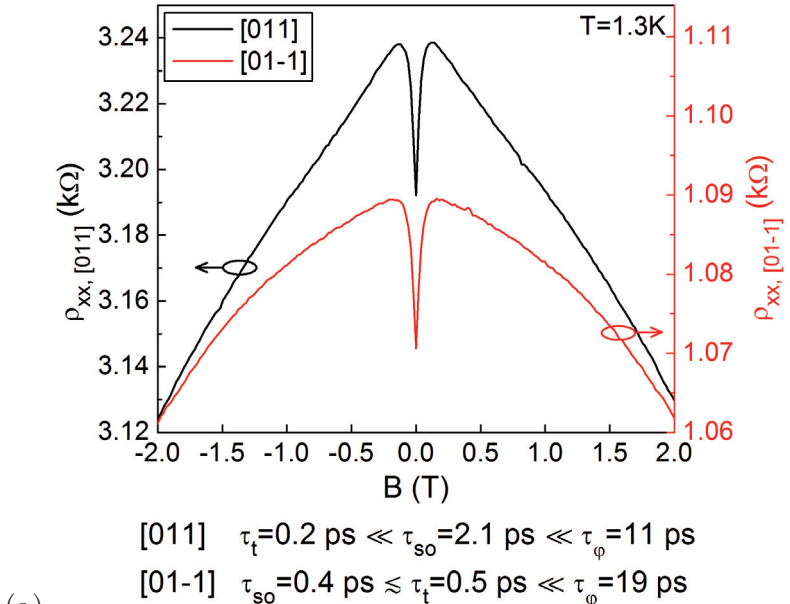

(a)

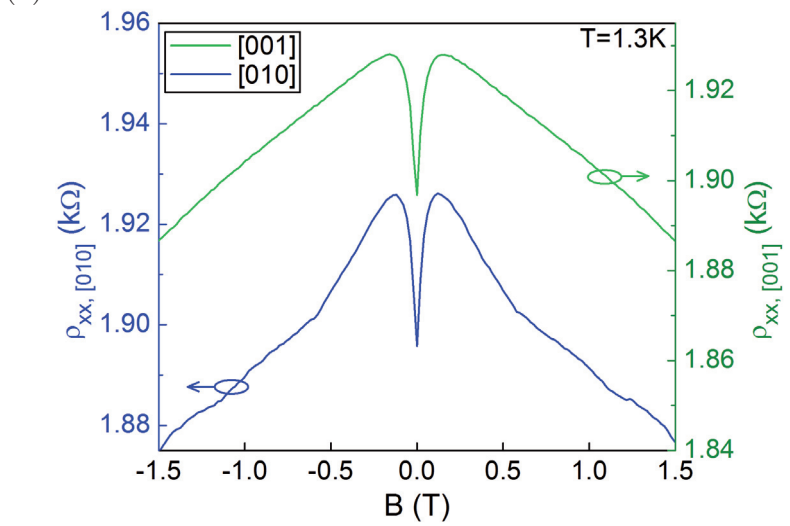

(b)

Figure 5.15: *Longitudinal magnetoresistance of sample B recorded along different crystallographic directions at 1.3 K. All four directions show a sharp WAL resistance minimum. In addition, a weak-localization peak is clearly recognizable along the [011] and [001] directions and very pronounced along [010] direction. The scattering times were extracted by fitting the experimental data with the HLN theory Eq. 5.2. The relations between the scattering times point out very strong spin-orbit interaction along the [01$\bar{1}$] direction.*

the data. We extracted the phase-coherence time and the spin-orbit scattering time. Their values at 1.3 K are listed in Fig. 5.15 under the corresponding curve. The scattering times are different if the crystallographic direction of current flow was

changed. A striking anisotropy comes out if we try to order them. Along $[01\bar{1}]$ direction, the scattering times obey the relation $\tau_{so} \lesssim \tau_t \ll \tau_\varphi$. Surprisingly, the relation changes to $\tau_t < \tau_{so} \ll \tau_\varphi$ if the scattering times along [011], [001] and [010] directions are compared.

The first regime, where $\tau_{so} < \tau_t \ll \tau_\varphi$, can be assigned to a strong spin-orbit interaction, reported also by Grbic *et al.* [17] in a carbon-doped GaAs/AlGaAs QW. In this regime, the spin-orbit interaction cannot be treated as a weak perturbation as it is done in common theoretical calculations. We estimated the characteristic field $B_{so,[01\bar{1}]} = 0.05\,\mathrm{T}$, where the WAL positive magnetoresistance should turn into the WL negative magnetoresistance, [17]. The value of B_{so} is beyond the transport field $B_{t,[01\bar{1}]} = 0.03\,\mathrm{T}$, for which the theory is valid. This explains qualitatively why we observed only the WAL dip without the WL peak in the longitudinal magnetoresistance, cf. red curve in Fig. 5.15(a).

The second case, where $\tau_t < \tau_{so} \ll \tau_\varphi$, corresponds to the more common regime. The characteristic field $B_{so,[011]} = 0.03\,\mathrm{T}$ is within the transport field $B_{t,[011]} = 0.30\,\mathrm{T}$. The shape of the low-field magnetoresistance indicates that the sharp WAL resistance minimum is superimposed on a broader WL resistance peak, see Fig. 5.15(a). Similarly, the diagonal directions [001] and [010], shown in Fig. 5.15(b), belong to the normal regime. In summary, both discussed regimes are recognizable in the form of the longitudinal-magnetoresistance curve in the vicinity of $B = 0\,\mathrm{T}$ and in comparison of the spin-orbit and transport scattering times. We noticed that this anisotropy was maintained at all measured temperatures from 20 mK to 4.2 K.

For completeness it should be mentioned that Koga *et al.* [63] revealed a transition from the positive (WAL) to negative (WL) magnetoresistance as they tuned the structure inversion asymmetry of the InGaAs QW. The authors demonstrated that with decreasing degree of SIA of the QW the spin-orbit interaction was reduced (τ_{so} increased) and the WAL minimum changed to WL peak, see also Fig. 2.5(b). Here, we report a clear change of the shape of the magnetoresistance curve, if measured along different crystallographic directions. To the best of our knowledge, such a dependence of the WAL on crystallographic direction was not shown in literature yet and is missing also in the theoretical predictions.

Finally, we determined the phase-coherence length of holes in these heterostructures with high indium content. From the expression $l_\varphi = \sqrt{D\tau_\varphi}$, the phase-coherence length is $l_{\varphi,[011]} = 0.5\,\mu\mathrm{m}$, $l_{\varphi,[01\bar{1}]} = 0.6\,\mu\mathrm{m}$ in sample A and $l_{\varphi,[011]} = 0.3\,\mu\mathrm{m}$, $l_{\varphi,[01\bar{1}]} = 0.9\,\mu\mathrm{m}$ in sample B at 700 mK. The results are comparable with a similar structure doped with manganese, [156]. It demonstrates that the fabrication of phase-coherent devices on these heterostructures is possible.

In conclusions, the indium-containing heterostructures exhibit a very strong WAL resistance minimum. To quantitatively analyze the WAL effect, we used the HLN theory, which excellently matched with the experimental data. In the first part, we studied the temperature dependence of the characteristic scattering times. The phase-breaking rate was found to increase as $\sim T$ for $T < 1\,\mathrm{K}$ and as $\sim T^2$ for $T > 1\,\mathrm{K}$. The linear dependence of $1/\tau_\varphi$ originates in the hole-hole scattering with small-energy transfer. Meanwhile, the quadratic increase of $1/\tau_\varphi$ can be

sign of both: hole-phonon scattering or hole-hole scattering with large-energy transfer. The spin-orbit scattering time remains constant up to 4 K and then it starts to decrease with increasing temperature. In the second part, we described a peculiar anisotropy of the phase-coherent transport. Depending on the crystallographic direction of current flow either a WAL dip superimposed on WL peak or only a WAL dip was developed in the longitudinal magnetoresistance.

5.4.4 Hole-hole interaction induced magnetoresistance

Apart from the SdH oscillations, the second most obvious feature in the longitudinal-resistance curve is the negative parabolic magnetoresistance in the intermediate field range. It was observed in all indium-containing samples along all investigated crystallographic directions. Moreover, it depends strongly on the temperature, as shown in Fig. 5.10(a).

There are several sources of a negative magnetoresistance reported on 2D systems such as a quasiclassical memory effect [157], a weak localization [158], or an electron-electron interaction effect [126, 127]. To identify which effect is the cause of the strong parabolic background in our samples, we compared their T- and B-dependencies with our observations. A parabolic shape of the negative magnetoresistance can be induced by the electron-electron interaction effect or the memory effect. Since we observed strong T-dependence of the parabolic background, the memory effect, which was reported to be temperature-independent at low temperatures [126], can be excluded as possible origin. Further, a negative magnetoresistance can be caused by weak-localization effect. However, the weak localization as a quantum interference of time-reversed paths is suppressed already by a weak magnetic field. This is in contrast to our measurements, where the parabolic background spreads out to ± 3 or ± 6 T, depending on the sample. Nevertheless, we already observed indications of the weak-localization peak, which superimposed at low magnetic fields the negative parabolic magnetoresistance, see Section 5.4.3.

On the basis of these considerations, we attributed the effect observed in our samples to the electron-electron interaction in the diffusion channel. The theoretical description was done by Altshuler and Aronov [124] and it was confirmed by investigations on 2DEGs in GaAs/AlGaAs [125, 159], or GaN/AlGaN [158, 155], heterostructures. Since, there is no equivalent theory for the 2D holes, we applied the theory developed for electrons on our 2DHG to evaluate the hole-hole interaction effect. In the following, we used the method introduced by Choi *et al.* [125] to calculate the hole-hole interaction time τ_{hh}. The magnetoresistance can be written as [158]:

$$\rho_{xx}(B) = \rho_0^2(\omega_c^2\tau^2 - 1)\delta\sigma_{hh}. \tag{5.5}$$

Here, $\rho_0 = 1/\sigma_0$ is the Drude resistivity and τ is the Drude scattering time. From perturbation theory, the correction to the Drude conductivity σ_0 caused by the hole-hole interaction in the diffusion channel is given in 2D as [125]:

$$\delta\sigma_{hh} = -\left[4 - 3\frac{2+F}{F}\ln\left(1+\frac{F}{2}\right)\right]\left(\frac{e^2}{2\pi^2\hbar}\right)\ln\left(\frac{\hbar}{k_B T\tau_{hh}}\right). \tag{5.6}$$

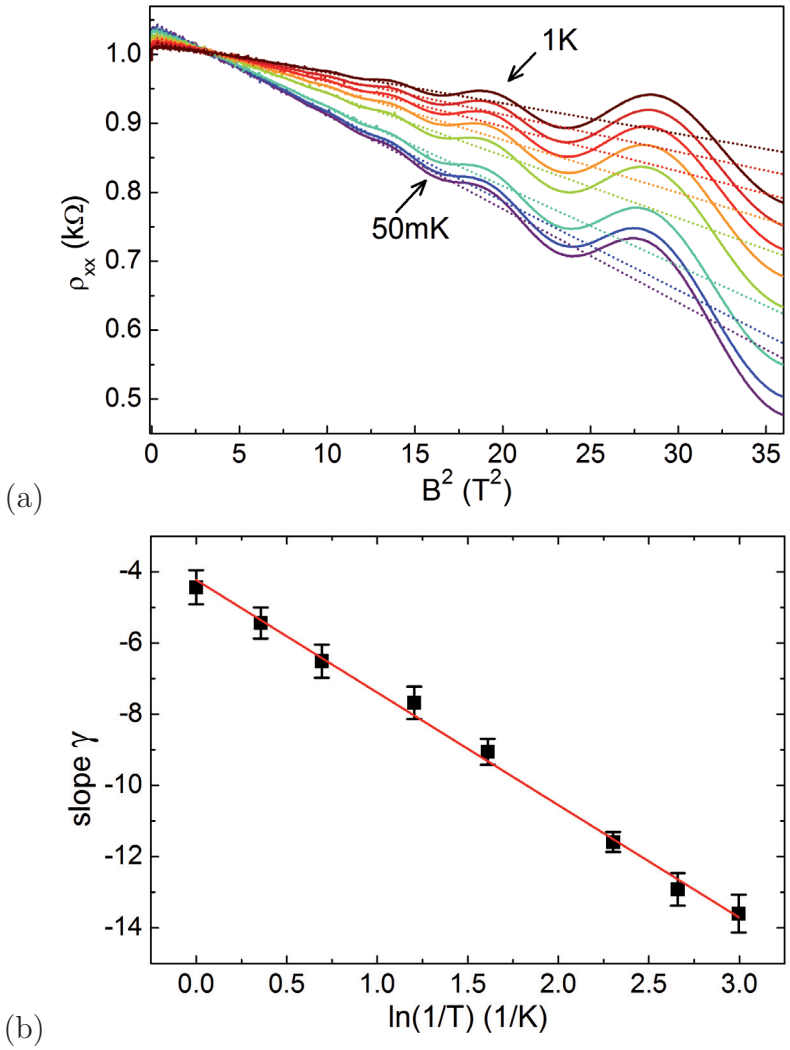

Figure 5.16: *(a) Longitudinal magnetoresistance of sample A (solid lines) and linear fits according to Eq. 5.5 (dashed lines) as a function of B^2 along the [011] direction for temperatures between 50 mK and 1 K. (b) Slope γ of the linear fits in (a) plotted versus* $\ln(1/T)$. *The red line represents the fit with Eqs. 5.5 and 5.6.*

The Hartree factor F represents an angular average over the statically screened Coulomb interaction $F = \int \frac{d\theta}{2\pi}(1 + \frac{2k_F}{\kappa} sin(\frac{\theta}{2}))^{-1}$, k_F is the Fermi wave vector and κ is the inverse screening length in 2D.

In order to quantitatively describe our measurements, we have to specify the temperature regime first. The theory (Eq. 5.6) is valid in the diffusive regime, where $k_B T \tau_t/\hbar < 1$. Using the transport scattering time τ_t, listed in Table 5.5, the expression $k_B T \tau_t/\hbar$ takes values from 0.001 to 0.05 $\ll 1$ in the temperature range between 20 mK and 1 K, respectively. Thus, the condition of the diffusive transport is satisfied and we can apply Eq. 5.6. In Fig. 5.16(a), ρ_{xx} is plotted as a function of B^2 for a variety of temperatures and follows a clear linear dependence (see Eq. 5.5) with a slope γ. The slope γ is temperature-dependent as a function of $\ln(1/T)$,

shown in Fig. 5.16(b). Combining Eq. 5.5 and Eq. 5.6 we fitted the data in Fig. 5.16(b) and evaluated the interaction time τ_{hh}. The factor F was the second fitting parameter.

The experimental data were analyzed also in relation to the crystallographic direction. For sample A containing $x = 0.75$ indium we obtained the interaction time of $\tau_{hh,[01\bar{1}]} = 2.2\,\mathrm{ps}$ along the $[01\bar{1}]$ and a lower value of $\tau_{hh,[011]} = 2.0\,\mathrm{ps}$ along [011] direction. Interestingly, the diagonal directions [010] and [001] achieve the same hole-hole interaction time of $\tau_{hh,[010],[001]} = 1.7\,\mathrm{ps}$. The accuracy established from the fitting procedure is $\pm 0.1\,\mathrm{ps}$. Further, we investigated this effect also in sample B with $x = 0.60$ indium. Here, the calculated interaction times are: $\tau_{hh,[01\bar{1}]} = 0.87\,\mathrm{ps}$ and $\tau_{hh,[011]} = 0.83\,\mathrm{ps}$ along the orthogonal directions $[01\bar{1}]$ and [011] respectively, determined with an accuracy of $\pm 0.07\,\mathrm{ps}$. In full agreement with the previous results, we got the longest hole-hole interaction time along the high-mobility direction $[01\bar{1}]$. For all fitting procedures the Hartree factor F stays in the range between $F = 1.5$ to 1.7. In an AlGaAs/GaAs 2DEG of much higher mobility, the Hartree factor was reported to be $F = 0.45$ [125] and $F = 0.25$ in an AlGaN/GaN 2DEG, [158]. In addition, we evaluated the hole-hole interaction effect in samples with low indium content, too. The results on samples with different indium content are summarized in Fig. 5.17. We found that τ_{hh} rises with increasing hole density even by one order of magnitude. This is supported by the fact that the negative parabolic magnetoresistance is diversely pronounced in different samples. While in sample A the parabolic background spreads out in the range of approximately $\pm 6\,\mathrm{T}$, in sample C it reaches only to $\pm 3\,\mathrm{T}$ corresponding to the long/short interaction time τ_{hh} in sample A/sample C, respectively. The data in Fig. 5.17 seem not to show any dependence on the indium content. Moreover, with higher hole density, τ_{hh} increases pointing out decreasing hole-hole interactions. To our best knowledge, a density dependence of the hole-hole interaction time was not investigated in literature yet.

The strength of the carrier-carrier interaction in 2D systems is usually parameterized by the interaction parameter r_s. It is defined as the ratio of the Coulomb energy to the Fermi energy and depends on the carrier density and effective mass as $r_s \propto m_{eff}/\sqrt{p}$, [8]. From this, it follows that the importance of the interactions increases as the hole density decreases. This fact is widely used and 2DHGs of high effective mass and low hole density are prepared to study the physics of strongly interacting many-body systems, [70, 8, 108]. We found that the hole-hole interaction time is short in low-density samples and long (even of one order of magnitude longer) in samples with high hole density.

In contrast to the manganese-doped 2DHGs, where the presence of two different slopes in the plot of γ versus $\ln(1/T)$ was reported, [85], the slope in Fig. 5.16 is well-defined and single-linear. Wurstbauer *et al.* explained the behavior in Mn-doped samples as the phase transition from a paramagnetic to a ferromagnetic phase, which occurs at a transition temperature $T = 600\,\mathrm{mK}$. Unlike the magnetic manganese doping, our non-magnetic carbon doping is not expected to cause such an effect.

In conclusion, the strong negative parabolic magnetoresistance which

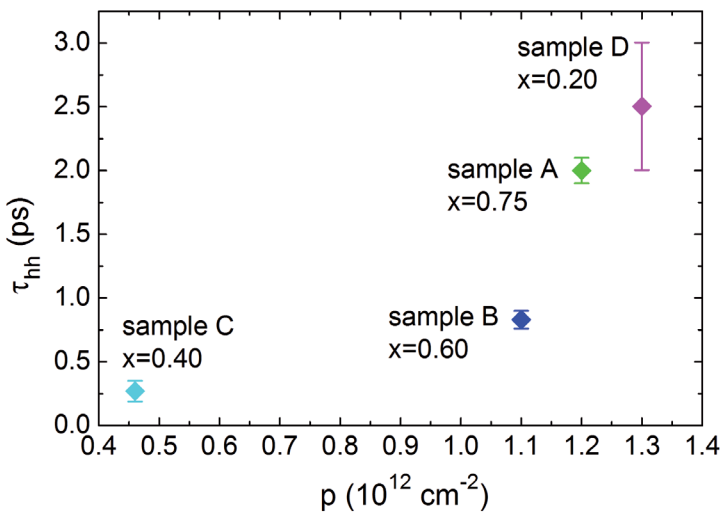

Figure 5.17: *Hole-hole interaction time τ_{hh} versus hole density p, determined along [011] direction. The points correspond to samples A - D having different In content and different carrier density. The error bars were estimated from the fitting procedure, see text.*

dominates the ρ_{xx} curve in the intermediate field range can unambiguously be attributed to the hole-hole interaction in the diffusion channel, mainly due to its B^2- and $\ln(1/T)$-dependence on the magnetic field and the temperature, respectively. Comparing different samples, we found that the calculated τ_{hh} increases rapidly with the hole density, and also the parabolic background becomes more pronounced, pointing out the important role of the carrier density on the strength of the hole-hole interaction.

5.4.5 Crystal direction anisotropy of transport parameters

In the previous sections we discussed the magnetotransport properties of the In-containing heterostructures. For these measurements, a strong anisotropy of the zero-field resistivity and related hole mobility was observed. This phenomenon will be investigated in this section.

As the main scattering sources limiting the low-temperature mobility in the $In_xGa_{1-x}As/In_xAl_{1-x}As$ heterostructures, ionized-impurity scattering (due to the background impurities and remote acceptors) and alloy-disorder scattering (originating in the random incorporation of the indium and gallium atoms into the crystal lattice of the ternary compound) were reported, [160, 82, 161, 162, 163]. Alloy-disorder scattering is most dominant in the $In_xGa_{1-x}As$ QW and can be eliminated by inserting an InAs channel as a binary compound into the QW. This led to an enhancement of the electron mobility, see Ref. [83, 82].

Since both mentioned scattering mechanisms are isotropic, there must be another anisotropic scattering mechanism responsible for the pronounced differences in the carrier mobility in dependence on the crystallographic direction of the current flow, which was also observed in 2DEGs and manganese-doped 2DHGs in similar heterostructures, [85, 161]. The highest mobility was determined along the $[01\bar{1}]$ direction, the lowest along [011]. In literature, different explanations for this behavior can be found. First, the anisotropy is attributed to the anisotropic spatial variations in the residual strain, which are correlated with the cross-hatch morphology of the

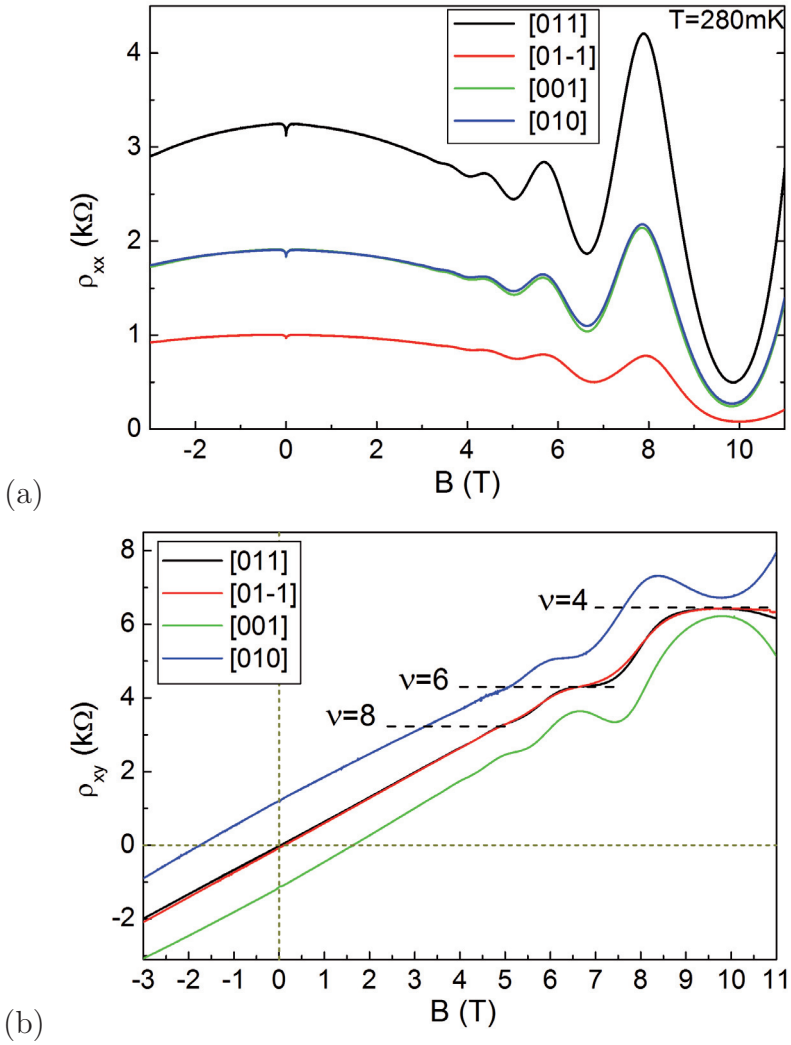

Figure 5.18: *(a) Longitudinal and (b) Hall resistance of sample B, measured at 280 mK along [011], [01$\bar{1}$], [001] and [010] crystal directions.*

surface. It is thought to come from the asymmetric in-plane strain relaxation concomitant with nonuniform misfit dislocation densities [164, 165, 166, 130, 167, 135]. Second, the origin can also be interface roughness scattering due to the cross-hatch pattern, which exhibits different periodicities of undulation along the [011] and [01$\bar{1}$] directions in these heterostructures, [79, 160, 163]. Third, a recent study presented by Ercolani *et al.* [80] shows that there are variations in the indium concentration of the ternary alloy of about 5% correlated with the cross-hatch morphology of the surface. The authors demonstrated that these fluctuations induce a periodic modulation of the conduction-band-edge energy. Fourth, piezoelectric effects may occur in presence of shear strain, [165, 168, 169], or due to a combination of lattice mismatch and interface roughness, [170], and can act as an additional scattering source.

We investigated the transport properties in the L-bar geometry not only of the standard [011] and [01$\bar{1}$] crystal directions but also of the diagonal [010] and

[001] directions, not reported in literature yet. For demonstration of the dependence of the longitudinal and transversal magnetoresistance on the crystallographic direction of the current flow, we chose sample B with $x = 0.60$ indium containing a 2 nm thick InAs channel embedded in the $In_{0.60}Ga_{0.40}As$ QW. However, qualitatively the same behavior was observed in all samples. The SdH and Hall measurements at 280 mK done on L-shaped Hall bars are shown in Fig. 5.18.

Crystal direction anisotropy in longitudinal magnetoresistance

The ρ_{xx} curves exhibit strongly different values depending on the crystallographic direction, see Fig. 5.18(a). We found the highest zero-field resistivity (lowest μ) along the [011] direction and in turn the lowest resistivity (highest μ) was achieved along the $[01\bar{1}]$ direction. The difference exceeds $\sim 70\%$. Interestingly, the ρ_{xx} curves along [010] and [001] are almost identical having intermediate values of the zero-field resistivity and hole mobility, see Table 5.7. The high-mobility 2DHGs discussed in Chapter 4 exhibited a resistivity anisotropy $\leq 10\%$ between the [011] and $[01\bar{1}]$ directions. The resistivity anisotropy is directly reflected in the hole mobility: in comparison to the $[01\bar{1}]$ direction, the hole mobility is reduced along [011] by about 70% and along [001] and [010] by about 47%, 48%, respectively.

AFM investigations discussed in Section 5.1.1 have shown that the surfaces of the In-containing samples exhibit a cross-hatch pattern with strongly anisotropic parameters, see Fig. 5.19. Table 5.7 and Table C.1 in Appendix C compare the roughness parameters and transport properties along a particular direction and show that both are directly correlated. The high mobility direction $[01\bar{1}]$ exhibits long periodicity of 2.4 μm with a very low RMS roughness of 1.8 nm. These facts point to a rather smooth modulation of the 2DHG along this direction. In contrast, the [011] direction exhibits a short periodicity of 0.76 μm accompanied with high RMS roughness of 3.4 nm. Probably, this leads to enhanced scattering of holes along this direction resulting in an increase of the zero-field resistivity and a reduction of the mobility as a consequence. Along both diagonal directions [010] and [001], we found intermediate periodicity of 1.2 μm with intermediate RMS roughness. This is in good agreement with the transport properties, where both directions reveal intermediate hole mobility. In summary, the reduced periodicity of the cross-hatch

Crystal direction	p ($10^{12}\,\mathrm{cm}^{-2}$)	$\rho_{xx}(B = 0\,\mathrm{T})$ (Ω)	μ ($\mathrm{cm}^2/\mathrm{Vs}$)	RMS roughness (nm)	Periodicity (μm)
[011]	0.9	3120	2100	3.4 ± 0.5	0.76 ± 0.05
$[01\bar{1}]$	0.9	970	7000	1.8 ± 0.3	2.4 ± 0.3
[001]	0.9	1840	3700	2.6 ± 0.4	1.2 ± 0.1
[010]	0.9	1840	3600	2.3 ± 0.4	1.2 ± 0.1

Table 5.7: *Table of magnetotransport properties recorded at 280 mK and surface morphology parameters of sample B.*

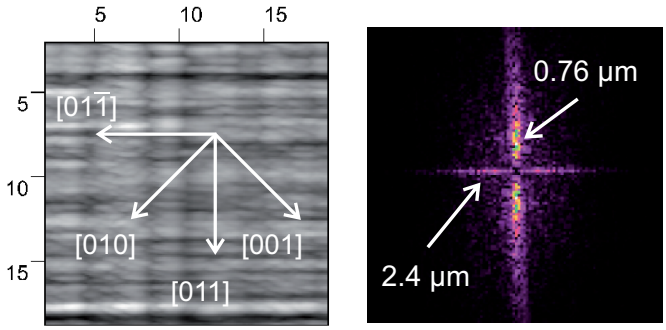

Figure 5.19: *(left) AFM image revealing the cross-hatch morphology of the surface of sample B. The grey scale goes from (black) -29 nm to (white) 27 nm. (right) 2D Fourier transformation of the surface (left) clearly showing different periodicities along the [011] and [01$\bar{1}$] directions.*

morphology along [011] of 68% and along [001] and [010] of 50% in analogy to [01$\bar{1}$] corresponds well to the variations of the hole mobility, see above. The AFM images indicate that the transport characteristics are correlated with the reduced periodicity of the cross-hatch morphology. Now we will treat the most important anisotropic scattering mechanism in more detail.

First, we will consider interface roughness scattering. Since all In-containing heterostructures have a one-sided-doped QW, which is strongly asymmetric, the hole wave function penetrates into the spacer layer, see calculations of the band structure in Fig. 5.21. Hence, the 2D holes are strongly influenced by the interface morphology. AFM investigation of the surface confirm a cross-hatch pattern of significant anisotropy. Because the cross-hatch pattern is a direct consequence of the buffer layer growth, all interfaces in the active layer are modulated in such a way.[8] As a consequence, the non-isotropic topography of the QW/spacer interface can modulate the 2DHG and introduce an additional scattering potential.

Second, according to the calculations in Ref. [80], the interface roughness scattering itself cannot explain the observed anisotropy because it provides only a small contribution to the observed anisotropy. Thus, we decided to investigate all In-containing structures. Below, we will examine only the orthogonal directions [01$\bar{1}$] and [011] demonstrating the most pronounced differences. In order to compare different samples, we defined the mobility anisotropy as $\Delta\mu = (\mu_{[01\bar{1}]} - \mu_{[011]})/\mu_{[01\bar{1}]}$. In Fig. 5.20, $\Delta\mu$ is plotted in dependence on the thickness of the InAs channel embedded in the $In_xGa_{1-x}As$ QW, for samples with different indium content x. Most samples exhibit a very high anisotropy of $\Delta\mu = 60 - 75\%$. Interestingly, in sample A the anisotropy was almost completely suppressed by the introduction of a relatively wide InAs channel into the QW.

For a better understanding of this phenomenon, we calculated the valence-band edge and the carrier density profile using the 8×8-band $\mathbf{k} \cdot \mathbf{p}$ method; for further information see Sections 3.5 and 5.3. Fig. 5.21 illustrates three examples of different QW designs: (a) an $In_{0.40}Ga_{0.60}As$ QW, without channel, sample C, (b) a 2 nm thick InAs channel in the $In_{0.75}Ga_{0.25}As$ QW, sample E, and (c) a 4 nm thick InAs channel in the $In_{0.75}Ga_{0.25}As$ QW, sample A. In all cases, only the first subband is occupied. In the case (a), the density profile is localized in the QW and

[8]The surfaces of the buffer-layer samples, grown in this work, were studied by M. Lohr using X-ray diffraction, [98]. All samples exhibited cross-hatch patterns.

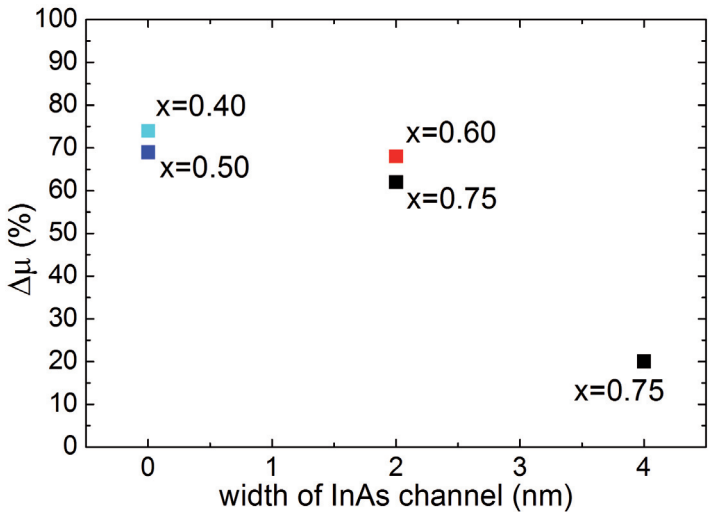

Figure 5.20: *Mobility anisotropy of samples with different indium content plotted according to the width of the InAs channel. The thickness of 0 nm corresponds to the InGaAs QW without an InAs channel.*

its maximum is positioned near the barrier/QW interface. On the contrary, in the cases (b) and (c), the maximum of the density profile is located in the channel region while its tails penetrate strongly into the surrounding QW.

On the basis of these investigations, we can explain the reduced anisotropy in sample A. According to Ref. [80], variations of the In concentration correlated with the interface morphology can take place in the ternary compound of the $In_xGa_{1-x}As$ QW. This leads to a modulation of the valence-band-edge energy, [80]. Since in our case the interface exhibits the cross-hatch morphology, which is strongly anisotropic as discussed before, in analogy to Ref. [80] it results in anisotropic transport properties. The insertion of the InAs layer reduced the mobility anisotropy, because in a binary alloy, no compositional fluctuation can occur. In sample A, about 83% of the density profile is concentrated in the binary compound and only about 17% penetrates into the surrounding QW, see Fig. 5.21(c). This results in low mobility anisotropy only of $\Delta\mu \sim 20\%$. In contrast, about 59% of the density profile of sample E lies within the 2 nm wide channel and about 41% percolates into the ternary compound of the QW, where it is influenced by the compositional fluctuations, see Fig. 5.21(b). This explains why sample E shows such a high anisotropy of $\Delta\mu \sim 62\%$ despite the embedded InAs channel. Furthermore, embedding a thicker InAs channel also led to the reduction of the alloy disorder scattering, [83], and resulted in an enhancement of the overall hole mobility, discussed in Section 5.1.2.

Third, important information about the strain relaxation in sample B was achieved from X-ray diffraction measurements, done in cooperation with M. Utz. The indium concentration in the active layer was evaluated as $(57.5 \pm 1.4)\%$ with the relaxed lattice constant $a = (5.890 \pm 0.005)$ Å, which is in good agreement with the supposed $x = 0.60$ indium content from the indium cell calibration, see Section 5.1. The results show that the crystal lattice relaxes anisotropically with different lattice constants $a_{[01\bar{1}]} = 5.884\,\text{Å} > a_{[011]} = 5.867\,\text{Å}$. Told in another way, along the $[01\bar{1}]$ direction the lattice is almost completely relaxed with a relaxation degree of 97.5%, but the [011] direction is still compressively strained with a relaxation degree of 90.4% pointing out anisotropic strain. The lattice constant in the growth

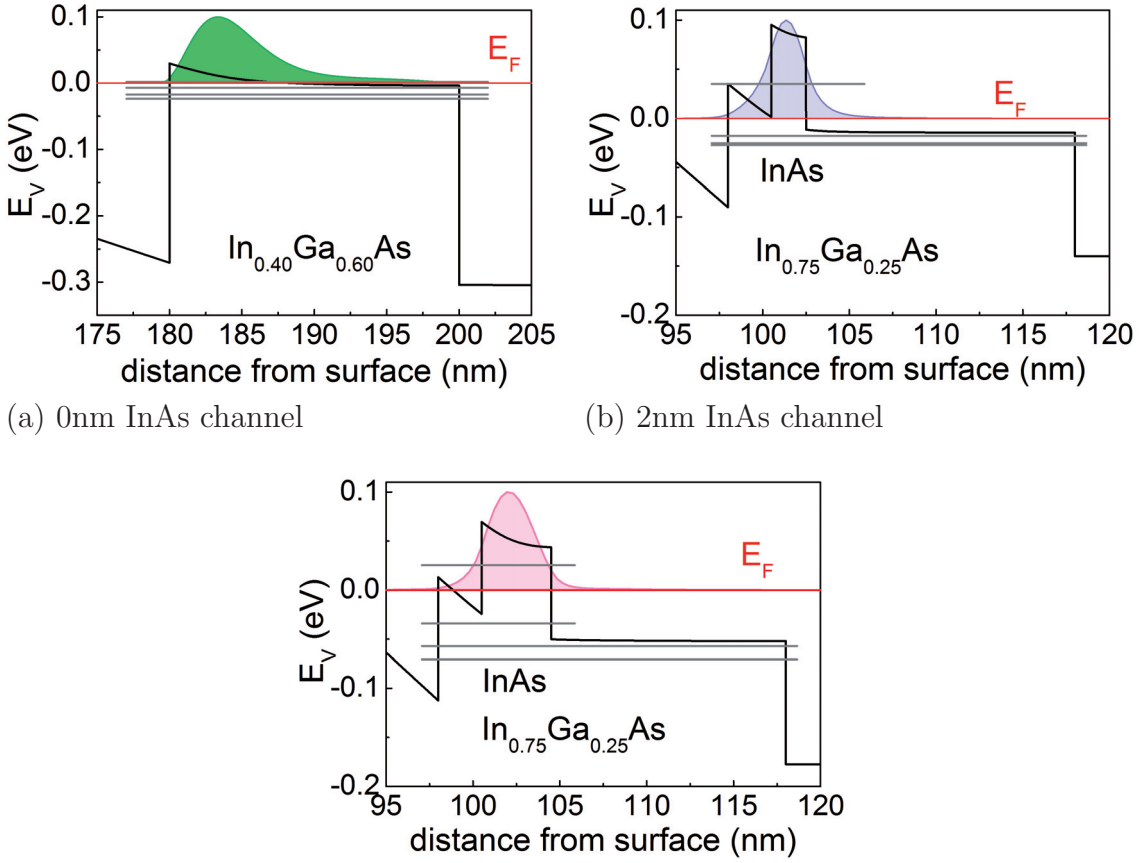

(a) 0nm InAs channel (b) 2nm InAs channel

(c) 4nm InAs channel

Figure 5.21: *Valence-band edge (black line) relative to the Fermi energy (red line) and carrier density profile (shaded area) for the QW (a), (b) and (c) of sample C, E and A, respectively; as calculated using the 8 × 8-band* $\mathbf{k} \cdot \mathbf{p}$ *method. The grey lines indicate the 2D subband energies in the QW.*

direction (perpendicular to the plane of the 2DHG) was estimated as $a = 5.904\,\text{Å}$. This indicates that there are anisotropic spatial variations in the residual strain in sample B, which can contribute to the observed transport anisotropy.

In conclusion, we identified three anisotropic scattering mechanisms in our In-containing heterostructures, which come from: interface roughness, variations of the In concentration in the ternary alloy modulated by the cross-hatch morphology, and anisotropic strain relaxation. We demonstrated that the mobility anisotropy can be significantly reduced by embedding a relatively wide InAs channel into the QW. However, some residual anisotropy stays present owing to the leakage of the carrier density profile into the surrounding QW. Finally, we wish to emphasize that not only the hole mobility and the zero-field resistivity exhibit a dependence on the crystallographic direction, but also other parameters, such as the transport scattering time, the quantum scattering time, the hole-hole interaction time or the weak-antilocalization effect, as was shown in the previous sections.

Crystal-direction anisotropy in Hall resistance

Fig. 5.18(b) displays the transversal magnetoresistance of sample B recorded along different crystallographic directions. As expected, the Hall curves measured along [011] and [01$\bar{1}$] start at zero resistance at zero magnetic field. Interestingly, this was not the case if the current was applied along the diagonal directions [001] and [010]. Here, the Hall resistance is shifted from $0\,\Omega$ at $B = 0\,\mathrm{T}$ to $\rho_{xy} = 1180\,\Omega$ along [010] and to the opposite direction of $\rho_{xy} = -1130\,\Omega$ along [001]. Thus, there is some Hall voltage already at $B = 0\,\mathrm{T}$. The symmetry of the offset is surprising. We want to stress that this behavior was observed in other samples, too. Usually the offset voltage is a sign of the not-exactly-opposite-made contacts, which result in some contribution of the longitudinal resistance to the Hall resistance. But in our case of the L-bar structures, fabricated by optical lithography, this explanation seems to be highly improbable. A possible origin of the offset voltage may be the asymmetry of the cross-hatch morphology exhibiting different periodicities along the main directions [011] and [01$\bar{1}$]. From Figs. 5.19 and 5.4 it is apparent that the orthogonal directions [011] and [01$\bar{1}$] exhibit a mirror symmetry. The grating on the surface proceeds parallel to these directions. On the contrary, for the diagonal directions [001] and [010], which are rotated of 45° to the cross-hatch pattern, the mirror symmetry is broken. Possibly, the holes passing along these crystal directions can be scattered to the opposite side of the Hall-bar structure already at $B = 0\,\mathrm{T}$ resulting in the non-zero Hall voltage. Hence, there must be direction-dependent scattering originating in the asymmetry of the cross-hatch morphology. Further, piezoelectric effects and applied strain were also reported to cause an offset voltage, [171].

As a consequence of the offset, the quantum Hall plateaus arise at other resistance values than observed along [011] and [01$\bar{1}$] directions and expected from the relation $R = R_H/\nu$ for a given hole density. In addition, the plateaus exhibit some non-typical shape, see Fig. 5.18(b). An overshoot of the quantum Hall resistance at integer filling factors was reported on InGaAs/InP by Ramvall *et al.* [162] and on Si/SiGe heterostructures by Sailer *et al.* [172]. In the latter, the authors presented a model of the integer quantum Hall effect based on a screening theory and explain this anomalous phenomenon as confinement of current into the co-existing evanescent incompressible strips of different filling factors.

5.4.6 Magnetotransport on inverted-doped structures

In order to compare our carbon-doped structures with the manganese-doped structures from Ref. [24], and to get more information about carbon diffusion, we prepared C-doped inverted structures, where the carbon-doping layer was grown before the QW. As demonstrative example we chose sample *inv* with a 1 nm strained InAs channel symmetrically embedded in the 20 nm wide $In_{0.50}Ga_{0.50}As$ QW. The $In_{0.50}Al_{0.50}As$ layer homogeneously doped with carbon is separated from the QW by a 20 nm thick spacer layer, see Table 5.2. The layer sequence is schematically shown in Fig. 5.3(c).

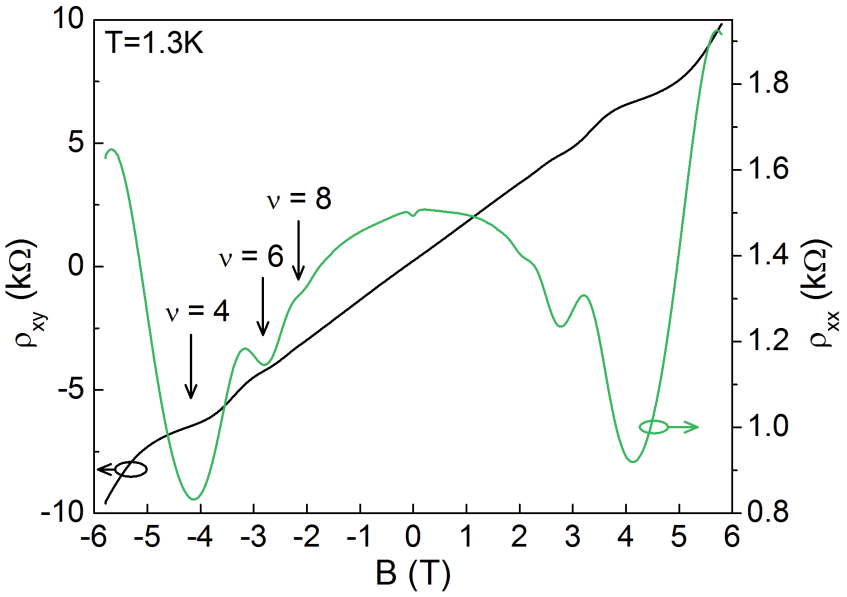

Figure 5.22: *Magnetotransport on the inverted-doped structure (sample inv) with* $x = 0.50$ *In content exhibiting a 2DHG confined in an InAs channel, measured at 1.3 K.*

Magnetotransport of sample *inv* was investigated in the van-der Pauw geometry at low temperatures. Positive slope of the Hall curve verifies p-type conductivity. The sample achieves a hole density of $p = 3.8 \times 10^{11}\,\mathrm{cm}^{-2}$ and a hole mobility of $\mu = 4500\,\mathrm{cm}^2/\mathrm{Vs}$ at 1.3 K. The ρ_{xx} and ρ_{xy} curves are shown in Fig. 5.22. In the Hall resistance, the Landau quantization leads to distinct quantum Hall plateaus at even filling factors $\nu = 4, 6, 8$. Similarly to normal-doped structures, the longitudinal resistance of sample *inv* can be separated into three ranges according to the magnetic field. At higher magnetic fields, the SdH oscillations dominate. Between ± 3 T, the ρ_{xx} curve is superimposed by a negative parabolic magnetoresistance, which arises due to the hole-hole interaction effect. Finally, at very low magnetic fields, there is an apparent weak-antilocalization dip. Its presence confirms that also in this sample the spin-orbit interaction is very strong. All these effects were extensively described on the normal-doped structures in Sections 5.4.4 and 5.4.3. In summary, the magnetotransport data of the inverted-doped structure do not show any deviation with regard to the normal-doped samples. Moreover, we can assume that the carbon segregation and diffusion is very low in these ternary compounds as it demonstrates comparably high hole mobility. If the carbon diffused during the growth process into the QW, the hole mobility of the 2DHG would be substantially reduced due to enhanced scattering on ionized impurities.

Unlike the manganese-doped inverted structures studied in Ref. [25, 24], no such dramatic increase of the low-field resistance, corresponding to the insulator-to-metal transition driven by a magnetic field, appeared in our samples. Instead of the strong hole localization, we observed sharp WAL. The absence of this feature in our nonmagnetic carbon-doped heterostructures confirms that it can be assigned to the magnetic nature of the manganese impurity. Furthermore, asymmetric broad-

ening of the manganese-doping layer was reported in InAlAs/InGaAs/InAs heterostructures and the presence of Mn ions in the QW was unambiguously detected by SIMS[9] analysis [173]. The diffusion of manganese is well-known, [174, 175]. On the contrary, previous studies on GaAs verified that carbon shows low diffusion and segregation, [92]. Following the results of our inverted-doped structure carbon segregation and diffusion is supposed to be low also in the In-containing compounds.

In conclusion, we have shown that carbon doping is widely applicable and makes it possible to produce even inverted-doped structures exhibiting a high-quality 2DHG with quantized transport phenomena. This example of a sample with an $x = 0.50$ indium content in the active layer has demonstrated that the strained InAs channel can be embedded even in QWs with low indium content without causing serious damage of the crystal structure. The results point out low carbon segregation and diffusion, which is an important advantage for future applications.

5.5 Engineering of the spin splitting in the In-containing heterostructures

Now, we will report our results on tuning the spin splitting by performing a simple change in the structure design. Both sample A and sample C were extensively studied experimentally (Section 5.4) and theoretically (Section 5.3). The investigations revealed strong spin splitting of the uppermost HH subband in sample C. On the contrary, no indication of spin splitting was experimentally observed in the magnetotransport measurements of sample A. In the calculations of its valence-band structure only small spin splitting occurred. This is in stark contrast to theoretical expectations concerning the high In content and the spin splitting presented in Ref. [15]. In this section the interesting phenomenon will be examined in detail.

The structure of sample A is much more asymmetric due to the smaller spacer layer of only 5 nm in comparison to the 20 nm spacer in sample C. The lower the thickness of the spacer layer the higher is the electric field $\mathcal{E}_z$ perpendicular to the 2DHG-plane in the sample and also the Rashba spin splitting, which is in first order proportional to $\mathcal{E}_z$ (see Eq. 2.17) and for ssd-QW $\mathcal{E}_z \propto p$. This is further supported by the enhancement of the 2D hole density. In sample A, the hole density exceeds $p = 1.1 \times 10^{12}\,\mathrm{cm}^{-2}$, which is twice as high as those obtained in sample C, $p = 0.47 \times 10^{12}\,\mathrm{cm}^{-2}$. According to Ref. [15], the spin splitting of the HH states in the QW increases with the total density as $\Delta p/p \propto p^{3/2}$ in the cubic approximation. Moreover, the indium content in the active layer plays an important role. Since with more indium the spin-orbit coupling increases, the spin splitting should be more pronounced in sample A with $x = 0.75$ indium than in sample C containing $x = 0.40$. On the basis of these considerations, one would expect very strong spin splitting in sample A. Interestingly, this is not the case.

Here, we reduced the spin splitting of the HH subband in sample A, embedding a thin InAs channel into the $In_{0.75}Ga_{0.25}As$ QW. As a consequence of

[9] Secondary Ion Mass Spectroscopy

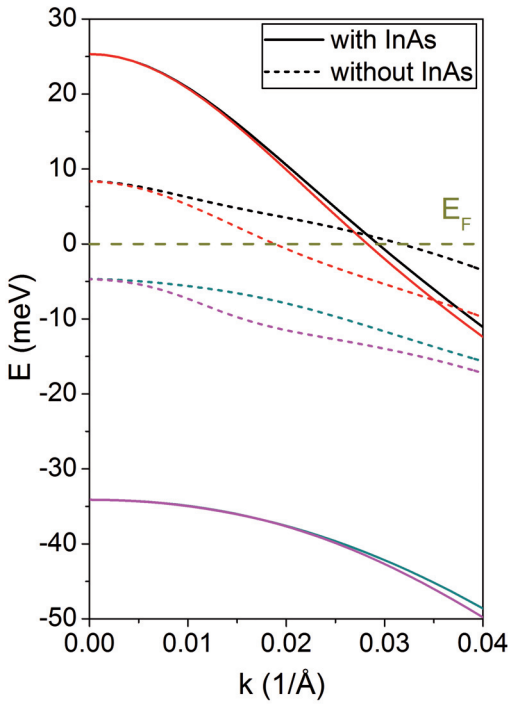

Figure 5.23: *Calculated valence-band structure of sample A with $x = 0.75$ indium with (solid lines) and without (dashed lines) a 4 nm thick InAs channel embedded in the $In_{0.75}Ga_{0.25}As$ QW. E_F marks the Fermi energy. The presence of the InAs channel crucially influences the HH-LH separation and the Rashba-induced spin splitting. In the simulations the BIA was not included.*

the enhancement of the quantum confinement due to the only 4 nm thick channel, the gap between the HH and LH subband increased rapidly. This is obvious from the simulations of the subband structure done with the 8×8-band $\mathbf{k} \cdot \mathbf{p}$ method, compare Fig. 5.8(a) with (b). For better illustration we simulated the valence-band structure of the sample A without the InAs channel (the simple $In_{0.75}Ga_{0.25}As$ QW). Fig. 5.23 summarizes both cases of sample A. Without the InAs channel the HH and LH subbands are much closer to each other and their distance decreased to 13 meV at the Γ point. Moreover, the dispersion demonstrates significant spin splitting, which exceeds 6 meV for the HH subband at the Fermi level. This unambiguously confirms that the InAs channel crucially influences the spin splitting introduced by the Rashba effect. We want to note that in the nextnano[3] theoretical simulations the BIA term was not included. Furthermore, the calculations, displayed in Fig. 5.21(c) for sample A, show that only the HH subband is present in the InAs channel; sample C is shown in Fig. 5.21(a). The LH subband is pushed far away and percolates into the surrounding $In_{0.75}Ga_{0.25}As$ QW. According to Ref. [15], the Rashba spin splitting of the HH states depends in contrast to electrons not only on the electric field $\mathcal{E}_z$ but also on the separation between the HH and LH subbands. The Rashba coefficient of the uppermost HH subband is given by [61]:

$$\beta_{R,1}^{h} = \frac{e\hbar^4}{m_0^2} a\gamma_3(\gamma_2+\gamma_3)\left[\frac{1}{\Delta_{11}^{hl}}\left(\frac{1}{\Delta_{12}^{hl}}-\frac{1}{\Delta_{12}^{hh}}\right)+\frac{1}{\Delta_{12}^{hl}\Delta_{12}^{hh}}\right], \tag{5.7}$$

where γ_2 and γ_3 are the Luttinger parameters and $\Delta_{\lambda\lambda'}^{\nu\nu'} \equiv \mathcal{E}_{\lambda}^{\nu} - \mathcal{E}_{\lambda'}^{\nu'}$ where $\mathcal{E}_{\lambda}^{h}$ and $\mathcal{E}_{\lambda}^{l}$ are the energies of the λth HH and LH subband, respectively. The numerical prefactor is equal to $a = 64/9\pi^2$ for an infinitely deep rectangular QW. It follows that an increasing HH-LH separation Δ_{11}^{hl} gives rise to a decreasing Rashba coefficient

$\beta^h_{R,1}$. Indeed, the spacing between HH and LH subband increases from $\Delta^{hl}_{11} \approx 9\,\mathrm{meV}$ in sample C to the enormous $\Delta^{hl}_{11} \sim 60\,\mathrm{meV}$ in sample A, cf. Fig. 5.8.

Our results confirm, that the HH-LH splitting reduces the Rashba coefficient and so overcomes the enhancement of the electric field and indium content in sample A concerning the Rashba-induced spin splitting. In conclusion, we have shown that in these In-containing heterostructures, where pronounced spin splitting is expected due to the strong spin-orbit interaction and high electric field, a small change in the design of the structure can suppress the spin splitting. For design of future spintronics devices, this simple trick can be of high importance.

Chapter 6

Conclusions

In this work, we investigated very high quality carbon-doped two-dimensional hole gases (2DHGs) in III-V semiconductor heterostructures; their molecular-beam-epitaxy (MBE) growth and magnetotransport properties. The first part compared high-mobility GaAs/AlGaAs quantum wells (QWs) of a different heterostructure design. These structures demonstrate excellent purity. In the second part, we studied asymmetric InGaAs/InAlAs QWs. Their specific characteristic is high spin-orbit coupling. Both the extreme high quality and the strong spin-orbit coupling are of special interest for future spintronics applications.

The quality of a 2DHG is expressed by the hole mobility. We introduced a concept of a double-sided-doped GaAs/AlGaAs QW (dsd-QW) structure with four carbon-doping layers and optimized its layout, doping and growth parameters. In a 15 nm GaAs QW with a 80 nm wide $Al_{0.25}Ga_{0.75}As$ spacer layer, we succeeded in obtaining a very high hole mobility $\mu = 2.1 \times 10^6\,\mathrm{cm^2/Vs}$ at 20 mK with a hole density of $p = 1.9 \times 10^{11}\,\mathrm{cm^{-2}}$. This value is on par with the current maximum reported in literature, [8]. The ratio of transport scattering time and quantum scattering time $\tau_t/\tau_q \approx 100$ indicates that long-range scattering potential dominates in this structure. Although carbon is not expected to create DX centers, as the silicon impurity does [22, 23], our investigations with illumination at low temperatures revealed persistent variations of the hole density in consensus with previous reports in literature, [20, 21]. Our experiments point out that some deep defect levels must be present in the band gap. With a careful adjustment of the temperature profile during the MBE growth we were able to produce samples exhibiting no persistent photoconductivity. This directly corresponds to the highest hole mobility in experiment.

The new dsd-QW structure design enables to adjust the QW more symmetrically, especially for controlling the spin splitting. The additional doping layers compensate surface states and substrate charges, respectively. Spin-splitting can be caused by: (a) the Dresselhaus effect originating in the bulk inversion asymmetry (BIA), (b) the Rashba effect, which comes from the structure inversion asymmetry (SIA). The spin splitting increases with the wave vector. Although the Fermi wave vector in the dsd-QW is substantially larger, the spin splitting of the heavy-hole subband is much smaller than in the single-sided-doped QW (ssd-QW). Comparison with the multiband $\mathbf{k} \cdot \mathbf{p}$ simulations of the valence-band structure without the

Dresselhaus term predict even smaller values of the spin splitting in the dsd-QW than in experiment. Hence, we assume that the BIA provides the dominating contribution to the spin splitting in this structure. In highly-doped ssd-QWs a relative carrier imbalance $\Delta p/p$ of up to 40% could be achieved. In all samples, we observed an anisotropy in $\Delta p/p$ between the [011] and [01$\bar{1}$] crystallographic directions. We interpret this phenomenon as a superposition of Rashba and Dresselhaus effects.

Further, we reported a striking anisotropy in the thermally activated transport of the fractional quantum Hall (FQH) states in the ssd-QW. Both highest-quality samples of the dsd-QW and ssd-QW structure demonstrate a large number of well-developed FQH states. From their temperature dependence we calculated their activation gaps. In the ssd-QW the activation gaps substantially differ along the [011] and the [01$\bar{1}$] crystallographic directions, reaching differences up to 40% for the FQH state $\nu = 5/3$. In contrast, the anisotropy vanishes in the dsd-QW. Moreover, no anisotropy was reported in the activated transport in the known literature yet. The observed anisotropy-to-isotropy transition can possibly be driven by changing the symmetry of the confinement potential from asymmetric to symmetric. First theoretical calculations based on the model of dissipative conductance in FQH states developed by d'Ambrumenil *et al.* [53] confirm the existence of two gaps [120].

Indium-containing ternary compounds are of importance for spintronics applications due to their strong spin-orbit interaction, [11, 12]. A great success of this work was the preparation of a carbon p-type doping in the $In_xAl_{1-x}As/In_xGa_{1-x}As/InAs$ heterostructures with high indium content x. Since carbon is a group IV member it can incorporate as acceptor (in GaAs) or donor (in InAs) in III-V semiconductor compounds. QW structures with a variety of In content x exhibit conductivity-type inversion from p- to n-type between $x = 0.60$ and $x = 0.75$. The C-doped 2DEGs with $x = 0.75$ indium content are of good quality exhibiting quantized transport phenomena. In order to get p-type conductivity also in the structure with $x = 0.75$ indium we developed a digital-alloy-doping design. In this way we succeeded in growing a 2DHG with a hole density of $p = 1.1 \times 10^{12}\,\mathrm{cm}^{-2}$ and a hole mobility of $\mu = 7200\,\mathrm{cm}^2/\mathrm{Vs}$ at 20 mK in an $In_{0.75}Al_{0.25}As/In_{0.75}Ga_{0.25}As$ QW with an embedded InAs channel. The transport measurements highlight well-pronounced quantum Hall states.

All In-containing samples show very distinct weak-antilocalization (WAL) resistance minima, which signal the presence of spin-orbit interaction in these systems. The WAL data were excellently fitted with the Hikami-Larkin-Nagaoka theory providing the phase-coherence time τ_φ and the spin-orbit scattering time τ_{so}. The phase-coherence time over a wide temperature range exhibited two functional dependencies on T. At low temperatures ($T < 1\,\mathrm{K}$) the phase-breaking rate is governed by hole-hole scattering with small-energy transfer. However, at higher temperatures both hole-phonon scattering and hole-hole scattering with high-energy transfer can contribute to hole dephasing. We found long phase-coherence lengths of $l_\varphi \approx 0.5 - 0.9\,\mu\mathrm{m}$. Our experimental data show a change of the spin-orbit scattering time with temperature, though it is typically supposed to be temperature independent. In the heterostructure with $x = 0.60$ indium content, we revealed a peculiar

anisotropy of the quantum-interference-related phenomena. According to the crystallographic direction of the current flow either a WAL minimum superimposed on a weak-localization peak or only a WAL minimum developed in the longitudinal magnetoresistance.

The intermediate B-field range of the longitudinal magnetoresistance is dominated by a strong negative parabolic magnetoresistance spreading out up to $\pm 6\,\mathrm{T}$. Due to its B^2- and $\ln(1/T)$-dependence, we attribute it to the hole-hole interaction effect. The calculated hole-hole interaction time τ_{hh} increases with increasing hole density.

The magnetotransport data of the In-containing heterostructures exhibit a strong anisotropy in all transport parameters such as: μ, τ_t, τ_q, τ_{hh}, τ_φ, τ_{so} concerning the crystallographic directions [011], [01$\bar{1}$], [001] and [010]. We identified three anisotropic scattering mechanisms, which came from: (a) the interface roughness, (b) variations of the In concentration in the ternary alloy modulated by the cross-hatch morphology, and (c) anisotropic strain relaxation. Further, we demonstrated that the mobility anisotropy can be significantly reduced by embedding an InAs channel into the InGaAs QW.

Our investigations on inverted-doped structures confirm that carbon doping makes it possible to produce inverted structures exhibiting a good-quality 2DHG with a hole density of $p = 3.8 \times 10^{11}\,\mathrm{cm}^{-2}$ and a hole mobility of $\mu = 4500\,\mathrm{cm}^2/\mathrm{Vs}$ in an $In_{0.50}Al_{0.50}As/In_{0.50}Ga_{0.50}As/InAs$ QW. This points out that carbon segregation and diffusion is rather low in these material compounds.

Finally, we highlighted the ability to engineer the spin splitting in the In-containing heterostructures by slightly changing the structure design. Against expectations, we reduced the spin splitting of the heavy-hole subband in a strongly asymmetric heterostructure with a high hole density and a high indium content $x = 0.75$ by embedding a thin InAs channel into the $In_{0.75}Ga_{0.25}As$ QW. The reason is that the Rashba coefficient does not only depend on the electric field, but also on the heavy-hole-light-hole separation, which can be enormously enhanced (up to $\Delta_{11}^{hl} \sim 60\,\mathrm{meV}$) owing to the high quantum confinement in the 4 nm thin InAs channel. Moreover, we demonstrated that—concerning the spin splitting—this effect can overcome the contribution of the high electric field and of the strong spin-orbit interaction due to the high indium content. For the design of future spintronics devices this simple trick can be of high importance.

In conclusion, we have shown that carbon is very promising doping material for spintronics. As an acceptor impurity it is widely applicable and allows to produce 2DHGs of excellent quality in a broad spectrum of different III-V semiconductor heterostructures.

Appendix A

Processing of Hall-bar structures

1. Optical lithography
    - Scribe (with tungsten carbide needle) and break 4 mm × 5 mm piece of sample from the wafer
    - Standard cleaning in acetone and isopropanol baths
    - Spin coating of the sample with a photoresist S1805
        - Spin on: 4600 rpm for 35 s
        - Soft bake: hotplate at 90°C for 2 min
    - Exposure to UV light for 35 s in a mask aligner
        - LW mask(width = 200 μm, length = 1600 μm)
        - #43 mask(width = 200 μm, length = 1000 μm)
    - Develop: Microposit 351 Developer : H_2O = 1 : 4 for 40 s
    - Stop in H_2O for 40 s, dry with N_2
    - Wet chemical etching for 1 min 30 s
        - Acetic acid (100%): H_2O_2(30%) : H_2O = 5 : 1 : 5
        - Stop in H_2O for 40 s, dry with N_2
    - Standard cleaning of the sample
    - Check of the etched depth with profilometer
2. Ohmic p-contacts
    - Make a scratch on the contact pads of the sample with a tungsten carbide needle
    - Put a drop of the InZn mixture (4-6% Zn, In 6N) on the scratches
    - Alloy the sample at 360°C in a forming-gas atmosphere for 90 s with a ramp of 60 s
3. Completion of the sample

- Solder the gold wires on contact pads of the sample with the InZn mixture
- Fix the sample on the carrier with the vacuum grease
- Solder the gold wires on the pins of the carrier

Appendix B

Fourier transformation of the SdH oscillations

Due to the bulk and structure inversion asymmetry, the HH subband is splitted in two spin subbands of different Fermi wave vectors k_{F1}, k_{F2} and different hole densities p_1, p_2 as well. This manifests itself in the magnetotransport as a beating pattern of the SdH oscillations in the range of low magnetic fields. In fact it is a superposition of two different frequencies f_1 and f_2. Applying fast Fourier transformation, the frequencies f_1, f_2 can be extracted and the hole densities can be calculated as, [176, 33]:

$$p_{1,2} = (e/h) \cdot f_{1,2} \cdot g_s, \tag{B.1}$$

e is the electron charge, h is Planck's constant, $g_s = 1$ if the spin degeneracy of the subband is lifted, and $g_s = 2$ for a spin-degenerate subband. In this work, the method, described in [177], was used. First, the data was corrected on the hysteresis of the magnet (here $\sim 35\,\mathrm{mT}$) and then the interval between -0.5 T and -0.1 T was cut out. Second, the parabolic background was subtracted and the data were scaled versus $1/B$. To increase the resolution of the Fourier transformation, a standard procedure of padding data with zeros at both ends of the data set was applied. In the Fourier spectrum of the low-field SdH oscillation, besides two peaks at f_1, f_2 also a third peak at the frequency f_{tot} can be present. The frequencies satisfy the relation $f_1 + f_2 = f_{tot}$, which reflects the fact that the subband densities p_1, p_2 sum up to the total density p_{tot}. At high magnetic fields, the Zeeman splitting is more dominant and there is only one peak at f_{tot} to be found in the Fourier spectrum corresponding. It corresponds to the total hole density. Due to the high effective mass of holes in contrast to electrons in 2DEGs, the measurements were carried out at a low temperature, 20 mK. Otherwise, no beating pattern in the SdH oscillations could be observed.

Appendix C

Surface parameters of the In-containing heterostructures

In content x	crystal direction	RMS roughness (nm)	period (μm)
0.75 (sample A)	[011]	2.0 ± 0.2	0.64 ± 0.02
	[01$\bar{1}$]	0.7 ± 0.1	1.23 ± 0.04
	[001]	1.3 ± 0.1	0.97 ± 0.03
	[010]	1.3 ± 0.1	0.95 ± 0.02
0.75 (sample E)	[011]	2.6 ± 0.7	0.42 ± 0.03
	[01$\bar{1}$]	1.1 ± 0.2	0.79 ± 0.04
	[001]	1.5 ± 0.2	0.53 ± 0.02
	[010]	1.7 ± 0.2	0.56 ± 0.02
0.75 (sample F)	[011]	2.8 ± 0.6	0.44 ± 0.02
	[01$\bar{1}$]	1.3 ± 0.3	0.70 ± 0.03
	[001]	2.2 ± 0.5	0.62 ± 0.04
	[010]	2.2 ± 0.3	0.62 ± 0.02
0.60	[011]	3.4 ± 0.5	0.76 ± 0.05
	[01$\bar{1}$]	1.8 ± 0.3	2.4 ± 0.3
	[001]	2.6 ± 0.4	1.2 ± 0.1
	[010]	2.3 ± 0.4	1.2 ± 0.1
0.50	[011]	2.6 ± 0.4	0.50 ± 0.02
	[01$\bar{1}$]	0.9 ± 0.3	1.18 ± 0.04
	[001]	2.1 ± 0.1	0.95 ± 0.02
	[010]	1.9 ± 0.3	0.95 ± 0.01
0.40	[011]	4.2 ± 0.4	0.56 ± 0.02
	[01$\bar{1}$]	1.8 ± 0.1	1.48 ± 0.07
	[001]	3.6 ± 0.3	1.01 ± 0.03
	[010]	3.5 ± 0.2	1.00 ± 0.02

continued on the next page...

In content x	crystal direction	RMS roughness (nm)	period (μm)
0.30	[011]	2.1 ± 0.2	0.56 ± 0.01
	[01$\bar{1}$]	1.0 ± 0.1	1.44 ± 0.02
	[001]	1.7 ± 0.2	1.02 ± 0.04
	[010]	1.7 ± 0.1	0.97 ± 0.03
0.20	[011]	2.5 ± 0.1	0.75 ± 0.01
	[01$\bar{1}$]	0.3 ± 0.1	1.22 ± 0.03
	[001]	1.9 ± 0.1	1.12 ± 0.01
	[010]	1.7 ± 0.1	1.11 ± 0.02

Table C.1: *Roughness parameters of samples with different In contents calculated along [011], [01$\bar{1}$], [001] and [010] crystallographic directions. The AFM topographs are shown in Fig. 5.4. The errors were estimated from the fluctuations of the investigated parameters in the AFM images.*

Bibliography

[1] R. Feynman. Simulating physics with computers. *International Journal of Theoretical Physics*, 21:467, 1982.

[2] R. W. Ogburn and J. Preskill. Topological Quantum Computation. In *Quantum Computing and Quantum Communications*, volume 1509 of *Lecture Notes in Computer Science*, page 341. Springer Berlin Heidelberg, 1999.

[3] J. Preskill. Fault-tolerant quantum computation. http://arxiv.org/abs/quant-ph/9712048, 1997.

[4] A. Yu. Kitaev. Fault-tolerant quantum computation by anyons. *Annals Phys.*, 303:2, 2003.

[5] M. H. Freedman, A. Kitaev, and Z. Wang. Simulation of topological field theories by quantum computers. *Commun. Math. Phys.*, 227:587, 2002.

[6] M. H. Freedman, M. Larsen, and Z. Wang. A Modular Functor Which is Universal for Quantum Computation. *Commun. Math. Phys.*, 227:605, 2002.

[7] V. Umansky, M. Heiblum, Y. Levinson, J. Smet, J. Nübler, and M. Dolev. MBE growth of ultra-low disorder 2DEG with mobility exceeding $35 \times 10^6\,\mathrm{cm}^2/\mathrm{Vs}$. *Journal of Crystal Growth*, 311(7):1658, 2009.

[8] J. D. Watson, S. Mondal, G. A. Csáthy, M. J. Manfra, E. H. Hwang, S. Das Sarma, L. N. Pfeifer, and K. W. West. Scattering mechanisms in a high-mobility low-density carbon-doped (100) GaAs two-dimensional hole system. *Phys. Rev. B*, 83:241305(R), 2011.

[9] C. Gerl, S. Schmult, H.-P. Tranitz, C. Mitzkus, and W. Wegscheider. Carbon-doped symmetric GaAs/AlGaAs quantum wells with hole mobilities beyond $10^6\,\mathrm{cm}^2/\mathrm{Vs}$. *Appl. Phys. Lett.*, 86(252105), 2005.

[10] B. Grbic. *Hole transport and spin-orbit coupling in p-type GaAs nanostructures*. PhD thesis, ETH Zurich, 2007.

[11] S. Datta and B. Das. Electronic analog of the electro-optic modulator. *Appl. Phys. Lett.*, 56:665, 1990.

[12] H. C. Koo, J. H. Kwon, J. Eom, J. Chang, S. H. Han, and M. Johnson. Control of Spin Precession in a Spin-Injected Field Effect Transistor. *Science*, 325:1515, 2009.

[13] T. Korn, M. Kugler, M. Griesbeck, R. Schulz, A. Wagner, M. Hirmer, C. Gerl, D. Schuh, W. Wegscheider, and C. Schüller. Engineering ultralong spin coherence in two-dimensional hole systems at low temperatures. *New J. Phys.*, 12:043003–1, 2010.

[14] M. Kugler, T. Andlauer, T. Korn, A. Wagner, S. Fehringer, R. Schulz, M. Kubová, C. Gerl, D. Schuh, W. Wegscheider, P. Vogl, and C. Schüller. Gate control of low-temperature spin dynamics in two-dimensional hole systems. *Phys. Rev. B*, 80:035325, 2009.

[15] R. Winkler. *Spin-Orbit Coupling Effects in Two-Dimensional Electron and Hole Systems*, volume 191 of *Springer Tracts in Modern Physics*. Springer-Verlag Berlin Heidelberg, 2003.

[16] M. Hirmer, M. Hirmer, D. Schuh, W. Wegscheider, T. Korn, R. Winkler, and C. Schüller. Fingerprints of the Anisotropic Spin-Split Hole Dispersion in Resonant Inelastic Light Scattering in Two-Dimensional Hole Systems. *Phys. Rev. Lett.*, 107:216805, 2011.

[17] B. Grbić, R. Leturcq, T. Ihn, K Ensslin, D. Reuter, and A. D. Wieck. Strong spin-orbit interactions and weak antilocalization in carbon-doped p-type GaAs/$Al_xGa_{1-x}As$ heterostructures. *Phys. Rev. B*, 77:125312, 2008.

[18] M. J. Manfra, E. H. Hwang, S. Das Sarma, L. N. Pfeiffer, K. W. West, and A. M. Sergent. Transport and Percolation in a Low-Density High-Mobility Two-Dimensional Hole System. *Phys. Rev. Lett.*, 99:236402, 2007.

[19] M. J. Manfra, R. de Picciotto, Z. Jiang, S. H. Simon, L. N. Pfeiffer, K. W. West, and A. M. Sergent. Impact of spin-orbit coupling on quantum Hall nematic phases. *Phys. Rev. Lett.*, 98:206804, 2007.

[20] M. J. Manfra, L. N. Pfeiffer, K. W. West, R. de Picciotto, and K. W. Baldwin. High mobility two-dimensional hole system in GaAs/AlGaAs quantum wells grown on (100) GaAs substrates. *Appl. Phys. Lett.*, 86:162106, 2005.

[21] C. Gerl. *Hochbewegliche zweidimensionale Lochsysteme in GaAs/AlGaAs Heterostrukturen*. PhD thesis, Univesity of Regensburg, 2009.

[22] P. M. Mooney. Deep donor levels (DX centres) in III-V semiconductors. *J. Appl. Phys.*, 67(3):R1, 1990.

[23] P. M. Mooney. Donor-related levels in GaAs and $Al_xGa_{1-x}As$. *Semicond. Sci. Technol.*, 6:B1, 1991.

[24] U. Wurstbauer, C. Sliwa, D. Weiss, T. Dietl, and W. Wegscheider. Hysteretic magnetoresistance and thermal bistability in a magnetic two-dimensional hole system. *Nature Physics*, 6:955, 2010.

[25] U. Wurstbauer. *Herstellung und Charakterisierung von Mangan dotierten III-V Halbleiterheterostrukturen.* PhD thesis, University of Regensburg, 2008.

[26] W. Wegscheider and D. Weiss. Vorlesungsskript Halbleiterphysik, University of Regensburg, 2006.

[27] T. Ihn. Halbleiter-Nanostrukturen, lecture notes, ETH Zurich, 2005.

[28] T. Ando. Theory of Quantum Transport in a Two-Dimensional Electron System under Magnetic Fields. IV. Oscillatory Conductivity. *J. Phys. Soc. Jpn.*, 37:1233, 1974.

[29] A. B. Fowler, F. F. Fang, W. E. Howard, and P. J. Stiles. Magneto-oscillatory conductance in silicon surfaces. *Phys. Rev. Lett.*, 16(20):901, 1966.

[30] F. F. Fang, A. B. Fowler, and A. Harstein. Effective mass and collision time of (100) Si surface electrons. *Phys. Rev. B*, 16(10):4446, 1977.

[31] D. Schneider, D. Rürup, A. Plichta, H. U. Grubert, A. Schlachetzki, and K. Hansen. Shubnikov-de Haas effect and effective mass in n-InP in dependence on carrier concentration. *Z. Phys. B*, 95:281, 1994.

[32] P. T. Coleridge, M. Hayne, P. Zawadzki, and A. S. Sachrajda. Effective masses in high-mobility 2D electron gas structures. *Surface Science*, 361/362:560, 1996.

[33] B. Habib, E. Tutuc, S. Melinte, M. Shayegan, D. Wasserman, S. A. Lyon, and R. Winkler. Spin splitting in GaAs (100) two-dimensional holes. *Physical Review B*, 69:113311, 2004.

[34] H. C. Manoharan, M. Shayegan, and S. J. Klepper. Signatures of a novel Fermi liquid in a two-dimensional composite particle metal. *Phys. Rev. Lett.*, 73:3270, 1994.

[35] S. Elhamri, R. S. Newrock, D. B. Mast, M. Ahoujja, W. C. Mitchel, J. M. Redwing, M. A. Tischler, and J. S. Flynn. $Al_{0.15}Ga_{0.85}N/GaN$ heterostructures: Effective mass and scattering times. *Phys. Rev. B*, 57(3):1374, 1998.

[36] P. T. Coleridge. Inter-subband scattering in a 2D electron gas. *Semicond. Sci. Technol.*, 5:961, 1990.

[37] P. T. Coleridge, R. Stoner, and R. Fletcher. Low-field transport coefficients in $GaAs/Ga_{1-x}Al_xAs$ heterostructures. *Phys. Rev. B*, 39(2):1120, 1989.

[38] J. Smet. Ballistischer Transport von Verbundfermionen in Halbleiternanostrukturen, Habilitation thesis, 1998.

[39] D. C. Tsui, H. L. Stormer, and A. C. Gossard. Two-Dimensional Magnetotransport in the Extreme Quantum Limit. *Phys. Rev. Lett.*, 48:1559, 1982.

[40] R. B. Laughlin. Anomalous Quantum Hall Effect: An Incompressible Quantum Fluid with Fractionally Charged Excitations. *Phys. Rev. Lett.*, 50:1395, 1983.

[41] J. K. Jain. Composite-fermion approach for the fractional quantum Hall effect. *Phys. Rev. Lett.*, 63:199, 1989.

[42] R. L. Willett. Experimental evidence for composite fermions. *Semicond. Sci. Technol.*, 12:495, 1997.

[43] R. R. Du, H. L. Stormer, D. C. Tsui, A. S. Yeh, L. N. Pfeiffer, and K. W. West. Drastic enhancement of composite fermion mass near Landau level filling $\nu = 1/2$. *Phys. Rev. Lett.*, 73:3274, 1994.

[44] H. L. Stormer. Nobel Lecture: The fractional quantum Hall effect. *Rev. Mod. Phys.*, 71:875, 1999.

[45] C. R. Dean. *A study of the fractional quantum Hall energy gap at half filling.* PhD thesis, McGill University, Montréal, Canada, 2008.

[46] E. Fradkin and S. A. Kivelson. Liquid-crystal phases of quantum Hall systems. *Phys. Rev. B*, 59:8065, 1999.

[47] R. R. Du, D. C. Tsui, H. L. Sotrmer, L. N. Pfeiffer, K. W. Baldwin, and K. W. West. Strongly anisotropic transport in higher two-dimensional Landau levels. *Solid State Commun.*, 109:389, 1999.

[48] M. P. Lilly, K. B. Cooper, J. P. Eisenstein, L. N. Pfeiffer, and K. W. West. Evidence for an anisotropic state of two-dimensional electrons in high Landau levels. *Phys. Rev. Lett.*, 82:394, 1999.

[49] A. G. Davies, R. Newbury, M. Pepper, J. E. F. Frost, D. A. Ritchie, and G. A. C. Jones. The fractional quantum Hall effect in high mobility two-dimensional hole gases. *Surface Science*, 263:81, 1992.

[50] J. P. Eisenstein, H. L. Stormer, L. Pfeiffer, and K. W. West. Evidence for a phase transition in the fractional quantum Hall effect. *Phys. Rev. Lett.*, 62(13):1540, 1989.

[51] R. G. Clark, S. R. Haynes, A. M. Suckling, J. R. Mallett, P. A. Wright, J. H. Harris, and C. T. Foxon. Spin configurations and quasiparticle fractional charge of fractional-quantum-Hall effect ground states in the $N = 0$ Landau level. *Phys. Rev. Lett.*, 62(13):1536, 1989.

[52] K. Muraki and Y. Hirayama. Spin transition of a two-dimensional hole system in the fractional quantum Hall effect. *Phys. Rev. B*, 59(4):R2502, 1999.

[53] N. d'Ambrumenil, B. I. Halperin, and R. H. Morf. Model for dissipative conductance in fractional quantum Hall states. *Phys. Rev. Lett.*, 106:126804, 2011.

[54] M. W. Wu, J. H. Jiang, and M. Q. Weng. Spin dynamics in semiconductors. *Physics Reports*, 493:61, 2010.

[55] O. Madelung, editor. *Semiconductors: group IV elements and III-V compounds*. Data in Science and Technology. Springer-Verlag Berlin Heidelberg, 1991.

[56] B. Jusserand, D. Richards, H. Peric, and B. Etienne. Zero-Magnetic-Field Spin Splitting in the GaAs Conduction Band from Raman Scattering on Modulation-Doped Quantum Wells. *Phys. Rev. Lett.*, 69(5), 1992.

[57] U. Rössler and J. Kainz. Microscopic interface asymmetry and spin-splitting of electron subbands in semiconductor quantum structures. *Solid State Communications*, 121:313, 2002.

[58] J. P. Lu, J. B. Yau, S. P. Shukla, M. Shayegan, L. Wissinger, U. Rössler, and R. Winkler. Tunable spin-splitting and spin-resolved ballistic transport in GaAs/AlGaAs two-dimensional holes. *Physical Review Letters*, 81(6):1282, 1998.

[59] R. Winkler. Rashba spin splitting in two-dimensional electron and hole systems. *Physical Review B*, 62(7):4245, 2000.

[60] B. Habib, E. Tutuc, S. Melinte, M. Shayegan, D. Wasserman, S. A. Lyon, and R. Winkler. Negative differential Rashba effect in two-dimensional hole systems. *Appl. Phys. Lett.*, 85(15):3151, 2004.

[61] R. Winkler, H. Noh. E. Tutuc, and M. Shayegan. Anomalous Rashba spin splitting in two-dimensional hole systems. *Phys. Rev. B*, 65:155303, 2002.

[62] A. Wong and F. Mireles. Spin Hall and longitudinal conductivity of a conserved spin current in two dimensional heavy-hole gases. *Phys. Rev. B*, 81:085304, 2010.

[63] T. Koga, J. Nitta, T. Akazaki, and H. Takayanagi. Rashba spin-orbit coupling probed by the weak antilocalization analysis in InAlAs/InGaAs/InAlAs quatum wells as a function of quantum well asymmetry. *Phys. Rev. Lett.*, 89(4):046801, 2002.

[64] S. Hikami, A. I. Larkin, and Y. Nagaoka. Spin-orbit interaction and magnetoresistance in the two dimensional random system. *Prog. Theor. Phys.*, 63(2):707, 1980.

[65] S. V. Iordanskii, Yu. B. Lyanda-Geller, and G. E. Pikus. Weak localization in quantum wells with spin-orbit interaction. *JETP Lett.*, 60:199, 1994.

[66] W. Knap, C. Skierbiszewski, A. Zduniak, E. Litwin-Staszewska, D. Bertho, F. Kobbi, J. L Robert, G. E. Pikus, F. G. Pikus, S. V. Iordanskii, V. Mosser, K. Zekentes, and Yu. B. Lyanda-Geller. Weak antilocalization and spin precession in quantum wells. *Phys. Rev. B*, 53(7):3912, 1996.

[67] W. Desrat, F. Giazotto, V. Pellegrini, M. Governale, and F. Beltram. Anticrossings of spin-split Landau levels in an InAs two-dimensional electron gas with spin-orbit coupling. *Phys. Rew. B*, 71:153314, 2005.

[68] L. E. Golub. Weak antilocalization in high-mobility two-dimensional systems. *Phys. Rev. B*, 71:235310, 2005.

[69] B. Grbic, C. Ellenberger, T. Ihn, K. Ensslin, D. Reuter, and A. D. Wieck. Magnetotransport in C-doped AlGaAs heterostructures. *Appl. Phys. Lett.*, 85:2277, 2004.

[70] T. M. Lu, Z. F. Li, D. C. Tsui, M. J. Manfra, L. N. Pfeiffer, and K. W. West. Cyclotron mass of two-dimensional holes in (100) oriented GaAs/AlGaAs heterostructures. *Appl. Phys. Lett.*, 92:012109, 2008.

[71] H. Zhu, K. Lai, D. C. Tsui, S. P. Bayrakci, N. P. Ong, M. Manfra, L. Pfeiffer, and K. West. Density and well width dependences of the effective mass of two-dimensional holes in (100) GaAs quantum wells measured using cyclotron resonance at microwave frequencies. *Solid State Communications*, 141:510, 2007.

[72] A. Kumar, N. Samkharadze, G. A. Csáthy, M. J. Manfra, L. N. Pfeiffer, and K. W. West. Particle-hole asymmetry of fractional quantum Hall states in the secon Landau level of a two-dimensional hole system. *Phys. Rev. B*, 83:201305(R), 2011.

[73] S. P. Koduvayur, Y. Lyanda-Geller, S. Khlebnikov, G. Csathy, M. J. Manfra, L. N. Pfeiffer, K. W. West, and L. P. Rokhinson. Effect of Strain on Stripe Phases in the Quantum Hall Regime. *Phys. Rev. Lett.*, 106:016804, 2011.

[74] B. Grbic, R. Leturcq, T. Ihn, K. Ensslin, D. Reuter, and A. D. Wieck. Aharonov-Bohm Oscillations in the Presence of Strong Spin-Orbit Interactions. *Phys. Rev. Lett.*, 99:176803, 2007.

[75] J. Wunderlich, B.-G. Park, A. C. Irvine, L. P. Zârbo, E. Rozkotová, P. Nemec, V. Novák, J. Sinova, and T. Jungwirth. Spin Hall effect transistor. *Science*, 330:1801, 2010.

[76] Ch. Heyn, S. Mendach, S. Löhr, S. Beyer, S. Schnüll, and W. Hansen. Growth of shallow InAs HEMTs with metamorphic buffer. *J. Cryst. Growth*, 251:832, 2003.

[77] F. Capotondi, G. Biasiol, I. Vobornik, L. Sorba, F. Giazotto, A. Cavallini, and B. Fraboni. Two-dimensional electron gas formation in undoped $In_{0.75}Ga_{0.25}As/In_{0.75}Al_{0.25}As$ quantum wells. *J. Vac. Sci. Tehcnol. B*, 22:702, 2004.

[78] F. Capotondi, G. Biasiol, D. Ercolani, V. Grillo, E. Carlino, F. Romanato, and L. Sorba. Strain induced effects on the transport properties of metamorphic InAlAs/InGaAs quantum wells. *Thin solid Films*, 484:400, 2005.

[79] A. Richter, M. Koch, T. Matsuyama, Ch. Heyn, and U. Merkt. Transport properties of modulation-doped InAs-inserted-channel $In_{0.75}Al_{0.25}As/In_{0.75}Ga_{0.25}As$ structures grown on GaAs substrates. *Appl. Phys. Lett.*, 77:3227, 2000.

[80] D. Ercolani, G. Biasiol, E. Cancellieri, M. Rosini, C. Jacoboni, F. Carillo, S. Heun, L. Sorba, and F. Nolting. Transport anisotropy in $In_{0.75}Ga_{0.25}As$ two-dimensional electron gases induced by indium concentration modulation. *Phys. Rev. B*, 77:235307, 2008.

[81] L. Sun, W. Zhou, G. Yu, L. Shang, K. Gao, Y. Zhou, T. Lin, L. Cui, Y. Zeng, and J. Chu. Strong spin-orbit interactions in a InAlAs/InGaAs/InAlAs two-dimensional electron gas by weak antilocalization analysis. *Jpn. J. Appl. Phys.*, 48:063004, 2009.

[82] F. Capotondi, G. Biasiol, D. Ercolani, and L. Sorba. Scattering mechanisms in undoped $In_{0.75}Ga_{0.25}As/In_{0.75}Al_{0.25}As$ two-dimensional electron gases. *Journal of Crystal Growth*, 278:538, 2005.

[83] D. Ercolani. *Transport properties of InGaAs based devices.* PhD thesis, University of Modena and Reggio Emilia, 2007.

[84] X. Li, K. F. Longenbach, and W. I. Wang. Observation of piezoelectric field induced carriers in AlGaAs/InGaAs strained-layer heterostructures. *Appl. Phys. Lett.*, 60:1513, 1992.

[85] U. Wurstbauer and W. Wegscheider. Magnetic ordering effects in a Mn-modulation-doped high mobility two-dimensional hole system. *Phys. Rev. B*, 79:155444, 2009.

[86] M. A. Herman and H. Sitter. *Molecular beam epitaxy - Fundamentals and current status.* Springer series in materials science 7. Springer-Verlag Berlin Heidelberg, second edition edition, 1996.

[87] J. Ehehalt. *Optimierung und optische Eigenschaften von Quantenstrukturen hergestellt durch Überwachsen von Spaltflächen.* PhD thesis, University of Regensburg, 2009.

[88] production company Veeco.

[89] M. Reinwald. *Herstellung und Charakterisierung von ferromagnetischem GaMnAs auf der GaAs(001)- und (311)A-Oberfläche*. PhD thesis, University of Regensburg, 2005.

[90] J. J. Heremans, M. B. Santos, K. Hirakawa, and M. Shayegan. Mobility anisotropy of two-dimensional hole systems in (311)A GaAs/$Al_xGa_{1-x}As$ heterojunctions. *J. Appl. Phys.*, 76(3):1980, 1994.

[91] S. V. Ivanov, P. S. Kop'ev, and N. N. Ledentsov. Interplay of beryllium segregation and diffusion in heavily doped GaAs ad AlGaAs grown by molecular beam epitaxy (thermodynamic analysis). *J. Cryst. Growth*, 108:661, 1991.

[92] N. Kobayashi, T. Makimoto, and Y. Horikoshi. Abrupt p-type doping profile of carbon atomic layer doped GaAs grown by flow-rate modulation epitaxy. *Appl. Phys. Lett.*, 50(20):1435, 1987.

[93] C. Gerl, J. Bauer, and W. Wegscheider. Growth and subband structure determination of high mobility hole gases on (001) and (110) GaAs. *J. Crystal Growth*, 301-302:145, 2007.

[94] R. J. Malik, R. N. Nottenberg, E. F. Schubert, J. F. Walker, and R. W. Ryan. Carbon doping in molecular beam epitaxy of GaAs from a heated graphite filament. *Appl. Phys. Lett.*, 53(26):2661, 1988.

[95] H. Ito and T. Ishibashi. Carbon Incorporation in (AlGa)As, (AlIn)As and (GaIn)As Ternary Alloys Grown by Molecural Beam Epitaxy. *Jap. J. Appl. Phys.*, 30:L944, 1991.

[96] M. Kamp, R. Contini, K. Werner, H. Heinecke, M. Weyers, H. Lüth, and P. Balk. Carbon incorporaion in MOMBE-grown $Ga_{0.47}In_{0.53}As$. *J. Cryst. Growth*, 95:154, 1989.

[97] M. Hirmer, D. Schuh, and W. Wegscheider. Carbon doped InAlAs/InGaAs/InAs heterostructures: Tuning from n- to p-doping. *Appl. Phys. Lett.*, 98:082103, 2011.

[98] M. Lohr. Strukturuntersuchung an InAlAs/InGaAs Heterostrukturen. Master's thesis, University of Regensburg, 2008.

[99] L. J. van der Pauw. A method of measuring specific resistivity and Hall effect of discs of arbitrary shape. *Philips Res. Repts.*, 13(1):1, 1958.

[100] University of Regensburg. Anleitung zum Fortgschrittenen-Praktikum, Der Quanten-Hall-Effekt.

[101] B. Hacker. Aufbau eines Messplatzes zur elektrischen Charakterisierung von GaMnAs bei Raumtemperatur. Master's thesis, University of Regensburg, 2010.

[102] M. Sexl. *Verspannte und gitterrelaxierte In(GaAl)As Heterostrukturen*. PhD thesis, Walter Shottky Institut, TU Munich, 1997.

[103] S. Birner, S. Hackenbuchner, M. Sabathil, G. Zandler, J. A. Majewski, T. Andlauer, T. Zibold, R. Morschl, A. Trellakis, and P. Vogl. Modeling of semiconductor nanostructures with nextnano^3. *Acta Physica Polonica A*, 110(2):111, 2006.

[104] C. Schüller. *Elektronische Ramanstreuung an p-dotierten GaAs/GaAlAs Quantentrogstrukturen*. PhD thesis, Julius Maximilian University Würzburg, 1994.

[105] http://www.nextnano.de/nextnano3/.

[106] C. Reichl. personal communication.

[107] M. Hirmer. Optimierung eines Annealingverfahrens zur Verbesserung der elektrischen und magnetischen Eigenschaften epitaktisch hergestellter GaMnAs Schichten. Master's thesis, University of Regensburg, 2007.

[108] J. D. Watson, S. Mondal, G. Gardner, G. A. Csáthy, and M. J. Manfra. The 19th international conference on Electronic Properties of Two-Dimensional Systems (EP2DS19),Tallahassee, Florida. 2011.

[109] M. J. Chou, D. C. Tsui, and G. Weimann. Negative photoconductivity of two-dimensional holes in GaAs/AlGaAs heterojunctions. *Appl. Phys. Lett.*, 47(6):609, 1985.

[110] W. Kraak, N. Ya. Minina, A. M. Savin, A. A. Ilievsky, I. V. Berman, and C. B. Sorensen. Persistent photoconductivity in p-type $Al_{0.50}Ga_{0.50}As/GaAs/Al_{0.50}Ga_{0.50}As$ heterostructures. *Nanotechnology*, 12:577, 2001.

[111] H. J. Queisser. Nonexponential relaxation of conductance near semiconductor interfaces. *Phys. Rev. Lett.*, 54(3):234, 1985.

[112] P. Krispin, R. Hey, and H. Kostial. Intrinsic origin and composition dependence of deep-level defects at the inverted $GaAs/Al_xGa_{1-x}As$ interface grown by molecular-beam epitaxy. *J. Appl. Phys.*, 77(11):5773, 1995.

[113] M. Grayson and F. Fischer. Measuring carrier density in parallel conduction layers of quantum Hall systems. *Journal of Applied Physics*, 98(013709), 2005.

[114] M. Hirmer. *Elektronische Ramna-Streuung und die Spin-Bahn-Wechselwirkung in p-dotierten GaAs/AlGaAs Quantentrögen*. PhD thesis, University of Regensburg, 2012.

[115] W. Nakwaski. Effective masses of electrons and heavy holes in GaAs, InAs, AlAs and their ternary compounds. *Physica B*, 210:1, 1995.

[116] G. S. Boebinger, A. M. Chang, H. L. Stormer, and D. C. Tsui. Magnetic Field Dependence of Activation Energies in the Fractional Quantum Hall Effect. *Phys. Rev. Lett.*, 55(15):1606, 1985.

[117] A. Hadzibrahimovic, A. F. Dethlefsen, D. Reuter, A. D. Wieck, H.-P. Tranitz, W. Wegscheider, and R. J. Haug. A comparison: 2D electron- and hole systems in the fractional quantum Hall regime. *Physica E*, 40:1258, 2008.

[118] M. Shayegan, H. C. Manoharan, S. J. Papadakis, and E. P. De Poortere. Anisotropic transport of two-dimensional holes in high Landau levels. *Physica E*, 6:40, 2000.

[119] S. H. Simon. Comment on "Evidence for an Anisotropic State of Two-Dimensional Electrons in High Landau Levels". *Phys. Rev. Lett.*, 83:4223, 1999.

[120] N. d'Ambrumenil. personal communication, 2011.

[121] L. Li, Y. Y. Proskuryakov, A. K. Savchenko, E. H. Linfield, and D. A. Ritchie. Magnetoresistance of a 2D electron gas caused by electron interactions in the trasition from the diffusive to teh ballistic regime. *Phys. Rev. Lett.*, 90(7):076802, 2003.

[122] Y. Y. Proskuryakov, A. K. Savchenko, S. S. Safonov, M. Pepper, M. Y. Simmons, and D. A. Ritchie. Hole-hole interaction effect in the conductance of the two-dimensional hole gas in the ballistic regime. *Phys. Rev. Lett.*, 89(7):076406, 2002.

[123] C. Mitzkus. *Transportuntersuchungen an dichtemodulierten zweidimensionalen Elektronensystemen.* PhD thesis, University of Regensburg, 2005.

[124] B. L. Altshuler and A. G. Aronov. *Electron-Electron Interactions in Disordered Systems.* Elsevier, Amsterdam, 1985.

[125] K. K. Choi, D. C. Tsui, and S. C. Palmateer. Electron-electron interactions in GaAs-$Al_xGa_{1-x}As$ heterostructures. *Phys. Rev. B*, 33:8216, 1986.

[126] I. V. Gornyi and A. D. Mirlin. Interaction-Induced Magnetoresistance: From the Diffusive to the Ballistic Regime. *Phys. Rev. Lett.*, 90(7):076801, 2003.

[127] I. V. Gornyi and A. D. Mirlin. Interaction-induced magnetoresistance in a two-dimensional electron gas. *Phys. Rev. B*, 69:045313, 2004.

[128] I. Vurgaftman, J. R. Meyer, and L. R. Ram-Mohan. Band parameters for III-V compound semiconductors and their alloys. *J. Appl. Phys.*, 89(11):5815, 2001.

[129] H. Föll. Semiconductor Skript, University of Kiel, 2007.

[130] S. Mendach, C. M. Hu, Ch. Heyn, S. Schnüll, H. P. Oepen, R. Anton, and W. Hansen. Strain relaxation in high-mobility InAs inserted-channel heterostructures with metamorphic buffer. *Physica E*, 13:1204, 2002.

[131] E. A. Fitzgerald, Y.-H. Xie, D. Monroe, P. J. Silverman, J. M. Kuo, A. R. Kortan, F. A. Thiel, and B. E. Weir. Relaxed Ge_xSi_{1-x} structures for III-V integration with Si and high mobility two-dimensional electron gases in Si. *J. Vac. Sci. Technol. B*, 10:1807, 1992.

[132] A. M. Noori, R. S. Sandhu, S. L. Hayashi, E. D. Meserole, V. Hardev, A. Cavus, M. Lange, C. Monier, R. Hsing, D. Sawdai, M. Wojtowicz, T. R. Block, A. Gutierrez-Aitken, and M. S. Goorsky. Strain relexation and surface roughness of $In_xAl_{1-x}As$ graded buffer layers grown on InP for 6.05 Å applications. *J. Vac. Sci. Technol. B*, 22:2303, 2004.

[133] K. H. Chang, R. Gibala, D. J. Srolovitz, P. K. Bhattacharya, and J. F. Mansfield. Crosshatched surface morphology in strained III-V semiconductor films. *J. Appl. Phys.*, 67:4093, 1990.

[134] J. A. Olsen, E. L. Hu, S. R. Lee, I. J. Fritz, A. J. Howard, B. E. Hammons, and J. Y. Tsao. X-ray reciprocal-space mapping of strain relaxation and tilting in linearly graded InAlAs buffers. *J. Appl. Phys.*, 79:3578, 1996.

[135] D. E. Jones, J. P. Pelz, Y. Hong, I. S. T. Tsong, Y.-H. Xie, and P. J. Silverman. Strain field imaging on Si/SiGe(001)-(2x1) surfaces by low-energy electron microscopy and scanning tunneling microscopy. *Appl. Phys. Lett.*, 69:3145, 1996.

[136] R. Beanland, M. Aindow, T. B. Joyce, P. Kidd, M. Lourenco, and P. J. Goodhew. A study of surface cross-hatch and misfit dislocation structure in $In_{0.15}Ga_{0.85}As$/GaAs grown by chemical beam epitaxy. *J. Cryst. Growth*, 149:1, 1995.

[137] S. Yu. Shiryaev, F. Jensen, and J. Wulff Petersen. On the nature of cross-hatch patterns on compositionally graded $Si_{1-x}Ge_x$ alloy layers. *Appl. Phys. Lett.*, 64:3305, 1994.

[138] A. M. Andrews, A. E. Romanov, J. S. Speck, M. Bobeth, and W. Pompe. Development of cross-hatch morphology during growth of lattice mismatched layers. *Appl. Phys. Lett.*, 77:3740, 2000.

[139] S. J. Pearton, U. K. Chakrabarti, C. R. Abernathy, and W. S. Hobson. Carbon implantation in InP. *Appl. Phys. Lett.*, 55:2014, 1989.

[140] J. J. Heremans, M. B. Santos, and M. Shayegan. Observation of magnetic focusing in two-dimensional hole systems. *Appl. Phys. Lett.*, 61:1652, 1992.

[141] R. Winkler, D. Culcer, S. J. Papadakis, B. Habib, and M. Shayegan. Spin orientation of holes in quantum wells. *Semiocond. Sci. Technol.*, 23:114017, 2008.

[142] V. N. Zverev, M. Muhammad, S. Rahman, P. Debray, M. Saglam, J. Sigmund, and H. L. Hartnagel. Magnetotransport properties of two-dimensional electron gas in AlSb/InAs quantum well structures designed for device applications. *J. Appl. Phys.*, 96(11):6353, 2004.

[143] I. B. Berkutov, V. V. Andrievskii, Yu. F. Komnik, O. A. Mironov, M. Mironov, and D. R. Leadley. Shubnikov-de Haas oscillations of the conductivity of a two-dimensional gas in quantum wells based on germanium and silicon. Determination of the effective mass and g factor. *Low Temp. Phys.*, 35(2):141, 2009.

[144] C. H. Möller, Ch. Heyn, and D. Grundler. Spin splitting in narrow InAs quatum wells with $In_{0.75}Ga_{0.25}As$ barrier layers. *Appl. Phys. Lett.*, 83:2181, 2003.

[145] G. M. Minkov, A. A. Sherstobitov, A. V. Germanenko, O. E. Rut, V. A. Larionova, and B. N. Zvonkov. Antilocalization and spin-orbit coupling in the hole gas in strained $GaAs/In_xGa_{1-x}As/GaAs$ quantum well heterostructures. *Phys. Rev. B*, 71:165312, 2005.

[146] S. Wind, M. J. Rooks, V. Chandrasekhar, and D. E. Prober. One-Dimensional Electron-Electron Scattering with Small Energy Transfers. *Phys. Rev. Lett.*, 57(5):633, 1986.

[147] J. J. Lin and J. P. Bird. Recent experimental studies of electron dephasing in metal and semiconductor mesoscopic structures. *J. Phys.: Condens. Matter*, 14:R501, 2002.

[148] K. K. Choi, D. C. Tsui, and K. Alavi. Dephasing time and one-dimensional localization of two-dimensional electrons in $GaAs/Al_xGa_{1-x}As$ heterostructures. *Phys. Rev. B*, 36(14):7751, 1987.

[149] J. J. Lin. Inelastic electron dephasing scattering times in disordered metals. *Physica B*, 279:191, 2000.

[150] T. Kawamura and S. Das Sarma. Temperature dependence of the low-temperature mobility in ultrapure $Al_xGa_{1-x}As/GaAs$ heterojunctions: Acoustic-phonon scattering. *Phys. Rev. B*, 42:3725, 1990.

[151] Y. Yaish, O. Prus, E. Buchstab, G. B. Yoseph, U. Sivan, I. Ussishikin, and A. Stern. Two band transport and the question of a metal-insulator transition in GaAs/GaAlAs two dimensional holes. *arXiv:cond-mat/0109469v1*, 2001.

[152] S. A. Studenikin, P. T. Coleridge, N. Ahmed. P. J. Poole, and A. Sachrajda. Experimental study of weak antilocalization effects in a high-mobility $In_xGa_{1-x}As$/InP quantum well. *Phys. Rev. B*, 68:035317, 2003.

[153] S. Knott, T. Ch. Hirschmann, U. Wurstbauer, W. Hansen, and W. Wegscheider. Magnetoresistance effects and phase coherent transport phenomena in a magnetic nonplanar two-dimensional hole system. *Phys. Rev. B*, 84:205302, 2011.

[154] G. M. Minkov, A. V. Germanenko, O. E. Rut, A. A. Sherstobitov, L. E. Golub, B. N. Zvonkov, and M. Willander. Weak antilocalization in quatum wells in tilted magnetic fields. *Phys. Rev. B*, 70:155323, 2004.

[155] N. H. Thillosen. *Spin-Bahn-Wechselwirkung in niedrigdimensionalen $Al_xGa_{1-x}N$/GaN-Elektronengasen.* PhD thesis, RWTH Aachen University, 2006.

[156] S. Weishäupl. Phasenkohärente Effekte in InAs:Mn. Master's thesis, University of Regensburg, 2010.

[157] A. D. Mirlin, D. G. Polyakov, F. Evers, and P. Wölfle. Quasiclassical negative magnetoresistance of a 2D electron gas: interplay of strong scatterers and smooth disorder. *Phys. Rev. Lett.*, 87:126805, 2001.

[158] A. F. Brana, C. Diaz-Paniagua, F. Batallan, J. A. Garrido, E. Munoy, and F. Omnes. Scattering times in AlGaN/GaN two-dimensional electron gas from magnetoresistance measurements. *J. Appl. Phys.*, 88:932, 2000.

[159] M. A. Paalanen, D. C. Tsui, and J. C. M. Hwang. Parabolic magnetoresistance from the interaction effect in a two-dimensional electron gas. *Phys. Rev. Lett.*, 51:2226, 1983.

[160] S. Gozu, T. Kita, Y. Sato, S. Yamada, and M. Tomizawa. Characterization of high indium content metamorphic InGaAs/InAlAs modulation-doped heterostructures. *J. Cryst. Growth*, 227-228:155, 2001.

[161] P. Ramvall, N. Carlsson, P. Omling, L. Samuelson, W. Seifert, M. Stolze, and Q. Wang. $Ga_{0.25}In_{0.75}As$/InP quantum wells with extremely high and anisotropic two-dimensional electron gas mobilities. *Appl. phys. Lett.*, 68:1111, 1996.

[162] P. Ramvall, N. Carlsson, P. Omling, L. Samuelson, W. Seifert, Q. Wang, K. Ishibashi, and Y. Aoyagi. Quantum transport in high mobility modulation doped $Ga_{0.25}In_{0.75}$/InP quantum wells. *J. Appl. Phys.*, 84:2112, 1998.

[163] A. Gold. Scattering time and single-particle relaxation time in a disordered two-dimensional electron gas. *Phys. Rev. B*, 38:10798, 1988.

[164] J. C. P. Chang, J. Chen, J. M. Fernandez, H. H. Wieder, and K. L. Kavanagh. Strain relaxation of compositionally graded $In_xGa_{1-x}As$ buffer layers for modulation-doped $In_{0.3}Ga_{0.5}As/In_{0.29}Al_{0.71}As$ heterostructures. *Appl. Phys. Lett.*, 60:1129, 1992.

[165] R. S. Goldman, H. H. Wieder, K. L. Kavanagh, K. Rammohan, and D. H. Rich. Anisotropic structural, electronic, and optical properties of InGaAs grown by molcular beam epitaxy on misoriented substrates. *Appl. Pys. Lett.*, 65:1424, 1994.

[166] S. Löhr, S. Mendach, T. Vonau, Ch. Heyn, and W. Hansen. Highly anisotropic electron transport in shallow InGaAs heterostructures. *Phys. Rev. B*, 67:045309, 2003.

[167] K. Rammohan, D. H. Rich, R. S. Goldman, J. Chen, H. H. Wieder, and K. L. Kavanagh. Study of μm-scale spatial variations in strain of a compositionally step-graded $In_xGa_{1-x}As/GaAs(001)$ heterostructure. *Appl. Phys. Lett.*, 66:869, 1995.

[168] I. A. Larkin, J. H. Davies, A. R. Long, and R. Cuscò. Theory of potential modulation in lateral suface superlattices. II. Piezoelectric effect. *Phys. Rev. B*, 56:15242, 1997.

[169] P. M. Asbeck, C.-P. Lee, and M.-C. F. Chang. Piezoelectric effects in GaAs FET's and their role in orientation-dependent device characteristics. *IEEE Transactions on Electron Devices*, 31:1377, 1984.

[170] D. N. Quang, V. N. Tuoc, and T. D. Huan. Roughness-induced piezoelectric scattering in lattice-mismatched semiconductor quantum wells. *Phys. Rev. B*, 68:195316, 2003.

[171] Y. Kanda and A. Yasukawa. Hall-effect devices as strain and pressure sensors. *Sensors and Actuators*, 2:283, 1982.

[172] J. Sailer, A. Wild, V. Lang, A. Siddiki, and D. Bougeard. Quantum Hall resistance overshoot in two-dimensional (2D) electron gases: theory and experiment. *New J. Phys.*, 12:113033, 2010.

[173] U. Wurstbauer, M. Soda, R. Jakiela, D. Schuh, D. Weiss, J. Zweck, and W. Wegscheider. Coexistence of ferromagnetism and quantum Hall effect in Mn modulation-doped two-dimensional hole systems. *J. Cryst. Growth*, 311:2160, 2009.

[174] R. Schulz, T. Korn, D. Stich, U. Wurstbauer, D. Schuh, W. Wegscheider, and C. Schüller. Ultrafast optical studies of diffusion barriers between ferromagnetic Ga(Mn)As layers and non-magnetic quantum wells. *Physica E*, 40:2163, 2008.

[175] R. Schulz. *Optische Spektroskopie an zweidimensionalen Lochsystemen in GaAs/AlGaAs-quantenwells und an GaAs/AlGaAs/GaMnAs Schichtstrukturen*. PhD thesis, University of Regensburg, 2010.

[176] R. Winkler, S. J. Papadakis, E. P. De Poortere, and M. Shayegan. Anomalous Magneto-Oscillations in Two-Dimensional Systems. *Physical Review Letters*, 84(4):713, 2000.

[177] J. Bauer. Transporteigenschaften zweidimensionaler Lochsysteme. Master's thesis, University of Regensburg, 2006.

Publications

Carbon doped InAlAs/InGaAs/InAs heterostructures: Tuning from n- to p-doping
M. Hirmer, D. Schuh, and W. Wegscheider
Applied Physics Letters **98**, 082103 (2011)

Fingerprints of the anisotropic Rashba spin-split hole dispersion in resonant inelastic light scattering on two-dimensional hole systems
M. Hirmer, M. Hirmer, T. Korn, D. Schuh, W. Wegscheider, R. Winkler, and C. Schüller
Physical Review Letters **107**, 216085 (2011)

Spin dynamics in two-dimensional electron and hole systems revealed by resonant spin amplification
T. Korn, M. Griesbeck, M. Kugler, S. Furthmeier, C. Grandl, M. Hirmer, D. Schuh, W. Wegscheider, K. Korzekwa, P. Machnikowski, T. Kuhn, M. M. Glazov, E. Ya. Sherman, C. Schüller
Proc. SPIE **8461**, Spintronics V, 84610O (2012)

Inelastic light scattering of hole spin excitations in p-modulation-doped GaAs-AlGaAs single quantum wells
M. Hirmer, M. Hirmer, T. Korn, D. Schuh, W. Wegscheider, R. Winkler, and C. Schüller
Proc. SPIE **8100**, 81000N (2011)

Decoherence-assisted initialization of a resident hole spin polarization in a p-doped semiconductor quantum well
M. Kugler, K. Korzekwa, P. Machnikowski, C. Gradl, S. Furthmeier, M. Griesbeck, M. Hirmer, D. Schuh, W. Wegscheider, T. Kuhn, C. Schüller, and T. Korn
Physical Review B **84**, 085327 (2011)

Optical polarization of localized hole spins in p-doped quantum wells
M. Studer, M. Hirmer, D. Schuh, W. Wegscheider, K. Ensslin, and G. Salis
Physical Review B **84**, 085328 (2011)

Engineering ultralong spin coherence in two-dimensional hole systems at low temperatures
T. Korn, M. Kugler, M. Griesbeck, R. Schulz, A. Wagner, M. Hirmer, C. Gerl, D. Schuh, W. Wegscheider, and C. Schüller
New Journal of Physics **12**, 043003 (2010)

Gate control of low-temperature spin dynamics in two-dimensional hole systems
M. Kugler, T. Andlauer, T. Korn, A. Wagner, S. Fehringer, R. Schulz, M. Kubová, C. Gerl, D. Schuh, W. Wegscheider, P. Vogl, and C. Schüller
Physical Review B **80**, 035325 (2009)

Acknowledgement

My best thanks go to my supervisor Prof. Dr. Werner Wegscheider for giving me the opportunity to perform my PhD research on the MBE growth and for his kind support all the time. Special thanks go to Prof. Dr. Dieter Weiss for accepting to be a co-examiner of my PhD thesis and for the interesting discussions. My great thanks go to Prof. Dr. Dominique Bougeard for the stimulating discussions and the amount of time, which they have cost, and Dr. Dieter Schuh for his readiness to the discussions and technical support. I would like to thank following people and groups:

- Prof. Dr. Dieter Weiss for the opportunity to use his clean room and dilution refrigerator and the people from his group (especially Sabine Weishäupl, Dieter Vogel, Christian Betthausen, Cornelia Linz, Claudia Rahm, Uli Gürster) for the kind collaboration in the laboratory.

- Prof. Dr. Dominique Bougeard for giving me the chance to do my measurements on ^{3}He cryostat, spectromag in his group on Walter Schottky Institute in Munich and his WSI team for the technical support.

- the team of Prof. Dr. Werner Wegscheider on ETH Zurich for stimulating discussions and technical support.

- the people from our group at University of Regensburg: our secretaries Annemarie Dinkel and Renate Creuzburg for the support in administration tasks; Martin Utz for X-ray diffraction measurements; Imke Gronwald for AFM pictures; Jörg Ehehalt for the nextnano^3 support; and the whole group for exciting and pleasant working atmosphere.

- Prof. Dr. Christian Schüller, Dr. Tobias Korn and the whole group for discovering new applications for my samples, for large number of joint publications coming out and for their permanent readiness to discuss the results.

- Prof. Dr. Wolfgang Hansen and Dr. Ursula Wurstbauer for inviting me to present and discuss my results with them.

- Prof. Dr. Roland Winkler and Dr. Nicholas d'Ambrumenil for the theoretical simulations on the interesting field of activated transport of FQH states.

I am grateful to the Dominique, Elisabeth, Tobias, Michael H., and Robert for the proofreading and Michael K., Michael G., Roland and Pamela for

English corrections. Last and most I want to thank my husband for its constructive suggestions and his never-ending patience.